

Mitigation of Wind-Induced Vibrations in Long-Span Bridges using a Distributed Flap System

THÈSE N° 7069 (2016)

PRÉSENTÉE LE 19 AOÛT 2016

À LA FACULTÉ DE L'ENVIRONNEMENT NATUREL, ARCHITECTURAL ET CONSTRUIT
LABORATOIRE DE SYSTÈMES ET ALGORITHMES INTELLIGENTS DISTRIBUÉS
PROGRAMME DOCTORAL EN ROBOTIQUE, CONTRÔLE ET SYSTÈMES INTELLIGENTS

ÉCOLE POLYTECHNIQUE FÉDÉRALE DE LAUSANNE

POUR L'OBTENTION DU GRADE DE DOCTEUR ÈS SCIENCES

PAR

Klara Maria BOBERG

acceptée sur proposition du jury:

Dr D. Gillet, président du jury
Prof. A. Martinoli, Dr G. Feltrin, directeurs de thèse
Dr A. Larsen, rapporteur
Prof. N. Correll, rapporteur
Prof. K. Beyer, rapporteuse



ÉCOLE POLYTECHNIQUE
FÉDÉRALE DE LAUSANNE

Suisse
2016



Acknowledgements

This thesis could not have been completed without the help and support of many kind and wise people. First of all I would like to thank my advisers Alcherio Martinoli and Glauco Feltrin for giving me the opportunity to come to Lausanne for a PhD, and for guiding me through this experience. Furthermore, I am very grateful to my thesis committee: Dr. Denis Gillet, Prof Katrin Beyer, Prof. Nikolaus Correll, and Dr. Allen Larsen, for taking their time to review this work and for providing valuable feedback. I am much obliged to have had the pleasure to work with several excellent students. Nicolò Valigi stayed one summer and helped me getting familiar with the different anemometers we have available in the wind tunnel. Vincent Mazoyer, was a very hard working semester student, who helped me by evaluating the prototype flap, and contributed with many insightful suggestions for improving the design. Tiago Morais, was a creative student who on his own accord brought a sewing machine into the wind tunnel facilities. Furthermore, I am very grateful to our lab engineer, Emmanuel Droz, who have provided design suggestions for the SmartBridge, and have been a valuable support when things go wrong in the wind tunnel (and they do). Furthermore, I much enjoyed working with our former lab engineer, Pascal Gilbert, for the short time that our contracts overlapped. I am also grateful to have worked next to the formidable Corinne Farquharson and Denis Rochat, who have helped me with many administrative and technical issues. My former and current colleagues at DISAL are like family. They have really made working here for the last couple of years an amazing experience. My fellow PhD students and postdocs (in order of appearance): Thomas Lochmatter, Grégory Mermoud, Amanda Prorok, Sven Goyal, Alexander Bahr, Chris Evans, Adrian Arfire, Ezequiel Di Mario, José Nuno Pereira, Steven Roelofsen, Miloš Vasić, Bahar Haghighat, Jorge Soares, Duarte Dias, Zeynab Talebpour, Ali Marjovi, Felix Schill, Iñaki Navarro, Alicja Wasik, Anwar Quraishi, and Faezeh Rabhar. Thank you for all the lunches, coffee breaks, discussions, game nights, dinners, beers, festivals, and travels; I couldn't have had a greater time!

My deepest gratitude goes out to my family who have supported me in so many ways. My mother Sonja whose kindness and love has helped not only me, but also my son, through many intense work periods, and my father Lasse has also been a wholehearted supporter of mine. I would also like to thank my extended family, Yvonne and Christer, who have been a tremendous help, whenever the most needed. I am eternally grateful to my fiancée, Daniel, and our wonderful son, Oskar. Your love and support carried me through. Thank you for your patience.

Lausanne, 16 May 2016

Maria Boberg



Abstract

Since the collapse of the Tacoma Narrows Bridge more than 75 years ago suppressing wind-induced instabilities has been a key aspect of the design of long-span bridges. The intensive experimental and theoretical research in wind engineering allowed researchers and practitioners to not only understand the physics of aeroelastic instability phenomena such as flutter, but also to develop reliable testing procedures, models, and design rules for preventing these instabilities during the lifetime of a bridge. As a consequence, the civil engineering community has adopted a series of design standards for wind effect mitigation of long-span bridges typically called passive measures. A passive solution, although safe in respect to wind perturbations, is intrinsically a static compromise for a dynamic system response to a variable and uncertain perturbation and as such it implies numerous limitations. Therefore, in the last two and a half decades researchers have investigated active measures for preventing aeroelastic instabilities, especially flutter. The underlying motivation is that an active damping mechanism can adapt to dynamic wind and structure conditions and has therefore the potential of being more efficient than a passive solution despite its higher complexity and cost. One of the most investigated and potentially highly effective active measures to enhance the flutter performance of bridges is to endow their decks with arrays of movable flaps.

The overall aim of this dissertation is to investigate, experimentally as well as theoretically, the feasibility and effectiveness of an intelligent, distributed flap system for enhancing the flutter performance of long-span bridges. The main contributions of this thesis are three-fold. First, we have designed a unique, dedicated, experimental setup consisting of a bridge section model, endowed with actively controlled flap arrays, as well as all the necessary instrumentation for measuring and perturbing the system states under controlled wind conditions, in a boundary layer wind tunnel. Secondly, we have developed an analytical model, building on top of theoretical frameworks commonly used in civil engineering for long-span bridges, and in aeronautics for wings equipped with ailerons and tabs. We have systematically evaluated the theoretical model effort with wind tunnel experiments. Thirdly, we leveraged our experimental setup and analytical model in order to thoroughly investigate different flap control coordination strategies, an unprecedented study that we are uniquely equipped for.

Key words: Mitigation of Wind-Induced Vibrations; Wind-Structure Interaction; Active Flutter Control; Distributed Flap System.



Résumé

Depuis l'effondrement du pont du détroit de Tacoma il y a plus de 75 ans, la suppression des instabilités causé par le vent est un aspect clé pour la conception des ponts suspendus. La recherche intensive en ingénierie du vent, à la fois expérimentale et théorique, a permis au chercheurs et praticiens de non seulement comprendre la physique des phénomènes aéroélastiques instables telle que le flottement, mais aussi à développer des procédures de teste fiables, des modèles et des règles de conception afin de prévenir ces instabilités pour toute la durée de vie du pont. En conséquence, la communauté du génie civil a adopté une série de standards de conception pour l'atténuation des effets du vent pour les ponts suspendus, appelé typiquement mesures passives. Nonobstant la fiabilités des mesures passives du point de vu des perturbations dues au vent, elles sont intrinsèquement un compromis statique pour une réponse dynamique d'un système variable et des perturbations incertaines, ce qui implique de nombreuses limitations. Pour cette raison, durant les deux dernières décennies, des chercheurs ont examiné la possibilité de mesures actives pour prévenir les instabilités aéroélastiques, en particulier le flottement. La motivation sous-jacente est qu'un mécanisme d'amortissement active peut s'adapter au dynamiques du vent et conditions structurelles et a donc un le potentiel d'être plus efficient que les mesures passives malgré un coût et une complexité plus élevés. Une des mesures actives les plus examinées et potentiellement hautement efficace pour améliorer la performance des ponts vis-à-vis du flottement est de doter leur tablier de séries de volets. L'objectif global de cette thèse est examiner, à la fois de façon expérimental et théorique, la faisabilité et l'efficacité d'un système distribué et intelligent de volets pour améliorer la performance des ponts suspendus vis-à-vis du flottement. La contribution de cette thèse est triple. Premièrement, nous avons conçu une installation expérimentale dédiée unique, consistant en un modèle réduit de la section d'un pont, doté de deux séries de volets contrôles activement, de même que tout les instruments de mesures et éléments pour perturber l'état du système, le tout installé dans une soufflerie à couche limite dont les conditions du vents peuvent être contrôlé. Deuxièmement, nous avons développé un modèle analytique, construit à partir de cadres théorique communément utilisé, soit par le génie civil pour la conception de ponts à longue portée, soit par l'aéronautique dans le cas d'ailes dotés d'ailerons ou de volets. Nous avons systématiquement évalué nos modèles théoriques avec des expériences en soufflerie. Troisièmement, nous avons utilisé notre installation expérimentale et nos modèles analytiques pour minutieusement étudier différentes stratégies de contrôle et de coordination des volets, une étude pour lequel nous sommes seuls capable de réaliser grâce à notre équipement unique.

Acknowledgements

Mots clefs : Atténuation de vibrations induit par le vent ; interaction vent-structure ; contrôle actif du flottement ; contrôle de volet distribué.

Contents

Acknowledgements	i
Abstract (English/Français)	iii
I Introduction	1
1 Problem Statement	3
1.1 Long-Span Bridges and Aeroelastic Instabilities	3
2 Related Work	7
2.1 Structural Methods	7
2.1.1 Static Structural Methods	7
2.1.2 Mobile Structural Methods	8
2.2 Aerodynamic Methods	9
2.2.1 Static Aerodynamic Methods	9
2.2.2 Mobile Aerodynamic Methods	9
3 Scope of the Thesis	13
3.1 Objectives and Outline	13
3.2 Contributions	14
3.2.1 Contributions of Predecessors and Collaborators	16
II Mechatronic Design	19
4 Related Work	21
4.1 Physical Bridge Models for Wind Tunnel Testing	21
4.1.1 Section Models Equipped with Mobile Flaps	21
4.1.2 Sensing Systems for Section Models	24
4.1.3 Perturbing Techniques for Section Models	25
4.2 Concluding Remarks	25
5 Hardware Development and Experimental Site	27
5.1 Design of an Active Bridge Section Model	27
5.1.1 Deck Design	27
	vii

Contents

5.1.2	Deck Anchoring and Support Structure	29
5.1.3	Flap Design	32
5.1.4	Sensing Capabilities and Embedded System Architecture	35
5.1.5	User Interface	38
5.2	Experimental Site	38
6	Characterizing a Single Flap	43
6.1	Premise	43
6.1.1	Material and Methods	44
6.2	Model Design	44
6.2.1	The Plant: DC Motor and Flap	45
6.2.2	PID Position Control	46
6.2.3	Modeling External Forces	46
6.3	Model Validation	49
6.3.1	Plant Model	49
6.3.2	Gravity Model	50
6.3.3	Wind Model	50
6.3.4	Overall System Model	51
6.4	Tuning Control Parameters	51
6.5	Evaluation of Results	53
7	Conclusion	55
III	Model	57
8	Related Work	59
8.1	Historical View of Flutter	59
8.2	Two-Dimensional Analytical Model of Bridge Flutter	60
8.2.1	Aerodynamic Model of a Deck with Mobile Flaps	60
8.2.2	Structural Dynamics of a Deck with Mobile Flaps	60
8.2.3	Experimental Validation of Analytical Models of Controlled Decks . . .	61
8.3	Other Modeling Techniques for a Deck with Mobile Flaps	62
8.3.1	Multi-Mode Analytical Model	62
8.3.2	Numerical Models	62
8.4	Concluding Remarks	63
9	Two-Dimensional Analytic Flutter Model	65
9.1	Flutter Model of a Canonical Bridge Deck	65
9.1.1	Structural Model	65
9.1.2	Aerodynamic Model	66
9.2	Flutter Model of a Bridge Deck Endowed with Flaps	67
9.2.1	Structural Model	68

9.2.2	Aerodynamic Model	68
9.3	Estimating the Flutter Wind Speed	70
9.3.1	The Flutter Condition	70
9.3.2	Theodorsen's Method for the Canonical Bridge Deck	71
9.3.3	Theodorsen's Method Extended for Bridge Deck with Flaps	73
9.4	Simplified Approaches for Estimating the Flutter Condition	75
10	System Identification of Model Parameters from Wind Tunnel Experiments	79
10.1	Experimental Premise	79
10.2	System Identification Method	81
10.2.1	Selecting Experimental Data	84
10.2.2	Filtering Experimental Data	85
10.3	Identifying Structural Model Parameters	85
10.3.1	Results for the Uncontrolled Deck	85
10.3.2	Results for the Controlled Deck	88
10.4	Identifying Aerodynamic Model Parameters	92
10.4.1	Results for the Uncontrolled Deck	92
10.4.2	Results for the Controlled Deck	93
10.5	Estimation of the flutter wind speed	100
10.5.1	Determining the Flutter Wind Speed Experimentally	102
10.5.2	Flutter Condition for the Implemented Control Configuration	103
10.5.3	Experimental Verification of Flutter Condition for Different Phase-Shifts	104
10.6	Model Reduction	105
10.6.1	Canonical Deck	105
10.6.2	Controlled Deck	107
11	Conclusion	111
IV	Control	113
12	Related Work	115
12.1	Passively Controlled Mobile Flaps	115
12.1.1	Experimental Studies	115
12.1.2	Theoretical Studies	116
12.2	Actively Controlled Mobile Flaps	116
12.2.1	Experimental Studies	116
12.2.2	Theoretical Studies	117
12.3	Concluding Remarks	118
13	Technical Approach	119
13.1	Control of the Section Model	119
13.1.1	The Section Model in the Third Dimension	119

Contents

13.1.2 Synchronized and Decentralized Control Strategies	120
13.1.3 Performance Metrics	122
13.2 Experimental Scenarios	124
13.2.1 Asymmetric Deck	125
13.2.2 Modifying the Wind Profile	126
14 Synchronized Flap Control	133
14.1 Synchronized Control: Flap Combinations along the X-Axis	133
14.1.1 Theoretical Analysis	134
14.1.2 Wind Tunnel Experiments	136
14.2 Synchronized Control: Flap Combinations along the Y-Axis	139
14.2.1 Varied Actuation Rate in Normal Wind Conditions	141
14.2.2 Varying Controlled Flap Coverage for a Nonuniform Wind Profile	143
15 Decentralized Flap Control	147
15.1 Control Law Comparison in Normal Wind Conditions	147
15.1.1 Decentralized vs. Synchronized Control: Baseline	147
15.1.2 Asymmetric Aerodynamic Profile of the Deck	149
15.1.3 Decentralized vs. Synchronized Control: Flap Combinations	149
15.2 Control Law Comparison for Nonuniform Wind Profiles	151
15.2.1 Funnel Perturbation	151
15.2.2 Ramp Perturbation	153
16 Conclusion	155
V Conclusion	159
17 Conclusion	161
17.1 Summary	161
17.2 Discussion and Outlook	163
A Solution of the Flutter Equations	165
B Expressing Flap Positions in the Form of the Bridge State	173
Bibliography	177
Curriculum Vitae	185

Introduction Part I

1 Problem Statement

AROUND 10'000 BC, mankind started to abandon the hunter-gatherer lifestyle in favor for a sedentary culture; building houses, villages and eventually cities. What was true then, and also today, is that these buildings and infrastructure were built not only to facilitate our everyday lives but also to protect us from the surrounding environment. It is a very compelling idea that we instead create structures that profit from, rather than endures, the environment. However, the conditions around us are constantly changing; seasonally, daily, hourly, or even by the second. The traditional static architecture can possibly profit in a specific situation, but is unable to adapt to a changing environment. This is where a dynamic architecture can make the difference. Wind is one element that has traditionally been considered mainly a safety risk in civil engineering. Meanwhile, in many other fields, such as aerospace and wind engineering, it has been utilized for its energy potential. This begs the question if we can somehow benefit from the wind also in the civil engineering case? The research conducted in this thesis has been towards the realization of a smart bridge that is capable of not only enduring its environment, but also using the wind force to its advantage.

1.1 Long-Span Bridges and Aeroelastic Instabilities

Long-span bridges are particularly vulnerable to wind loads, owing to their inherently low structural damping, low natural frequencies and adjacent fundamental torsional and vertical mode frequencies. This leads to wind-induced instabilities causing potential damage to the whole structure. Bridges are typically subdued to several aeroelastic phenomena such as flutter, divergence and buffeting. Flutter is the most critical wind-induced oscillation, for instance, it was the cause of the Tacoma Narrows Bridge collapse in the 1940's [1]. This catastrophic event is well-documented, and a photograph capturing the collapse can be seen in Figure 1.1. Ever since the collapse of the Tacoma Narrows Bridge suppressing wind-induced instabilities has been a key aspect of the design of long-span bridges. The intensive experimental and theoretical research in wind engineering allowed researchers and practitioners to not only



Figure 1.1 – The collapse of the Tacoma Narrows Bridge [3].

understand the physics of aeroelastic instability phenomena such as flutter but also to develop reliable testing procedures, models, and design rules for preventing these instabilities during the lifetime of a bridge. As a consequence, the civil engineering community has adopted a series of design standards for wind effect mitigation of long-span bridges. Most solutions for this problem deployed on real bridges are passive elements [2]. A passive solution, although safe in respect to wind perturbations, is intrinsically a static compromise for a dynamic system response to a variable and uncertain perturbation and as such it implies numerous limitations. An active vibration mitigation mechanism can adapt to dynamic wind and structure conditions and has therefore the potential of being more efficient than a passive solution despite its higher complexity and cost. One possible active solution is to install multiple mobile flaps along the bridge girder in order to alter its aerodynamic profile, enabling stabilizing forces on the structure, a concept illustrated in Fig. 1.2. Furthermore, the angular positions of the adjustable flaps are controlled as a function of the wind field and/or the displacement of the structure whose dynamic state can be measured with an underlying sensor network.

Although wind tunnel experiments using single-flap bridge section models have demonstrated their feasibility and effectiveness, up to date no effort has been undertaken to implement active flaps on real bridges. High complexity, low reliability, and high implementation and maintenance costs are some of the typical reasons having discouraged their implementation. In the near future, this situation will change. First, the continuous progress in sensor, actuator, and embedded computation technology will enable to manufacture self-contained, modular mechatronic devices showing an unprecedented degree of reliability and affordability thus significantly reducing the barriers for a large-scale deployment on real bridges. Second, recent research outcomes in the robotics, mechatronics, and automatic control communities provide examples of successful distributed control strategies that are able to coordinate large number of sensor-actuator systems to achieve a specific objective under the presence of noisy, real-world conditions.

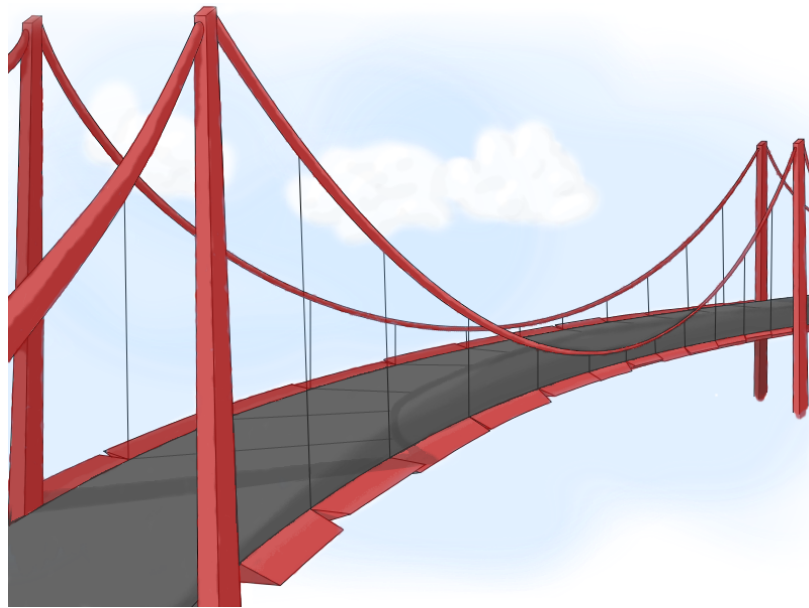


Figure 1.2 – Conceptual figure of the multi-flap wind mitigation strategy.

An actively controlled bridge deck has the potential to push the envelope of the physical limit inherent to the main span length of suspension bridges of today. For instance, allowing bridges to be built across huge distances that are currently not possible, such as the Messina Strait Bridge, or the impressive endeavor to connect Europe and Africa over the Gibraltar Strait. Furthermore, the advantages of an actively controlled bridge deck is not limited to the pursuit of longer bridge spans. Reducing the vibrations of the bridge deck would naturally lessen the fatigue of a bridge also for regular sized spans, and thus cut down the maintenance costs.

The overall aim of this thesis has been to investigate, experimentally as well as theoretically, the feasibility and effectiveness of an intelligent, distributed flap system for enhancing the flutter performance of long-span bridges. Although being outside the scope of this thesis, such a flap-based mitigation system could be considered not only for mitigating further wind-induced phenomena in long-span bridges (e.g., torsional divergence, buffeting) but also for a deployment on many types of long and slender structures that are typically vulnerable to wind-induced vibrations, such as towers or tall buildings.

Summary

In this chapter we introduce the topic of this thesis: active flutter control of long-span bridges enabled by flap arrays along the deck girder. We provide a short introduction to the sensitivity to aeroelastic instabilities inherent to bridge decks. In the following chapter we will further introduce the related work within vibration control of long-span bridges.

2 Related Work

INCREASING the flutter wind speed of a long-span bridge can be achieved by improving the total, structural and aerodynamic, stiffness and/or damping [1]. Several different methods have been developed ever since the Tacoma Narrows Bridge collapsed. One can categorize these methods into two groups: structural and aerodynamic methods. On an orthogonal axis, these methods can be further categorized as static or mobile, depending on whether the components are completely static and anchored to the bridge structure, or if they can be characterized by movable parts. Finally, mobile solutions can be further classified as active or passive, depending on whether the actuation requires an external energy supply or not. The classification of the different techniques to improve aeroelastic stability is visualized in Figure 2.1. In this section we will first briefly describe some of the structural methods, then provide a more thorough presentation of the aerodynamic solutions.

2.1 Structural Methods

Structural methods improve the flutter stability of the bridge without influencing its aerodynamic response. In this section we present a few structural methods, that are categorized either as static or mobile.

2.1.1 Static Structural Methods

A standard static structural method is to improve the torsional stiffness of the bridge section. However, if the bridge's span length is increased, then so must the cross-section in order to achieve sufficient stiffness. Since an increased cross-section implies greater wind loads, the demands on the bridge's structural strength are in turn increased. These circumstances set an upper limit of a bridge's span length that can be obtained from purely improving the structural stiffness [1]. Moreover, Andersen et al. [4] suggested a non-traditional static structural approach by significantly reducing the torsional stiffness of the deck below that of the heaving stiffness, where in theory coupled flutter of a bridge deck never occur. Their

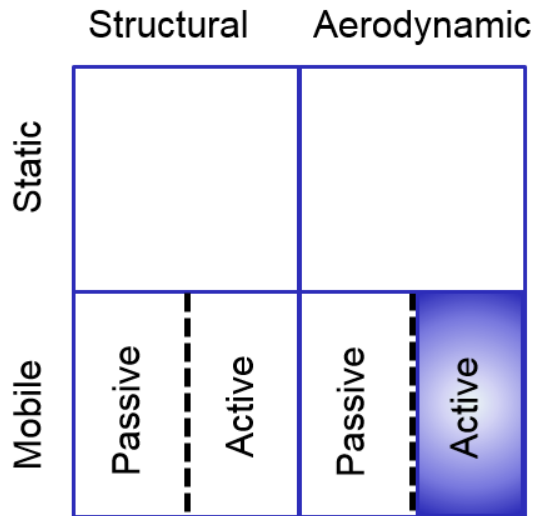


Figure 2.1 – The proposed categorization of flutter improvement strategies. The target methodology of this thesis has been highlighted in the figure.

initial wind tunnel experiments conducted on a two-dimensional section model showed an improved flutter behavior.

2.1.2 Mobile Structural Methods

Passive mobile structural methods

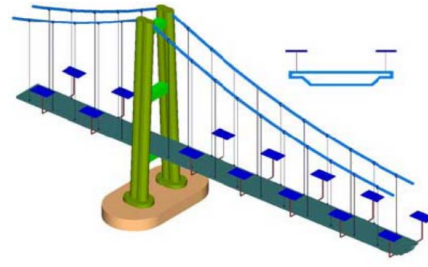
A passive, mobile, structural method to increase the flutter wind speed has been obtained by installing Tuned-Mass Dampers (TMDs) in the bridge deck, see for instance the work of Nobuto and Fujino [5]. The natural frequencies of the TMDs are tuned to the flutter frequency of the structure so that the structural damping is increased at this frequency. The TMD is thus effective at the flutter wind speed but at the same time bound to this frequency. Chen and Kareem [6] showed that TMD solutions can be efficient for soft-type flutter, i.e., when the wind speed is increased slowly until the flutter wind speed is reached. However, they are not for hard-type flutter, i.e., when the wind speed is increased rapidly and beyond the onset of flutter. They emphasize that an active or passive, mobile, aerodynamic solution is necessary to control hard-flutter instability.

Active mobile structural methods

Körllin and Starossek [7] investigated with wind tunnel experiments the performance of an active mass damper. By using linear control, they could increase the flutter wind speed of a sectional model by about 16.5%. More recently, Scheller and Starossek [8] validated with wind tunnel experiments a twin rotor damper, which was proposed previously by Starossek and Scheller [9]. They were able to raise the critical wind speed by more than 18%.



(a) The Bronx Whitestone bridge has wind fairings installed along the bridge deck.



(b) Rigid winglets as proposed by Raggett [11].

Figure 2.2 – Static aerodynamic methods.

Moreover, Dung et al. [10]. proposed a structural control method of the twisting moment of the deck, which can be realized through a rotating cylinder installed inside the deck. They provided an analytical analysis which supported the improvement of the flutter resistance of the bridge deck.

2.2 Aerodynamic Methods

Aerodynamic methods strive to minimize the effects of the wind by altering the aerodynamic profile of the bridge. They have the advantage over structural solutions that they actually lessen the overall forces acting on the bridge.

2.2.1 Static Aerodynamic Methods

One example of a static, aerodynamic method is the triangular wind fairings we see on many bridges today, for instance the Bronx Whitestone Bridge in Figure 2.2a. In 1987, Raggett [11] showed with theoretical and experimental results that mounting rigid winglets parallel to, and clear from, the bridge deck can be very effective in stabilizing bridges that might otherwise be aeroelastically unstable. More recent studies on this topic can be found in [12] and [13], see Figure 2.2b for an illustration of the concept.

2.2.2 Mobile Aerodynamic Methods

To the best of our knowledge mobile, aerodynamic methods have only been investigated using moving flap systems. In 1992, Kobayashi and Nagaoka [14] took Ragget's idea of rigid winglets one step further by introducing mobile flaps. During the last two and a half decades, both passively and actively controlled flap methods have been investigated, theoretically as well as experimentally. Below we introduce a, to the best of our knowledge, complete lineup of passive and active mobile aerodynamic investigations that have been undertaken

Chapter 2. Related Work

experimentally. Although we intend to develop an active flap control, we will dedicate close attention to both passive and active solutions, since they are so tightly coupled in terms of modeling and experimental setup. Additional details about these works will be provided and discussed throughout this manuscript, whenever relevant, and in particular in the related work sections in Part II, Part III, and Part IV.

Passive mobile aerodynamic methods

Mobile passive flaps solutions have been investigated experimentally by a few research groups. Sketches of the different mechanical solutions for the passive controls can be found in Figures 4.1a, 4.1b, 4.1c, and 4.1d, in Part II. In 1999, Wilde, Fujino and Kawakami [15] proposed a passive flap actuation driven by a pendulum, which was capable of increasing the flutter wind speed of the deck. In 2000, Kwon, Sungmoon Jung and Chang [16] designed passively actuated control surfaces being regulated by TMDs. The control surfaces were significantly different from a rotating flap or a static winglet: the flat surfaces were instead perpendicular to the wind flow linearly actuated in and out of slots from the bottom of the deck. The deck could be controlled using only the TMDs or using both TMDs and control surfaces. Their experimental results showed an increase of the flutter wind speed by 37% using only TMDs and an increase by 43% using the TMDs and control surfaces. In 2008, Starossek and Aslan [17] proposed a similar TMD control solution as the previous authors; however, with an ordinary flap design. The results from the wind tunnel experiments were however poor, allowing only for a 7-8% increase in flutter wind speed. In 2011, Phan and Kobayashi, proposed a passive flap control driven by a combination of cables and springs, a setup leveraged for the studies presented in [18], [19]. Notably, they managed to increase the flutter wind speed by 250%. Moreover, Phan and Nguyen employed the same setup in order to evaluate their simulated results in [20].

A general disadvantage of these passive solutions is that it is much more complicated to change the control parameters in the experimental setup, since the components need to be changed physically, whereas for active controls there is only a need to reprogram the controller. Indeed, this could be one of the reasons why Zhao, Gouder, Limebeer, and Graham chose to emulate their passive mechanical actuation design with active devices in their experimental work presented in [21]–[23]. They increased the flutter wind speed by 18% using their experimental setup illustrated in Figure 4.2d.

Active mobile aerodynamic methods

There are to the best of our knowledge only two research groups who have investigated flutter suppression using actively controlled flaps. In 1998, Kobayashi [24] followed up his previous pioneering study; he conducted it using a new setup, integrating the flaps into the deck instead of attaching them above it, as was done in the earlier study. Kobayashi and colleagues showed with wind tunnel experiments that the critical flutter wind speed of a bridge section model could be increased by a factor of two when actively controlling the flaps [14]. Hansen

and Thoft-Christensen constitute the second group of researchers that have studied actively controlled flaps. Their research is well-documented and is presented in several publications [25]–[31]; particularly the theoretical aspects of Hansen’s thesis [29] have been a valuable source of information for the research conducted in this thesis. The experimental setups developed for these studies are illustrated in Figures 4.2a, 4.2b, and 4.2c, in Part II.

Summary

In this chapter we introduce, and categorize, different types of flutter control strategies that can be found in the literature. We mainly limit our research to that of a mobile, actively controlled aerodynamic solution. We provide an overview of all the related works for such a concept that has been studied experimentally. We will further discuss these works, as well as other theoretical contributions, throughout the manuscript.

3 Scope of the Thesis

VIBRATION control of long-span bridges using actively controlled flap arrays is the focus of this thesis. We have investigated, experimentally as well as theoretically, the feasibility and effectiveness of an intelligent, distributed flap system for enhancing the flutter performance of long-span bridges. In this chapter we outline the focus of this thesis and define the three pillars on which our research stands. Finally, we describe our contributions and how they are linked to our published record.

3.1 Objectives and Outline

The thesis focuses on the three different research thrusts visualized in Figure 3.1; the mechatronic design of a physical model, the development of an analytical model, and the investigation of different control strategies of a bridge deck equipped with mobile, active, flap arrays. These areas are strongly intertwined and changes in one component often have an effect on the other two. Thus, the investigation and development of these thrusts have partially been an iterative process. However, the structure of this manuscript roughly follows the chronological order, since the different parts generally build on top of each other.

1. **Mechatronic design of an actively controlled bridge section model**

In this part (**Part II** of this manuscript), we present the mechatronic system design process that culminated in the realization of the SmartBridge, a bridge section model equipped with eight independently controllable flaps. The design challenges included defining appropriate system requirements such as the dimensions and structural properties of the section model, and the operating conditions of a single flap actuator.

2. **Analytical model of an actively controlled bridge deck**

In this part (**Part III** of this manuscript), we present an analytical model of the flutter phenomenon in regards to a bridge section model equipped with a leading and a trailing edge flap. In addition to deriving the theoretical formulation describing the system's aeroelastic behavior, we have validated our modeling approach with wind

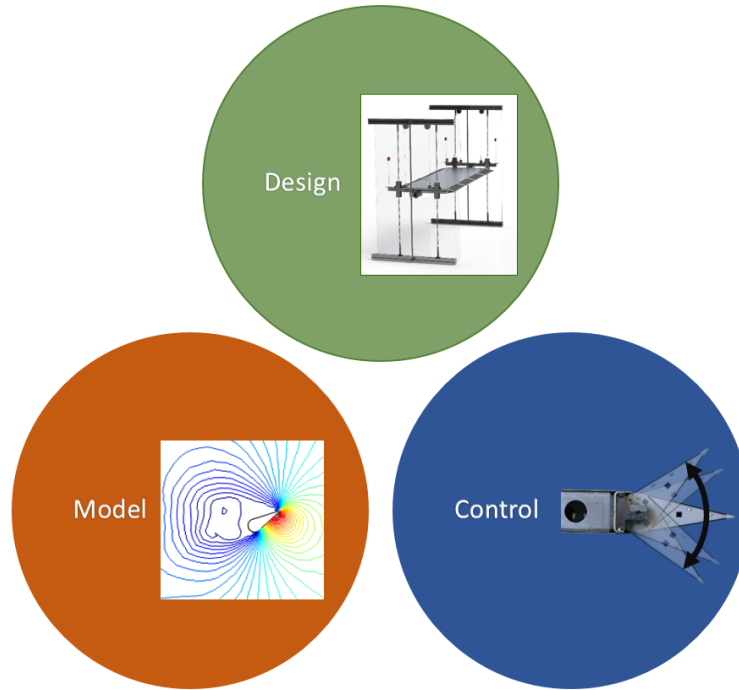


Figure 3.1 – The three main pillars of this thesis.

tunnel experiments.

3. Control coordination approaches for the flap arrays

In this part (**Part IV** of this manuscript), we present the control effort of the thesis. The analytical model has been leveraged in order to evaluate a baseline control law that moves all of the flaps within the arrays in a synchronized fashion. Moreover, an extensive systematic experimental effort has been conducted in order to evaluate the control performances of different coordination strategies of the flaps in both regular, laminar, flow conditions, and under perturbed scenarios.

3.2 Contributions

1. Mechatronic design of an actively controlled bridge section model

We have designed a dedicated experimental setup consisting of a bridge section model endowed with flap arrays as well as all the necessary instrumentation for measuring and perturbing the system states under controlled wind conditions, carefully generated in a wind tunnel available at EPFL. The mechatronic design of the setup was per se challenging and represents a significant contribution to the state of the art since, to the best of our knowledge, experimental studies in this area have exclusively been carried out using a single flap on both sides of the bridge section. Although we have not considered wireless monitoring technology, we have designed the SmartBridge

in such a way that many state variables can be monitored in real-time (e.g., heave and pitch motions of the section; discrete pressure distribution on section and flaps; position, speed, and torque of flaps), and allowed us to perform repeatable and reliable experimental series. We have paid particular attention to a proper integration of all the components in a self-contained, modular, mechatronic device – an intelligent flap – in order to minimize the potential intervention on the structure to be controlled and to maximize the deployment scalability as a function of the structural and environmental requirements. Relevant publications for this part are:

- **M. Boberg**, G. Feltrin, and A. Martinoli, “Model and control of a flap system mitigating wind impact on structures”, in *Robotics and Automation (ICRA), 2014 IEEE International Conference on*, May 2014, pp. 264–269. DOI: 10.1109/ICRA.2014.6906620.
- **M. Boberg**, G. Feltrin, and A. Martinoli, “A novel bridge section model endowed with actively controlled flap arrays mitigating wind impact”, in *Robotics and Automation (ICRA), 2015 IEEE International Conference on*, May 2015, pp. 1837–1842. DOI: 10.1109/ICRA.2015.7139437.

2. Analytical model of an actively controlled bridge deck

We conducted an in-depth effort to properly capture the dynamics of our bridge deck equipped with moving leading and trailing edge flaps with an analytical model. Building on top of theoretical frameworks commonly used in civil engineering for long-span bridges, and in aeronautics for wings equipped with ailerons and tabs, we derive a physically sound analytical model. Leveraging our experimental setup, we estimated the model parameters from free vibration tests in the wind tunnel. We show that the experimentally obtained model parameters capture the dynamics of the bridge deck well. Moreover, we are the first to validate experimentally an analytical flutter model of a bridge deck with mobile flaps that consider structural and aerodynamic effects of flaps. We show that this added model complexity significantly improves the flutter wind speed prediction. In fact, the flutter prediction of the model proved quite reliable also for control parameters significantly different from those used for the system identification of the model parameters. However, although the theoretical model is adequate in respect to controlling leading and trailing edge flaps independently, we observed that controlling both sides simultaneously greatly decreases the model accuracy, thus indicating that the aerodynamic forces acting on downwind elements are perturbed by moving upwind elements, an effect that has not been modeled. Finally, we performed a crude sensitivity analysis, by investigating possible redundancies in the formulation of the aerodynamic model. Relevant publications for this part are:

- **M. Boberg**, G. Feltrin, and A. Martinoli, “Experimental validation of the wing-aileron-tab combination applied to an actively controlled bridge section model”, in *14th International Conference on Wind Engineering (ICWE)*, Jun. 2015.
- **M. Boberg**, G. Feltrin, and A. Martinoli, “An analytical and experimental investigation of an actively controlled bridge section model”, *Journal of Wind Engineering*

and Industrial Aerodynamics, in preparation.

3. Control coordination approaches for the flap arrays

We provide the first experimental study that have considered not only a single flap, but an array of flaps, on the leading and trailing edges of the section model. This unique setup has allowed us to evaluate the control coordination among flaps from several angles. The coordination between leading and trailing edge flaps have to some extent been studied in related works. By performing an ample theoretical and experimental study, we provided additional insight regarding the coordination between the leading and trailing flaps. Note that the results from the experimental validation of the analytical model in Part III is additionally a solid contribution also from a control perspective. Moreover, we leveraged our experimental setup in order to thoroughly investigate the flap control coordination within the flap arrays, a study that we are uniquely equipped for. This pioneering work has been profoundly experimental. We proposed different performance metrics for the flutter control and evaluated the different strategies based on these. Moreover, we defined a synchronized and a decentralized version of the same control law, so that the effect of using a local control input could be assessed. The robustness of the two coordination approaches were furthermore evaluated under more realistic, perturbed scenarios, for which we show that while in general the synchronized control performs better, it degenerates quickly to the level of the decentralized approach even in the case of small disturbances. A relevant publication for this part is:

- **M. Boberg**, G. Feltrin, and A. Martinoli, “Flutter suppression of a bridge section model endowed with actively controlled flap arrays”, in *Intelligent Robots and Systems (IROS)*, 2015 *IEEE/RSJ International Conference on*, Sep. 2015, pp. 5936–5941. DOI: 10.1109/IROS.2015.7354221.

3.2.1 Contributions of Predecessors and Collaborators

I would like to clearly state that the research towards an actively controlled bridge deck was already ongoing (project started in 2008) when I started my doctoral studies. Consequently, a few of the design contributions that are described in Part II were already in place when I entered the scene.

In particular, a spring-suspended canonical bridge section model had been designed and built by my predecessor, Shravan Kumar Sajja, who was associated with the project during one year. The same suspension structure has been recycled for the work presented in this thesis. Furthermore, his investigation and conclusions regarding the construction of canonical bridge section models have been valuable during the design process of the active setup.

Moreover, Albrecht Lindner worked as a research assistant for four months on the project, with the focus on finalizing the assembly of the structure around the section model, so that wind tunnel experiments could be achieved. In particular, he installed the wooden frames around the suspension system, and performed the first free vibration experiments in the channel.

Both of my predecessors collaborated very closely to our former lab engineer, Pascal Gilbert. His main contribution was to develop the backbone of the embedded system architecture. In particular, he designed and manufactured the electronic boards that communicate and control the laser sensors and electromagnets.

Thus, there had already been substantial progress made on the infrastructure on top which the SmartBridge has been developed.

Moreover, the two electronic board used for the supervision and the control in the embedded architecture are of the type of R&D board that has been developed by our lab engineer, Emmanuel Droz. He has additionally provided me valuable feedback during the design process of the SmartBridge.

Summary

In this chapter, we established the outline and contributions of this thesis. We categorize our research into the three main themes that are consistent with the division of the main parts of the manuscript. Furthermore, we provide an overview of the main contributions and our relevant publications within each of the defined areas; the mechatronic design of an actively controlled section model, the analytical modeling effort of the controlled bridge deck, and the evaluation of different coordination strategies of the flap control.

Mechatronic Design Part II

4 Related Work

WIND tunnel testing is an essential tool for evaluating aerodynamic and aeroelastic properties of bridge decks. We will in this chapter describe experimental setups of bridge decks equipped with mobile flaps, as well as common wind tunnel testing techniques for canonical bridge decks. Moreover, we will describe common sensing and perturbation techniques used for wind tunnel tests of physical bridge models.

4.1 Physical Bridge Models for Wind Tunnel Testing

There are typically three types of physical models used for suspension bridges: section models, taut strip models, and full-bridge models. Every research group introduced in Chapter 2 ([11], [12], [14]–[17], [24]–[29]), performed their experimental investigations of aerodynamic flutter suppression (realized by static winglets or mobile flaps) with a bridge section model. This model has the simplest structure and is also the least expensive type, yet it suffices to determine the bridge section's aeroelastic stability and it is therefore well-suited for initial experiments of new concepts [37].

4.1.1 Section Models Equipped with Mobile Flaps

In this section we will review design choices and experimental setups developed for mobile (passively and actively controlled) flaps used in aerodynamic bridge stabilization methods.

Passive mobile aerodynamic methods

To the best of our knowledge, four different section models have been built that control mobile flaps using purely mechanical elements: Wilde, Fujino and Kawakami [15] proposed a pendulum solution; Kwon, Sungmoon Jung and Chang [16] proposed a passive flap control using TMDs; Aslan and Starossek [17] proposed a similar TMD control solution as the previous

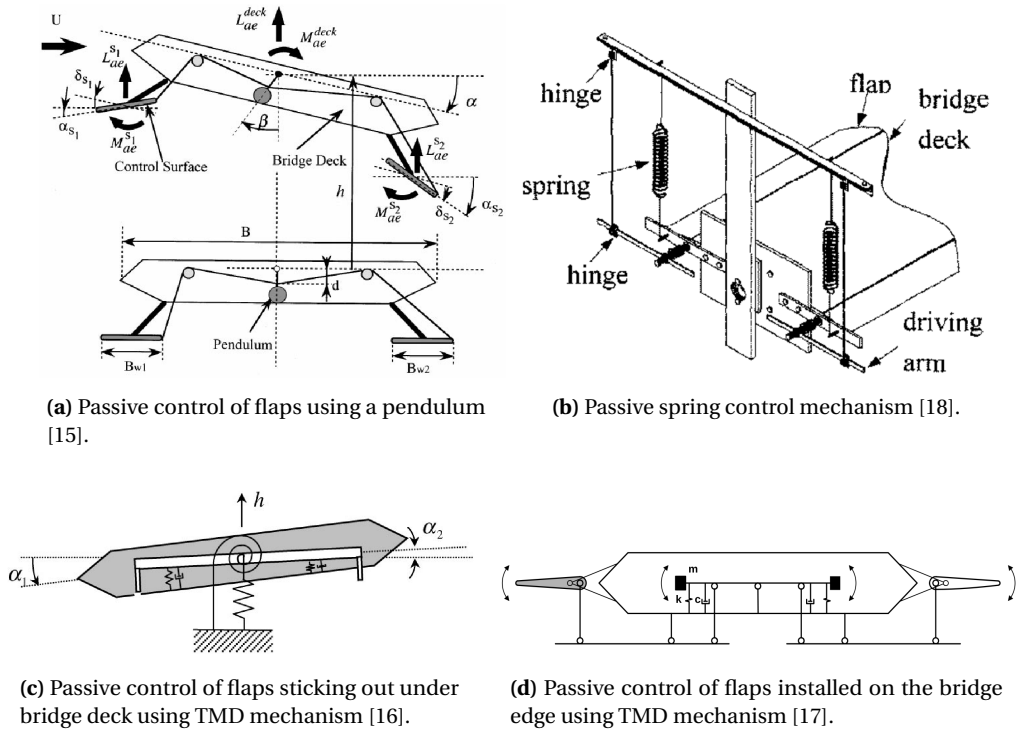


Figure 4.1 – Passively controlled experimental setups.

authors, however, with a different flap design; and Phan and Kobayashi [18] realized a passive control through a combination of hinges and springs. The different mechanical solutions for the passive controls are illustrated in Figures 4.1a, 4.1b, 4.1c, and 4.1d. Although we have categorized these methods as the same type, we can observe that the embodied solutions are highly diverse, in addition to the driving mechanism, the flap placement and design are distinctly different.

Active mobile aerodynamic methods

Kobayashi and Nagaoka [14] were the first to experimentally investigate actively controlled flaps. Their flaps, clearly influenced by Ragget's design, were installed above, and separated from, the bridge section, as illustrated in Figure 4.2a. A few years later Kobayashi et al. introduced a new setup with the flaps integrated to the deck [24], as shown in Figure 4.2b. In both designs the flaps were actuated by motors placed inside the deck. Hansen constructed a section model equipped with actively controllable flaps that have been described in detail in her thesis [27]. The physical setup, with the servo system for the flap control placed inside the deck, is depicted in Figure 4.2c. The author declared that they had major difficulties obtaining a reliable system (due to time delays, noisy measurements and unforeseen events), causing a one-year delay in their time plan. This highlights the fact that the mechatronic engineering factor for constructing an active bridge section model is both nontrivial and critical for the

4.1. Physical Bridge Models for Wind Tunnel Testing

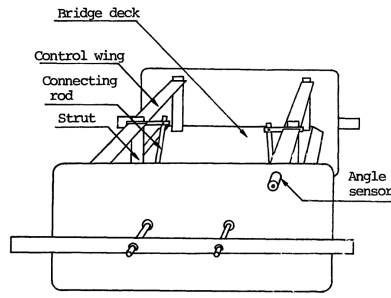
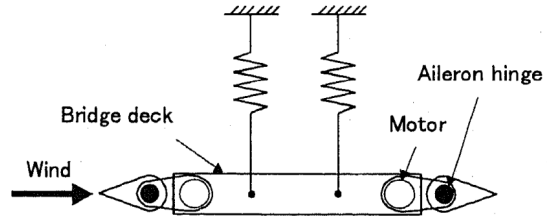
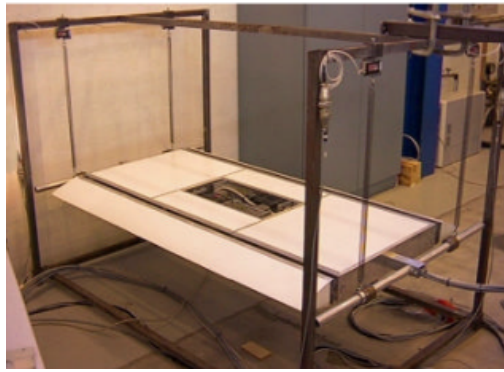


Fig.3 Model with control wings

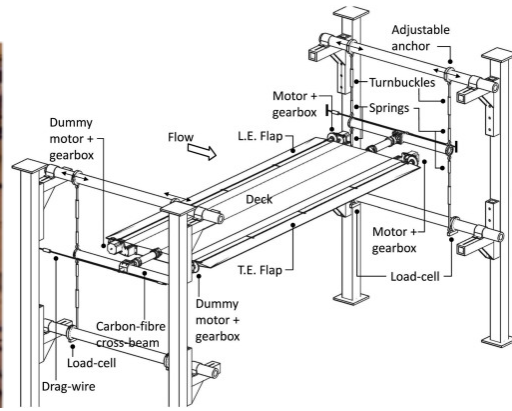
(a) The first setup developed by Kobayashi et al. [14].



(b) The second setup designed by Kobayashi et al. [24].



(c) Bridge section model with movable flaps as designed by Hansen [27]. Note that the control system is located inside the bridge deck.



(d) Bridge section model with movable flaps as designed by Zhao et al. [22].

Figure 4.2 – Actively controlled experimental setups.

success of the project. Although Zhao et al. investigate a passive control concept, it is realized by active elements [22]. The flaps are actuated by stepper motors attached to the section model, as illustrated in Figure 4.2d.

Theoretical studies of flap positions and deck anchoring

In a patent written by Ostfeld [1], possible flap designs and placements have been discussed theoretically. The author concludes that placing the flaps above the bridge deck is sub-optimal due to the higher turbulence level and suggests two alternative flap designs as seen in Figure 4.3a and Figure 4.3b, where the advantage of the latter is that it would be cheaper to implement and aesthetically nicer [1].

Moreover, Wilde et al. compared [38] different placements of the flap hinges, as seen in Figure 4.3c. The hinges placed on the edge of the deck (Figure 4.3c, case 1) and hinges placed on the middle of the flap (case 2) performed best in terms of stability and robustness of the

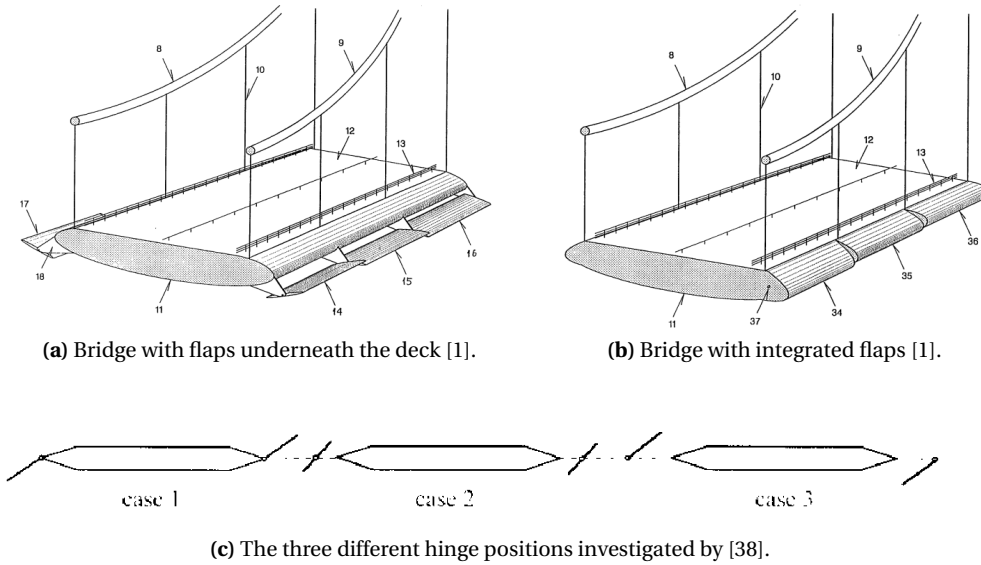


Figure 4.3 – Possible flap placements and hinge positions.

system. However, hinges on the deck (case 1) required smaller flap width and were therefore considered more suitable. Although this conclusion is solely based on analytical theory (no experimental validation), it should still provide an indication of the potential performance.

4.1.2 Sensing Systems for Section Models

Monitoring the deck's position

All of the experimental work mentioned above monitor the bridge deck's heaving and pitching motion. However, only Hansen et al. [27] and Zhao et al. [21] disclose what type of sensor they used, which in both cases are load cells attached to the spring suspension system. On the other hand, also other sensor types such as accelerometers [39] and laser sensors [12] have been employed for monitoring the displacement of canonical, passive bridge section models.

Sensing local surface pressure

Furthermore, Kwon et al. [16] measured the pressure distribution around the bridge deck, in addition to the displacement, using a 36-channel pressure transducer system. The approach of combining local pressure measurements and forced vibration tests (described in the following section) has also been employed for canonical bridge section models, for comparing experimental and analytical results (e.g., Cao and Sarkar [40] and Argentini et al. [41]) or experimental and numerical models (e.g., Sarkic, Fisch, Hoeffler and Bletzinger [42]).

4.1.3 Perturbing Techniques for Section Models

Aeroelastic stability of bridge section models is typically investigated either by forced vibration or by free vibration experiments [43]. Free vibration tests imply analyzing the motion of the bridge section model in the wind flow after being released from an initial displacement. Whereas forced vibration tests analyze the forces acting on the bridge section model in the wind flow while undergoing forced, sinusoidal, harmonic motion. The free vibration tests require mechanically simpler and cheaper perturbation systems than those based on forced vibrations (a few examples of perturbation systems are found in Cao et al. [40], Neuhaus et al. [44] and Chen et al. [39]); however, they imply more complex system identification methods. All the experimental works investigating mobile flaps described in this section have employed the free vibration procedure, except for Kwon et al. [16], who performed forced vibration tests.

4.2 Concluding Remarks

The section model is a standard tool that is well-suited for investigating the aeroelastic behavior of bridge decks. Moreover, it is the only type of model that has been constructed for the investigation of actively controlled decks. Therefore, we have chosen to design our physical model as a sectional type. Furthermore, we have decided to design a section model with the flaps integrated to the deck, which theoretical and simulated results having indicated has several favorable properties. Moreover, we have opted for a free vibration perturbation mechanism for our bridge section because of its simple and cheap design.

Summary

In this chapter we describe commonly used wind tunnel test methodologies for determining the aeroelastic behavior of a bridge deck. In particular, we focused on the design choices made by other researches who have conducted experimental studies of bridge decks endowed with flaps controlled passively and actively. In the following chapters we will carefully describe the development of our setup, the SmartBridge.

5 Hardware Development and Experimental Site

IN this chapter, we present the SmartBridge, a novel bridge section model equipped with actively controlled arrays of flaps, whose primary scope is to provide a flexible, physical test-bed to investigate mitigation solutions for wind-induced vibrations of long-span bridges. The mechatronic design of an active section model, as well as its support structure, is described in detail and the key design choices are motivated. Moreover, we introduce the experimental site, a boundary layer wind tunnel, and the wind tunnel testing tools we have at our disposal. Our bridge section model equipped with multiple, individually controllable flaps, is unique in the field, and the overall supporting structure is essential for allowing reliable and repeatable experimental procedures in the wind tunnel.

5.1 Design of an Active Bridge Section Model

The SmartBridge is a bridge section model equipped with eight actively and independently controllable flaps. The mechanical design of the deck and the flaps was carried out using the Computer Aided Design (CAD) software Solidworks¹. This tool allowed us to insure a smooth integration process of the individual parts, and additionally to evaluate the physical and the mechanical properties of the system before it was manufactured as a whole.

Modularity was a key aspect throughout the design process. Given the experimental and pioneering nature of the project, we natively aimed at a solution broken down in well-defined components which could be potentially replaced later on with different solutions without having to redesign the complete system.

5.1.1 Deck Design

A traditional, canonical, bridge section model deck has a simple, low-cost design, yet providing a high stiffness-to-weight ratio. For instance, these properties can be realized by a sandwich

¹<http://www.solidworks.com/>

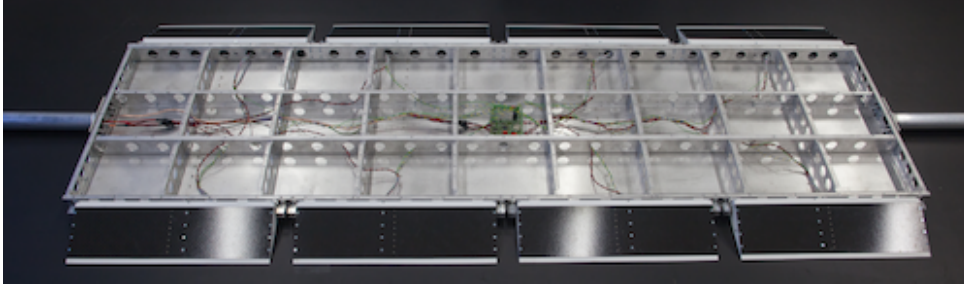


Figure 5.1 – Active deck, with a rib and spar structure.

Table 5.1 – Measured System Parameters

Parameter	SmartBridge	Hansen	Kobayashi
m [kg]	21.5	26.6	n/a
B' [mm]	500	625	160
B [mm]	740	938	240
D [mm]	48	94	14
L [mm]	1800	1480	450
f_α [Hz]	4.6	1.61	2.7
f_h [Hz]	3.5	0.83	2.1
B/D	15.4	10	17.1
L/B	2.4	1.6	1.9
$0.5(B - B')/B'$	0.24	0.25	0.25
f_α / f_h	1.3	1.9	1.3

structure with a foam core coated with aluminium plates. However, we are required to place electronics inside the deck, as well as drawing cables and pressure tubes through the deck, which eliminates the possibility of a filled structure. Furthermore, the additional weight of the flaps put further constraints on the total mass of the SmartBridge. Therefore, we designed a novel, lightweight, hollow bridge deck in aluminium, which is inspired from airplane wing construction with its spar and rib structure, as depicted in Figure 5.1. The ribs and spars are perforated with many circular holes that significantly reduce the weight as well as provide a flexible infrastructure for cables and tubes. These elements are permanently riveted together, while the coating panels are screwed on, so that the interior remains easily accessible. The characteristics of the bridge section model are given in Table 5.1, we have also reported the corresponding parameters for the active bridge section models of Hansen et al. [28] and Kobayashi et al. [24], for comparison purpose. Note that the total mass, m , corresponds to the minimum weight as it only considers the mass of the deck and flaps (14.1 kg) and the support structure (7.4 kg). The total mass can be substantially altered by adding equipment or dummy masses. Furthermore, the natural frequencies reported here for the SmartBridge can be easily altered to suit a specific experiment, as will be explained in the following section.

In order to approximate a flat plate, the deck depth, D , should in principle be as thin as possible ($D \rightarrow 0$). In our design, the minimal depth is constrained by the size of the flaps' actuators.

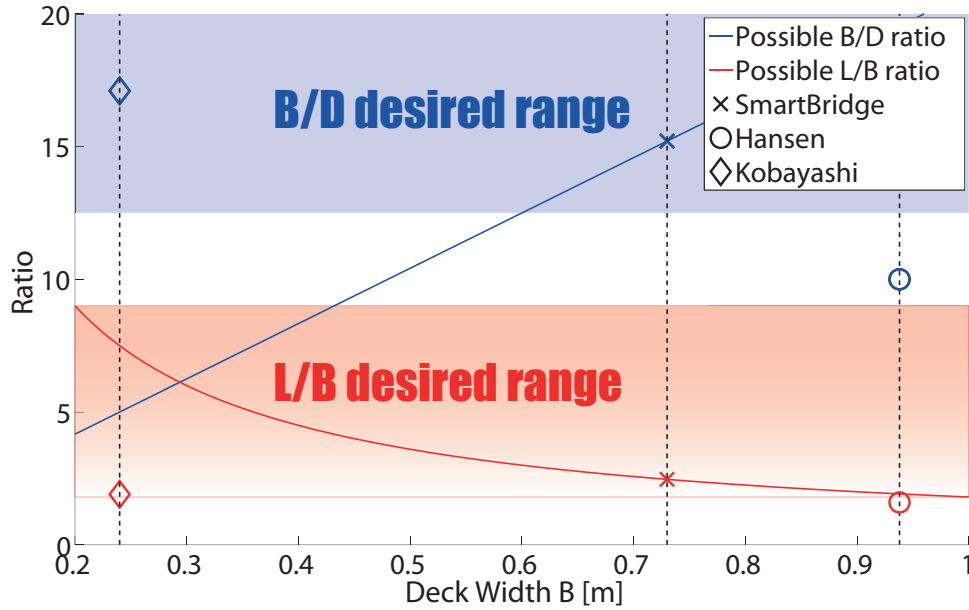


Figure 5.2 – Effects of changing the deck width on the B/D and L/B ratios.

Moreover, it is common that the deck length, L , is set as long as possible, or more precisely that the L/B ratio (or aspect ratio) is high [45]. In our case, the bridge length is limited by the width of the channel, and although the distance between the channel's walls is 2 m, 10 cm margin per side has been spared to allow bridge motion as well as to avoid the turbulent wind regions close to the walls [45]. The bridge width (including flaps), B , is not restricted physically, although, in order to achieve a high L/B ratio, a narrower deck is preferred. Brownjohn et al. [46] (citing an private email conversation with Hjorth-Hansen) recommend an aspect ratio between 3 and 8, in order to minimize the effect of deck flexibility in rigid body modes.

According to Matsumoto et al. [47] a B/D ratio larger than 12.5 leads to a deck exhibiting coupled flutter, with increasing instability up to a ratio of 20. Normally, this region is avoided in a passive design; however, this is an aeroelastic instability that we desire to study and control with the flaps. As can be seen in Figure 5.2, changing the deck width, B , (L and D are fixed values according to Table 5.1) has contradictory effects of the desired B/D and L/B ratios. Finally, a compromise was found by selecting a high B/D ratio in order to obtain a deck as sensitive as possible to coupled flutter while keeping the L/B ratio within the desired range, and distinctively higher than those of Hansen et al. and Kobayashi et al.

5.1.2 Deck Anchoring and Support Structure

Spring suspension

The SmartBridge is anchored to a suspension system, as depicted in Figure 5.3. The deck is carried by two support bars that are suspended by eight springs attached to the wind tunnel

structure. The design and construction of the suspension system (as for the deck) has been significantly influenced by the suggestions given in [45].

The natural frequencies in the heave Degree of Freedom (DOF), f_h , and the pitch DOF, f_α have a great impact on the system behavior, in particular the frequency ratio, f_α/f_h , influences the flutter behavior as described in [47]. By adjusting the natural frequencies, we can obtain specific system responses, for instance achieve a certain wind speed where the bridge deck starts to flutter. To this purpose we have designed a system where the natural frequencies can easily be manipulated by changing the mass (e.g., by adding dummy masses to the support bars), the spring stiffness, and/or the distance between the springs. According to [46] the stiffness of the suspension springs determines f_h and f_α , as follows

$$f_h = \sqrt{\frac{K_h}{m_T} \frac{1}{2\pi}} = \sqrt{\frac{8k}{m_T} \frac{1}{2\pi}} \quad (5.1a)$$

$$f_\alpha = \sqrt{\frac{K_\alpha}{I_T} \frac{1}{2\pi}} = \sqrt{\frac{K_h a^2}{I_T} \frac{1}{2\pi}} = \sqrt{\frac{8k a^2}{I_T} \frac{1}{2\pi}} \quad (5.1b)$$

where, m_T and I_T , are the total mass and the total mass moment of inertia of the deck, K_h and K_α , are the stiffness in the heave and pitch DOFs respectively, k , is the stiffness of a single spring, and a is the half-distance between the springs.

In the configuration given in Table 5.1, the stiffness k of one spring is 1298 N/m, the half-inter-spring-distance, a , is 0.29 m, the mass, m_T , is 21.5 kg, and the mass moment of inertia, I_T , is approximated as 0.99 kgm². Under these conditions, the theoretical value for f_h is 3.5 Hz, according to Eq. 5.1a. The measured frequency is 3.5 Hz, and corresponds well to the theoretical value. According to Eq. 5.1b, the theoretical value for f_α is 4.7 Hz, and it is close to the measured frequency of 4.6 Hz. These results support the estimation of the natural frequencies according to Eq. 5.1a and Eq. 5.1b.

Pull-up system

The system parameters (e.g., natural frequencies and damping coefficients) can be identified through free vibration tests [43]. In order to perform repeatable free vibration tests on the SmartBridge we have installed a remotely controllable pull-up mechanism. This mechanism is realized with four electromagnets and four DC motors, as seen in Figure 5.3; the magnets can latch to the support bars and be pulled up by the motors until the deck reaches the desired set-point (the loop is closed with the bridge deck position data from the laser sensors). The step response is triggered as the magnets simultaneously release the deck and is left to oscillate freely.

We have defined three different types of step responses; purely in the heave DOF, a mixture of the heave and the pitch DOFs, and finally a mixture of the heave, the pitch, and the roll

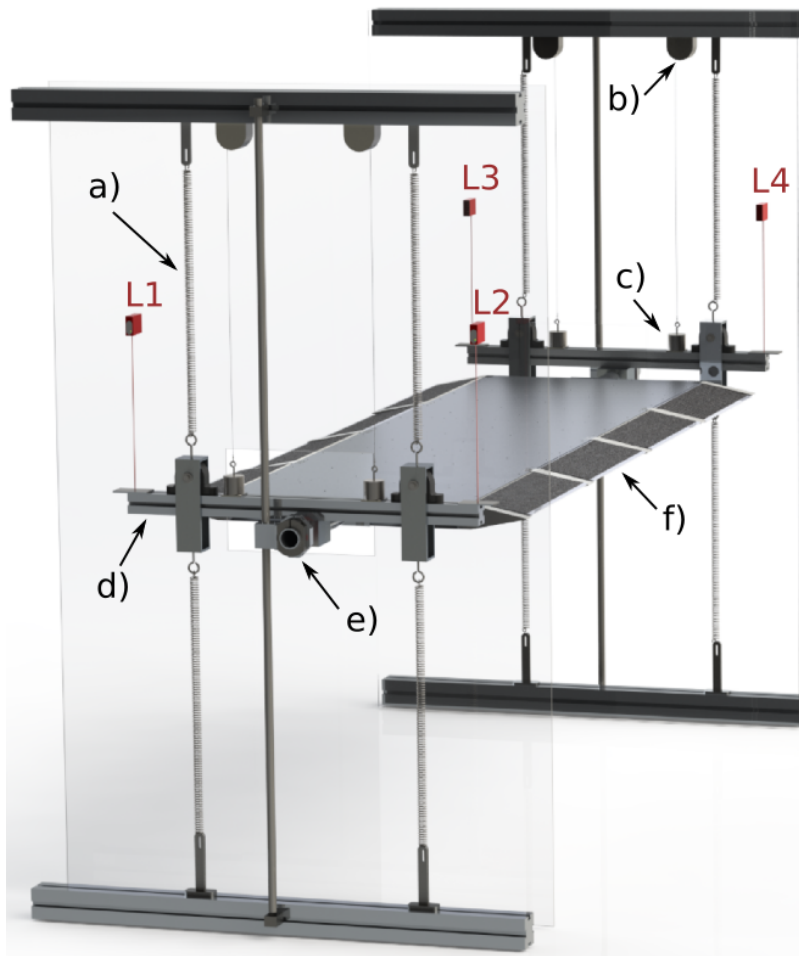


Figure 5.3 – A faithful CAD model of the SmartBridge anchored to the suspension system. Some key elements of the set up are highlighted in the figure: a) spring for the suspension system, b) DC motor for the pull-up system, c) electromagnet for the pull-up system, d) support bar, e) decoupling system, and f) active flap. Moreover, four laser sensors are measuring the corner positions of the deck and are marked with L1-4.

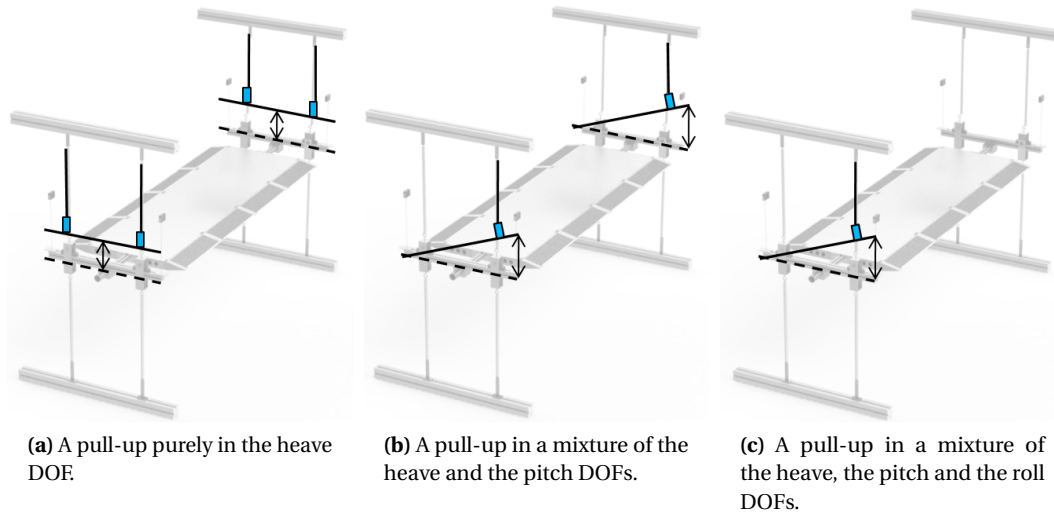


Figure 5.4 – The different pull-up types.

DOFs. The different types of pull-ups, visualized in Figure 5.4, are realized by using a subset of the magnets. Note that the setup allows for mirrored step responses to the ones presented in Figure 5.4b and Figure 5.4c.

Decoupling system

In order to further facilitate the system identification of the setup, we have designed a guiding and decoupling system that restricts the deck to the heave and pitch DOFs, as seen in Figure 5.3 and Figure 5.5. The heaving motion is guided with a linear bushing along a steel shaft and can be fixed by locking the linear bushing. The pitch motion is facilitated with a ball bearing and can be locked at any angle with a collar. A similar guiding system used for identifying system parameters of a canonical, passive deck, using steel shafts, linear bushings, and ball bearings was presented by Sarkar et al. [48]. Furthermore, the decoupling system is easy to add or remove depending on the type of experiment performed. In addition, drag wires [45] are permanently installed in order to prevent deck motion in the horizontal DOF even when the decoupling system is disconnected. Roughly 3 m long piano wires were used for this purpose. The wires add geometrical stiffness in the heaving mode. However, introducing springs on the downwind side of the bridge deck reduces this effect.

5.1.3 Flap Design

A particularly important aspect of the active deck design is its actuator, the flap. In order to assert the flap performance we made two iterations of its design. The first iteration, the prototype flap, was evaluated in-depth, before the second generation, and final design, was produced. In Chapter 6 we present this initial effort of characterizing the single actuator unit.

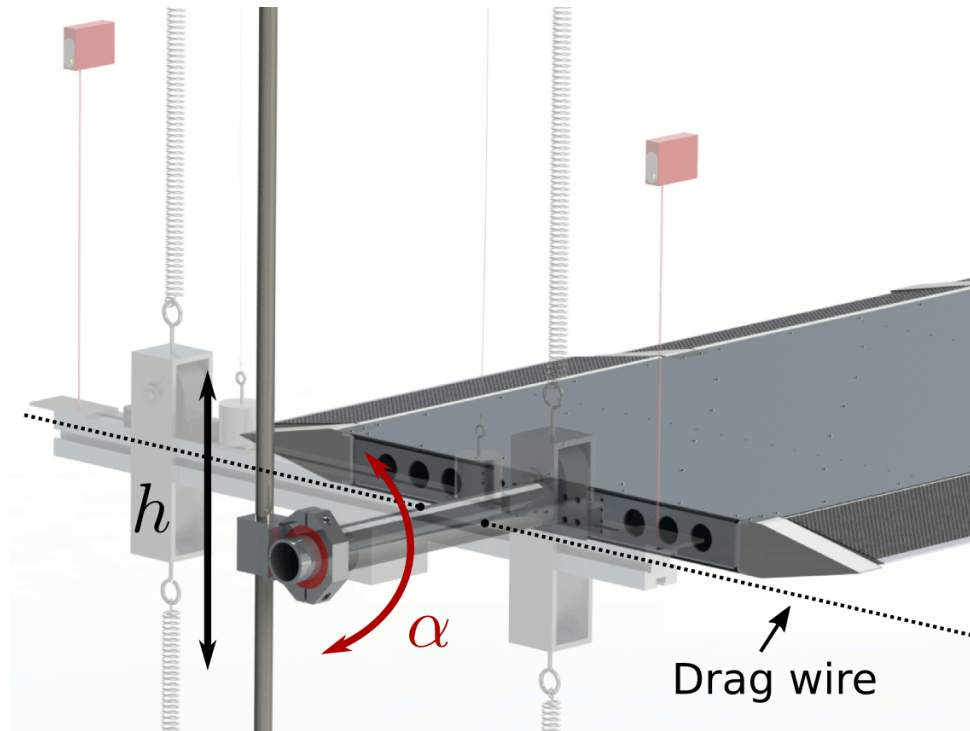


Figure 5.5 – The guiding system allows heave and pitch motion. Additionally, each DOF can be locked independently. The drag wires prevent motion of the deck in the horizontal DOF.

Prototype flap

We intentionally kept the shape of the flap simple; optimizing its aerodynamic profile is not within the scope of this thesis. The design is symmetric (width: 400 mm, chord length: 134 mm, max thickness: 49 mm), and was manufactured completely using a 3D printer, a procedure that allowed us significant design freedom and fast production.

Differently from Hansen et al. [27] and Kobayashi et al. [24], we have chosen to place the motor and control unit inside the flap. This simplifies the construction of the deck, and since the motor and control unit coincide with the rotational axis, illustrated in Figure 5.6b, they do not impose a significant extra momentum on the flap. In our setup we used a 20W DC motor with graphite brushes (model: 118751), gear reduction rate of 53:1 (model: 144035) optical encoder (model: 225778), and a digital positioning controller (model: 390003), all from Maxon Motor Inc². We dimensioned the flap size, the gearbox unit, and the motor in such a way that the maximal estimated aerodynamic forces in the worst angle of attack could be reasonably overcome by the active flap. In order to investigate the flap performance, with and without wind, we built a dedicated test rig, as seen in Figure 5.6a. More details of this evaluation are given in Chapter 6.

²<http://www.maxonmotor.com>

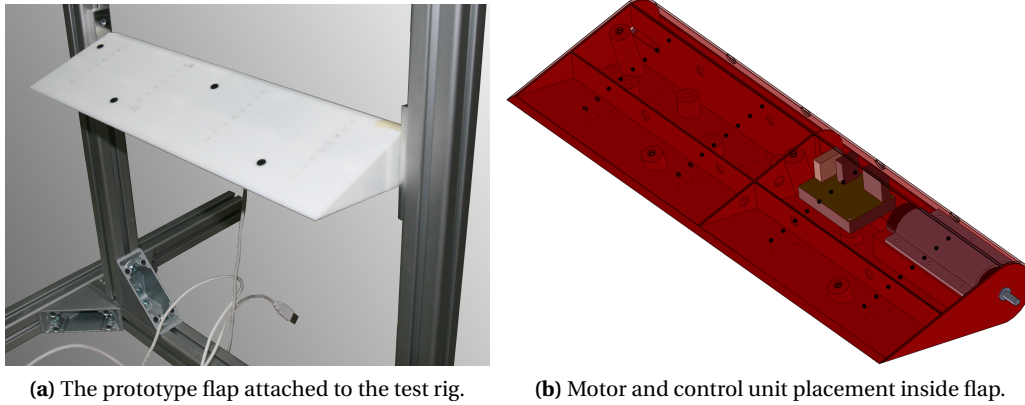


Figure 5.6 – The prototype flap and setup.

Furthermore, our flap prototype allowed us to test a 64-channel pressure sensing instrument. This instrument is described in section 5.1.4 and can be used for measuring the pressure distribution on the entire active bridge section model.

Final flap design

The final design of the flap is similar to that of the prototype, and can be found in Figure 5.7b. The same actuator unit is used also for the second generation. However, several improvements were made to the flap design, the most important being the rigidity and robustness of the structure. The frame of the flap is still 3D printed plastic, however the torsional rigidity was improved by increasing the wall thickness of the ribs, introducing square carbon fiber tubes through the structure, and by covering the flat sides with carbon fiber sheets (the bottom side is glued on and the upper side is screwed on so that the interior remains accessible). Although, the assembly process is a little more complex than for the prototype flap, the resulting design is cheaper to manufacture, weighs slightly less, and has significantly more torsional rigidity. The total weight of one flap including motor, driver, cables, and screws is 550 g. The overall shape of the flap was kept as before; however, the dimensions (length: 400 mm, width: 139 mm, max thickness: 48 mm) were slightly adjusted to better fit the active deck requirements. Although their width is 139 mm, the flaps on each side of the girder are only adding 2x120 mm to the extended bridge width B , since they are partially incorporated within the deck structure. This means that the effective flap width is 24% of the core deck width (without flaps), B' , a value that is comparable to the 25% of Hansen et al. [28] and Kobayashi et al. [24] as reported in Table 5.1.

Flaps and deck anchoring

The flaps are directly attached to the deck with hinges, as depicted in Figure 5.7a. Furthermore, hollow, 3D printed thin shells are attached to cover the hinges and avoid turbulence at the flap

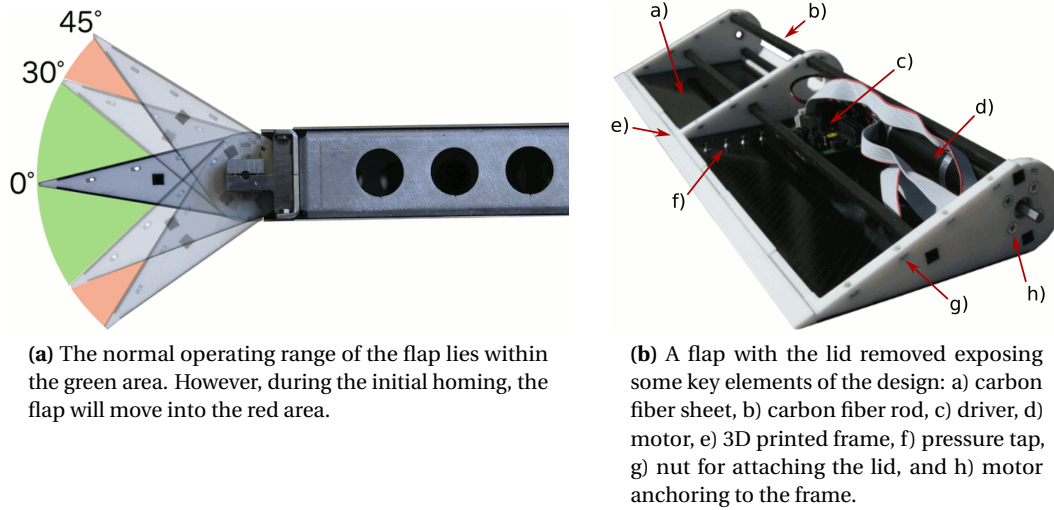


Figure 5.7 – The final flap design and its attachment to the bridge deck.

fixation points, as seen in Figure 5.8. There are two main advantages of partially introducing the flap into the deck; firstly, by minimizing the physical gap between the parts, air leakage and turbulence effects are reduced; secondly, the configuration allows for a simple and reliable homing solution. At start up the flaps require homing to localize themselves. This is achieved by moving the flaps upward until the physical limit at approximately 45° is reached; at this point, the motor current consumption increases above a threshold value which defines the home position; subsequently, the flap moves to an offset position that corresponds to a 0° angle. Finally, a software limit is set to $\pm 30^\circ$, a value defining our operating range. The allowed movements of the flap are visualized by Figure 5.7a.

5.1.4 Sensing Capabilities and Embedded System Architecture

Deck position from laser sensors

The bridge deck position is measured with 0.1 mm resolution by four laser sensors (ODSL 8 from Leuze Electronics³) at a sampling rate of 200 Hz. The sensors are placed above each corner of the deck, as seen in Figure 5.3. The deck's heave (h), pitch (α), and roll (β) can be

³<http://www.leuze.ch>

calculated from the measured distance from each sensor to the deck as follows

$$h = \frac{1}{4} \sum_{i=1}^4 L_i \quad (5.2a)$$

$$\alpha = \arctan\left(\frac{L2 - L1 + L4 - L3}{2d}\right) \approx \left(\frac{L2 - L1 + L4 - L3}{2d}\right) \quad (5.2b)$$

$$\beta = \arctan\left(\frac{L4 - L2 + L3 - L1}{2l}\right) \approx \left(\frac{L4 - L2 + L3 - L1}{2l}\right) \quad (5.2c)$$

where $L1$, $L2$, $L3$, and $L4$, are the bridge deck positions given by the laser sensors, and d is the horizontal distance between a laser sensor pair on the same side of the wind tunnel wall. Furthermore, l , is the cross channel distance between the laser sensors. The distance d is 820 mm in the current setup, and the distance l is fixed at 2245 mm. Note that since we operate at small pitch and roll angles of the deck, we can use a linearized approximation of α and β for the on-board micro controller calculations.

Flap state from motor encoders

The positions of the flaps are tracked with the motor's encoders, with a resolution of 108544 steps per revolution. Although the sampling rate can be set freely up to the limit of the CAN bus (see also the embedded system architecture section below), we have chose to set to 200 Hz for consistency with the deck state monitoring. Moreover, while we are currently only using the position feedback, other states, such as speed, or the measured motor current (as a proxy for the torque) could provide useful feedback for modeling or control purposes.

Pressure sensing system

In order to better understand the underlying physical mechanisms of the active deck dynamics, the pressure distribution around the deck and flaps can be measured and analyzed. To this purpose we leverage a 64-channel pressure sensing system⁴ available in our laboratory equipment. The sampling rate is user defined, and is maximally 500 Hz per channel in fast mode. The measurement data is communicated to the PC via an Ethernet connection, as depicted in Figure 5.9. The pressure measurement system is decoupled from the embedded system architecture, and batches of data are analyzed a posteriori. Thus, we cannot currently use the pressure sensor data for real-time control without a major integration effort. However, this is an interesting possibility that could be studied in future work.

Kwon et al. [16] also measured and analyzed the pressure distribution for their passively controlled model. Moreover, the approach of using local pressure measurements to compare experimental and analytical results has also been employed for canonical passive bridge section models [40]–[42].

⁴<http://www.meas-spec.com>

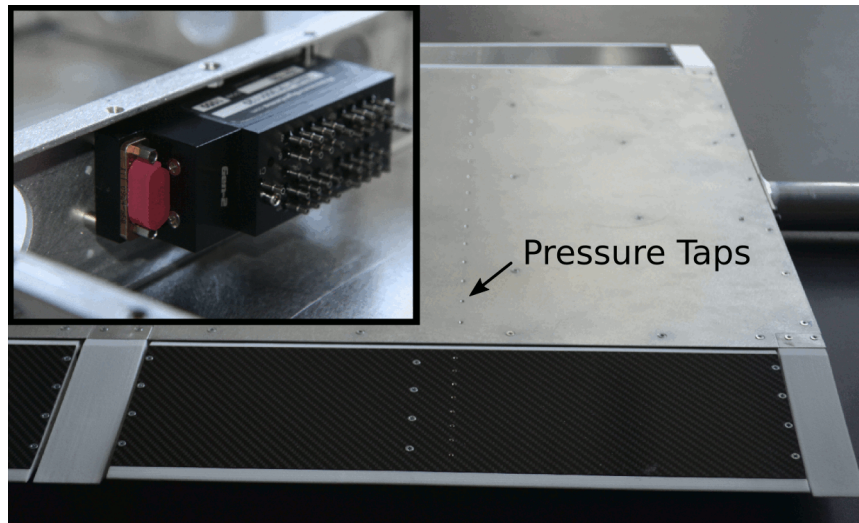


Figure 5.8 – The pressure taps are located along the streamline from the leading to the trailing edge flap, crossing over bridge deck. Upper left corner: pressure sensor attachment inside the deck.

The SmartBridge has thus been designed to accommodate the pressure sensing system. The pressure is measured locally at the surface of the model, at so-called pressure taps. Pressure taps are connected to the measuring unit with tubing elements that must be kept short in order to avoid noisy measurements. Therefore, it is necessary to place the pressure measuring unit inside the deck. Furthermore, depending on the experimental purpose, it will be interesting to measure the pressure at different places. Therefore, a great number of tap locations (264) have been made throughout the bridge deck and flaps. A few tap placements as well as the pressure measurement unit are presented in Figure 5.8.

Embedded system architecture

The system overview is shown in Figure 5.9. All nodes in the system, except for the laser sensors and the PC which are communicating via RS232, are hooked up to a CAN bus implementing a CANopen protocol (in particular CiA: DS-301 and CiA: DSP-402⁵). The supervisor microcontroller is the master node and is communicating information to and from the whole network to the PC and a Labview⁶ interface, from which all nodes in the network are managed. The synchronized laser sensor boards are receiving data from the laser sensors and forwarding them on the CAN bus together with a time stamp. Furthermore, the laser boards are controlling the electromagnets used for the pull-up mechanism, whereas the pull-up board is solely managing the motors used for the pull-ups. The control board is reading the deck position data and calculating set-points for the flaps, thus executing the control algorithm for the flap actuation.

⁵<http://www.can-cia.org>

⁶<http://www.ni.com/labview/>

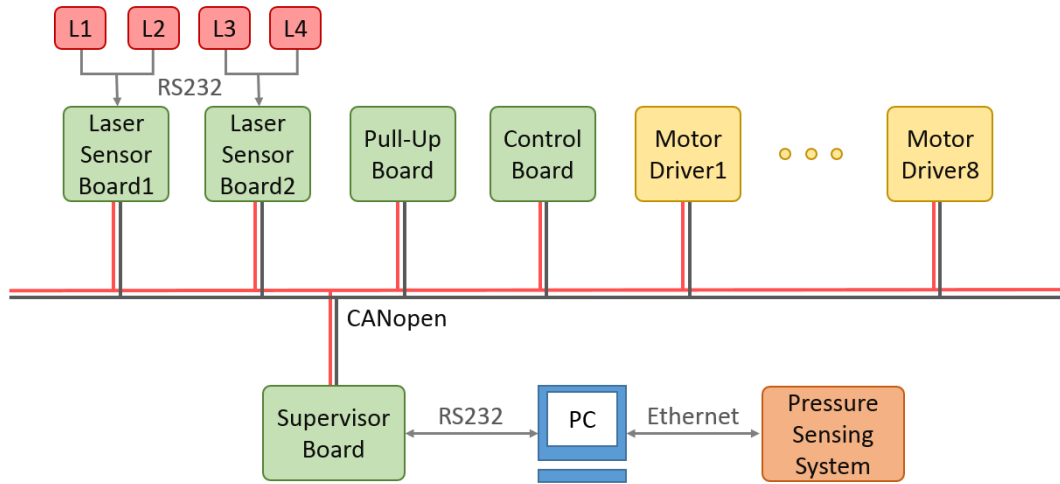


Figure 5.9 – A system overview of all the nodes in the network.

In the current configuration the speed of the CAN bus is set to 1 Mbit/s and each laser sensor board is sending the measured distances together with a time stamp at 200 Hz; each motor driver is receiving a set-point and sending its actual position at 200 Hz as well. Considering that each CAN data frame takes approximately $100\ \mu\text{s}$ to send, a complete control loop involving 2 sensor boards and 8 motor drivers occupies the bus for 1.8ms ($100\ \mu\text{s} * 2 + 100\ \mu\text{s} * 2 * 8$), i.e. a control loop at 200Hz requires 36% of the CAN bus capacity. Since the bus is not heavily loaded, it could be further used to send additional information (e.g., state of nodes) and/or increasing the update rate for the driver nodes (e.g., at 475 Hz the maximal recommended bus load of 80% would be reached).

5.1.5 User Interface

A dedicated Labview interface has been developed for the SmartBridge, from which a screenshot is shown in Figure 5.10. From this central point all the nodes in the embedded network can be reached, and most functionalities used. For instance, the control law and their corresponding parameters can be specified, homing of flaps executed, step responses semi-automatically performed, and communication rates set. Furthermore, the wind measurement data from the pitot tube is synchronized to the bridge state data and logged to file. Moreover, the wind tunnel fan can be operated. Although, the fan is usually operated manually, the wind is automatically turned off in case the software detects that the deck has moved outside the user-defined safety limit.

5.2 Experimental Site

All experimental work in this thesis have been carried out in a boundary layer wind tunnel on campus, see Figure 5.11. The wind tunnel consists of two testing channels arranged one above

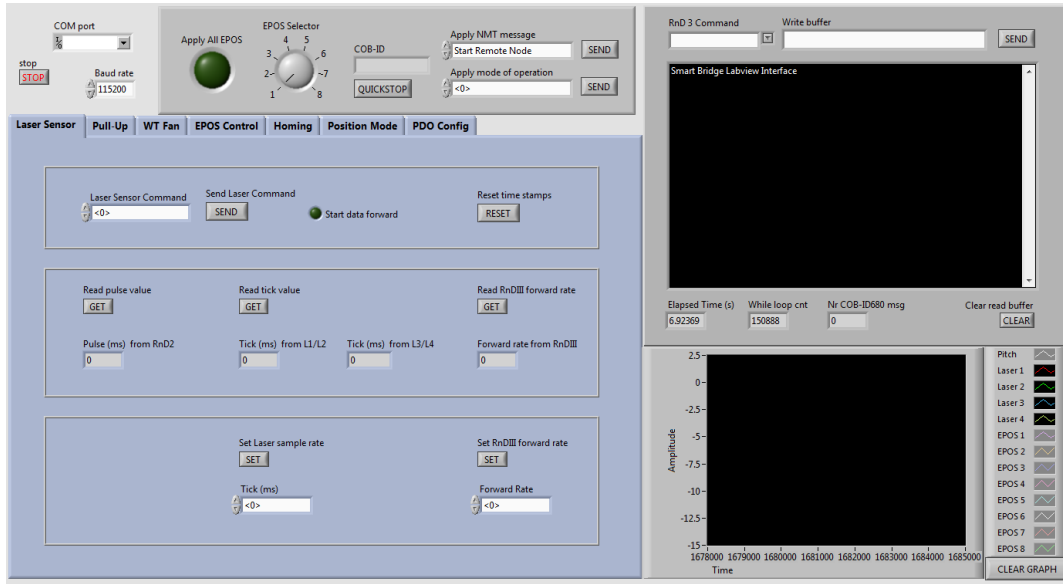


Figure 5.10 – Labview interface for the SmartBridge.

the other. The upper channel has a $4 \times 2 \text{ m}^2$ cross section while the lower one shows a $2 \times 1.45 \text{ m}^2$ cross section. The SmartBridge is installed in the lower channel that allows for the highest wind speed test, as seen in Figure 5.11c. Furthermore, the prototype flap test rig was placed closer to the contraction cone during the preliminary studies. The wind tunnel can be configured into open-loop or closed-loop operation. Since the highest wind speeds and the most laminar and uniform flow is achieved with the closed loop configuration, our experiments are run in this condition. The rotational speed of the fan is limited, thus constraining the wind speed to ca 16 m/s. Although, this software limit in principle can be exceeded to reach a wind speed up to 24 m/s, we have not done so for safety reasons (after a recent renovation, the infrastructure has not been validated yet for safe operation at such high wind speed range). We measure the wind speed locally with a pitot-tube fixed slightly upwind, and slightly above, the deck.

The lower channel is furthermore equipped with a multi-axis traversing system, as can be seen in the background of Figure 5.11a. For instance, wind sensing equipment can be attached to the robotic arm of the system and moved to precise points in the three dimensions of the channel to take measurements. This robotic system has not directly been used for experiments with the SmartBridge. However, it has been used to properly characterize the wind flow for the different operational configurations of the wind tunnel (e.g., open-/closed-loop, tilting of fan blades), thus determining the best experimental conditions. Note that the traversing system was moved downwind of the SmartBridge during experiments in order to avoid creating a turbulent flow over the deck.

The deck is installed inside the channel as can be seen in Figure 5.11a. However, the suspension system is located outside of the channel as to minimize its influence on the flow, and to maximize the possible length of the deck section. The channel wall is perforated on both sides

Chapter 5. Hardware Development and Experimental Site

so that the aluminum rods carrying the deck can pass through. These holes allow air to pass through and can create turbulence. In order to avoid this effect, airtight doors are installed on both sides of the channel wall, thus framing the whole suspension system, as seen in Figure 5.11b.

Summary

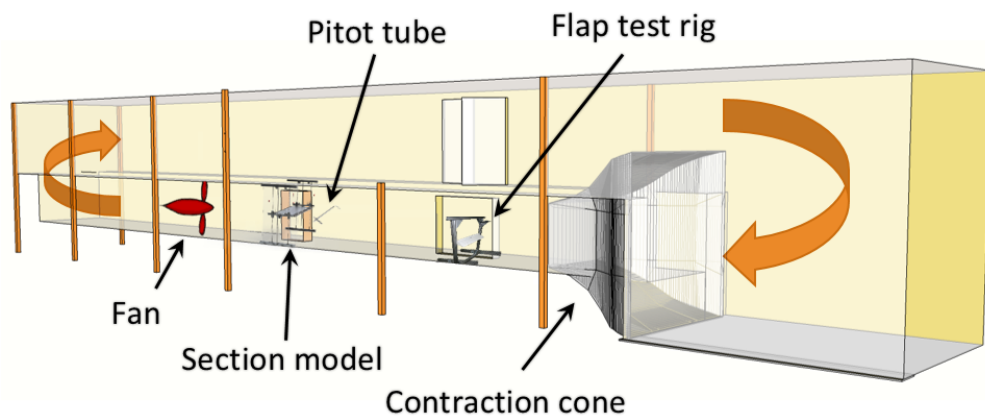
In this chapter we describe the hardware and software development of the SmartBridge and its dedicated suspension system, pull-up mechanism, and decoupling system. In particular, the design and dimensions of the deck are described and motivated. The flap design has been carefully evaluated in two iterations, resulting in a sturdy modular device containing both DC motor and driver. Moreover, we introduced the wind tunnel facilities and the different tools we have available there.



(a) The deck installed in the wind tunnel. In the background the traversing system is seen.



(b) Frame in wood around the deck suspension.



(c) Overview of the wind tunnel and setup.

Figure 5.11 – The SmartBridge experimental setup and the single prototype flap test rig placements in the lower channel of the boundary layer wind tunnel. The arrows indicate how the wind flows in the closed loop configuration.

6 Characterizing a Single Flap

PRIOR to building the SmartBridge, the single actuator unit was carefully assessed. In this chapter we present the primitive modeling and control effort conducted on the prototype flap described in Chapter 5. Our primary intentions were to verify that the prototype fulfilled the expected requirements for controlling the active deck, and to gain insights into modeling the nonlinear, noisy wind force that is exerted on the flap. Furthermore, we investigated a model-based control tuning for a single flap in order to further push the performance limits.

6.1 Premise

Towards the goal of realizing an actively controlled bridge section model, we carefully studied the dynamics of a single flap situated in a wind flow. A core challenge for an effective control law design is to properly capture the nonlinear, noisy wind force exerted on the flap. Neither Kobayashi nor Hansen, who aimed to investigate the feasibility of active flutter control using flaps, directly addressed the issue of position control of a single flap. Fowler and D’Andrea performed wind tunnel experiments researching aircraft flight formation [49]. They employed a manually tuned linear control law for the flap actuation. The flap angle was controlled in an open-loop fashion by a servo motor, while the control signal to the servo motor was generated in a closed-loop fashion taking into account the yaw and roll of the airfoil. The dynamic response of the system to the control input was captured by a fourth-order state-space model. However, they did not model the actual underlying physical mechanism of the interaction between the flap and the surrounding wind field.

In this chapter, we present a model-based approach, well-anchored to physical reality, allowing for fine tuning of a linear control law and its corresponding parameters. Not only does the model-based approach provide a safe control tuning environment, but also a flexible and fast platform for testing new control laws. Furthermore, a method for identifying the model parameters from experimental data is proposed, and the approach was validated with our prototype flap in the wind tunnel, as seen in Figure 5.6 in Chapter 5. The model was developed

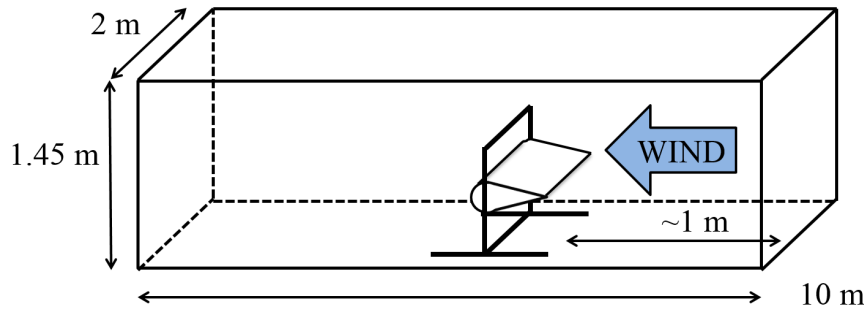


Figure 6.1 – The test rig placed inside the wind tunnel (not to scale).

in Matlab Simulink¹.

6.1.1 Material and Methods

We based the motor's speed and torque requirements upon approximate calculations and previous work within this field. The required flap speed depends on the motion of the bridge deck it controls since it will probably move at the same frequency, but with a different amplitude. The flap in Hansen's experimental setup moved at a frequency of 1.5 Hz and a maximal amplitude of $\pm 15^\circ$, and with 2.4 Hz and $\pm 5^\circ$ amplitude in Kobayashi's setup. We investigated a worst case scenario in terms of the flap's operating range and frequency, with movements of $\pm 30^\circ$ at the motor's top speed and acceleration, when a step takes approximately 80 ms and corresponds to 6.25 Hz.

As stated in Chapter 5, we used a 20 W DC motor with graphite brushes, gear reduction rate of 53:1, optical encoder, and a digital positioning controller, all from Maxon Motor Inc. The manufacturer provides an auto-tuning function that allows quick tuning of the motor control parameters (proportional, integral, and derivative coefficients). The tuning criterion can be set between a hard and a soft response, however, full tuning transparency is not provided. Running the auto-tuning procedure for the control parameters when the motor is placed inside the flap is possible. However, even when the flap is subjected to low wind speeds, the software aborts the tuning operation due to the nonsteady forces. Therefore, in this chapter whenever auto-tuned parameters are mentioned, they were tuned with the flap mounted, but without wind. The experiments were carried out in the wind tunnel, where the test rig was placed near the inlet, as seen in Figure 6.1 and in Figure 5.11c in Chapter 5.

6.2 Model Design

Our aim is to capture the dynamics of the experimental setup with a model that is well anchored to the physical reality. A control system is typically represented by a controller and a

¹<http://www.mathworks.com/products/simulink/>

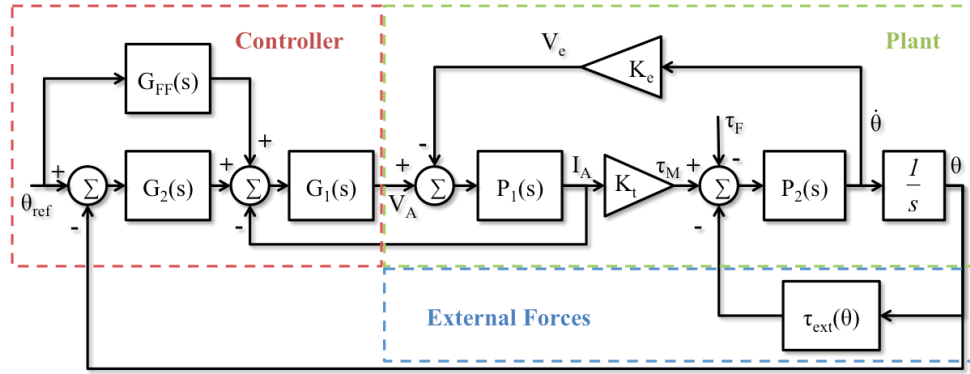


Figure 6.2 – Overview of the model.

plant, which in our case corresponds to the flap with the control unit and the motor mounted inside. Moreover, there are external forces that disturb our system, i.e., the gravity and the wind force. A schematic overview of the system is presented in Figure 6.2.

The manufacturer provides a position control with a cascade structure with an inner PI current control loop G_1 , an outer PID position control loop G_2 , and augmented by a speed and acceleration feed forward block G_{FF} . The flap and the DC motor are modeled by the process blocks P_1 , P_2 , the back EMF constant K_e , and the motor torque constant K_t . The external forces acting on the flap, gravity and wind, are assumed to be nonlinear functions of the flap angle and are modeled by the external torque block τ_{ext} in Figure 6.2. The various parts of the model are represented in the frequency domain by Laplace transforms. In the following sections each part of the model is described in detail.

6.2.1 The Plant: DC Motor and Flap

The DC motor is modeled with an electrical part (P_1 , K_e and K_t) and a mechanical part (P_2). The back EMF voltage is proportional to the motor speed, $V_e = K_e \dot{\theta}$, and following Lenz's law it is always counteracting the armature voltage, V_A . The resulting voltage generates the motor armature current, I_A , and is modeled by P_1 . The electrical torque produced by the motor is proportional to the armature current, $\tau_M = K_t I_A$. The total mechanical torque (including losses) generates the motor speed and is modeled by P_2 . The process blocks P_1 and P_2 are given by

$$P_1(s) = \frac{1}{Ls + R} \quad (6.1a)$$

$$P_2(s) = \frac{1}{Js + b} \quad (6.1b)$$

where L is the motor inductance, R is the motor resistance, J is the rotor inertia, b is the viscous friction constant and s is the Laplace variable.

Chapter 6. Characterizing a Single Flap

Mounting the motor in the flap increases the plant's inertia and friction force (mechanical and air resistance). This is simply accounted for by adjusting the mechanical parameters (J and b) and by adding a constant friction force τ_F , as seen in Figure 6.2.

6.2.2 PID Position Control

The motor position control is modeled by three parts: an inner current control loop, an outer position control loop, and a speed and acceleration feed forward,

$$G_1(s) = K_{P1} + \frac{1}{K_{I1}s} \quad (6.2a)$$

$$G_2(s) = K_{P2} + \frac{1}{K_{I2}s} + \frac{K_{D2}s}{K_{D2}/(NK_{P2})s + 1} \quad (6.2b)$$

$$G_{FF}(s) = \frac{1}{K_\omega s} + \frac{1}{K_\alpha s^2} \quad (6.2c)$$

where K_{P1} , K_{I1} , K_{P2} , K_{I2} , K_{D2} , N , K_ω and K_α are the control parameters. All parameters except the filter coefficient N (predefined value is 16) can be modified by the user. Furthermore, the output of blocks G_1 , G_2 are limited by 18 Volt and 3 Ampere, respectively. An anti-wind up method is implemented in order to avoid a growing integral part when the blocks are saturated. The details about the method the controller unit uses is not disclosed by the manufacturer; in our Matlab Simulink model a conditional integration method (also called integrator clamping) is used [50].

6.2.3 Modeling External Forces

Gravity and wind are the external forces acting on the flap that are considered in our model. However, only the force components that are perpendicular to the flap's symmetry axis, as seen in Figure 6.3, contribute to the motor torque. In the following sections the gravity and wind force models are described in detail.

Gravity model

Since the flap's center of mass and axis of rotation are not aligned, the gravity will affect the motor torque. The gravity-induced torque τ_G is described by

$$\tau_G = r_G F_G \cos(\theta) = r_G m g \cos(\theta) \quad (6.3)$$

where m is the mass, g is the gravitational field acceleration (9.81 m/s^2), r_G is the distance between the flap's center of rotation, c_r , and center of mass, c_m , and θ is the angle of the flap.

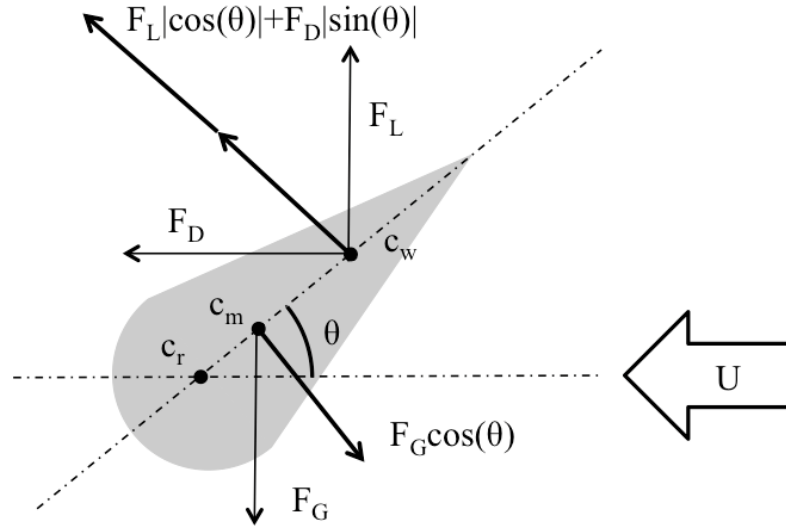


Figure 6.3 – External forces on the flap. The lift force, F_L , and the drag force, F_D , are functions of the wind speed, U . F_G is the gravity force. θ is the flap angle and c_r , c_m and c_w are the center of rotation, mass, and wind respectively.

Wind model

Assuming that the flap is flat (i.e. negligible thickness), the wind-induced torque τ_W is given by

$$\tau_W = r_W (F_L |\cos(\theta)| + F_D |\sin(\theta)|) \quad (6.4)$$

where F_L is the lift force, F_D is the drag force, r_W is the distance between the center of rotation, c_r , and the aerodynamic center, c_w , and θ is the flap's angle of attack. The aerodynamic center for a symmetric airfoil is typically located 1/4 of the chord length behind the leading edge and does not change position as the angle of attack does [51]. The drag and the lift forces are described by

$$F_D = \frac{1}{2} \rho U^2 C_D A \quad (6.5a)$$

$$F_L = \frac{1}{2} \rho U^2 C_L A \quad (6.5b)$$

where ρ is air density, U is the wind speed, A is the flap surface area, and C_D and C_L are the drag coefficient and lift coefficient, respectively. The drag and lift coefficients depend on the object's shape, surface roughness, Reynolds number, and fluid properties. Changing the flap's angle of attack is essentially equivalent to changing the object's shape. Therefore, the coefficients are functions of the flap's angle of attack, $C_D(\theta)$ and $C_L(\theta)$.

The drag and lift coefficients for different angles of attack can be estimated experimentally;

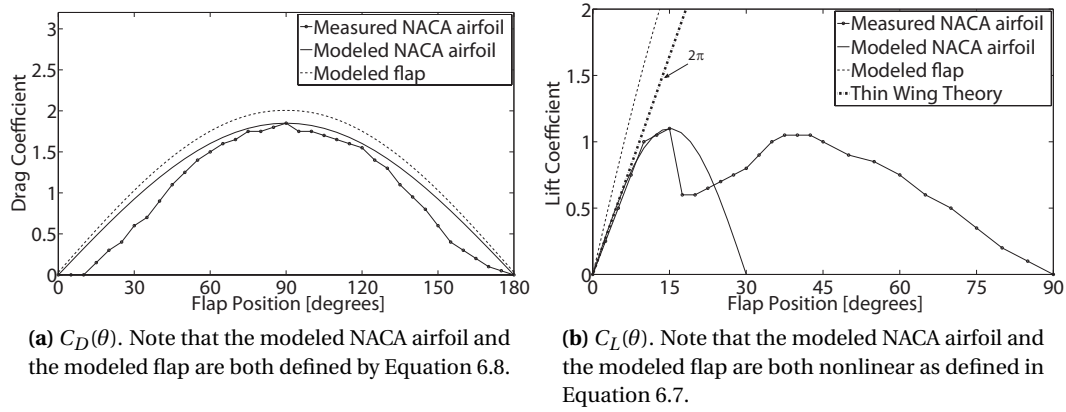


Figure 6.4 – Experimentally extracted $C_D(\theta)$ and $C_L(\theta)$ from a symmetric NACA airfoil [52]. The modeled flap curve is explained in Section 6.3.3.

Table 6.1 – Model Parameter Identification

Parameter	Range	Estimation	Data Sheet
J [gcm^2]	9.5:0.1:11	9.9	9.49
b [$\mu\text{Nms/rad}$]	0.5:0.1:1.5	1.0	0.87
τ_F [mNm]	0:0.02:0.12	0.1	-

extensive experimental results are available from wind tunnel tests on National Advisory Committee for Aeronautics (NACA) standard airfoils. Sheldahl and Klimas present an experimental study of extracting the lift and drag coefficients of a series of symmetric NACA airfoils [52], with angles of attack ranging from 0° to 180° . Although our flap cannot exactly be classified as a NACA airfoil, it is symmetric and the measured drag and lift coefficients for the airfoil with the closest dimensions to our flap (with a 15% thickness-to-chord length ratio compared to 37% for our flap) are given in Figure 6.4. The drag coefficient, in Figure 6.4a, is as one can expect maximized at 90° (vertical position) and zero at 0° and 180° (horizontal positions). In Figure 6.4b the effect of stall on the lift coefficient can be seen at approximately 15° . When the airfoil stalls, the airflow separates from the back, the pressure drops and the lift decreases. The angle at which stall occurs depends on the airfoil shape, the fluid properties, and the Reynolds number.

Furthermore, $C_L(\theta)$ can be approximated by the theory of thin wings for small angles of attack. To summarize the theory, any arbitrary airfoil is assumed to behave like a thin plate, with a proportional relationship between the angle of attack and the lift coefficient as described in [51]

$$C_L(\theta) = 2\pi\theta + C_{L0} \quad (6.6)$$

where θ is the angle of attack in radians and C_{L0} is the lift coefficient at 0° . When the airfoil is symmetric there is no lift at 0° , thus C_{L0} is zero. The proportional relationship in the stable

region (before stall) between C_L and θ can be verified by looking at Figure 6.4b, where the NACA airfoil experimental results are reasonably well modeled (until 10° roughly) by the thin wing theory in Equation 6.6. However, since the operating range of our flap include larger angles, a better model is required. We propose a nonlinear model that also captures the attenuation of $C_L(\theta)$ when the flap stalls,

$$C_L(\theta) = C_{L\theta_s} \sin\left(\frac{\pi}{2\theta_s}\theta\right) \quad (6.7)$$

where $C_{L\theta_s}$ is the maximal lift coefficient, which occurs at the stall angle, θ_s . It is seen in Figure 6.4b that the proposed model in Equation 6.7 applied to the NACA airfoil provides an improved lift model for large angles compared to the thin airfoil theory.

The drag coefficient can simply be approximated by

$$C_D(\theta) = C_{D90} \sin(\theta) \quad (6.8)$$

where C_{D90} is the drag coefficient at 90° . The model (6.8) is compared to the measured NACA airfoil result in Figure 6.4a.

6.3 Model Validation

Our approach for experimentally validating the above described models is detailed in the following sections.

6.3.1 Plant Model

The parameters for the DC motor model given in the data sheets were verified by comparing the model output and the measured output for the motor without flap or external forces. However, the mechanical parameters J , b and τ_F need to be re-evaluated for the motor mounted in the flap. In order to avoid gravity interference with the parameter estimation the flap was placed vertically. Usually, b and τ_F are estimated by performing a series of constant speed experiments, when there is no acceleration and a linear relationship between the measured armature current and motor speed is obtained, as can be seen in Equation 6.9. However, at high speeds, this method implies a flap movement of several rotations, an operation which is limited by cables in our test rig. Instead, we estimate all three parameters simultaneously with a series of position steps (varying the reference trajectories), where J , b and τ_F are tuned in order to minimize the Mean Square Error (MSE) between the measured and simulated position trajectories. Since the search space is small, a systematic parameter sweep, using the ranges given in Table 6.1, sufficed for estimating these parameters.

$$K_t I_A - \tau_F - \tau_{ext} = \mathcal{L}^{-1}\left(\frac{\omega(s)}{P_2(s)}\right) = J\ddot{\theta} + b\dot{\theta} \quad (6.9)$$

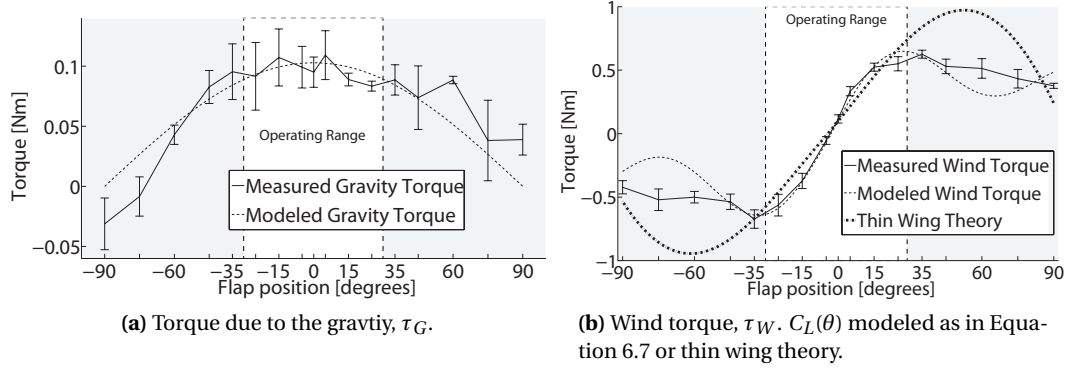


Figure 6.5 – Measured and modeled external torques, as a function of the angle of attack, θ . The error bars represent the standard deviation.

6.3.2 Gravity Model

The motor torque can be calculated from the measured armature current, as $\tau_M = K_t I_A$. While holding a static position, the motor torque is counteracting the external torque applied to the flap. The gravity torque can thus indirectly be measured when there is no wind force applied. The motor torque was measured at different flap angles (1536 samples taken at each position). The model parameters m and r_G were extracted from the CAD model of the flap. The mass of the motor and control unit was not considered since their center of mass is aligned with the flap's center of rotation.

The result from the static position measurements is compared to the gravity model described by Equation 6.3 in Figure 6.5a. The measured gravity torque is slightly asymmetric and noisy. The asymmetry might be due to the fact that the weight is not evenly distributed along the symmetry axis of the flap (top and down), or possibly due to asymmetries of the motor. However, the gravity model was not further developed, since the asymmetry effect is insignificant within the considered operating range ($\pm 30^\circ$), and the noise was ignored due to its negligible effect on the highly repeatable dynamic step responses (see Subsection 6.3.4).

6.3.3 Wind Model

The wind model was validated following the same experimental procedure as for the gravity model. The motor torque was measured at the same static angles, while the flap was under maximum wind load of 16 m/s. The measured motor torque then counteracts the combined effect of gravity, lift, and drag. The combined wind torque (lift and drag) was obtained by subtracting the mean measured gravity torque from the measured motor torque, and is presented in Figure 6.5b. Note that the flap stalls at approximately $\pm 30^\circ$, which also corresponds to our defined operating range.

The drag and lift coefficients, $C_D(\theta)$ and $C_L(\theta)$ cannot directly be estimated from the combined

wind torque. Except at a 90° angle, where there is only drag and no lift present, which allows C_{D90} in Equation 6.8 to be estimated (to a value of 2.0). Furthermore, by leveraging the drag coefficient model, $C_{L\theta_s}$ in Equation 6.7 can be estimated (to a value of 2.9) from the measured wind torque at the stall angle. The resulting models of $C_D(\theta)$ and $C_L(\theta)$ for the flap are seen in Figure 6.4a and Figure 6.4b respectively. We observe that the experimental drag coefficient of the NACA airfoil is well captured by our model, and is comparable to the drag coefficient of our modeled flap. On the other hand, while the experimental and the modeled lift coefficient of NACA airfoil are well aligned, the modeled lift coefficient of the flap is significantly different. However, it is to be expected that the lift coefficient is more affected by the difference in thickness-to-chord ratio between the flap and NACA airfoil.

The resulting combined wind torque models, from applying both the thin wing theory and our proposed lift coefficient model, are presented in Figure 6.5b. Even at small angles the thin wing theory does not capture the wind torque particularly well. This is not surprising since the approximation is stronger for the flap (larger thickness-to-chord ratio) compared to the airfoil. However, our wind model for the flap is validated within, and slightly beyond, the operating range.

6.3.4 Overall System Model

In order to validate the complete dynamic model, visualized in Figure 6.2, experimental data from position step responses at different wind speeds were compared with the model output. Note that the outcome of these steps, presented in Figure 6.6, is highly repeatable in any wind condition. The same control parameters were implemented on the physical and simulated control unit, and were set by the manufacturer's auto-tuning function. It is clear that the Matlab Simulink model is able to capture the flap dynamics and the wind effect.

6.4 Tuning Control Parameters

The flap position should ideally follow the reference trajectory closely. However, as seen in Figure 6.6, this is not the case: even without wind there is a noticeable overshoot. Therefore, we performed an offline optimization of the control parameters in our developed system model.

The control parameters that can be tuned in Equations 6.2 are K_{P1} , K_{I1} , K_{P2} , K_{I2} , K_{D2} , K_ω , and K_α . However, not all of them have the same impact in terms of overall system performance. For instance, the current control parameters (K_{P1} and K_{I1}) are already well tuned by the auto-tuning procedure and further optimization has only a minimal effect. Moreover, the speed feed forward K_ω was set to zero by the auto-tuning function, and our simulation confirms that increasing it only has a negative effect on the system performance. In the end, the following control parameters were tuned: K_{P2} , K_{I2} , K_{D2} , and K_α . Appropriate control parameter ranges were chosen manually (in simulation), and are presented in Table 6.2. The boundaries were

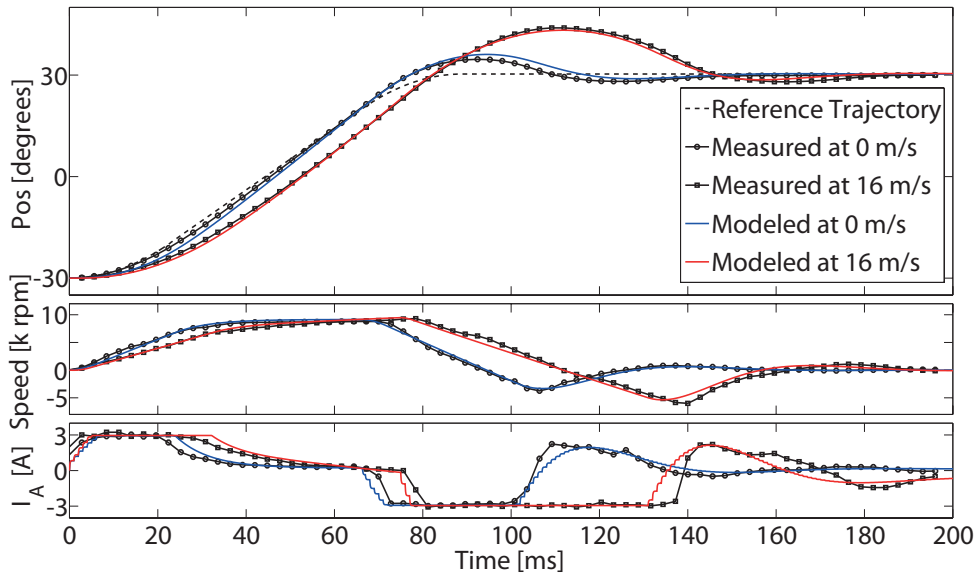


Figure 6.6 – Comparison of measured and simulated position steps of the flap at wind speeds of 0 m/s and 16 m/s.

Table 6.2 – Control Parameter Tuning

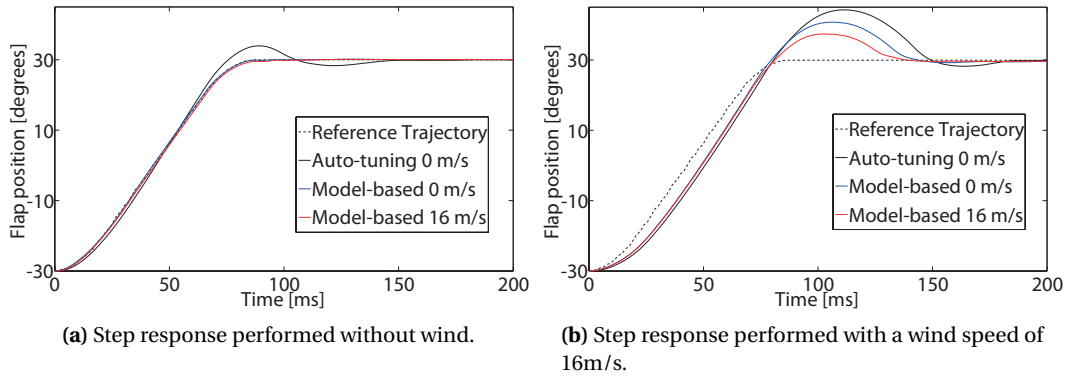
Parameter	Range	Auto-tuning	Model-based 0 m/s	Model-based 16 m/s
K_{P2}	100:25:500	148	325	400
K_{I2}	100:25:800	667	600	300
K_{D2}	150:25:600	176	325	400
K_{α}	25:25:250	23	100	250

chosen to avoid unstable regions or saturation effects. The increments were set as large as possible, while maintaining an insignificant effect on the performance. A systematic parameter sweep was made, with the MSE between the actual (simulated) position and the reference position as tuning criterion. The parameters were tuned for two wind speeds, 0 and 16 m/s, and the identified control parameters for the two scenarios are presented in Table 6.2.

The control parameters identified by auto-tuning and model-based tuning were validated with our experimental setup in the wind tunnel. Ten step responses of 60° were performed, both with and without wind, and for all three sets of control parameters (60 steps in total). Statistical results of these experiments are presented in Table 6.3. Note that the parameters tuned in the harshest environment worked well for all scenarios, while the parameters found for the case without wind did not perform as well for experiments with wind. Furthermore, model-based tuning, in any wind condition, but especially without wind, performs significantly better than auto-tuning. This is also evident in Figure 6.7, where a qualitative representation of the result is presented.

Table 6.3 – Control Performance Statistics

Scenario		Overshoot [%]			Reference Trajectory [°] MSE		
		Auto-tuned 0m/s	Model-based 0m/s	Model-based 16m/s	Auto-tuned 0m/s	Model-based 0m/s	Model-based 16m/s
0 m/s	mean	7.5	0.8	0.5	4.0	0.5	0.4
	std	0.08	0.04	0.04	0.1	0.02	0.02
16 m/s	mean	23.6	18.5	13.6	48.5	29.6	20.0
	std	0.22	0.22	0.28	0.95	0.64	0.56

**Figure 6.7** – Measured data from position steps, comparing the performance of the auto-tuning and model-based tuning procedures.

6.5 Evaluation of Results

In this chapter, we proposed and validated a physically grounded model for a flap system operating in diverse wind conditions. We used this model to design and optimize a linear control law for the position of the flap. While in this work we focused exclusively on the position control, the proposed model is detailed enough to allow tuning of control laws concerned with speed and torque.

The emphasis of this work has been on validating the model, while the tuning approach of the control parameters was crude and only to the point of showing a valid result. However, we showed that a parameter-tuning procedure based on our model outperforms the auto-tuning function provided by the manufacturer. Moreover, although more sophisticated optimization algorithms could be used, we believe we are approaching the performance limit of linear control principles, possibly also the physical limits of the motor, for this application.

Furthermore, the results indicate that little or nothing is gained by varying the control parameters depending on the wind speed. Control parameters tuned for the harshest conditions, the maximal wind speed in our case, perform very well also for lower wind speeds within the desired range of operation.

Although, the model-based tuning approach significantly improved the performance of the actuation, the reference trajectory is not satisfactory followed in the harshest wind condition.

Chapter 6. Characterizing a Single Flap

However, we investigated the worst case scenario here, with fast oscillation and very large amplitude, that is highly unlikely to be required during normal operation of the active deck. Ultimately, we did not experience any problems with the flap position control performance during our experiments with the active deck.

Summary

In this chapter, we have thoroughly investigated the performance of a single flap actuator unit. Furthermore, we proposed a model able to properly capture the nonlinear interaction between wind and the structure. Moreover, we optimized a linear control law for the flap position able to robustly cope with the nonlinear forces exerted on the flap. Finally, the model accuracy and the system performance were systematically validated by wind tunnel experiments.

7 Conclusion

WE have in this part presented the contribution of this thesis in terms of mechatronic design. We have thoroughly motivated the hardware and software design choices, and have situated our active bridge deck model in the context of related work. Moreover, we presented the intermediate, in-depth performance analysis of a single flap.

For the preliminary modeling and control effort in Chapter 6, we investigated the performance of the prototype flap attached to a dedicated test rig. A model capable of properly capture the nonlinear interaction between wind and the structure was developed. Moreover, we optimized a linear control law for the flap position able to robustly cope with the nonlinear forces exerted on the flap. Systematic wind tunnel experiments were made in order to validate the model accuracy and the system performance. Although, the model-based tuning approach significantly improved the performance of the actuation, the actuation still had a slower rise time, and a slight overshoot, in respect to the target trajectory, for the harshest experimental conditions. However, since the performance was still satisfactory, and the tested harsh case was extreme and unlikely for the normal operation, no further improvements in control or new hardware choices were made. Indeed, we did not encounter any problems with the flap actuation in terms of accuracy during our experiments with the active deck.

The analytical model of the full, active, section model is covered in Part III, and does not include the actuation dynamics of the single flap. Specifically, the full bridge model assumes that a flap is precisely and instantly moved to a desired set point. Naturally, in reality, there is an actuation lag, the one we observed and were able to reliably model in Chapter 6. However, the developed single flap model is quite complex and not well suited for this purpose. Instead, a simpler second, or even first, order system description (calibrated to the operating wind speed), would be a better option. The main purpose of the model developed here was instead to properly understand and improve the performance of the single actuator unit. Still, if the flap actuation dynamics was to be included into the full bridge deck analytical model in future work, the lessons learned here would be valuable.

Chapter 7. Conclusion

The hardware development phase resulted in the SmartBridge, a novel bridge section model equipped with actively controlled flaps, as presented in Chapter 5. Furthermore, we developed a dedicated suspension system, a pull-up mechanism, and a decoupling system that complete the overall setup. This supporting structure is an essential part of the setup that allows us to conduct reliable and repeatable experiments on the SmartBridge. The design of the bridge deck allows for easy access to electronics, cables, and tubing. Furthermore, the design is modular and changeable, allowing modifications of system parameters such as natural frequencies, and providing a flexible platform for conducting pressure measurements.

Summary

In this chapter we conclude the mechatronic design part of the thesis. The main outcome of this effort is the SmartBridge and its dedicated support system. The SmartBridge is the first section model equipped with flap arrays and is unique in its modular design. The overall supporting structure allows for repeatable and quick experiments in the wind tunnel. Finally, we provided a thorough characterization of the performance of a single flap.

Model Part III

8 Related Work

AEROELASTIC phenomena are characterized by strong interactions between aerodynamic forces and structural motions. In particular, aeroelastic instabilities occur when aerodynamic forces acting on a structure yield a movement that in turn create stronger aerodynamic effects, so-called *self-excited* forces [37]. Although many types of aeroelastic phenomena can affect a long-span bridge, e.g., vortex shedding, galloping, torsional divergence, flutter, and buffeting response, we will mainly focus on the flutter instability problem in this thesis, since it is the most destructive phenomenon. Nevertheless, an actively controlled flap system is a promising approach also for controlling other types of aeroelastic instabilities. In this chapter we will provide a general introduction to flutter, as well as provide an overview of existing modeling methods for canonical bridge decks and particularly for those equipped with mobile flaps.

8.1 Historical View of Flutter

One century ago, in 1916, the first case of flutter was recognized for a Handley Page bomber airplane [53]. A milestone for the theoretical studies of the phenomenon was published in 1935 by Theodorsen [54], where he provided an exact solution for an harmonically oscillating theoretical flat plate (wing). It was only after the collapse of the Tacoma Narrows Bridge in 1940 that the flutter problem was recognized for bridge decks. However, the first attempt to link the theoretical models for a flat plate to a bridge deck proved difficult because of the bluff-body dynamics inherent to the deck. In the late 1960s flutter derivatives were commonly obtained from wind tunnel experiments [55]. A notable paper relating airfoil and bridge deck flutter was published by Scanlan and Tomko in 1971 [56].

During the last century, many sub-classes of flutter have been classified, e.g., classical, stall, single DOF, and panel flutter. We have limited our study to classical, sometimes called coupled, flutter, which implies that the heave and pitch DOF of the structure couple together, in wind-induced unstable oscillations [37]. Thus, from here on when flutter is mentioned in this manuscript, we refer to the classical flutter type.

8.2 Two-Dimensional Analytical Model of Bridge Flutter

The simplest analytical model describing the motion of a bridge section includes two DOFs: heaving and pitching motion. In near-flutter conditions, the system is described by two linear coupled differential equations. The lift and moment generated by the airflow around the section depend on the motion of the section thus creating a coupling between the heaving and pitching motion. The parameters describing the coupling are functions of the wind speed and the oscillation frequency, and are called Flutter Derivatives (FDs) [37]. The structure and definition of the FDs are essentially based on Theodorsen's circulatory function for thin airfoils [54]. Since most cross-sections of full-scale bridges cannot be approximated as thin plates, it is common practice to identify the FDs through wind tunnel tests. The coupled two DOFs model is considered the state-of-the-art engineering model for predicting the critical wind speed triggering flutter in bridges.

8.2.1 Aerodynamic Model of a Deck with Mobile Flaps

Actively controlled flaps were studied experimentally and theoretically in the pioneering work of Kobayashi et al. [14], [24]. They extended the analytical model for a canonical bridge deck to include flaps, by introducing additional flap flutter derivatives that were also calculated based on the thin airfoil theory (i.e., Theodorsen's circulatory function). Hansen [27] and Starossek et al. [17] both employ similar theoretical models, with additional flutter derivatives for the flaps described by Theodorsen's circulatory function.

Rational Function Approximation

A simplification of the approach of Kobayashi et al. [14] was presented by Wilde and Fujino [57] and later leveraged for their experimental study in [15]. Instead of using Theodorsen's frequency-dependent circulatory function, they approximate the unsteady aerodynamic forces with a Rational Function Approximation (RFA) approach, by deriving a parameter representation of the FDs that is frequency-independent. Thus, the equations of motion can be purely formulated in the time-domain, which is convenient since it allows the use of classical control analysis tools (e.g., root locus or Nyquist diagrams). RFA methods were also employed in the experimental work of Zhao et al. [21]–[23] and Phan et al. [19], as well as in several purely theoretical contributions for bridge decks equipped with mobile flaps [38], [57]–[68].

8.2.2 Structural Dynamics of a Deck with Mobile Flaps

Generally, when analytical models of bridge decks with mobile flaps are derived, independently of the exact formulation of the flap's aerodynamic forces, their contribution to the structural dynamics of the system is ignored, i.e., only the structural properties of the deck as a whole are considered. Nevertheless, Zhao et al. [67] did propose an analytical formulation that also

considers the flap's structural dynamics; however, it has not been validated experimentally since this approach was not leveraged for their wind tunnel study in [21].

8.2.3 Experimental Validation of Analytical Models of Controlled Decks

While there are many examples of theoretical studies using moving flaps to dampen bridge deck oscillations, particularly with respect to the flutter phenomenon, only the few research groups that were presented in Chapter 2 have provided experimental evaluations of the controlled decks.

Kobayashi et al. [14] showed with wind tunnel experiments that they could increase the flutter wind speed by 50%. However, the experimental and theoretical results (flutter always suppressed) did not match well, a fact that the authors mainly attributed to the occurrence of torsional divergence, an effect that was not taken into account in their model. Hansen et al. also designed a bridge deck capable of stabilizing the bridge vibrations, with actively controlled flaps attached to the deck using a similar control approach [29]. However, they also reported problems verifying their model because the torsional divergence wind speed was too close to the flutter wind speed. Wilde et al. proposed a pendulum solution for passively actuating flaps, and were able to increase the flutter wind speed by 57% experimentally [15]. However, the experimental and analytical results only concurred for very small gain values; authors hypothesized that this discrepancy was due to aerodynamic forces of the system not modeled correctly. Moreover, Starossek et al. designed a system with passively controlled flaps using Tuned Mass Dampers (TMDs) [17]. Although, they showed experimental results with increased deck vibration damping using controlled flaps, they did not disclose a comparison between experimental and theoretical results. Kwon et al. designed passively actuated control surfaces using TMDs and control surfaces that moved in and out of slots from the bottom of the deck [16]. They achieved an increase of the flutter wind speed by 43% with the TMDs augmented by the corresponding control surfaces, and by 37% using only the TMDs (control surfaces removed). They included structural properties of the TMDs in their model; however, they did not consider any aerodynamic force contributions from the control surfaces. Consequently, they showed a very good relation between the experimental and analytical result for the flutter control using only TMDs, and a large discrepancy for the flutter control using TMDs and control surfaces. Zhao et al. [21] emulated a passive control law, and showed that the flutter wind speed could be increased by 18.3%, compared to the model prediction of 20%. However, the absolute values do not correspond satisfactorily, for instance, the uncontrolled deck flutters at 17.5 m/s while the model predicts 20 m/s. The authors comment that this is likely due to the fact that theoretical aerodynamic parameters were implemented instead of experimentally extracted. Gouder, Zhao, Limebeer and Graham [23], leveraging the same experimental setup, noted that the theoretical damping prediction was higher than the one observed from experiments when only one flap was being controlled, and this was particularly evident concerning the trailing flap. They attribute the loss of efficiency for the trailing flap to the fact that it is operating in the separated wake of the deck and leading flap. However,

when they controlled both of the flaps simultaneously they noted that the theoretical damping prediction was instead lower than the observed one. They indicated that the reason for this discrepancy was due to the fact that the aerodynamic model parameters were not estimated from the setup.

Notably, an experimental estimation of all the aerodynamic parameters were reported by Phan et al. [19]. Although their experimental and model results appear to match well, they do not provide a comparison between simulated and real flutter wind speed, or between the theoretical and estimated flap flutter derivatives.

8.3 Other Modeling Techniques for a Deck with Mobile Flaps

The two-dimensional analytical model is widely used, and particularly for studies of section models. However, there exists other modeling techniques for predicting the aeroelastic behavior of a bridge deck. In this section we present two additional methods of importance.

8.3.1 Multi-Mode Analytical Model

The multi-mode model is in principle a 3D analytical model, where the two-dimensional formulation is leveraged and the third dimension is being modeled by the mode shapes of the bridge. Although Kwon et al. [16] did not include the flaps in the analytical model, they created a multi-mode model using the approach of Jain, Jones and Scanlan [69]. However, they do analyze the flutter behavior of the passively controlled setup, and calculate the FDs, by measuring the pressure around the section. However, the experimental results of the controlled setup do not compare well with the analytical 2D model (upon which their multi-mode model is based) in terms of predictions of the flutter wind speed. The multi-mode approach for an actively controlled bridge setup has also been investigated in purely theoretical work (e.g., Kwon et al. [70], Arco et al. [71], and Nissen et al. [72]).

8.3.2 Numerical Models

The aeroelastic stability of canonical bridge sections have been modeled with numerical Fluid-Structure Interaction (FSI) methods. Computational Fluid Dynamics (CFD) is used to model the fluid flow and is based on the numerical discretization of the Navier-Stokes equations. These equations are highly nonlinear and simulating the full equations is computationally very demanding. Therefore it is practical to employ simplified versions of the equations, using approximate turbulence models such as Large Eddy Simulation (LES) or Reynolds-Averaged Navier-Stokes (RANS). For example, Sun et al. [73] employed a RANS method to model a bridge section in 2D and 3D, and the obtained FDs were in good agreement with experimental results. Recently, the Unsteady RANS (URANS) method was used by Sarkic, Fisch, Hoeffler and Bletzinger [42] to simulate aeroelastic surface pressures, integrated forces, and to identify

FDs of a 2D bridge section. The work showed that good predictions of FDs are obtained for moderate wind velocities. LES has also been used to simulate the turbulent wind flow; for example Sarwar et al. [74] were able to validate the simulation with experimental results of the flutter phenomenon. Another, pioneering, example of a CFD simulation is the work of Larsen and Walther [75], [76]. They modeled the turbulence with the grid-free Discrete Vortex Method (DVM) and investigated flutter on several bridge sections in a 2D setting. The FDs extracted from their results displayed a fair agreement with experimentally obtained FDs. However, as pointed out by [73], although the DVM is computationally efficient, it has been criticized for not being readily extended to 3D flows. Furthermore, the flutter wind speed for a 2D bridge section has been investigated with Navier-Stokes equations for laminar flow (no turbulence model) by Frandsen [77], where the obtained flutter wind speed compared well to experimental results. However, normally a turbulence model should be employed when simulating a flow at such high Reynolds numbers. These works suggest that CFD methods have achieved a grade of maturity that allows simulating aeroelastic phenomena of canonical bridge section models.

Up to date, we have encountered two separate studies that have formulated a numerical framework for a bridge controlled by flaps. Preidikman and Mook [78] developed a time-domain numerical model in which a bridge section with a single movable winglet placed below the deck interacts with flowing air. The aerodynamic forces acting on the bridge deck and on the winglet were computed with a CFD model based on DVM. However, their work did not contain any experimental validation of the simulated results. Additionally, Li, Ge, and Zha [79] considered a two-dimensional section model being controlled with a twin-winglet system operating above the deck. They proposed a modeling framework where the aerodynamic forces acting on the deck and flaps are obtained from CFD simulations (URANS), and are iteratively calculated as the mesh is updated according to the changes in states produced by the control law. However, they did not either produce any experimental validation of their approach.

8.4 Concluding Remarks

While the extended two-dimensional analytical model is widely used for modeling bridge decks endowed with mobile flaps, it is currently unclear how well it is actually faithfully representing the real system. Although, it is the only modeling approach that have been leveraged for wind tunnel studies, the rare experimental results indicate that the assumptions made by the model are too strong.

In order to validate this baseline approach for an actively controlled bridge deck, we sought out to thoroughly investigate an analytical model by leveraging our experimental setup that was described in Part II. Other, more complex modeling techniques involving numerical or multi-mode models are outside the scope of this thesis.

Summary

In this chapter we introduced the aeroelastic phenomenon of flutter and different state of the art modeling techniques used to predict its influence on a long-span bridge. In particular, we focus our attention to modeling efforts that have considered mobile flaps. Most frequently, researchers and practitioners have employed a two-dimensional analytical model extended with aerodynamic parameters for the flaps. However, such an approach has not been extensively evaluated with wind tunnel experiments. Therefore, we will present our ambition to do so in the following chapters.

9 Two-Dimensional Analytic Flutter Model

IN this chapter we present analytical flutter models of traditional bridge decks as well as for bridge decks equipped with flaps. The structural model and the aerodynamic model are discussed individually; the complexity of the structural model we investigated is higher than what is usually considered in the literature. Furthermore, the closed-form solution to the flutter problem is presented for the uncontrolled deck, and an extended version of the solution is derived for a controlled bridge deck. Finally, we present different simplification methods of the flutter problem found in the literature.

9.1 Flutter Model of a Canonical Bridge Deck

The analytical model of the bridge section model is based on the heave and pitch DOFs, the two fundamental modes involved in coupled flutter. The two-dimensional model of the bridge deck and definitions of positive directions, are visualized in Figure 9.1.

9.1.1 Structural Model

The structural dynamics can be modeled as two harmonic oscillators in the heave and pitch DOFs, as described below [37]

$$m\ddot{h} + S\ddot{\alpha} + 2m\zeta_h\omega_h\dot{h} + m\omega_h^2 h = L_h \quad (9.1a)$$

$$S\ddot{h} + I\ddot{\alpha} + 2I\zeta_\alpha\omega_\alpha\dot{\alpha} + I\omega_\alpha^2 \alpha = M_\alpha \quad (9.1b)$$

where h and α are the heave and pitch positions, m is the mass per unit length of the deck, I is the mass moment of inertia per unit length of the deck, ζ_h and ζ_α are the damping ratios in the heave and pitch DOFs, ω_h and ω_α are their natural circular frequencies, and S is the static moment of the deck per unit length ($S = mr_e$, where r_e is the distance between the center of mass and the elastic center of the deck). Note that the structural dynamics are uncoupled if the center of mass and the elastic center overlap, i.e. if $r_e = 0$, which is a common assumption

for a symmetric bridge deck. The bridge deck is eccentric if $r_e \neq 0$; eccentric canonical bridge decks have been studied by e.g. Chen et al. [80] and Sarker et al. [81]. Moreover, L_h and M_α are external lift and moment exerted on the deck, thus if there is no wind acting on the deck the right-hand sides of Equations 9.1 are zero.

9.1.2 Aerodynamic Model

The model of the external lift and moment caused by the aerodynamic forces on a canonical bridge section model can be expressed in linear form with Theodorsen's flutter derivatives [54]. The aerodynamic forces are then described by [37]

$$L_h = \frac{1}{2} \rho U^2 B K \left[H_1^*(K) \frac{\dot{h}}{U} + H_2^*(K) \frac{B \dot{\alpha}}{U} + K H_3^*(K) \alpha + K H_4^*(K) \frac{h}{B} \right] \quad (9.2a)$$

$$M_\alpha = \frac{1}{2} \rho U^2 B^2 K \left[A_1^*(K) \frac{\dot{h}}{U} + A_2^*(K) \frac{B \dot{\alpha}}{U} + K A_3^*(K) \alpha + K A_4^*(K) \frac{h}{B} \right] \quad (9.2b)$$

where ρ is the air density, B is the bridge deck width, U is the wind speed, $K = B\omega/U$ is the reduced frequency, and H_1^*, \dots, H_4^* and A_1^*, \dots, A_4^* are the non-dimensional flutter derivatives for the deck. Note that the flutter derivatives are not constant model parameters, but dependent on the reduced frequency, K . The theoretical flutter derivatives for a flat plate are calculated as follows [37]

$$H_1^*(K) = -\frac{2\pi F(K)}{K} \quad (9.3a)$$

$$H_2^*(K) = -\frac{\pi}{2K} \left[1 + \frac{4G(K)}{K} + 2 \left(\frac{1}{2} - r_e \right) F(K) \right] \quad (9.3b)$$

$$H_3^*(K) = -\frac{\pi}{K^2} \left[2F(K) - \left(\frac{1}{2} - r_e \right) K G(K) + \frac{r_e K^2}{4} \right] \quad (9.3c)$$

$$H_4^*(K) = \frac{\pi}{2} \left[1 + \frac{4G(K)}{K} \right] \quad (9.3d)$$

$$A_1^*(K) = \frac{\pi F(K)}{K} \left(r_e + \frac{1}{2} \right) \quad (9.3e)$$

$$A_2^*(K) = -\frac{\pi}{2K} \left[\frac{\left(\frac{1}{2} - r_e \right)}{2} - \frac{2G(K)}{K} \left(r_e + \frac{1}{2} \right) + F(K) \left(r_e^2 - \frac{1}{4} \right) \right] \quad (9.3f)$$

$$A_3^*(K) = \frac{\pi}{2K^2} \left[\frac{K^2}{4} \left(r_e^2 + \frac{1}{8} \right) + 2F(K) \left(r_e + \frac{1}{2} \right) + K G(K) \left(r_e^2 - \frac{1}{4} \right) \right] \quad (9.3g)$$

$$A_4^*(K) = -\frac{\pi}{2} \left(\frac{r_e}{2} + \frac{2G(K)}{K} \left(r_e + \frac{1}{2} \right) \right) \quad (9.3h)$$

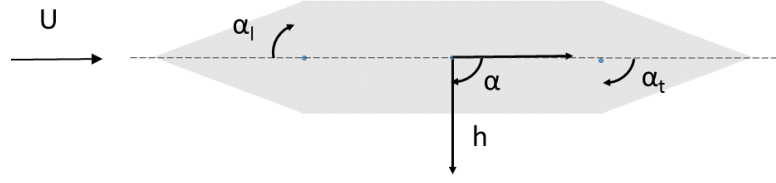


Figure 9.1 – Definitions of positive directions in the heave and pitch DOFs.

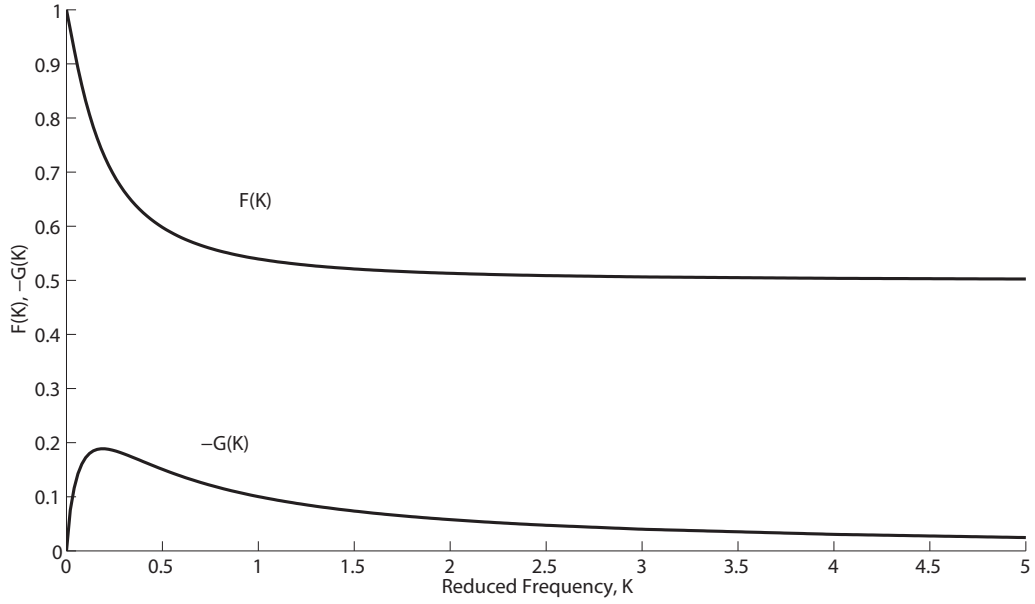


Figure 9.2 – The real (F) and imaginary (G) parts of Theodorsen's circulatory function as functions of the reduced frequency K.

where $F(K)$ and $G(K)$ are the real and imaginary parts of Theodorsen's circulatory function, $C(K) = F(K) + iG(K)$ [54]. We have implemented the approximation of the circulatory function found in [53], where the function's real and imaginary parts, plotted in Figure 9.2, are described by

$$C(K) = 1 - \frac{0.165}{1 - \frac{0.0455}{K}i} - \frac{0.335}{1 - \frac{0.3}{K}i} \quad (9.4)$$

9.2 Flutter Model of a Bridge Deck Endowed with Flaps

The flutter phenomenon is well studied in the aeronautic field, also for wings equipped with ailerons. The similarities of this application to that of a bridge deck equipped with flaps are

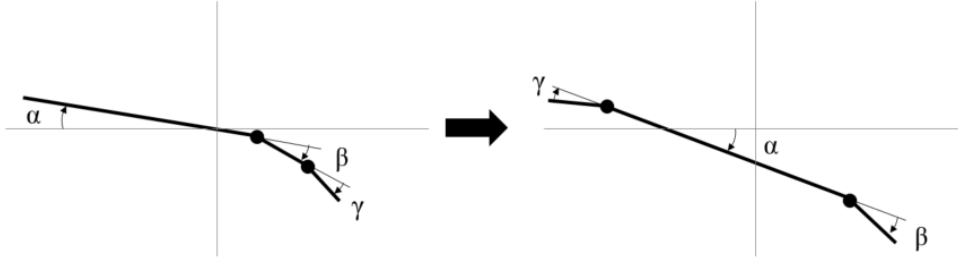


Figure 9.3 – The wing-aileron-tab combination and the transformation to a bridge deck with leading and trailing flaps.

significant. We are therefore expressing the structural dynamics of the bridge deck endowed with flaps analogously to a wing equipped with an aileron, and model the aerodynamic effects using an adapted version of the wing-aileron-tab formulation. The two-dimensional model of the bridge deck equipped with flaps and definitions of positive directions, are visualized in Figure 9.1.

9.2.1 Structural Model

The derivation of a structural (and aerodynamic) model of a wing equipped with an aileron is thoroughly described by Scanlan et al. [82]. We express the structural dynamics of the bridge deck equipped with a trailing and a leading flap, analogously to the wing and aileron, as

$$m\ddot{h} + S\ddot{\alpha} + S_t\ddot{\alpha}_t + S_l\ddot{\alpha}_l + 2m\zeta_h\omega_h\dot{h} + m\omega_h^2 h = L_h + L_t + L_l \quad (9.5a)$$

$$S\ddot{h} + I\ddot{\alpha} + (r_t S_t + I_t)\ddot{\alpha}_t + (r_l S_l + I_l)\ddot{\alpha}_l + 2I\zeta_\alpha\omega_\alpha\dot{\alpha} + I\omega_\alpha^2 \alpha = M_\alpha + M_t + M_l \quad (9.5b)$$

where α_t and α_l are the trailing and leading flap positions, S_t and S_l are the static moments per unit length about the trailing and leading flap hinges respectively, and I_t and I_l are the mass moments of inertia per unit length about the trailing and leading flap hinges, respectively. Moreover, r_t and r_l are the distances between the deck's center of rotation and the hinge positions of the trailing and leading flaps, respectively. Note that if the static moments and mass moments of inertia of the flaps are set to zero, the expression on the left hand side of Equations 9.5 revert to the ones in Equations 9.1, i.e., ignoring inertia effects of the flaps.

9.2.2 Aerodynamic Model

In order to consider the external lift and moment caused by the flaps the model can be extended with a modified version of the wing-aileron-tab configuration (transformed into a bridge deck with leading and trailing flaps) developed by Theodorsen and Garrick [83], as in Figure 9.3. The model can be applied to a bridge deck with flaps considering the following assumptions:

9.2. Flutter Model of a Bridge Deck Endowed with Flaps

- The wind speed is at the fluttering point, thus the deck oscillations are harmonic.
- Up-wind elements do not disturb the flow around the down-wind elements.
- Both the deck and flaps are flat plates (for theoretical FDs).
- Flaps move at the same frequency as the bridge deck.

Under these assumptions, the additional lifts and moments generated by the flaps can be superposed to those of the canonical deck, i.e., L_h and M_α in Equations 9.2. The reader is referred to the thesis of Hansen [27] for the derivation of the expressions for the flap lifts and moments. The aerodynamic forces due to the flaps are described by additional flutter derivatives as follows

$$L_t = \frac{1}{2} \rho U^2 B K \left[H_5^*(K) \frac{B \dot{\alpha}_t}{U} + K H_6^*(K) \alpha_t \right] \quad (9.6a)$$

$$M_t = \frac{1}{2} \rho U^2 B^2 K \left[A_5^*(K) \frac{B \dot{\alpha}_t}{U} + K A_6^*(K) \alpha_t \right] \quad (9.6b)$$

$$L_l = \frac{1}{2} \rho U^2 B K \left[H_7^*(K) \frac{B \dot{\alpha}_l}{U} + K H_8^*(K) \alpha_l \right] \quad (9.6c)$$

$$M_l = \frac{1}{2} \rho U^2 B^2 K \left[A_7^*(K) \frac{B \dot{\alpha}_l}{U} + K A_8^*(K) \alpha_l \right] \quad (9.6d)$$

where the additional flutter derivatives due to the flaps, H_5^*, \dots, H_8^* and A_5^*, \dots, A_8^* , are given in the following equations

$$H_5^*(K) = \frac{1}{2K} \left[T_4 - F(K) T_{11} - \frac{4G(K) T_{10}}{K} \right] \quad (9.7a)$$

$$H_6^*(K) = \frac{1}{K^2} \left[-\frac{K^2 T_1}{4} - 2F(K) T_{10} + \frac{KG(K) T_{11}}{2} \right] \quad (9.7b)$$

$$H_7^*(K) = \frac{T_4}{2K} \quad (9.7c)$$

$$H_8^*(K) = -\frac{T_1}{4} \quad (9.7d)$$

$$A_5^*(K) = \frac{1}{4K} \left[-T_1 + T_8 + cT_4 - \frac{T_{11}}{2} + \frac{F(K) T_{11}}{2} + \frac{2G(K) T_{10}}{K} \right] \quad (9.7e)$$

$$A_6^*(K) = \frac{1}{2K^2} \left[-T_1 - T_{10} - \frac{K^2(T_7 + cT_1)}{4} + F(K) T_{10} + \frac{KG(K) T_{11}}{4} \right] \quad (9.7f)$$

$$A_7^*(K) = -\frac{T_1 - T_8 - cT_4}{4K} \quad (9.7g)$$

$$A_8^*(K) = \frac{1}{2K^2} \left[-T_4 - \frac{K^2}{4} (T_7 + cT_1) \right] \quad (9.7h)$$

where the values for the Theodorsen constants [83], $T_1, T_4, T_7, T_8, T_{10}$ and T_{11} are only depending on the deck and flap dimensions, through the value $c = B'/B$, and are calculated as follows

$$\begin{aligned}
 T_1 &= -\frac{2+c^2}{3}\sqrt{1-c^2} + c\cos^{-1}c & T_8 &= -\frac{1+2c^2}{3}\sqrt{1-c^2} + c\cos^{-1}c \\
 T_4 &= c\sqrt{1-c^2} - \cos^{-1}c & T_{10} &= \sqrt{1-c^2} + \cos^{-1}c \\
 T_7 &= -\frac{c(7+2c^2)}{8}\sqrt{1-c^2} - \left(\frac{1}{8} + c^2\right)\cos^{-1}c & T_{11} &= (2-c)\sqrt{1-c^2} + (1-2c)\cos^{-1}c
 \end{aligned} \tag{9.8}$$

9.3 Estimating the Flutter Wind Speed

The structural and aerodynamic models of the bridge deck describe the system under flutter, and the linear expressions of the aerodynamic forces are only valid for this condition. However, determining the flutter condition is a nontrivial task because of the flutter derivatives dependence on the reduced frequency K .

In this section, we define the flutter condition and outline a full solution for the canonical bridge deck as well as for a deck endowed with flaps. Furthermore, various simplified solutions for determining the point of flutter are discussed.

9.3.1 The Flutter Condition

In order to solve the system of equations above it is convenient to express the structural and aerodynamic models in state-space form. In the case of the canonical bridge deck (represented by Equations 9.1 and 9.2), the flutter condition can be written as follows

$$M_s \ddot{Y} + (C_s - C_{se}) \dot{Y} + (K_s - K_{se}) Y = 0 \tag{9.9}$$

where

$$\begin{aligned}
 Y &= \begin{bmatrix} h \\ \alpha \end{bmatrix} & M_s &= \begin{bmatrix} m & S \\ S & I \end{bmatrix} \\
 C_s &= \begin{bmatrix} 2m\zeta_h\omega_h & 0 \\ 0 & 2I\zeta_\alpha\omega_\alpha \end{bmatrix} & K_s &= \begin{bmatrix} m\omega_h^2 & 0 \\ 0 & I\omega_\alpha^2 \end{bmatrix} \\
 C_{se} &= \frac{1}{2}\rho U B K \begin{bmatrix} H_1^*(K) & B H_2^*(K) \\ B A_1^*(K) & B^2 A_2^*(K) \end{bmatrix} & K_{se} &= \frac{1}{2}\rho U^2 K^2 \begin{bmatrix} H_4^*(K) & B H_3^*(K) \\ B A_4^*(K) & B^2 A_3^*(K) \end{bmatrix}
 \end{aligned} \tag{9.10}$$

When a bridge deck is fluttering, the heave and pitch modes couple and oscillate with a constant amplitude and the same circular frequency, known as the flutter frequency, ω_f ,

and with a phase-shift, ϕ_f , between the two DOFs. The value of the flutter frequency lies somewhere between the natural frequencies of the heave, ω_h , and pitch, ω_α [37]. The state variables of the system for the flutter condition can thus be simplified as follows

$$Y(t) = \begin{bmatrix} h_0 \\ \alpha_0 e^{-i\phi_f} \end{bmatrix} e^{i\omega_f t} \quad \dot{Y}(t) = i\omega_f Y(t) \quad \ddot{Y}(t) = -\omega_f^2 Y(t) \quad (9.11)$$

Which implies that the system in Equation 9.9 can be rewritten for the flutter condition as

$$Y(t) \underbrace{\left[-\omega_f^2 M_s + \omega_f (C_s - C_{se}) i + (K_s - K_{se}) \right]}_A = 0 \quad (9.12)$$

In order to find a non-trivial solution (i.e., $Y(t) \neq 0$), the determinant of the system matrix A has to be equal to zero in both real and imaginary parts. However, as stated above finding the solution to the flutter condition is complicated by the fact that the flutter derivatives are functions of the reduced frequency, $K = B\omega/U$, and are thus dependent both on the system frequency, ω , and the wind speed, U . Note that this is a general description of the reduced frequency, K , and that ω refers to the current frequency of the deck oscillations (in heave or pitch) at that specific wind speed, U . The flutter case is indicated by $K_f = B\omega_f/U_f$. The flutter condition is defined as the highest value of the reduced frequency, K , (i.e., the lowest wind speed) where the determinant of the system matrix A is zero,

$$\det(A) = 0 \quad (9.13)$$

Since this solution is dependent on both the wind speed and the frequency, the simplest way to solve this system is to calculate the determinant for different value pairs of ω and U and continuously check the condition until it is fulfilled. However, this is a cumbersome and time consuming approach. In the following section, the Theodorsen's method to solve the flutter condition in Equation 9.13 is outlined, while full details are provided in Appendix A.

9.3.2 Theodorsen's Method for the Canonical Bridge Deck

The main idea behind Theodorsen's method is to rearrange the system matrix A , so that the flutter condition is solved for the non-dimensional variable X , and having the system matrix only depending on the reduced frequency K . This solution premise is given in Simiu et al. [37] (note that more details are given in the second edition from 1986 than the third, although, only for six flutter derivatives). Moreover, the solution for the eight flutter derivatives is given in [84].

We introduce the variable $X = \omega/\omega_h$ and divide system matrix A by ω^2 . The new system matrix

Chapter 9. Two-Dimensional Analytic Flutter Model

$A' = \frac{A}{\omega^2}$ in the case of the canonical bridge deck is described by

$$A' = \begin{bmatrix} -m + \left(\frac{2m\zeta_h}{X} - \frac{\rho B^2}{2} H_1^* \right) i + \frac{m}{X^2} - \frac{\rho B^2}{2} H_4^* & -S - \frac{\rho B^3}{2} (H_2^* i + H_3^*) \\ -S - \frac{\rho B^3}{2} (A_1^* i + A_4^*) & -I + \left(\frac{2I\zeta_\alpha \gamma}{X} - \frac{\rho B^4}{2} A_2^* \right) i + \frac{I\gamma^2}{X^2} - \frac{\rho B^4}{2} A_3^* \end{bmatrix} \quad (9.14)$$

where $\gamma = \omega_\alpha / \omega_h$. Note that all the flutter derivatives are functions of K (omitted from equations for readability).

Solving the determinant of A' in Equation 9.14 also satisfies the flutter condition and the flutter wind speed and flutter frequency can be estimated. In Appendix A the derivation of matrix A' and the solution for the determinant are described. The determinant of matrix A' separated into the real and the imaginary part becomes

$$\begin{aligned} \Re(|A'|)X_r^4 = & \left[mI + m\frac{\rho B^4}{2} A_3^* + I\frac{\rho B^2}{2} H_4^* + \frac{\rho^2 B^6}{4} (H_1^* A_2^* + H_4^* A_3^* + H_2^* A_1^* - H_3^* A_4^*) \right. \\ & \left. - S^2 - \frac{\rho B^3}{2} (S(A_4^* + H_3^*)) \right] X_r^4 \\ & + \left[m\zeta_h \rho B^4 A_2^* + I\zeta_\alpha \gamma \rho B^2 H_1^* \right] X_r^3 \\ & + \left[-mI\gamma^2 - 4mI\zeta_h \zeta_\alpha \gamma - mI - m\frac{\rho B^4}{2} A_3^* - I\gamma^2 \frac{\rho B^2}{2} H_4^* \right] X_r^2 \\ & + mI\gamma^2 = 0 \end{aligned} \quad (9.15a)$$

$$\begin{aligned} \Im(|A'|)X_i^3 = & \left[m\frac{\rho B^4}{2} A_2^* + I\frac{\rho B^2}{2} H_1^* + \frac{\rho^2 B^6}{4} (H_1^* A_3^* + H_4^* A_2^* - H_2^* A_4^* - H_3^* A_1^*) \right. \\ & \left. - \frac{\rho B^3}{2} (S(A_1^* + H_2^*)) \right] X_i^3 \\ & + \left[-2mI\zeta_\alpha \gamma - 2mI\zeta_h - m\zeta_h \rho B^4 A_3^* - I\zeta_\alpha \gamma \rho B^2 H_4^* \right] X_i^2 \\ & + \left[-I\gamma^2 \frac{\rho B^2}{2} H_1^* - m\frac{\rho B^4}{2} A_2^* \right] X_i \\ & + 2mI\gamma(\zeta_h \gamma + \zeta_\alpha) = 0 \end{aligned} \quad (9.15b)$$

The Equations 9.15a and 9.15b are simultaneously solved for X_r and X_i for a range of values of the reduced frequency K . The flutter condition is defined as the point (X_f, K_f) where the curves of $X_r(K)$ and $X_i(K)$ cross, i.e., where $X_r(K) = X_i(K) = X_f(K_f)$. Since the amplitude of the system oscillations at the flutter condition is assumed to be constant, i.e. neither damped nor growing, only real solutions to the polynomials are considered. In the case of multiple crossings of the curves, the highest value of the reduced frequency K (i.e. the lowest wind speed U), corresponds to the flutter point. From the solution (X_f, K_f) the flutter frequency

and flutter wind speed are calculated as follows

$$\omega_f = X_f \omega_h \quad (9.16a)$$

$$U_f = B \omega_f / K_f \quad (9.16b)$$

In case the curves do not cross, the flutter condition is never fulfilled, and thus the system will, at least in theory, never flutter.

9.3.3 Theodorsen's Method Extended for Bridge Deck with Flaps

The bridge deck equipped with moving flaps is described in Equations 9.5 and 9.6 and the system is described by four DOFs; deck heave, pitch and leading and trailing flap angles. Since the wing-aileron-tab model assumes that the flaps are moving at the same frequency as the deck we can also express the flap DOFs in terms of the deck state variables and control parameters. Thus conveniently reducing the number of state variables. We will derive the theoretical solution to the flutter condition for an amplitude-gain and phase-shift control law of the deck's pitch DOF. Thus the following flutter solution for the controlled deck is restricted to flaps controlled with the deck pitch as control input. However, a solution for other control inputs (heave or edge), or control laws, could be derived in a similar fashion as for the pitch DOF.

Considering an amplitude-gain and phase-shift control law, we can express flap motion as follows

$$\alpha_l(t) = A_l e^{-i\phi_l} \alpha(t) \quad (9.17a)$$

$$\alpha_t(t) = A_t e^{-i\phi_t} \alpha(t) \quad (9.17b)$$

where A_l and A_t are the amplitude-gains, and ϕ_l and ϕ_t are the phase-shifts of the leading and trailing edge flaps, respectively.

The flap acceleration can be expressed in terms of pitch acceleration as follows

$$\ddot{\alpha}_x(t) = A_x e^{-i\phi_x} \ddot{\alpha}(t) = A_x (\cos(-\phi_x) + i \sin(-\phi_x)) \ddot{\alpha}(t) \quad (9.18)$$

thus the system dynamics of the deck with flaps given in Equations 9.5 can be expressed only

Chapter 9. Two-Dimensional Analytic Flutter Model

in terms of bridge deck state variables

$$m\ddot{h} + S_\alpha \ddot{\alpha} + S_t A_t (\cos(-\phi_t) + i \sin(-\phi_t)) \ddot{\alpha} + S_l A_l (\cos(-\phi_l) + i \sin(-\phi_l)) \ddot{\alpha} + 2m\zeta_h \omega_h \dot{h} + m\omega_h^2 h = L'_h \quad (9.19a)$$

$$S_\alpha \ddot{h} + I_\alpha \ddot{\alpha} + I'_t A_t (\cos(-\phi_t) + i \sin(-\phi_t)) \ddot{\alpha} + I'_l A_l (\cos(-\phi_l) + i \sin(-\phi_l)) \ddot{\alpha} + 2I_\alpha \zeta_\alpha \omega_\alpha \dot{\alpha} + I_\alpha \omega_\alpha^2 \alpha = M'_\alpha \quad (9.19b)$$

where L'_h and M'_α equivalent to the expressions in Equations 9.2a and 9.2b with the flutter derivatives H_2^* , H_3^* , A_2^* and A_3^* replaced by their modified counterparts $H_2^{*'}$, $H_3^{*'}$, $A_2^{*'}$ and $A_3^{*'}$. Full details of how to express the flap flutter derivatives in terms of the deck pitch are given in Appendix B. Below follows the resulting modified flutter derivatives for the proposed control laws in Equations 9.17a and 9.17b

$$H_2^{*'} = H_2^* + H_5^* A_t \cos(-\phi_t) + H_6^* A_t \sin(-\phi_t) + H_7^* A_l \cos(-\phi_l) + H_8^* A_l \sin(-\phi_l) \quad (9.20a)$$

$$H_3^{*'} = H_3^* - H_5^* A_t \sin(-\phi_t) + H_6^* A_t \cos(-\phi_t) - H_7^* A_l \sin(-\phi_l) + H_8^* A_l \cos(-\phi_l) \quad (9.20b)$$

$$A_2^{*'} = A_2^* + A_5^* A_t \cos(-\phi_t) + A_6^* A_t \sin(-\phi_t) + A_7^* A_l \cos(-\phi_l) + A_8^* A_l \sin(-\phi_l) \quad (9.20c)$$

$$A_3^{*'} = A_3^* - A_5^* A_t \sin(-\phi_t) + A_6^* A_t \cos(-\phi_t) - A_7^* A_l \sin(-\phi_l) + A_8^* A_l \cos(-\phi_l) \quad (9.20d)$$

Finally, Equations 9.19 fully represents the bridge deck with leading and trailing flaps without additional state variables compared to the canonical bridge deck. Since our system is now described analogously to the canonical deck, albeit a more complex system matrix, we can solve the flutter condition using Theodorsen's method. The rather cumbersome task to arrive at the final polynomials to solve for the real and imaginary part of the system matrix A' is

9.4. Simplified Approaches for Estimating the Flutter Condition

detailed in Appendix A, resulting in the following polynomials

$$\begin{aligned}
\Re(|A'|)X_r^4 = & \left[mI + m\frac{\rho B^4}{2}A_3^{*'} + I\frac{\rho B^2}{2}H_4^* + \frac{\rho^2 B^6}{4}(-H_1^*A_2^{*'} + H_4^*A_3^{*'} + H_2^{*'}A_1^* - H_3^{*'}A_4^*) \right. \\
& + \left(m + \frac{\rho B^2}{2}H_4^* \right) (I_t' A_t \cos(-\phi_t) + I_l' A_l \cos(-\phi_l)) \\
& - \frac{\rho B^2}{2}H_1^* (I_t' A_t \sin(-\phi_t) + I_l' A_l \sin(-\phi_l)) \\
& - S(S + S_t A_t \cos(-\phi_t) + S_l A_l \cos(-\phi_l)) - \frac{\rho B^3}{2}(S(A_4^* + H_3^{*'})) \\
& + A_4^*(S_t A_t \cos(-\phi_t) + S_l A_l \cos(-\phi_l)) - A_1^*(S_t A_t \sin(-\phi_t) + S_l A_l \sin(-\phi_l)) \Big] X_r^4 \\
& + \left[m\zeta_h \rho B^4 A_2^{*'} + I\zeta_\alpha \gamma \rho B^2 H_1^* + 2m\zeta_h (I_t' A_t \sin(-\phi_t) + I_l' A_l \sin(-\phi_l)) \right] X_r^3 \\
& + \left[-mI\gamma^2 - 4mI\zeta_h \zeta_\alpha \gamma - mI - m\frac{\rho B^4}{2}A_3^{*'} - I\gamma^2 \frac{\rho B^2}{2}H_4^* \right. \\
& \left. - m(I_t' A_t \cos(-\phi_t) + I_l' A_l \cos(-\phi_l)) \right] X_r^2 \\
& + mI\gamma^2 = 0
\end{aligned} \tag{9.21a}$$

$$\begin{aligned}
\Im(|A'|)X_i^3 = & \left[m\frac{\rho B^4}{2}A_2^{*'} + I\frac{\rho B^2}{2}H_1^* + \frac{\rho^2 B^6}{4}(H_1^*A_3^{*'} + H_4^*A_2^{*'} - H_2^{*'}A_4^* - H_3^{*'}A_1^*) \right. \\
& + m(I_t' A_t \sin(-\phi_t) + I_l' A_l \sin(-\phi_l)) + \left(\frac{\rho B^2}{2}H_1^* \right) (I_t' A_t \cos(-\phi_t) + I_l' A_l \cos(-\phi_l)) \\
& + \left(\frac{\rho B^2}{2}H_4^* \right) (I_t' A_t \sin(-\phi_t) + I_l' A_l \sin(-\phi_l)) \\
& - S(S_t A_t \sin(-\phi_t) + S_l A_l \sin(-\phi_l)) - \frac{\rho B^3}{2}(S(A_1^* + H_2^{*'})) \\
& + A_1^*(S_t A_t \cos(-\phi_t) + S_l A_l \cos(-\phi_l)) + A_4^*(S_t A_t \sin(-\phi_t) + S_l A_l \sin(-\phi_l)) \Big] X_i^3 \\
& + \left[-2mI\zeta_\alpha \gamma - 2mI\zeta_h - m\zeta_h \rho B^4 A_3^{*'} - I\zeta_\alpha \gamma \rho B^2 H_4^* \right. \\
& \left. - 2m\zeta_h (I_t' A_t \cos(-\phi_t) + I_l' A_l \cos(-\phi_l)) \right] X_i^2 \\
& + \left[-I\gamma^2 \frac{\rho B^2}{2}H_1^* - m\frac{\rho B^4}{2}A_2^{*'} - m(I_t' A_t \sin(-\phi_t) + I_l' A_l \sin(-\phi_l)) \right] X_i \\
& + 2mI\gamma(\zeta_h \gamma + \zeta_\alpha) = 0
\end{aligned} \tag{9.21b}$$

From Equation 9.21 the flutter point (X_f, K_f) is identified using the same approach as described in the previous section for the canonical deck.

9.4 Simplified Approaches for Estimating the Flutter Condition

There also exist simpler ways of determining the flutter wind speed for a canonical deck. We will in this section discuss a few of such approaches, without aiming at an exhaustive presenta-

Chapter 9. Two-Dimensional Analytic Flutter Model

tion of simplified methods. Some of them are reduced versions of the two-dimensional model described above, others were developed empirically, or semi-empirically.

One of the most restrictive methods was proposed by Selberg in 1961 [85]. The formula is derived for a theoretical flat plate, and include only mechanical parameters, thus, allowing for a flutter prediction of a bridge section model without performing wind tunnel tests. This prediction is naturally less accurate for bridge decks substantially differentiating from the flat plate geometry. However, it can provide a useful initial appreciation of the flutter conditions. The Selberg formula is given by

$$U_f = f_\alpha B 3.72 \sqrt{\frac{Im}{\rho B^3} \left(1 - \left(\frac{f_h}{f_\alpha} \right)^2 \right)} \quad (9.22)$$

By studying the theoretical formulation of the flutter derivatives in Equations 9.3, one can observe possible simplifications. For instance, we could set the derivative $H_1^* = -4A_1^*$ (assuming no eccentricity). Such inter-relations between flutter derivatives were investigated, for different bridge deck shapes, by Scanlan et al. in [55]. Although the results indicate that some theoretical relations hold for streamlined decks, they conclude that estimating all the flutter derivatives from wind tunnel tests is still essential. However, several attempts to simplify the determination of the flutter condition have been made using theoretical derivative inter-connections, sometimes combined with ignoring of structural damping terms, e.g., [86], [87]. For instance, Bartoli et al. suggested in [88] the following formulation for a simplified flutter condition

$$X = \left(\frac{\omega_\alpha}{\omega_f} \right)^2 = \left(\frac{\omega_\alpha}{\omega_h} \right)^2 \frac{A_2^* + r_\alpha^2 H_1^*}{A_2^* + \left(\frac{\omega_\alpha}{\omega_h} \right)^2 r_\alpha^2 H_1^*} \quad (9.23a)$$

$$A_2^* A_3^* + \left(\frac{\omega_\alpha}{\omega_h} \right)^2 r_\alpha^2 H_1^* A_3^* - r_\alpha^2 \frac{2m}{\rho B^2} A_2^* \left(\left(\frac{\omega_\alpha}{\omega_h} \right)^2 - 1 \right) = 0 \quad (9.23b)$$

where $r_\alpha^2 = I/(mB^2)$. Equation 9.23a give the flutter frequency, ω_f , for the flutter condition, that is determined by Equation 9.23b. The flutter wind speed is then determined from the definition of the reduced frequency K as $U_f = \omega_f B / K_f$. The authors comment that these major simplifications of the flutter problem applies to a thin plate, and therefore their approach is very similar to that of e.g. Selberg. However, since three aerodynamic parameters are still considered, the proposed formulation is more flexible. Furthermore, they suggest that the estimated flutter wind speed can be multiplied by the Aerodynamic Stability Performance Index (ASPI), an empirical coefficient that is calculated as the experimental flutter wind speed divided by the theoretical wind speed for the equivalent flat plate. The ASPI for a streamlined deck usually lies within the range of 0.8-1.1 [89].

Moreover, the first analytical formulation of the bridge deck flutter phenomenon by Scanlan and Tomko in 1971 [56] only included the first six flutter derivatives. The last two derivatives, H_4^* and A_4^* , are often difficult to estimate from experiments; however, their contribution to

9.4. Simplified Approaches for Estimating the Flutter Condition

the flutter prediction is “known to be marginal” [90]. Also Brownjohn et al. [46] mention that the last derivatives are difficult to estimate and were normally not considered 25 years ago from today. Thus, the former formulation of the flutter equations, only including the first six flutter derivatives, is another, viable, reduced representation.

Summary

In this chapter we have incrementally introduced the structural and aerodynamic modeling contributions of a bridge deck controlled with a leading and trailing edge flap. We have extended the widely used Theodorsen method for solving the flutter condition so that it applies to an eccentric deck equipped with controllable flaps. Finally, we have discussed different simplified approaches of predicting bridge deck flutter. In the following chapter these theoretical contributions will be compared to experimental results from wind tunnel tests.

10 System Identification of Model Parameters from Wind Tunnel Experiments

IN this chapter we present the results gathered from wind tunnel experiments, with the aim to investigate how faithfully the two-dimensional analytical model presented in Chapter 9 captures what we observe in reality. Our aim is to study the applicability of the analytical model based on Theodorsen's theory, and in particular investigate the importance of additional structural considerations in the model formulation and the relevance of estimating all the model parameters from the experimental setup. First the experimental procedure and the system identification method are described, followed by the experimental results for the structural and aerodynamic tests of four different control scenarios. Furthermore, we validate the resulting calibrated model by comparing its predictions to wind tunnel measurements for different control parameters that were not considered in the identification procedure. Finally, we discuss the possibilities of reducing the model complexity and how this would effect the faithfulness of the model results.

10.1 Experimental Premise

In order to extract all the model parameters experimentally we leveraged the pull-up mechanism to do systematic step responses of the SmartBridge. The step responses were made by pulling up the windward side of the deck by 25 mm and releasing it, resulting in a mixed step response of the deck in heave and pitch DOFs, as illustrated in Figure 5.4b. The structural model parameters were determined from step responses performed without wind and the aerodynamic parameters from step responses performed at wind speeds ranging between 3 to 11 m/s, with increments of 1 m/s.

First, all the model parameters were estimated for the uncontrolled deck. Then, the experiments were repeated for three different active control strategies. By introducing the leading and trailing edge flap control incrementally, the complexity of the system is slowly increased.

Chapter 10. System Identification of Model Parameters from Wind Tunnel Experiments

Thus, the following four control scenarios were investigated

- case I** Uncontrolled deck, all the flaps are fixed at a 0° angle
- case II** Leading edge flaps are controlled, all the trailing flaps are fixed to a 0° angle
- case III** Trailing edge flaps are controlled, all the leading flaps are fixed to a 0° angle
- case IV** All the flaps on both sides of the deck are controlled

The same control law and control parameters were implemented for all four cases above. The flap positions are controlled with the amplitude-gain and phase-shift control law previously reported (Equations 9.17), given here in an edge-independent form by

$$\alpha_x(t) = A_x e^{-i\phi_x} \alpha(t) \quad (10.1)$$

$$\phi_x = \omega_\alpha \tau_x \quad (10.2)$$

where A_x is the amplitude gain, ϕ_x is the phase-shift, and τ_x is a time delay, where x can indicate either the trailing or the leading flap.

The phase-shift was implemented as a (constant) time delay in the controller unit, which has the effect that the phase-shift in terms of frequency is depending on the frequency of the control input signal, i.e. the pitch, as described by Equation 10.2. The resulting step responses for the entire range of wind speeds for the uncontrolled deck (**case I**) are shown in Figure 10.2a, and for the leading flap control (**case II**) in Figure 10.2b. It is evident that the system damping and frequencies for both the heave and pitch are dependent on the wind speed. Since the pitch frequency is depending on the wind speed, we have to consider a dynamic phase-shift when analyzing the results from the experiments. The time delay, τ_x , was set to 135 ms, which for the flutter frequency of the uncontrolled deck ω_f yields a phase-shift close to 90° (in still air, the same time delay provides a phase-shift of 107.8°). We will later on in this chapter explain why this parameter choice is convenient. The amplitude-gain, A_x , was set to 1.2, a value deemed high enough to show a significant difference for the different control cases, yet low enough to not control the deck too efficiently (and thereby reducing the amount of data useful for estimation). Thus the control parameters were purposely not chosen to be efficient at suppressing flutter, but rather to provide usable data for parameter estimation of the system. The leading and trailing flap responses to the deck pitch motion during a step response without wind is shown in Fig. 10.1, where the phase-shifts are clearly detectable.

In order to estimate the structural and aerodynamic model parameters, a total of 200 step responses in the wind tunnel were performed (10 wind settings x 4 control types x 5 runs per setting).

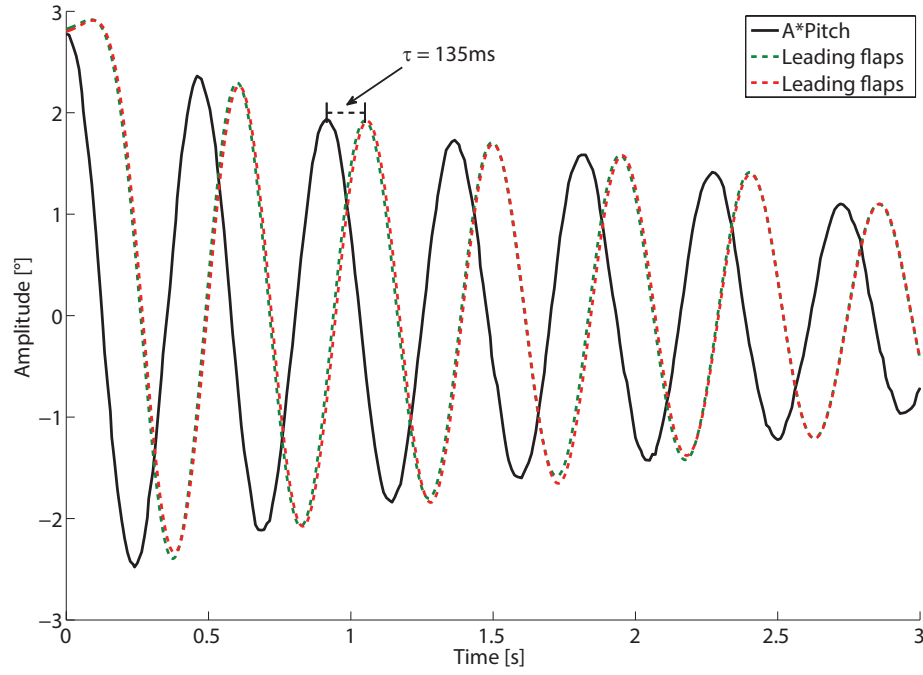


Figure 10.1 – Leading and trailing flaps trajectories at 0 m/s. The trajectories of the leading and trailing flaps are reported by the motor encoders, while the pitch is given by the laser measurements. The pitch is scaled by the amplitude gain of the control in the graph.

10.2 System Identification Method

In order to estimate the model parameters from our experimental data we describe our system in the form of a continuous, time-invariant, state-space model

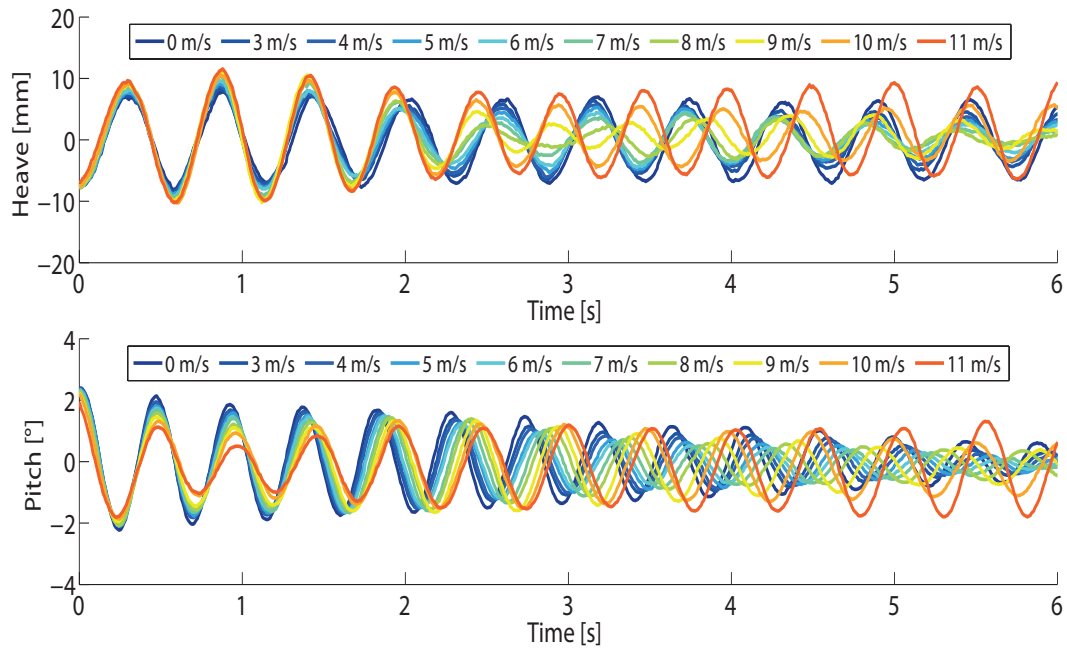
$$\dot{x}(t) = Ax(t) + Bu(t) \quad (10.3a)$$

$$y(t) = Cx(t) + Du(t) \quad (10.3b)$$

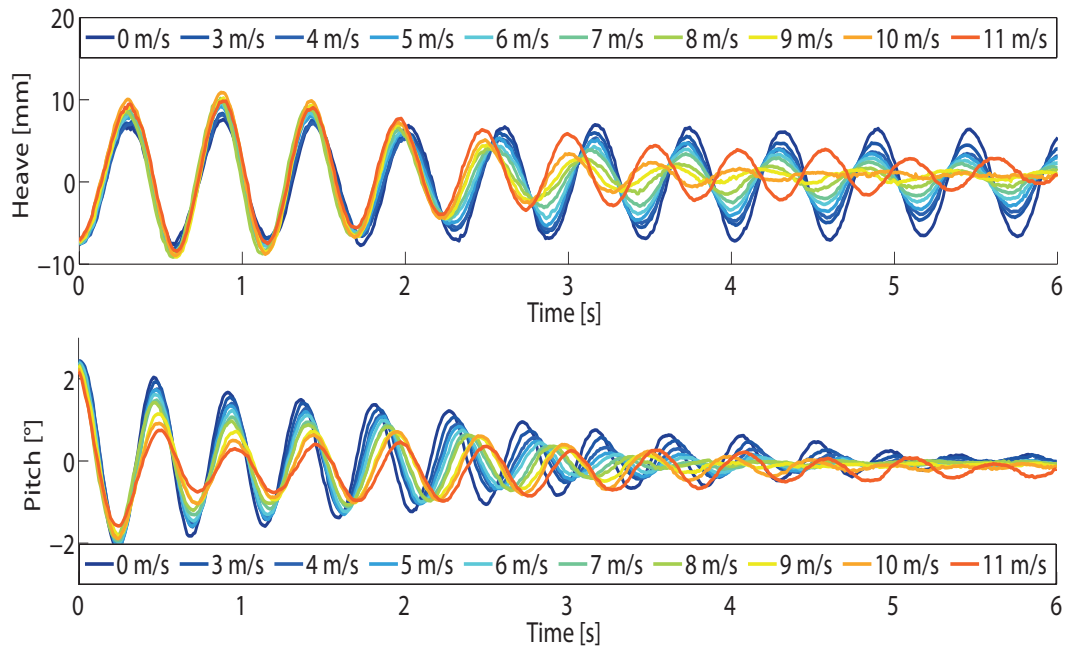
where

$$x(t) = \begin{bmatrix} h(t) \\ \alpha(t) \\ \dot{h}(t) \\ \dot{\alpha}(t) \end{bmatrix} \quad u(t) = 0$$

$$A = \begin{bmatrix} \mathbf{0} & \mathbf{I} \\ (K_{ae} - K_{mech}) & (C_{ae} - C_{mech}) \end{bmatrix} \quad B = \begin{bmatrix} 0 \\ 0 \\ 0 \\ 0 \end{bmatrix} \quad C = \begin{bmatrix} 1 & 0 & 0 & 0 \\ 0 & 1 & 0 & 0 \\ 0 & 0 & 1 & 0 \\ 0 & 0 & 0 & 1 \end{bmatrix} \quad D = \begin{bmatrix} 0 \\ 0 \\ 0 \\ 0 \end{bmatrix} \quad (10.4)$$



(a) The uncontrolled deck.



(b) The deck controlled by the leading edge flaps.

Figure 10.2 – Step responses for wind speeds ranging from 0 to 11 m/s.

The system model parameters are thus all contained in the state matrix A ¹. Experimental data from step responses performed without wind allow the structural model parameters in K_{mech} and C_{mech} to be determined from the obtained matrix A . While the aerodynamic parameters in K_{ae} and C_{ae} , i.e. the flutter derivatives, are determined from step responses performed to the deck with wind present. Additionally, performing the same analysis when the deck is being controlled allows the structural parameters for the flaps (without wind) and the aerodynamic parameters for the flaps (with wind) to be obtained. The procedure to determine each of the parameters will be described in the following sections. Note that the system parameters are determined by estimating the matrix A based on the step responses in pitch and heave of the deck, thus the actual flap positions are not considered when performing the parameter estimation.

There are numerous system identification methods available for finding appropriate values for the state matrix A so as to best explain the experimental data, $x(t)$. In our preliminary modeling effort [34] we employed two different estimation methods: an Eigensystem realization method (EIG) [91] and the Modified Ibrahim Time-Domain (MITD) method [92]. However, these methods did not provide a satisfactory estimation of the system matrix A . Therefore, we implemented a different approach using Matlab's System Identification Toolbox². The predefined function `ssest` leverages a subspace algorithm for estimating the state space model parameters from the observed data [93]. The function automatically assigns important weight matrices used in the algorithm according to the Multivariable Output Error State Space algorithm (MOESP) algorithm by Verhaegen [94] or the Canonical Variable Algorithm (CVA) by Larimore [95]. We perform our iterative estimation procedure as follows:

1. An initial estimation is made A_0 .
2. From the initial guess A_0 , we restrict the system matrices, so that only the stiffness and damping elements, $A(3:4,1:4)$, are free parameters, i.e., all other elements are fixed to zeros and ones as given in Equation 10.4. Thus, the initial guess is slightly modified A'_0 .
3. Three new estimations are performed leveraging the restricted initial guess A'_0 . The different estimations have different focus, i.e., the errors between the measured and the modeled outputs are weighed differently at specific frequencies during the minimization of the prediction error.
 - (a) A_1 : Focus on making a good fit for simulation
 - (b) A_2 : Focus on producing good predictors
 - (c) A_3 : Focus on producing good predictors with model stability enforced
4. Finally, we choose the estimation A'_0 , A_1 , A_2 , or A_3 that generates the best fit compared to the experimental data. The fit is defined as the normalized root-mean-square error (NRMSE).

Note that for all non-flutter cases A_1 always provided the best estimation; however, for diverg-

¹Note that the state matrix A defined in Equation 10.3 is different from the system matrix A described for solving the flutter condition in Chapter 9, Equation 9.13, (e.g. size 4x4 vs 2x2).

²<http://www.mathworks.com/products/sysid/>

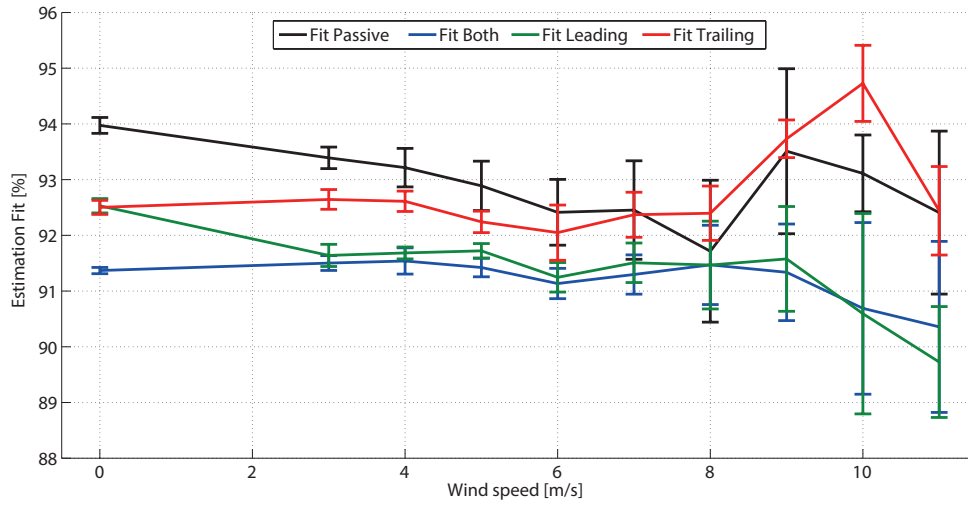


Figure 10.3 – Fit for reconstructed data and experimental data for the different control scenarios.

ing amplitudes the stability criteria estimation A_3 , or even the initial restricted guess A'_0 could get selected.

10.2.1 Selecting Experimental Data

An important factor is how to choose what part of the experimental data should be used for the estimation algorithm. Generally speaking, the longer the time series, the more information about the process we have, and the more reliable the estimation. After a step response is performed, the amplitude of the oscillations are damped over time (unless the deck flutters) to a point where the small amplitude oscillations have a very low signal-to-noise ratio. Therefore, a compromise in terms of length of time series has to be found. Moreover, such empirically optimized length is typically different for different scenarios and wind speeds. Indeed, on the one hand, as it can be seen from Figures 10.2, as long as the system is in a sub-flutter regime, the higher the wind speed, the stronger is the damping of the oscillations generated by the step stimulus. On the other hand, when the system is above the critical wind speed for flutter, the system becomes rapidly unstable and only short time histories can be recorded before the wind is automatically turned off. For all these reasons, the length of the time series used for parameter estimation were empirically chosen to be 6 s for the uncontrolled deck (**case I**) and the deck controlled with trailing flaps (**case III**), where the implemented phase-shift is non-effective for flutter control. The leading flap control (**case II**) and using all flaps for control (**case IV**), on the other hand, are damping the oscillations of the deck so efficiently that the data acquisition for system identification was cut 3 s after the step release. The estimation fits from 6 s data performed on the different control cases for the increasing wind speeds are shown in Figure 10.3. Note that the estimation fit for the leading flap control and controlling the flaps on both edges are in general lower, and drop at high wind speeds, which is due to the fast damping of the oscillations for these control configurations.

10.2.2 Filtering Experimental Data

The experimental data is consisting of the deck position recorded by the four laser sensors and the flap positions reported with individual motor encoders, and is sampled at a rate of 200 Hz, as described in Chapter 5. Occasionally the data samples received through the Labview interface are missing or corrupt. Note that this data loss is due to UART communication issues, and does not effect the CAN bus where the control loop is executed, thus the flap actuation is not perturbed in these rare cases. The logged data is therefore primarily checked for irregularities, and in the cases of data loss, the missing points are reconstructed through linear interpolation.

The heave and pitch position values are calculated as described in Equations 5.2a and 5.2b. Since we only directly measure positions, we have to calculate the time derivatives of the position values in each DOF in order to attain the corresponding velocities. However, the calculated velocities are quite noisy, and they are therefore filtered with a 3rd order, low-pass Butterworth filter (with normalized cut-off frequency, $W_n = 0.0742$). Furthermore, the bias was removed from the position data (to insure that the heave and pitch oscillate around zero). In Figures 10.4a and 10.4b example runs of the raw and filtered step responses for two different wind conditions are given. Note that Figure 10.4b shows the wind condition that is the most difficult to estimate for the uncontrolled deck (lowest estimation fit percentage).

10.3 Identifying Structural Model Parameters

As already mentioned, performing the system identification procedure on step responses performed without wind allows us to estimate the structural model parameters. That is the system matrix, A in Equations 10.4, is reduced to

$$A = \begin{bmatrix} \mathbf{0} & \mathbf{I} \\ -K_{mech} & -C_{mech} \end{bmatrix} \quad (10.5)$$

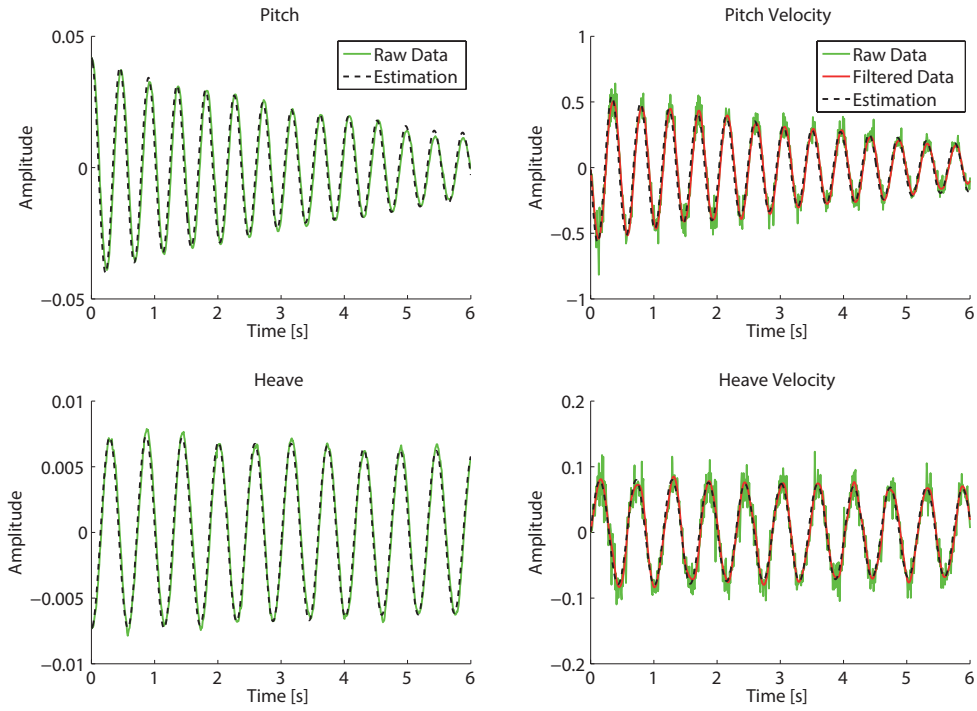
First, we estimate the model parameters for the uncontrolled deck, then we investigate the active control cases in order to estimate the model parameters inherent to the flap motions.

10.3.1 Results for the Uncontrolled Deck

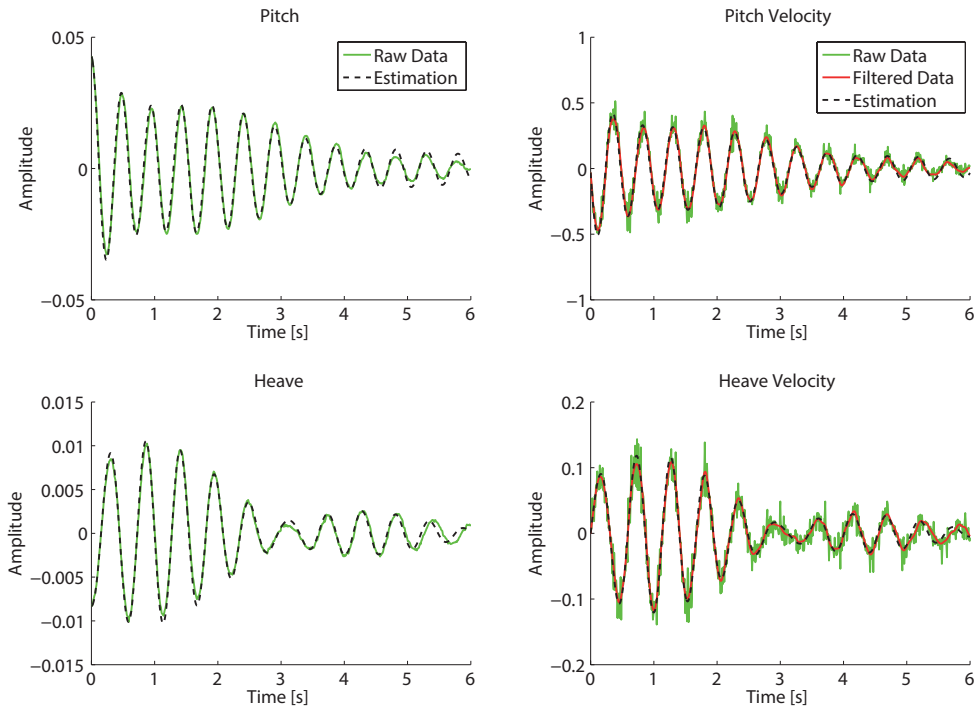
In Chapter 9 we show that the uncontrolled deck is described by Equations 9.1, which in the case of no wind (no external forces) equals

$$m\ddot{h} + mr_e\ddot{\alpha} + 2m\zeta_h\omega_h\dot{h} + m\omega_h^2 h = 0 \quad (10.6a)$$

$$mr_e\ddot{h} + I\ddot{\alpha} + 2I\zeta_\alpha\omega_\alpha\dot{\alpha} + I\omega_\alpha^2 \alpha = 0 \quad (10.6b)$$



(a) Step response at 0 m/s.



(b) Step response at 8 m/s.

Figure 10.4 – Comparison of experimental and reconstructed data for the uncontrolled deck.

10.3. Identifying Structural Model Parameters

Table 10.1 – Resulting stiffness and damping matrices for the uncontrolled deck.

	Estimation μ	Estimation σ	SNR = $\frac{\mu}{\sigma}$	Reconstruction ^{a,b}
K_{mech}	$\begin{bmatrix} 119.76 & 0.30 \\ 8.09 & 192.99 \end{bmatrix}$	$\begin{bmatrix} 0.062 & 0.052 \\ 0.61 & 0.10 \end{bmatrix}$	$\begin{bmatrix} 1933 & 5.8 \\ 13.4 & 1895 \end{bmatrix}$	$\begin{bmatrix} 119.76 & 0.34 \\ 7.4 & 192.99 \end{bmatrix}$
C_{mech}	$\begin{bmatrix} 0.068 & -0.002 \\ 0.12 & 0.40 \end{bmatrix}$	$\begin{bmatrix} 0.002 & 0.0032 \\ 0.044 & 0.0067 \end{bmatrix}$	$\begin{bmatrix} 33.4 & -0.55 \\ 2.8 & 59.1 \end{bmatrix}$	$\begin{bmatrix} 0.068 & 0.0007^a \\ 0.0001^a & 0.40 \end{bmatrix}$

We rearrange the equations so that our system can be put in the desired state-space form (Equation 10.5)

$$\ddot{h} = \frac{1}{\left(1 - \frac{m}{I} r_e^2\right)} \left(-2\zeta_h \omega_h \dot{h} - \omega_h^2 h + r_e 2\zeta_\alpha \omega_\alpha \dot{\alpha} + r_e \omega_\alpha^2 \alpha\right) \quad (10.7a)$$

$$\ddot{\alpha} = \frac{1}{\left(1 - \frac{m}{I} r_e^2\right)} \left(-2\zeta_\alpha \omega_\alpha \dot{\alpha} - \omega_\alpha^2 \alpha + r_e 2\zeta_h \omega_h \dot{h} + r_e \omega_h^2 h\right) \quad (10.7b)$$

This accurate description of the model will make the calculation of the system parameters somewhat complicated. However, we can make the assumption that $1/(1 - (m/I)r_e^2) = 1$ for small values of r_e , as we will show is our case. Thus we can form the relevant stiffness and damping matrices for the uncontrolled deck

$$K_{mech}^a = \begin{bmatrix} \omega_h^2 & -r_e \omega_\alpha^2 \\ -r_e \frac{m}{I} \omega_h^2 & \omega_\alpha^2 \end{bmatrix} \quad C_{mech}^a = \begin{bmatrix} 2\zeta_h \omega_h & -r_e 2\zeta_\alpha \omega_\alpha \\ -r_e 2\zeta_h \omega_h & 2\zeta_\alpha \omega_\alpha \end{bmatrix} \quad (10.8)$$

Another, simpler approach, is to make the assumption that the coupling terms $m r_e \ddot{h}(t) = -m r_e \omega_h^2 h(t)$ and $m r_e \ddot{\alpha}(t) = -m r_e \omega_\alpha^2 \alpha(t)$ in Equations 10.6, which is perfectly true for an undamped system. This approach leaves us with the following stiffness and damping matrices

$$K_{mech}^b = \begin{bmatrix} \omega_h^2 & -r_e \omega_\alpha^2 \\ -r_e \frac{m}{I} \omega_h^2 & \omega_\alpha^2 \end{bmatrix} \quad C_{mech}^b = \begin{bmatrix} 2\zeta_h \omega_h & 0 \\ 0 & 2\zeta_\alpha \omega_\alpha \end{bmatrix} \quad (10.9)$$

Note that both assumptions yield the same stiffness matrix, whereas there are coupling terms in damping for the first assumption (a) and no coupling in the latter (b).

The resulting stiffness and damping matrices obtained from the estimation procedure for the uncontrolled deck are presented in Table 10.1. The mean μ and standard deviation σ are given for the 5 experiments done without wind. We define here the Signal-to-Noise-Ratio (SNR) as the mean divided by the standard deviation, as to give us a normalized measure of reliability for the estimated values. It is clear that the diagonal terms are clearly distinguished, in particular the stiffness matrix. The cross-diagonal terms, i.e. coupling terms, are much noisier, in particular for the damping matrix where the the noise level compares to the signal strength.

Table 10.2 – Estimation of the deck's structural model parameters

	ω_h [rad/s]	ω_α [rad/s]	ζ_h	ζ_α	m [kg/m]	I [kgm ² /m]	r_e [mm]
Mean	10.94	13.89	0.0031	0.014	17.92	0.514	-1.8
Std	0.0028	0.0037	9e-05	2.4e-04	0.009	2.7e-04	0.19

The resulting calculations of the model parameters are found in Table 10.2. All the parameters, except for r_e , are calculated in a straightforward manner from the diagonal terms of K_{mech} and C_{mech} . The estimated mass (per unit length) m is calculated from the heave frequency ω_h and is a little higher than the measured deck, which is 17 kg/m. However, the measurement did not include additional weight for the suspension springs, some of the cables, screws etc. Thus, the estimations are deemed reliable, and the values in Table 10.2 have been used for the analysis.

The distance between the deck's elastic center and the center of mass r_e can be estimated from the cross-diagonal elements in K_{mech} , and in the case of assumption (a), in C_{mech} . However, because of the noisy nature of the coupling terms in damping we estimate r_e only from the stiffness matrix. It is calculated from the mean value of $K_{mech}(1,2)$ and $K_{mech}(2,1)$ weighted by their respective SNR. The estimated value of r_e indicates indeed a small eccentricity of the deck, 1.8 mm. Nevertheless, such a small distance explains to a large extent the coupling terms in stiffness, as can be seen in the reconstructed (from the estimated model parameters) matrix $K_{mech}^{a,b}$ in Table 10.1. Furthermore, we can confirm that the assumption that $1/(1 - (m/I)r_e^2) = 1$ holds; in fact the exact value is 1.0001.

The relevance of coupling terms of the damping is not clear. Although the value of the mean estimation of $C_{mech}(2,1)$ in Table 10.1 is significant (0.12, in the same order of magnitude as the diagonal terms), it also has a relatively high standard deviation. Nevertheless, it is clear that the eccentric model does not explain the observed coupling terms in damping, the reconstructed terms are orders of magnitude lower than the observed, for such a small value of r_e . Furthermore, we observe that the less strict assumption (b), explains the results as well as assumption (a). Finally, we do not deem it meaningful to pursue an alternative damping model for the uncontrolled deck because of the high noise level of the observed coupling terms in damping.

10.3.2 Results for the Controlled Deck

In Chapter 9 we show that the controlled deck is described by Equations 9.5, which in the case of no wind (external forces) equals

$$m\ddot{h} + S\ddot{\alpha} + S_t\ddot{\alpha}_t + S_l\ddot{\alpha}_l + 2m\zeta_h\omega_h\dot{h} + m\omega_h^2 h = 0 \quad (10.10a)$$

$$S\ddot{h} + I\ddot{\alpha} + (r_t S_t + I_t)\ddot{\alpha}_t + (r_l S_l + I_l)\ddot{\alpha}_l + 2I\zeta_\alpha\omega_\alpha\dot{\alpha} + I\omega_\alpha^2 \alpha = 0 \quad (10.10b)$$

10.3. Identifying Structural Model Parameters

In order to form the appropriate state-space matrix with four state variables, we express the flap positions in terms of the pitch DOF and the control parameters for the amplitude-gain and phase-shift control. Furthermore, as for the uncontrolled deck in assumption (b), we assume that the coupling terms $\ddot{h}(t) = -\omega_h^2 h(t)$ and $\ddot{\alpha}(t) = -\omega_\alpha^2 \alpha(t)$ resulting in

$$-\omega_\alpha^2 [S + S_t A_t (\cos(-\phi_t) + i \sin(-\phi_t)) + S_l A_l (\cos(-\phi_l) + i \sin(-\phi_l))] \alpha + m\ddot{h} + 2m\zeta_h \omega_h \dot{h} + m\omega_h^2 h = 0 \quad (10.11a)$$

$$-S\omega_h^2 h - \omega_\alpha^2 [I'_t A_t (\cos(-\phi_t) + i \sin(-\phi_t)) + I'_l A_l (\cos(-\phi_l) + i \sin(-\phi_l))] \alpha + I_\alpha \ddot{\alpha} + 2I_\alpha \zeta_\alpha \omega_\alpha \dot{\alpha} + I_\alpha \omega_\alpha^2 \alpha = 0 \quad (10.11b)$$

where $I'_x = r_x S_x + I_x$. Furthermore, we can remove the imaginary part of the equation by substituting $i\omega_\alpha \alpha(t) = \dot{\alpha}(t)$ (true for a simple harmonic oscillator), thus

$$-\omega_\alpha^2 (S + S_t A_t \cos(-\phi_t) + S_l A_l \cos(-\phi_l)) \alpha - \omega_\alpha (S_t A_t \sin(-\phi_t) + S_l A_l \sin(-\phi_l)) \dot{\alpha} + m\ddot{h} + 2m\zeta_h \omega_h \dot{h} + m\omega_h^2 h = 0 \quad (10.12a)$$

$$-S\omega_h^2 h - \omega_\alpha^2 (I'_t A_t \cos(-\phi_t) + I'_l A_l \cos(-\phi_l)) \alpha - \omega_\alpha (I'_t A_t \sin(-\phi_t) + I'_l A_l \sin(-\phi_l)) \dot{\alpha} + I_\alpha \ddot{\alpha} + 2I_\alpha \zeta_\alpha \omega_\alpha \dot{\alpha} + I_\alpha \omega_\alpha^2 \alpha = 0 \quad (10.12b)$$

Thus, the structural matrices for the controlled deck are written

$$K_{mech}^c = \begin{bmatrix} \omega_h^2 & -\frac{\omega_\alpha^2}{m} (S + S_t A_t \cos(-\phi_t) + S_l A_l \cos(-\phi_l)) \\ -\frac{S}{I} \omega_h^2 & \omega_\alpha^2 (1 - \frac{1}{I} (I'_t A_t \cos(-\phi_t) + I'_l A_l \cos(-\phi_l))) \end{bmatrix} \quad (10.13a)$$

$$C_{mech}^c = \begin{bmatrix} 2\zeta_h \omega_h & -\frac{\omega_\alpha}{m} (S_t A_t \sin(-\phi_t) + S_l A_l \sin(-\phi_l)) \\ 0 & 2\zeta_\alpha \omega_\alpha - \frac{\omega_\alpha}{I} (I'_t A_t \sin(-\phi_t) + I'_l A_l \sin(-\phi_l)) \end{bmatrix} \quad (10.13b)$$

Note that in contrast to the uncontrolled deck we now observe a coupling term in damping. In fact, all terms of the stiffness and damping matrices are linked to the pitch DOF, i.e. the second column, are affected by inertial effects of the controlled flaps.

The resulting step responses for all the different control configurations without wind are shown in Fig. 10.5. From a qualitative point of view it is clear that controlling the flaps with the deck pitch as input has a clear impact on the pitch damping, and seemingly no significant impact on the heave damping or on the system frequencies. The resulting pitch damping when controlling the trailing flaps is equivalent to the control of leading flaps, and with a larger damping when controlling both sides. This initial assessment indicates that the inertial effects of the flaps are symmetric and are significant for the structural dynamics.

In Table 10.3 all the estimated stiffness and damping matrices are reported, we repeat also the uncontrolled deck results for comparison. Also from the estimation results it is clear that the biggest effect of controlling the flaps is on the pitch damping parameter, i.e. $C_{mech}(2,2)$. Furthermore, we observe from the SNR matrices that the diagonal terms are still highly

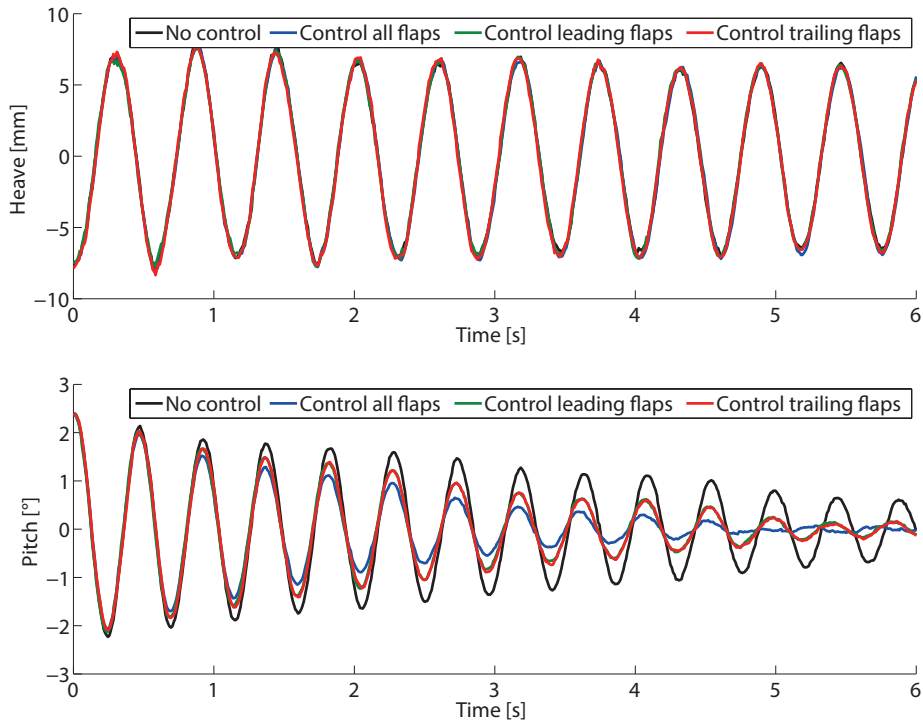


Figure 10.5 – Uncontrolled vs. controlled deck step response 0 m/s.

distinguished.

The estimation of the flap's structural model parameters are presented in Table 10.4. We include here the estimation of flap static moment and mass moment inertia (per unit length) based on our Solidworks CAD model of the flap. Note that we here report $I'_x = r_x S_x + I_x$, and not the flap mass inertia around the hinge, I_x ; and for a symmetric set-up $I_l = I_t$, $S_l = -S_t$ and thus also $I'_l = I'_t$. The parameters calculated from the estimated stiffness and damping matrices are also reported. The values from the CAD model shows a fair resemblance to the experimental estimations. It is however, evident that the static moments per unit length, S_x , are difficult to determine from the experimental results, we therefore chose the CAD estimated static moments in our analysis. The estimations of I'_x , both from damping and stiffness matrices, are coherent and with small variations, we therefore choose the mean experimental estimation of the mass inertia per unit length (around the axis of rotation) for our model.

Finally, we rebuild the system matrices using the estimated model parameters applied to Equations 10.13a and 10.13b, as reported in Table 10.3. Although there are some discrepancies between the reconstructed matrices and the (mean) observed data, the main effects regarding the pitch damping, also pitch frequency, are well captured.

10.3. Identifying Structural Model Parameters

Table 10.3 – Resulting stiffness and damping matrices for the controlled deck.

		Estimation μ	Estimation σ	SNR = $\frac{\mu}{\sigma}$	Reconstruction ^c
No control	K_{mech}	$\begin{bmatrix} 119.76 & 0.30 \\ 8.09 & 192.99 \end{bmatrix}$	$\begin{bmatrix} 0.062 & 0.052 \\ 0.61 & 0.10 \end{bmatrix}$	$\begin{bmatrix} 1933 & 5.8 \\ 13.4 & 1895 \end{bmatrix}$	$\begin{bmatrix} 119.76 & 0.34 \\ 7.4 & 192.99 \end{bmatrix}$
	C_{mech}	$\begin{bmatrix} 0.068 & -0.002 \\ 0.12 & 0.40 \end{bmatrix}$	$\begin{bmatrix} 0.002 & 0.0032 \\ 0.044 & 0.0067 \end{bmatrix}$	$\begin{bmatrix} 33.4 & -0.55 \\ 2.8 & 59.1 \end{bmatrix}$	$\begin{bmatrix} 0.068 & 0 \\ 0 & 0.40 \end{bmatrix}$
Leading	K_{mech}	$\begin{bmatrix} 119.91 & 0.22 \\ 9.53 & 194.37 \end{bmatrix}$	$\begin{bmatrix} 0.073 & 0.079 \\ 1.34 & 0.17 \end{bmatrix}$	$\begin{bmatrix} 1648 & 2.8 \\ 7.1 & 1137 \end{bmatrix}$	$\begin{bmatrix} 119.76 & 0.25 \\ 7.4 & 194.50 \end{bmatrix}$
	C_{mech}	$\begin{bmatrix} 0.05 & -0.029 \\ 0.056 & 0.75 \end{bmatrix}$	$\begin{bmatrix} 0.0027 & 0.0057 \\ 0.053 & 0.016 \end{bmatrix}$	$\begin{bmatrix} 18.84 & -5.09 \\ 1.06 & 46.15 \end{bmatrix}$	$\begin{bmatrix} 0.068 & -0.022 \\ 0 & 0.73 \end{bmatrix}$
Trailing	K_{mech}	$\begin{bmatrix} 119.91 & 0.24 \\ 8.19 & 194.52 \end{bmatrix}$	$\begin{bmatrix} 0.03 & 0.025 \\ 0.65 & 0.19 \end{bmatrix}$	$\begin{bmatrix} 3927 & 9.85 \\ 12.55 & 1020 \end{bmatrix}$	$\begin{bmatrix} 119.76 & 0.45 \\ 7.4 & 194.50 \end{bmatrix}$
	C_{mech}	$\begin{bmatrix} 0.063 & 0.022 \\ 0.13 & 0.73 \end{bmatrix}$	$\begin{bmatrix} 0.0025 & 0.0015 \\ 0.028 & 0.0085 \end{bmatrix}$	$\begin{bmatrix} 25.13 & 14.82 \\ 4.72 & 86.20 \end{bmatrix}$	$\begin{bmatrix} 0.068 & 0.022 \\ 0 & 0.73 \end{bmatrix}$
Both	K_{mech}	$\begin{bmatrix} 119.83 & 0.29 \\ 7.01 & 195.26 \end{bmatrix}$	$\begin{bmatrix} 0.067 & 0.019 \\ 0.37 & 0.29 \end{bmatrix}$	$\begin{bmatrix} 1744 & 15.25 \\ 18.93 & 668 \end{bmatrix}$	$\begin{bmatrix} 119.76 & 0.34 \\ 7.4 & 196.0 \end{bmatrix}$
	C_{mech}	$\begin{bmatrix} 0.054 & -0.0035 \\ 0.11 & 1.04 \end{bmatrix}$	$\begin{bmatrix} 0.002 & 0.0042 \\ 0.042 & 0.011 \end{bmatrix}$	$\begin{bmatrix} 26.54 & -0.83 \\ 2.51 & 98.69 \end{bmatrix}$	$\begin{bmatrix} 0.068 & 0 \\ 0 & 1.07 \end{bmatrix}$

Table 10.4 – Estimation of the flap's structural model parameters

	S_l [kgm/m]	S_t [kgm/m] [rad]	I'_l [kgm ² /m]	I'_t [kgm ² /m]
CAD	-0.0257	0.0257	0.0089	0.0089
Stiffness	-0.021±0.021	-0.015±0.0063	0.0104±0.0013	0.0113±0.0014
Damping	-0.032±0.0066	0.028±0.0018	0.0119±5e-04	0.0113 ±3e-04
Selected	-0.0257	0.0257	0.0113	0.0113

10.4 Identifying Aerodynamic Model Parameters

The aerodynamic model parameters are estimated from step responses performed with wind. In this case the system matrix, A in Equations 10.4, is described by

$$A = \begin{bmatrix} \mathbf{0} & \mathbf{I} \\ (K_{ae} - K_{mech}) & (C_{ae} - C_{mech}) \end{bmatrix} \quad (10.14)$$

Recall that the aerodynamic stiffness matrix, K_{ae} , and damping matrix, C_{ae} , contain the flutter derivatives that are depending on the reduced frequency, K . Thus, we have to perform the estimation procedure for a range of wind speeds.

In the following subsection, we first estimate the aerodynamic model parameters for the uncontrolled deck, then we incrementally investigate the actively controlled cases in order to estimate the flutter derivatives inherent to the flap motions.

10.4.1 Results for the Uncontrolled Deck

In Chapter 9 we show that the uncontrolled deck is described by Equations 9.2, which can be written in the required state-space form as

$$C_{ae} = \frac{1}{2} \rho U B K \begin{bmatrix} H_1^*/m & B H_2^*/m \\ B A_1^*/I & B^2 A_2^*/I \end{bmatrix} \quad K_{ae} = \frac{1}{2} \rho U^2 K^2 \begin{bmatrix} H_4^*/m & B H_3^*/m \\ B A_4^*/I & B^2 A_3^*/I \end{bmatrix} \quad (10.15)$$

The flutter derivatives are calculated from the estimated system matrix A and is thus dependent also on the previous estimation of the structural model. The deck's mass and inertia terms reoccur also in the aerodynamic stiffness and damping matrices, but more importantly, the structural stiffness and damping matrices, K_{mech} and C_{mech} , are primarily deducted from the estimation of A . In order to assess how the structural coupling terms influence the flutter derivatives estimation, we have compared three different sets of structural matrices:

- a** K_{mech} and C_{mech} as estimated from step responses without wind,
- b** K_{mech} and C_{mech} reconstructed with eccentric model,
- c** K_{mech} and C_{mech} reconstructed without eccentric model.

The resulting flutter derivatives from the three different experimental estimations are presented in Figure 10.6, as well as their corresponding theoretical values, plotted against the reduced wind velocity ($U_{red} = 2\pi/K = Uf/B$). The direct flutter derivatives are found in Figure 10.6a, and since they are independent of the coupling terms (thereof the prefix direct), the result is identical for all sets of structural matrices (**a**, **b** and **c**). In Figure 10.6b the cross flutter derivatives are presented. Note that the coupling terms in damping are neglected both in case **b** and **c**, thus the estimation of the corresponding derivatives A_1^* and H_2^* are identical. Thus,

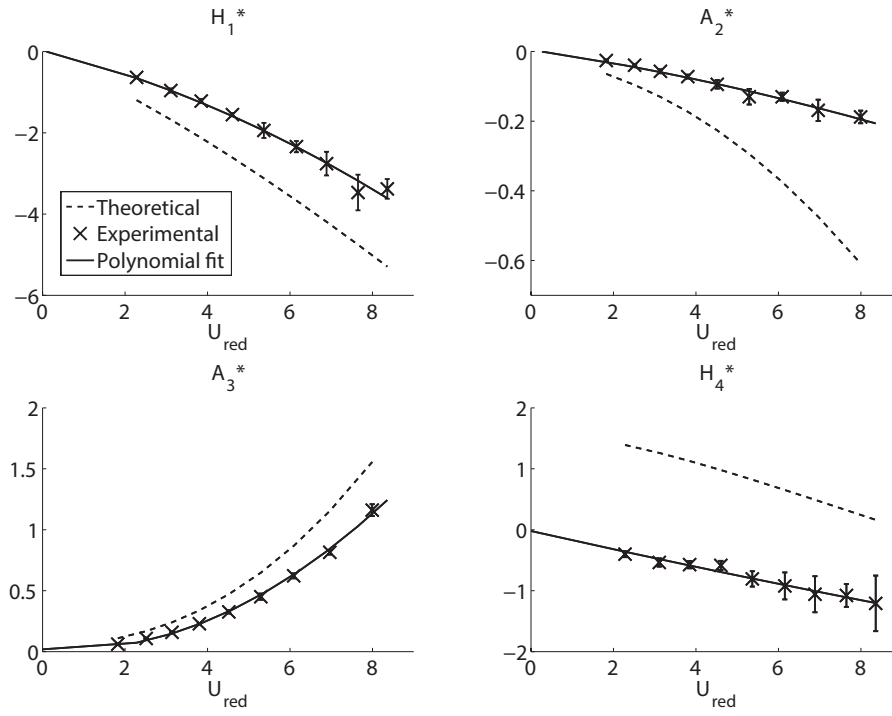
only the derivatives H_3^* and A_4^* yield a different result between **b** and **c**. In any case, the effect of the structural coupling terms are very small for the cross flutter derivatives, except for A_4^* . In this case the estimations considering the coupling (**a** and **b**) are much closer to the theoretical one. Furthermore, the reconstructed matrices including deck eccentricity (**b**) correspond well to the direct estimation (**a**).

This comparison shows us that the coupling terms in the structural model can potentially have a large effect on the estimated flutter derivatives. Furthermore, it shows that our eccentric model of the deck (**b**), despite the quite small misalignment, is able to reproduce to a large extent the result from directly identifying (**a**) the aerodynamic parameters. In the following analysis we use the flutter derivatives estimated using K_{mech} and C_{mech} of **a**, thus incorporating, albeit small, effects that has not been modeled.

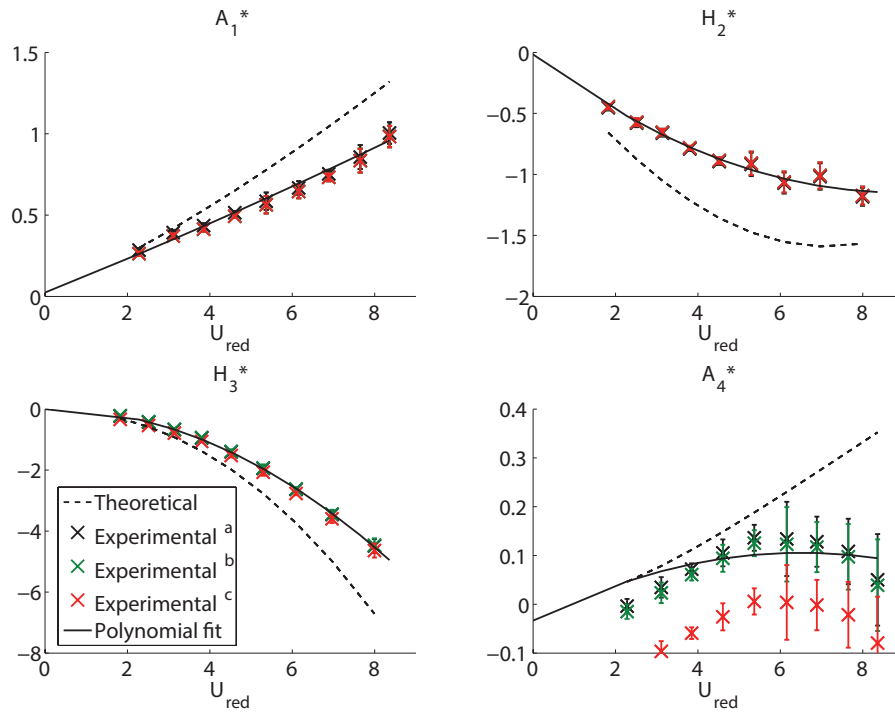
In general, the estimated flutter derivatives have a steady trend that correspond roughly with the theoretical ones in Figure 10.6. Note that it is expected that the identified parameters will diverge to some extent from the theoretical ones, since in fact our bridge deck is not a flat plate. Furthermore, the estimations have a low variance, although growing in some cases for higher wind speeds. Moreover, we observe that the most inconsistent, and noisy, results are from the H_4^* and A_4^* flutter derivatives. Nevertheless, as has been stated in Section 9.4, it is well documented that these flutter derivatives are the most difficult to estimate, and were not even considered in the original formulation of flutter.

10.4.2 Results for the Controlled Deck

We have seen that the leading flap control and the trailing flap control have a symmetric effect on damping given the same control parameters without wind. However, the symmetry is broken for the aerodynamic and aeroelastic behavior. In Figure 10.7 we compare the resulting step responses for the different control configurations at 11 m/s. At this wind speed the uncontrolled deck is fluttering, i.e., it has a growing amplitude in heave and pitch. The same is observed for the deck controlled using only the trailing edge flaps, although in this case much more unstable. This is because the chosen phase-shift value is unfavorable when applied to the trailing edge; again, the criteria for the selection of control parameters for these experiments were to facilitate the estimation procedure, not to efficiently control flutter. The leading edge flaps are successfully dampening the deck, thus consolidating the claim of asymmetry regarding the aerodynamic and aeroelastic effects. Even though the control using all the flaps is capable of controlling the flutter, it is doing so less efficiently than the leading flaps only, a reasonable outcome since moving also the trailing flaps with the current phase-shift degrades the overall performance. However, it is curious that the performance using all flaps is significantly closer to that of the leading flaps, rather than (evenly) in between the leading and the trailing flaps. This might suggest that the model assumption of superposed flap forces is too rigid. In fact, the model assumes that upwind elements do not disturb the flow over downwind elements, which is a strong assumption probably not valid in reality.



(a) Direct flutter derivatives.



(b) Cross flutter derivatives.

Figure 10.6 – Identified flutter derivatives for the uncontrolled deck derived from different structural matrices.

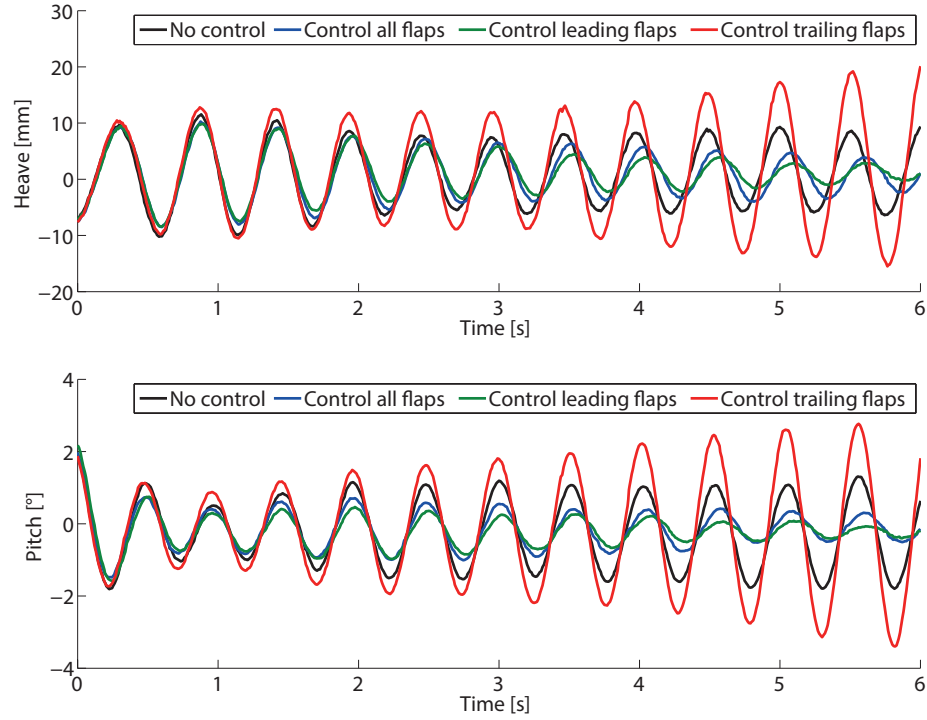


Figure 10.7 – Uncontrolled vs. controlled deck step response at 11 m/s.

In Chapter 9, we show that the controlled deck can still be described in the form of Equations 9.2, which in the required state-space is given by

$$C_{ae} = \frac{1}{2} \rho U B K \begin{bmatrix} H_1^*/m & B H_2^{*'}/m \\ B A_1^{*}/I & B^2 A_2^{*'}/I \end{bmatrix} \quad K_{ae} = \frac{1}{2} \rho U^2 K^2 \begin{bmatrix} H_4^*/m & B H_3^{*'}/m \\ B A_4^{*}/I & B^2 A_3^{*'}/I \end{bmatrix} \quad (10.16)$$

since the modified flutter derivatives $H_2^{*'}$, $H_3^{*'}$, $A_2^{*'}$ and $A_3^{*'}$ from Equations 9.20 contain the flap flutter derivatives used in the control law described by Equation 10.1.

The theoretical flap flutter derivatives are depending on the Theodorsen's constants, which are calculated for $c = B'/B = 0.6757$ and given in Table 10.5.

Table 10.5 – Theoretical Theodorsen constants

	T_1	T_4	T_7	T_8	T_{10}	T_{11}
Value	-0.0436	-0.3308	0.0106	0.09	1.5661	0.6850

Effect of the structural estimation

The effect of the structural matrices on the flutter derivatives estimation is again investigated. Here, we compare the following sets of structural matrices for the leading edge flap control:

- a** K_{mech} and C_{mech} as estimated from step responses without wind (with control),
- b** K_{mech} and C_{mech} reconstructed with eccentric deck and flap inertia model,
- c** K_{mech} and C_{mech} as estimated from step responses without wind (without control).

The resulting flutter derivatives from the three different estimations for the leading flap control experiments are presented in Figure 10.8, as well as their corresponding theoretical values.

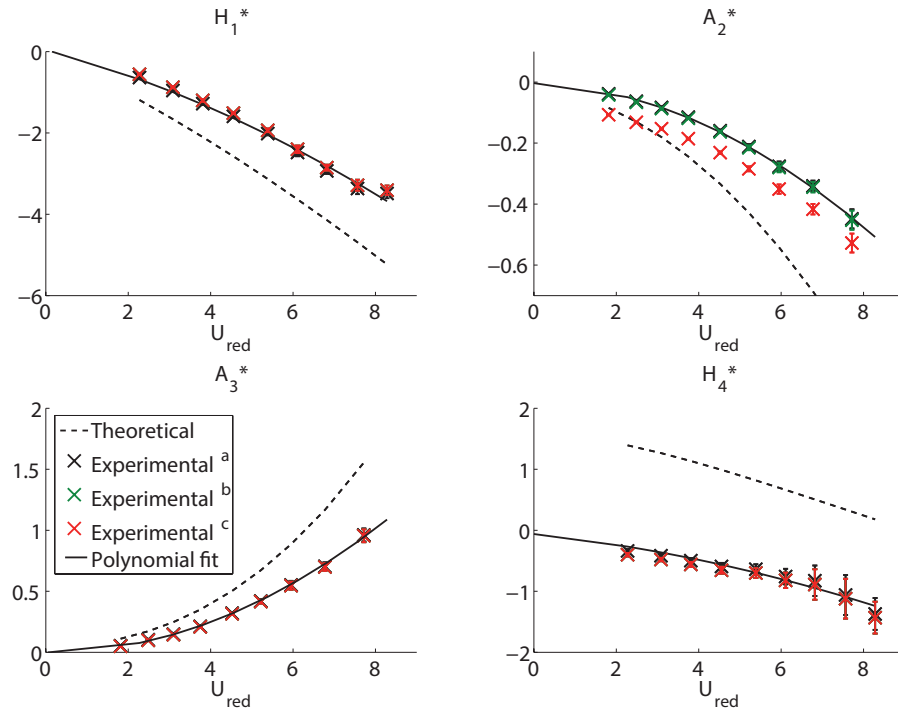
In contrast to the uncontrolled deck, we do observe different estimations also for the direct flutter derivatives, that are found in Figure 10.8a. In general, we observe that for most cases there is little impact on the estimated derivatives when not considering flap inertia terms (**c**) as the eccentric deck and flap inertia model (**b**) is able to reproduce to a large extent the resulting flutter derivatives from directly identifying the structural parameters (**a**). Not surprisingly, the derivatives (A_2^* and H_2^*) associated to the pitch velocity, i.e., the pitch damping, are the most effected by not taking into account the flap inertia effects (**c**).

In analogy to the analysis of the eccentric structural model for the uncontrolled deck, we can conclude that flap inertia can potentially affect the flutter derivatives' estimation for an actively controlled deck. Furthermore, we see that including deck eccentricity and flap inertia to our structural model (**b**), allow us to reproduce, to a large extent, the result from directly identifying (**a**) the structural and aerodynamic parameters of the controlled deck. Although not reported here, similar analyses have been carried out with similar results for the cases of controlling the deck with trailing flaps and using all flaps. In the following analysis we employ, as for the uncontrolled deck, the flutter derivatives estimated using K_{mech} and C_{mech} from (**a**).

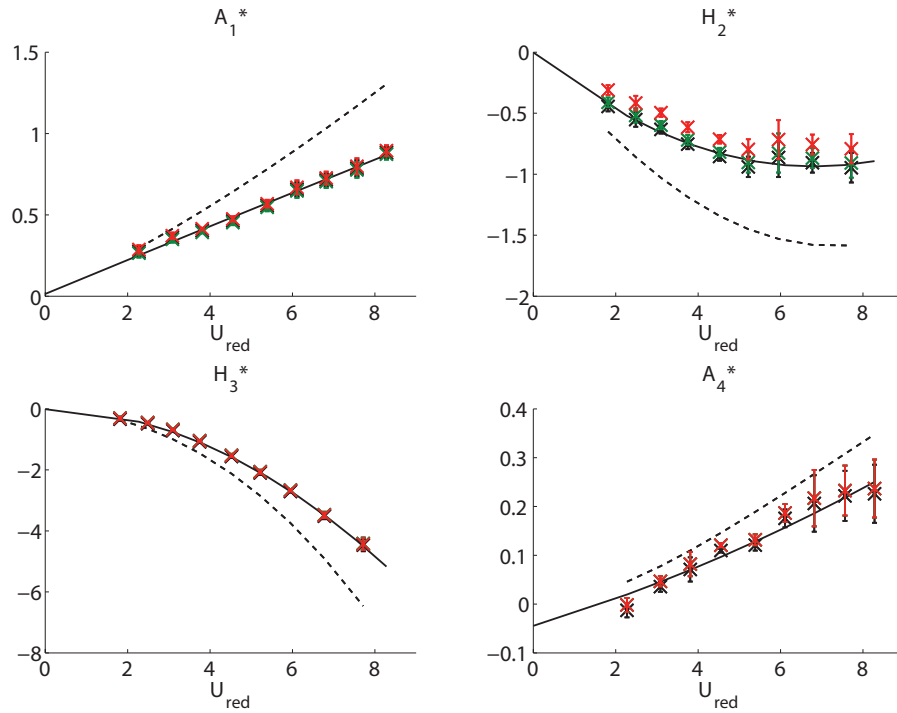
Estimation of aggregated aerodynamic parameters

The estimated flutter derivatives for all control cases are given in Figure 10.9. Note that according to the theoretical model H_1^* , H_4^* , A_1^* , and A_4^* should be unaffected by the flap control, while the modified parameters $A_2^{*'}$, $A_3^{*'}$, $H_2^{*'}$, and $H_3^{*'}$ are functions of the corresponding uncontrolled deck derivatives (A_2^* , A_3^* , H_2^* , and H_3^*) as well as the leading and trailing flap derivatives ($H_{5..8}^*$ and $A_{5..8}^*$) as described in Equations 9.20. In general, diagonal elements for the direct and cross flutter derivatives are indeed somewhat coherent. The worst match is (again) for the known difficult derivative A_4^* . The flutter derivatives that theoretically should be dependent on the control, i.e., $A_2^{*'}$, $A_3^{*'}$, $H_2^{*'}$, and $H_3^{*'}$, are also so in our experiments. The most significant effects are observed for $A_2^{*'}$ and $H_2^{*'}$. Although, the theoretical values do not correspond exactly to the attained values, the different control scenarios affect the flutter derivatives in a similar fashion; this is especially clear for $H_2^{*'}$. The experimentally obtained $A_3^{*'}$ on the other hand, does not change significantly between the different control cases, in contrast to the theoretical values. Although $H_3^{*'}$ has a predicted a small change depending on

10.4. Identifying Aerodynamic Model Parameters

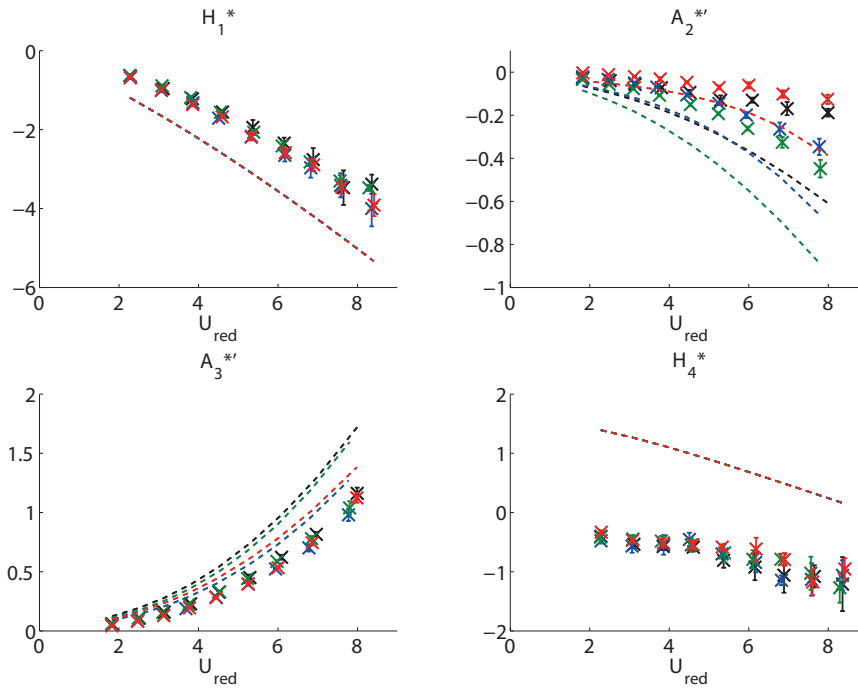


(a) Direct flutter derivatives.

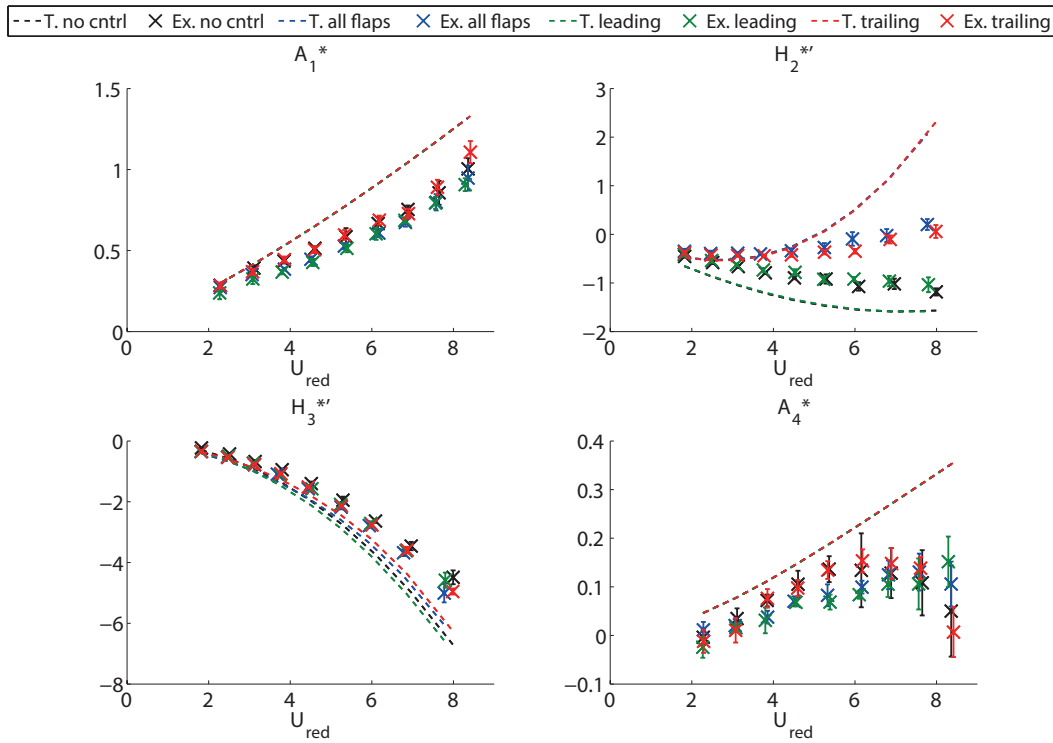


(b) Cross flutter derivatives.

Figure 10.8 – Comparing flutter derivatives, identified using different structural matrices, for the deck controlled with leading flaps.



(a) Direct (modified) flutter derivatives.



(b) Cross (modified) flutter derivatives.

Figure 10.9 – Identified flutter derivatives for the different control cases.

the control, which is also observed experimentally, experiments and theory shows an opposite trend.

In conclusion, as for the uncontrolled deck, the estimated flutter derivatives have steady trends that correspond roughly with the theoretical ones, as well as low estimation variances. Thus, the experimentally obtained aggregated flutter derivatives do seem plausible and reliable.

Estimation of individual flap aerodynamic parameters

The aggregated aerodynamic derivatives are however only sufficient to predict the flutter behavior for the particular control law implemented during the estimation procedure. Thus, in order to achieve a general flutter model it is necessary to estimate the individual flap flutter derivatives ($H_{5,8}^*$ and $A_{5,8}^*$). One indirect approach is to calculate them from the aggregated derivatives. Here we present the results from estimating the flap flutter derivatives from the experiments performed with controlling only the leading flaps and only the trailing flaps. The experiments performed using all the control surfaces serve to validate our estimations of individual flap parameters.

After restructuring the expressions describing the modified flutter derivatives in Equations 9.20, we find that the trailing flap flutter derivatives are given by

$$H_5^* = \frac{1}{A_t} (\cos(-\phi_t)(H_2^{*'} - H_2^*) - A_t \sin(-\phi_t)(H_3^{*'} - H_3^*)) \quad (10.17a)$$

$$H_6^* = \frac{1}{A_t} (\sin(-\phi_t)(H_2^{*'} - H_2^*) + A_t \cos(-\phi_t)(H_3^{*'} - H_3^*)) \quad (10.17b)$$

$$A_5^* = \frac{1}{A_t} (\cos(-\phi_t)(A_2^{*'} - A_2^*) - A_t \sin(-\phi_t)(A_3^{*'} - A_3^*)) \quad (10.17c)$$

$$A_6^* = \frac{1}{A_t} (\sin(-\phi_t)(A_2^{*'} - A_2^*) + A_t \cos(-\phi_t)(A_3^{*'} - A_3^*)) \quad (10.17d)$$

and analogously the leading flap flutter derivatives are calculated as

$$H_7^* = \frac{1}{A_l} (\cos(-\phi_l)(H_2^{*'} - H_2^*) - A_l \sin(-\phi_l)(H_3^{*'} - H_3^*)) \quad (10.18a)$$

$$H_8^* = \frac{1}{A_l} (\sin(-\phi_l)(H_2^{*'} - H_2^*) + A_l \cos(-\phi_l)(H_3^{*'} - H_3^*)) \quad (10.18b)$$

$$A_7^* = \frac{1}{A_l} (\cos(-\phi_l)(A_2^{*'} - A_2^*) - A_l \sin(-\phi_l)(A_3^{*'} - A_3^*)) \quad (10.18c)$$

$$A_8^* = \frac{1}{A_l} (\sin(-\phi_l)(A_2^{*'} - A_2^*) + A_l \cos(-\phi_l)(A_3^{*'} - A_3^*)) \quad (10.18d)$$

Note that we chose to implement a phase-shift of 90° for the estimation so that the above terms are reduced. However, as previously mentioned, the actual observed phase-shift values were not precisely 90° , and varying with the wind speed. As formerly stated, we have used the actual values for the analysis, thus, the cosine terms were not completely suppressed, although, the sine terms of Equations 10.17 and 10.18 were still dominant.

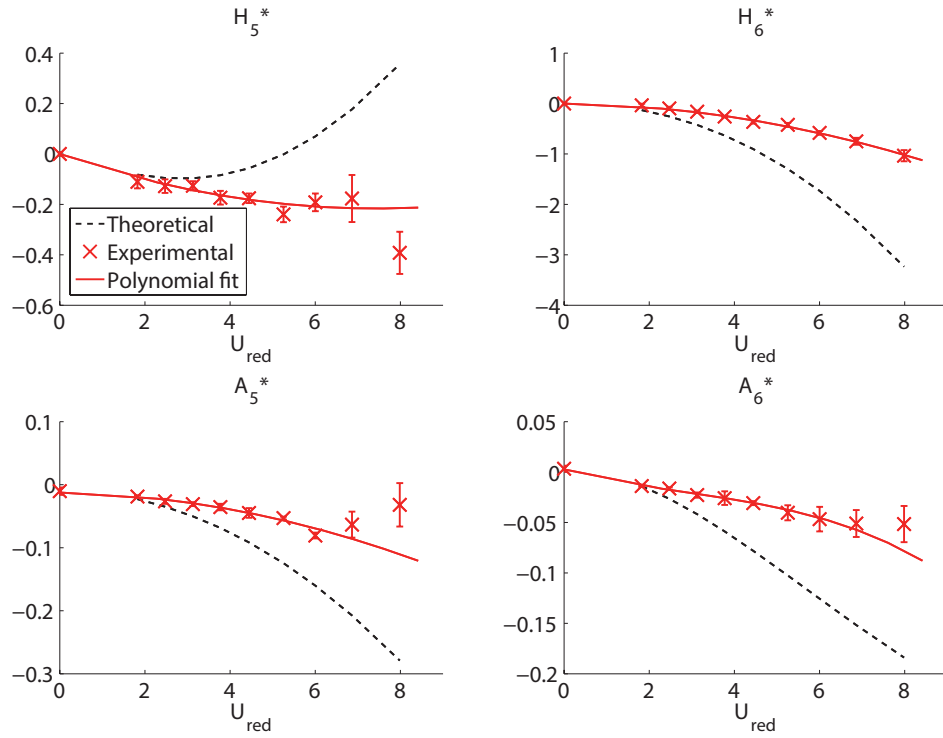
The flap flutter derivatives estimations are presented in Figure 10.10. The results in Figure 10.10a were obtained from the estimations made with control using only the trailing flaps, and the results in Figure 10.10b were obtained from the estimations gathered with control using only the leading flaps. In general, the resulting flap flutter derivatives have less consistent trends compared to the modified flutter derivatives for the controlled deck. The leading flap's derivatives are quite noisy, except for A_8^* which corresponds very well to the theoretical prediction. The estimations of trailing flap's flutter derivatives are less noisy, and consistent in their trends, although, they are distinctly different from the theoretical ones. The reliability of the estimated flap derivatives will be better understood from the flutter prediction analysis in the following section.

Note that the flap flutter derivatives also can be estimated directly using the flap trajectories, thus extending the state vector x in Equations 10.3, and estimating a 6×6 state matrix, A in Equations 10.4. We have not presented such an analysis here since the estimation methodology that was reliable for estimating $A_{4 \times 4}$ did not converge to meaningful results for a larger set of model parameters. Thus, we are not utilizing all the available information in the current analysis. However, in our case adding more parameters to the estimation procedure, seemed to increase the risk of getting stuck in local optima. It is thus unclear whether such an approach would finally give more insightful results; nevertheless, we recommend such an analysis for further work.

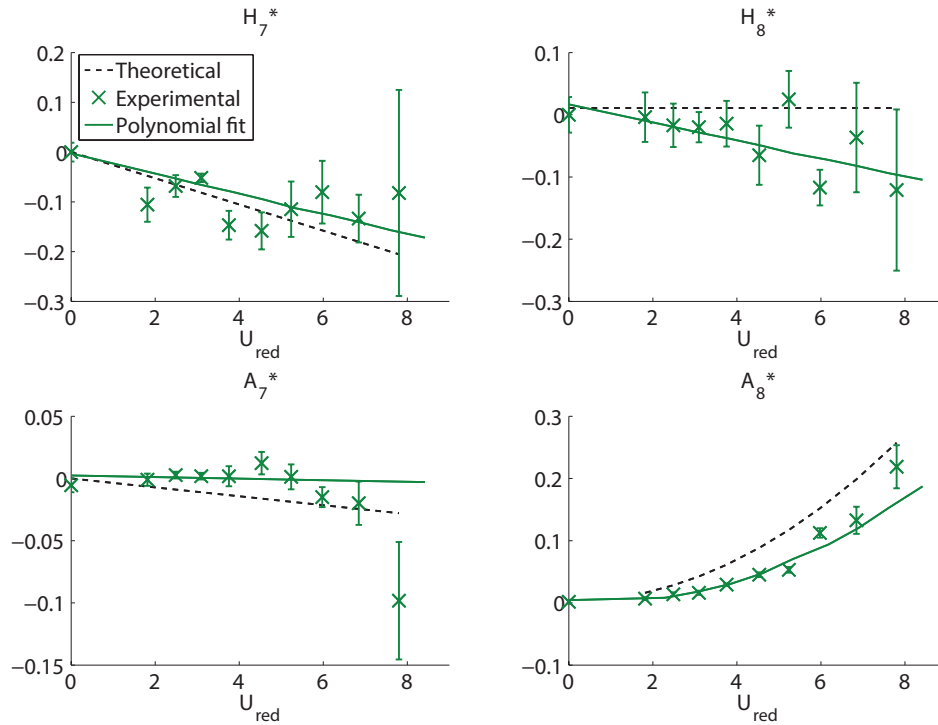
10.5 Estimation of the flutter wind speed

A proper estimation of the model parameters are vital for a correct flutter condition estimation. We will leverage the structural and aerodynamic model parameters presented in the previous section, in order to predict the flutter wind speed of the uncontrolled and controlled bridge deck, and compare these to the predicted theoretical values.

In Chapter 9, we have described Theodorsen's method to calculate the flutter condition. Recall, that it is necessary to solve the flutter determinant, i.e., solving Equations 9.21a and 9.21b, for a range of reduced frequencies K . Therefore, we cannot directly use the estimated experimental data points, instead we need to express the flutter derivatives as a function of K . We use a weighted polynomial fit for this purpose, where each flutter derivative's mean value, at a certain wind speed, is weighted by the inverse of its standard deviation, thus decreasing the importance of noisy data points. Furthermore, assigning the order of the polynomial fit is a delicate decision: by choosing a too high order we risk to over fit the data while selecting a too low one might result in losing valuable information and decreasing the model accuracy.



(a) Trailing flap flutter derivatives, identified from the trailing flap only control case.



(b) Leading flap flutter derivatives, identified from the leading flap only control case.

Figure 10.10 – Identified additional flutter derivatives for the leading and trailing flaps.

Table 10.6 – Polynomial orders of the flutter derivatives curve fit

H_1^*	H_2^*	H_3^*	H_4^*	A_1^*	A_2^*	A_3^*	A_4^*	H_5^*	H_6^*	H_7^*	H_8^*	A_5^*	A_6^*	A_7^*	A_8^*
2	2	2	1	1	2	2	1	2	2	1	1	2	3	1	2

In general, the order of the chosen polynomials has been set as low as possible, while still reasonably capturing the trends of the derivatives. Moreover, the theoretical curves resulting from Theodorsen's circulatory function were used as a guideline for the polynomial shape expectation. The order of the polynomial assigned to each flutter derivative is given in Table 10.6; and the resulting fitted curves are plotted in Figures 10.6 and 10.10 for the deck and flaps, respectively. Note that the last data points of the trailing flap flutter derivatives (at $U_{red} = 8$) in Figure 10.10a were well above the flutter condition and that the resulting estimations break the observed trends of the sub-flutter derivatives, especially for H_5^* and A_5^* . Therefore, we decided to not include these points for the curve fitting procedure of the trailing flap flutter derivatives.

10.5.1 Determining the Flutter Wind Speed Experimentally

The flutter wind speed can be determined from wind tunnel experiments. However, we have not come across any guidelines or a clearly described experimental procedure for such an estimation. We will therefore outline in detail our methodology and discuss how to interpret the results.

In the previous sections, the model parameters were estimated from step responses. From these experiments we can easily observe when we are above the critical wind speed, when the oscillation amplitudes are increasing. However, determining more precisely the onset point of flutter is more difficult. We have defined the experimental flutter condition as the lowest wind speed for which growing amplitudes in the heave and pitch DOFs are observed. In practice, if any of the individual laser sensors at the deck corners measure an amplitude higher than 4 cm, the bridge deck is considered to be in flutter mode and the wind is automatically turned off. However, the theoretical definition states that the point of flutter is where the oscillations maintain a constant amplitude. Thus, our approach would assign a slightly higher critical speed than the one defined theoretically.

Another important factor is the initial perturbation applied to the deck. It is noteworthy that if no initial perturbation is applied, i.e., the deck is resting, we do not observe flutter even at significantly higher wind speeds than the observed critical speed experimentally determined for step responses. For instance, the uncontrolled deck does not flutter without an initial step perturbation even at the highest wind speed considered (16 m/s). Thus, the initial perturbation of the deck is essential for triggering the flutter response. Furthermore, we also noticed that the amplitude of the step response influences our estimation of the flutter condition. In Figure 10.11, we observe that as the amplitude of the initial step perturbation (pull-up height) is

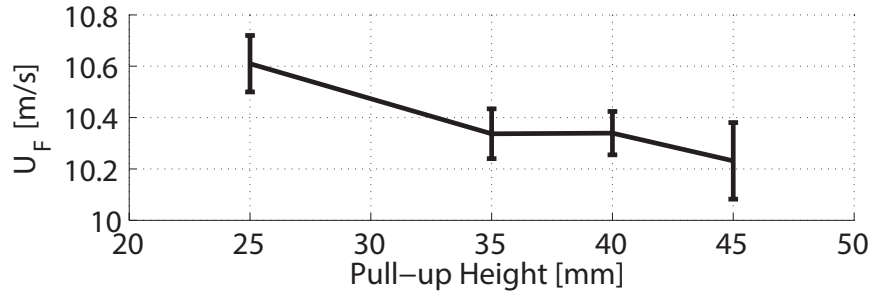


Figure 10.11 – Experimental flutter wind speeds obtained for different pull-up amplitudes.

increased, the experimentally obtained flutter wind speed U_f is decreased. Note that we report only one step response per amplitude, thus the standard deviation represent fluctuations of the wind speed during a single experiment as measured by the pitot-tube, and not over multiple runs. Although we did not investigate this effect rigorously, the dependence of the critical wind speed on the initial perturbation amplitude outline the nonlinear nature of the dynamical system under observation.

Thus, the presented experimental flutter wind speeds are estimated given the outlined approach, and should be viewed as an indication of the flutter region rather than a precise point of flutter. However, although the "actual" flutter wind speed might be slightly higher or lower, it is consistent among the various experimental scenarios since determined with the same procedure. Therefore, we are not too concerned with the decimal precision when comparing our experimental flutter wind speeds to the model predictions, but rather more interested in reliably capturing trends.

10.5.2 Flutter Condition for the Implemented Control Configuration

A comparison between the experimentally determined and the model-based predictions of the flutter wind speeds are listed in Table 10.7. The estimations listed with (+mass) indicate that the eccentric deck and flap inertia effects were considered, the other estimations were made assuming a symmetric deck with negligible structural effects of the flaps. Note that for experiments involving either the control of the leading edge flaps or both edge flaps no flutter was observed experimentally up to the considered maximal wind speed of 16 m/s. The theoretical model predictions are in general lower in all control cases, although improved to various degrees when the deck eccentricity and flap inertia are included. The model predictions based on the experimentally estimated aerodynamic parameters are overall closer to the observed values than those generated by their exclusively theoretical counterpart. Indeed, the model predictions for the uncontrolled deck, as well as those for the single edge flap control, correspond very well to the experimentally obtained critical wind speeds when the eccentric deck and flap inertias are considered. However, this is not the case for the flutter wind speed estimation when all flaps are controlled: in these conditions, all model predictions are far lower than what we observed in the wind tunnel. Again, as we observed

Table 10.7 – Estimation of flutter wind speed

U_f	No control	Leading control	Trailing control	Both control
Experimental	10.58	>16	10.11	>16
Theoretical FDs	10.06	13.45	9.15	9.71
Theoretical FDs (+ mass)	10.53	15.51	9.15	10.50
Estimated FDs	10.23	13.49	10.21	10.87
Estimated FDs (+mass)	10.62	∞	10.20	12.41

from the response step trajectories in Figure 10.7, the outcome of using all flaps in the control appears closer to that of the leading flap control only, pointing out that aerodynamic coupling between leading and trailing flap edges do play a role in the estimation of the critical wind speed and none of our model variants really take this into account. It is noteworthy that our experimental results show a significantly more efficient control than predicted by the theory, which is consistent with the findings of Gouder et al. [23]. Moreover, we show that this discrepancy is not completely explained by experimentally extracted aerodynamic parameters, which was the assumption made by Gouder et al.

10.5.3 Experimental Verification of Flutter Condition for Different Phase-Shifts

The comparison between the predicted flutter wind speeds in the previous subsection was made by considering the control parameters that were used during the estimation procedure. In order to test the versatility of our modeling approach, we will now compare the flutter wind speed predictions given the full range of possible phase-shift values for the leading and trailing edge flap controls.

Experimental flutter wind speeds were obtained for 15 different phase-shift values covering the entire possible range between 0° and 360° , and are compared to the model predictions in Figure 10.12. Note that even though the same, roughly uniformly distributed, phase-shift values were implemented in terms of time delay for the leading and trailing flap control, the resulting effective phase-shifts in degrees varies depending on the pitch frequency. This explains the uneven distribution of the reported experimental points, and the slight difference in phase-shift location between leading and trailing flap control. Moreover, there were two data points where flutter was not achieved up to the maximal wind speed, 16 m/s, for the leading flap control, marked by \triangle in Figure 10.12b.

The results for the leading flap show that the predictions made from theoretical flutter derivatives are relatively close to the predictions of the estimated aerodynamic parameters. This in turn indicates that the theoretical aerodynamic model captures rather well the dynamics of the controlled deck. In both the cases of theoretical and experimental flutter derivatives, the structural model including an eccentric deck and flap inertia improves the prediction substantially.

The results for the trailing flap control in Figure 10.12a show that the theoretical model prediction is significantly different from the estimated prediction and experimental observation. This suggests that the theoretical trailing flap flutter derivatives do not capture well the aerodynamic effects. A conclusion that is consistent with the divergent trends of the experimental and theoretical flap flutter derivatives in Figure 10.10a. Moreover, it is consistent with the finding that the trailing edge's damping efficiency is overestimated theoretically, as reported by Gouder et al. [23]. However, our extended structural model captures again better the experimental results, although just marginally for the theoretical parameter estimations.

Overall, the flutter wind speed predicted using the estimated aerodynamic model parameters in combination with the extended structural model best captures the experimental wind tunnel results, both for the leading and the trailing flap control cases.

Furthermore, we observe that the flap inertia effects boost the leading edge flap control performance, while it dampens the effect of the trailing one. This behavior is explained by the structural symmetry combined with the aerodynamic asymmetry when controlling the leading or trailing flaps. In the case of the leading flap control, the phase-shifts that give positive effects on the structural damping, also yield positive effects in the aerodynamic damping, while the inverse relation is observed for the trailing flap control.

10.6 Model Reduction

In the previous section, we compared the flutter wind speed predictions for a model with 16 flutter derivatives (theoretical and estimated). However, some of the derivatives were difficult to estimate and affected by noise. A fact that poses the question whether we can reduce the number of model parameters and still achieve a quantitatively comparable result while achieving additional repeatability because of the removal of noisy estimates. Such simplified approaches are common for the canonical bridge deck, as presented in Chapter 9; we therefore aim to investigate the reduction possibilities also for the controlled deck.

10.6.1 Canonical Deck

In a first step, we benchmark the methods presented in Section 9.4, for the uncontrolled deck. The results for theoretical and estimated flutter derivatives, with and without eccentricity included, are given in Table 10.8. We observe that the most restrictive methods, Selberg, in Equation 9.22, and Bartoli, in Equations 9.23, both underestimate the flutter wind speed. Even correcting the Bartoli estimation with the ASPI value (the experimental flutter wind speed divided by the estimated theoretical one), as proposed by the authors, does not impact significantly the results. Note that the Selberg estimation is made considering only structural parameters (for a symmetric deck), thus the predicted wind speed is the same in all cases, yet it is closer to the observed experimental wind speed than that achieved with the Bartoli method. The full Theodorsen solution (eight FDs) differ significantly from the original six FDs

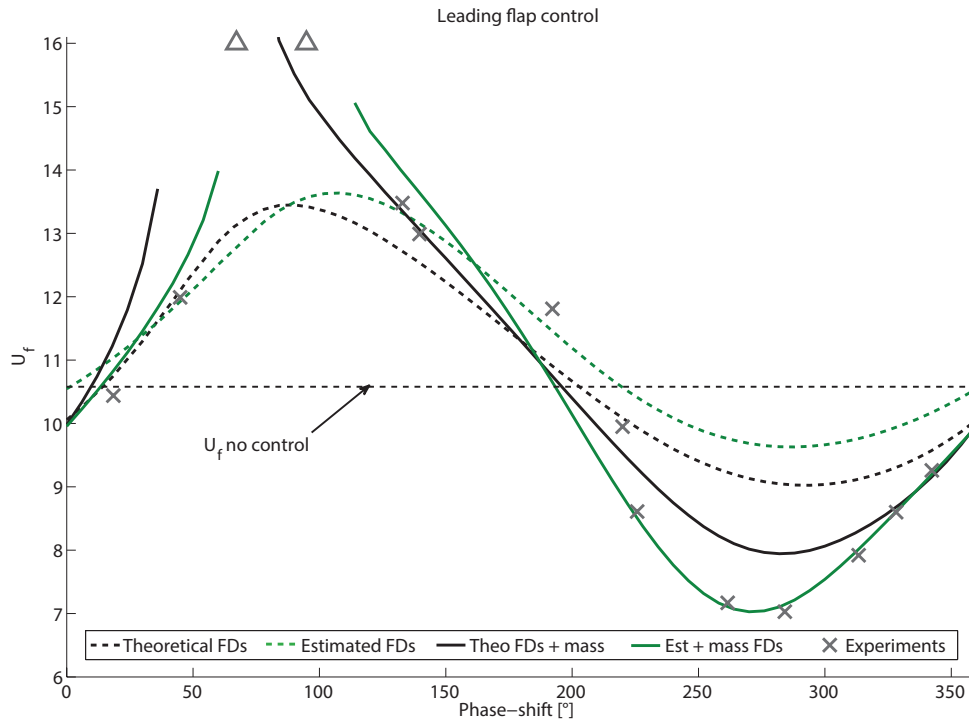
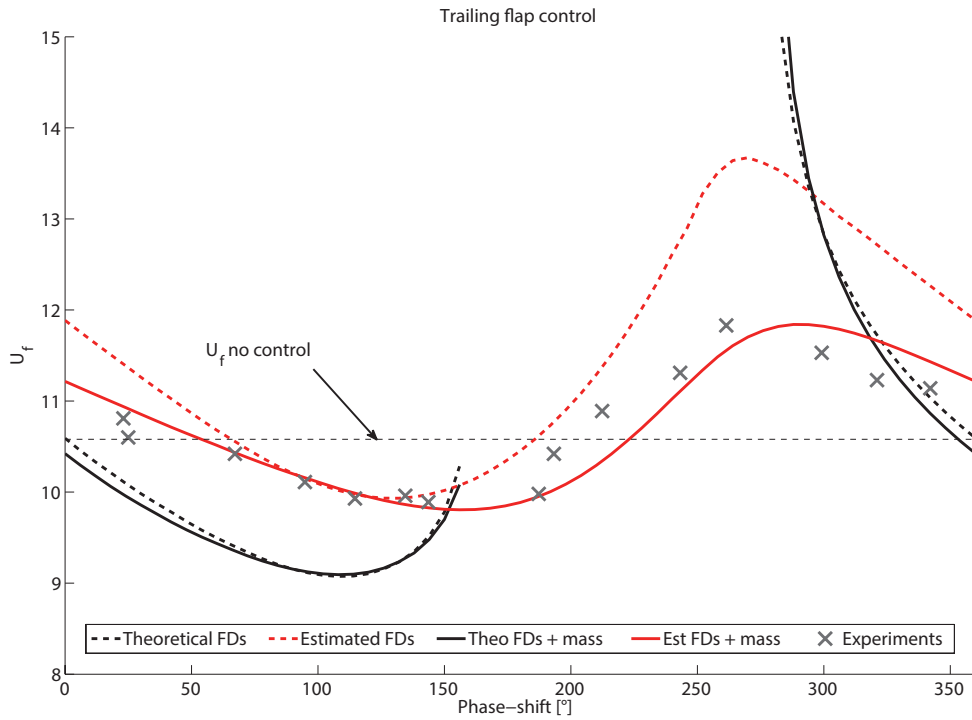


Figure 10.12 – Model prediction compared to experimentally obtained flutter wind speeds.

Table 10.8 – Reduced models U_f estimations for canonical deck

U_f	Experi- mental	Theoretical FDs	Theoretical FDs (+ ecc)	Estimated FDs	Estimated FDs (+ ecc)
Selberg				9.02	
Bartoli (incl. ASPI)	10.58	8.17 (8.59)	8.18 (8.22)	8.98 (9.29)	8.98 (8.94)
Theodorsen (8 FDs)		10.06	10.53	10.23	10.63
Theodorsen (6 FDs)		12.12	13.56	10.95	11.39
Theodorsen (no H_4^*)		10.03	10.52	10.45	10.79
Theodorsen (no A_4^*)		12.12	13.64	10.79	11.23

solution (neither H_4^* , nor A_4^* considered), especially for the theoretically estimated aerodynamic parameters. Furthermore, we have investigated the impact of removing H_4^* and A_4^* separately: we observe that removing H_4^* yields a prediction close to the full solution, while removing A_4^* is closer to the six FDs estimation, in all cases. In fact, removing H_4^* has a smaller impact on the prediction than not modeling deck eccentricity. Moreover, the theoretical and experimentally estimated values of the H_4^* derivative are significantly different, see Figure 10.6a, thus suggesting that this derivative, in general, has little influence on the predicted flutter wind speed. In conclusion, predictions of the flutter wind speed for the canonical deck are deemed to be reliably estimated without including H_4^* .

10.6.2 Controlled Deck

When analyzing the effects of reducing the model parameters for the controlled deck we will look at the whole range of phase-shift values, from 0° to 360° . In Figure 10.13 the mean square errors between the full eight FDs estimation and the reduced models, over the whole phase-shift range, are shown. Note that the reduced models sometime miss to predict a complete flutter suppression (false negative), which is noted by $-X^\circ U_f$, where X denotes the range of phase-shift values that misses the prediction. Similarly, the reduced model might predict additional regions where flutter is completely suppressed (false positive), marked with $+X^\circ U_f$. As for the canonical deck, we observe that removing H_4^* has almost no impact on the model predictions of U_f , and that removing A_4^* is more or less equivalent to using six FDs (plus flap FDs). The prediction of Bartoli is also for the controlled deck quite poor; this is not surprising since H_2^* and H_3^* are not considered, i.e., derivatives that are affected by flap control. Since the Selberg prediction is completely disregarding any flap dynamics, it is meaningless to consider it for the controlled deck. Finally, we have plotted the prediction error when removing, one at a time, the flap flutter derivatives. The reduced predictions for the leading flap control are mostly very close to the full solution, especially when removing A_7^* ; however, removing A_8^* significantly changes the prediction. The estimated flutter wind speeds for the trailing flap control are moderately affected when removing either of the flap derivatives, except for H_5^* where the effect is quite small.

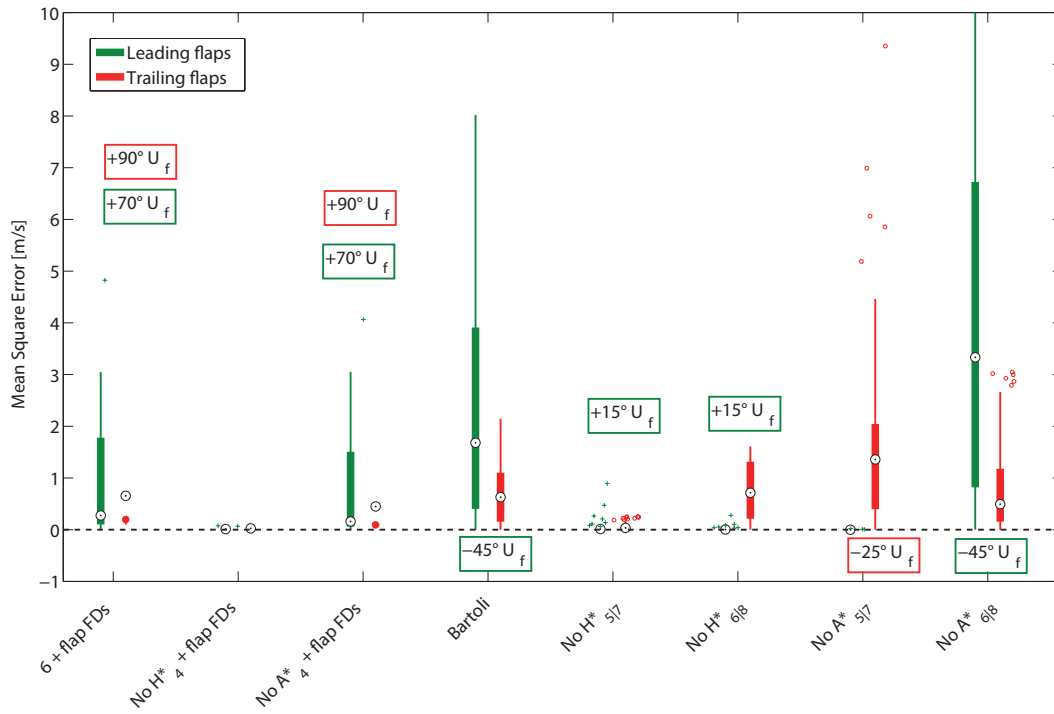
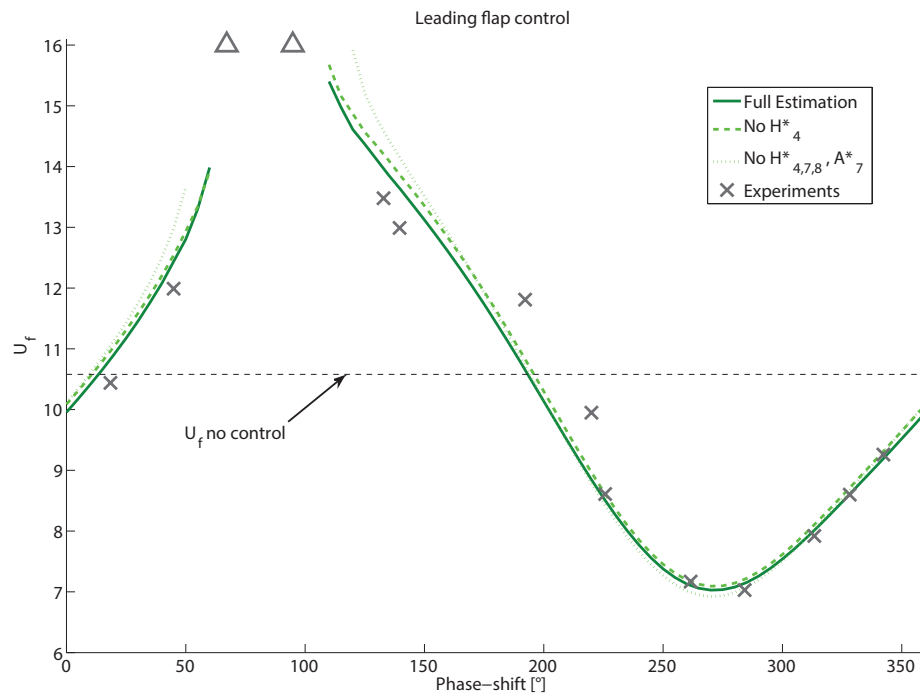
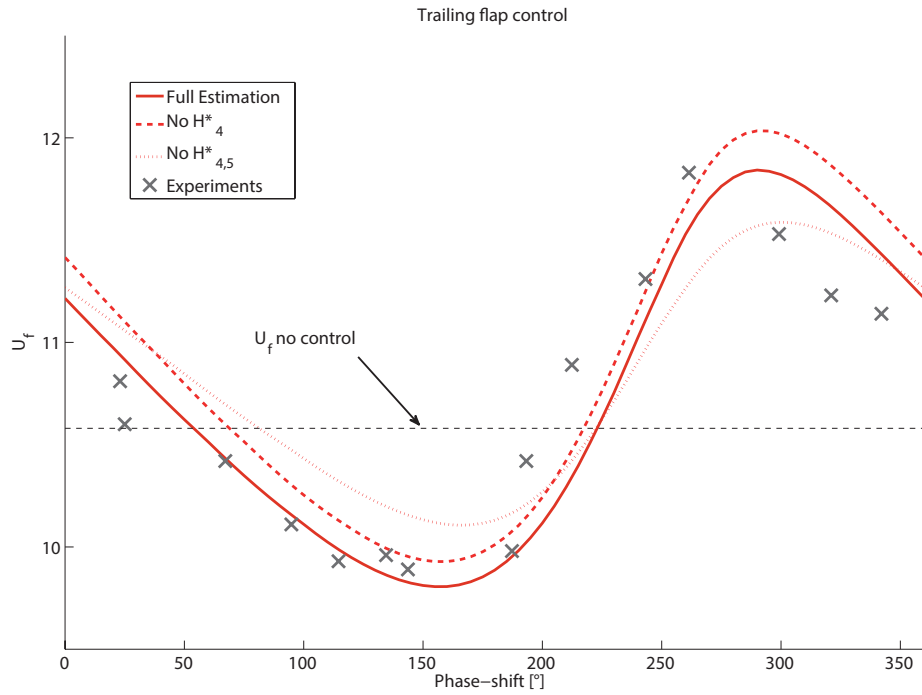


Figure 10.13 – Flutter wind speed prediction errors for different model reductions. Leading flaps in green, trailing flaps in red.

The most promising reductions for the leading and trailing flap control are presented in Figure 10.14. In Figure 10.14a, we observe that in case we remove H_4^* there is a constant positive bias compared to the full estimation for the trailing flap control. The leading flap control shows an almost negligible positive biased for the same simplified model in Figure 10.14b. Thus, the trailing flap control is less robust to the same model simplification. Moreover, we see that additionally removing the most promising trailing flap flutter derivative, H_5^* , has a quite big effect on the estimated flutter wind speed. On the other hand, we observe in Figure 10.14b that we can model the leading flap control case without significantly affecting the flutter prediction using only seven deck flutter derivatives and one for the leading flap. The most distinct estimated leading flap flutter derivative, A_8^* , in Figure 10.10b is thus by far the most important component for describing the control effect.

Finally, an acceptable prediction of the flutter wind speed can be obtained for a deck controlled either with leading or trailing flaps using a model with 12 FDs (removing H_4^* , H_7^* , H_8^* and A_7^*), instead of the 16 FDs of the full solution.



(b) Leading flap control case. Note that the experimental points marked Δ did not flutter, but was tested up to 16 m/s.

Figure 10.14 – Model reduction effects on flutter wind speed prediction compared to experimentally obtained flutter wind speeds.

Summary

In this chapter we described the methodology used to estimate the model parameters characterizing the two-dimensional model outlined in Chapter 9. Both structural and aerodynamic model parameters were estimated from step response experiments conducted in the wind tunnel. We show that the flutter wind speed of the uncontrolled deck and the deck controlled by either leading or trailing flaps can be estimated reliably using Theodorsen's method, also for a range of control parameters not used during the estimation procedure. Furthermore, we investigate the effects of estimating the flutter condition using a reduced number of model parameters.

11 Conclusion

THIS part of the dissertation covers the thorough investigation of the analytical model of a bridge deck equipped with moving leading and trailing edge flaps. We employed a systematic approach in order to estimate all the model parameters with wind tunnel tests, leveraging our experimental setup. We estimated model parameters from a total of 200 step responses for four different control strategies: using no control, controlling only leading flaps, controlling only trailing flaps, and controlling all flaps.

Modeling the aerodynamic effects of trailing or leading flaps in terms of additional flutter derivatives appears to sufficiently capture their impact on the overall deck response. However, an experimental estimation of model parameters, especially for the trailing flap flutter derivatives, is of great importance. In this work, we have estimated the flap flutter derivatives indirectly, from aggregated terms. An interesting approach for future work would be to attempt a direct estimation of the aerodynamic parameters associated with the flaps.

Including eccentricity and flap inertia effects into the structural model showed significant impact on the flutter prediction of the controlled deck, even for relatively small values. The importance of properly capturing the structural part (especially the flap inertia effects) of the model becomes clear when comparing the flutter predictions over a range of phase-shift values.

Although the inertia of the flap around its hinge can never be completely be removed, the static mass inertia of the flaps, S_x , can be reduced to zero with a proper mass balancing of the flap (i.e. center of mass and center of rotation overlap). Note that in this case the mass moment inertia terms due to the flaps would also be reduced to the flap inertia around its hinge, i.e., $I'_x = I_x$. Such a mass balancing would thus greatly reduce the flap inertia effects on the total deck dynamics, which is perhaps the assumption made by researchers who did not consider the flaps in their structural model. Moreover, regarding real bridges the effect of flap inertia will probably be negligible since the mass of the flaps is much smaller than the mass of the bridge deck.

Chapter 11. Conclusion

The proposed aeroelastic model, in combination with the experimentally obtained model parameters, is capable of predicting the flutter wind speed from wind tunnel tests for a wide range of phase-shift parameters, even for control configurations not used for the estimation procedure. Thus, the analytical model, with estimated model parameters, can be leveraged for designing and tuning control parameters with significantly more faithful results than using theoretical model parameters.

However, even though the model predictions are confirmed when only the leading edge flaps or trailing edge flaps are controlled, the prediction quality is not as good when both flaps are being controlled simultaneously. A possible explanation to the observed discrepancies is that the leading edge flaps are disrupting the flow over the deck and the trailing flaps, therefore diminishing their effects and, in turn, breaking one of the model assumptions. Since the control parameters chosen for system identification purposes are non-favorable in terms of vibration-damping effectiveness using the trailing edge flaps, this means that control effort of using both flaps is not poorly captured since under such conditions the impact of the trailing flaps is clearly reduced. This hypothesis appears to be confirmed by the experimental results gathered up to date. However, further investigations, for instance based on local pressure measurements on deck and flaps for the different control scenarios, could shed further lights on this hypothesis.

Finally, we have looked at possible redundancies in the aerodynamic model. We outlined that the bridge deck can be modeled almost identically to the full solution when ignoring one flutter derivative. Moreover, we showed that the forces due to the leading edge flap can to a great extent be captured with one aerodynamic parameter instead of the four characterizing the full solution. These results indicate that the model description has redundancies, that would be interesting to further analyze.

Summary

In this chapter we conclude the analytical model part of the thesis. The widely used analytical model based on Theodorsen's theory has been investigated. Our proposed, more complex, structural model for the flap dynamics proved better at predicting the flutter wind speed of the controlled deck than the model ignoring the flaps' structural dynamics. Moreover, we found that estimating the flutter derivatives from the experimental setup provides significantly better flutter wind speed predictions than those produced using theoretical values. However, we observed that, although the model serves well when the control is applied to either the leading or the trailing flaps, the predictions are not as accurate when both sides are controlled simultaneously.

Control Part IV

12 Related Work

SUPPRESSING flutter has been the main objective of every experimental study of bridge decks equipped with mobile flaps, both passively and actively controlled. In this chapter we provide an overview of the different control strategies that have been investigated for all such stabilization methods. In particular, we distinguish the research efforts evaluated with wind tunnel experiments from purely analytical or numerical studies.

12.1 Passively Controlled Mobile Flaps

In this section we review the passive control strategies of flaps that have been investigated experimentally and theoretically.

12.1.1 Experimental Studies

All research groups that have experimentally investigated a passive flap control were able to achieve a higher critical flutter wind velocity: Wilde et al. [15] by ca 50%; Aslan et al. [17] by ca 10%; Phan et al. [18] by 250% in smooth flow and by 200% in turbulent flow (turbulence intensity: 5%); Zhao et al. [21] by 18%; and Kwon et al. [16] improved the flutter wind velocity (in laminar flow and 0° angle of attack) with stable control by 43%. Furthermore, Kwon et al. studied the effect of adding turbulence (turbulence level not specified) and changing the wind's angle of attack by $\pm 3^\circ$. In a turbulent environment with 0° angle of attack they increased the flutter wind speed by 23%, and in a laminar flow with a small angle of attack the flutter wind speed was increased by 22%. The results indicate that even small disturbances (e.g., 3° difference in the wind's angle of attack) to the setup can have a major impact (e.g., 20% difference in flutter wind speed) on a passively controlled system. Moreover, these results are consistent with the findings of Phan et al., where the comparison between laminar and turbulent flow brought a 20% decrease to the flutter wind speed improvement. Considering that a real suspension bridge will be subjected to both turbulence effects and various angles

of attack of the wind this is an important limitation. In 2016 Gouder et al. [23] performed an experimental study comparing the control performance of the leading edge and the trailing edge, or both used in combination. As previously stated, they observed that the trailing edge is not damping the deck as efficiently as their model predicted. In fact, the leading edge seems to outperform the trailing edge flap, although, the exact same control gain values were not compared. Their control law is an amplitude-gain one that is using a combination of the deck's pitch and heave velocities as input. Note that since they restrict their active setup to a control law emulating a passive mitigation solution, they do not investigate the effect of adding or changing the phase-shift. Moreover, the same research group [22] performed a study of buffet loading and flutter suppression in the presence of turbulence of the controlled section model. Note that in all of their experimental work [21]–[23] they optimized the control parameters using \mathcal{H}_∞ theory (robust control) starting from the analytical model based on Theodorsen's theory.

12.1.2 Theoretical Studies

Moreover, Graham, Limebeer and Zhao [63] analyzed theoretically the somewhat contradicting requirements of a controlled bridge in terms of flutter and torsional divergence stability. Their results indicate that individual control strategies for the leading edge and trailing edge are preferable. They conclude that even though passive control strategies might be simpler to realize and more reliable, an active control strategy is advantageous considering that the wind conditions do change. Furthermore, they have shown that the system is effective to suppress also buffeting, in addition to flutter, using a single trailing flap [65]. Finally, the same authors investigated a symmetrical passive flap control [66], resulting in a wind direction independent solution, which is however not able to increase the critical wind speed for torsional divergence.

12.2 Actively Controlled Mobile Flaps

In this section we review the active control strategies of flaps that have been investigated experimentally and theoretically.

12.2.1 Experimental Studies

Kobayashi et al [14], [24] implemented a simple output feedback control law. They employed an amplitude-gain and a phase-shift of the bridge section's pitch displacement for the first study conducted with the flaps placed above the deck [14], and managed to increase the flutter wind speed by 50%. For the follow up project they employed a section model with flaps integrated to the deck, and introduced an amplitude-gain and phase-shift control law with a combined heave and pitch input [24]. Although, they analytically investigated the effects of both leading and trailing flap, they did only provide results from the trailing flap control experiment. Furthermore, they do not disclose by how much the flutter wind speed is

improved in this latter study. In both of these works, they point out that torsional divergence stability becomes an issue at high wind velocities, and is limiting the performance of the bridge stabilization control.

Hansen et al. (e.g., [27]) leveraged the same control strategy as Kobayashi et al. [14], i.e., an amplitude-gain and phase-shift control law and the bridge section's pitch displacements as input. Although, they confirmed that their controlled deck can reduce wind-induced vibrations, they do not perform flutter suppression experiments. Nevertheless, they showed that the flutter wind speed can be decreased when unfavorable phase-angles are implemented.

12.2.2 Theoretical Studies

Additionally, Hansen et al. [27] investigated additional linear (Proportional-Derivative) control strategies analytically: classical linear optimal closed-loop control; and instantaneous optimal closed-loop control. Both of the control laws were theoretically effective in limiting the vibrations.

Wilde and Y. Fujino [57], [59] proposed a variable-gain control law for the flaps. The RFA formulation of the two-dimensional analytical model, allows optimizing the control parameters in an operating range instead of exclusively at the flutter wind speed. The approach is motivated by the fact that the open-loop system properties (the bridge section's modal frequencies and damping ratios) vary with the wind speed. The performance of the variable-gain control strategy is compared to the control law optimized for specific wind speeds, and it is shown that it provides satisfactory result for the whole operating range while the laws for specific wind speeds perform much worse at the ranges they are not designed for.

Multi-mode investigations

Kwon et al. [70] also proposed an active control law; a linear optimal output feedback control, minimizing the control energy, applied to their multi-mode model. They investigate the performance of a bridge section controlled by one to five control surfaces, that are uniformly placed along the main span. Their results show that potentially independent control surfaces move in almost the same manner and that, while adding one controller has a significant impact, adding more than one controller only slightly improves the performance. However, they conclude that the robustness of the control is increased with multiple controllers in the case that one or more fails.

Nissen et al. [72] proposed a linear (Proportional-Derivative) control law for the flap position as a function of the bridge state. For their multi-mode model a local control input is given to the distributed flap system. Their theoretical results show that the critical wind speed for flutter instability is increased.

12.3 Concluding Remarks

The control approaches of the individual flaps presented above are quite similar; linear control laws with the heave and/or pitch DOFs as control input for the flaps. All of the experimental efforts have employed bridge section models endowed with a single flap on each side of the girder. We aim to extend the investigation of active flutter control to bridge section models endowed with multiple flaps on each side, so that the potential of a physically distributed mitigation system can be studied and validated experimentally. The spatial distribution of flaps, and the degree of operated elements, have been studied in a multi-mode analysis.

Summary

In this chapter we describe the different control strategies that have been investigated for a bridge deck equipped with mobile flaps. A handful of actively and passively controlled section models have been proven capable of suppressing flutter. Although multi-flap control have been studied theoretically, there exist no experimental precedent. We will in the following chapters present our theoretical, but foremost experimental, investigations of flap control on a local (flap), as well as global (inter-flap) level.

13 Technical Approach

WE will in this chapter outline the methodology employed for the control part of this thesis. We have defined a series of control approaches for the flaps and different external and internal disturbances of the system in order to investigate the rich capabilities of the research test-bed we have developed. Moreover, we have established several metrics that allow us to evaluate the cost, benefit, and performance of the proposed control strategies.

13.1 Control of the Section Model

In this section we will further describe the SmartBridge as a deck with independently controllable segments. Moreover, we will define how to appreciate the goodness of a control law by several performance metrics.

13.1.1 The Section Model in the Third Dimension

Up until this point we have only considered two dimensions of the section model, the heave and the pitch DOFs. Although we restrict the deck in many directions, it is still free to rotate also in the roll DOF, as visualized in Figure 13.1. Note that the movements in yaw, and along the x-axis, are restricted by the drag wires, and that motion along the y-axis is assumed to be negligible. Moreover, under the conditions investigated so far, i.e., with a symmetrical and synchronized flap control in a uniform wind flow, the roll of the deck was comparatively insignificant. However, when one or several of these conditions are perturbed, the importance of the roll DOF is augmented. We have systematically investigated such scenarios in Chapter 14 and Chapter 15, and we therefore also consider roll in the following analysis.

Furthermore, we have defined four subsections of the bridge section model along the y-axis, as depicted in Figure 13.1. Thus, each leading and trailing edge flap pair form a subsection.

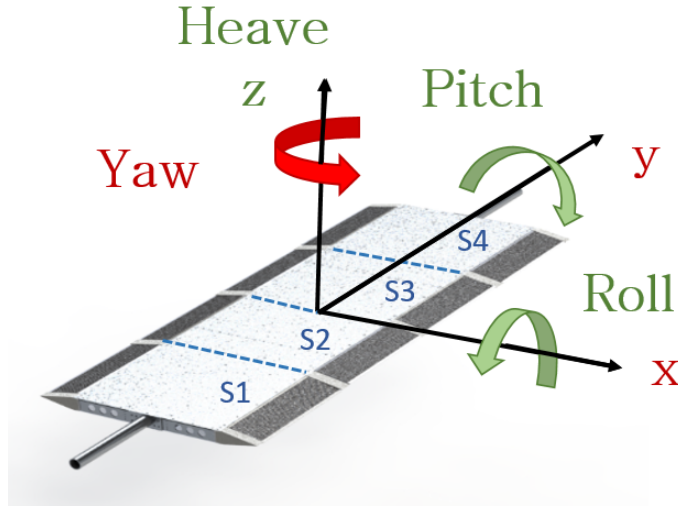


Figure 13.1 – Visualization of the six DOFs of the deck. Note that movements along the y-axis and x-axis, as well as motion in the yaw DOF, are restricted in our setup (all represented in red). The division of the four subsections are denoted S1, S2, S3 and S4.

13.1.2 Synchronized and Decentralized Control Strategies

In Part III we demonstrated that when the flaps are controlled with a linear amplitude-gain and a phase-shift control law modulated by the pitch of the deck, flutter of the section model can be suppressed. Moreover, we indirectly proposed a simple coordination between flaps along the x-axis when studying the resulting flutter wind speed for a range of the phase-shift values of the leading and the trailing edge flap control laws. We furthermore concluded that the aerodynamic forces produced by the flaps are asymmetric when identical control parameters are implemented for the leading and trailing edge flaps. Thus, studying a synchronized flap control along the x-axis is not effective. Instead, using a synchronized control law along the y-axis of the deck appeared to be a natural and effective choice in absence of significant heterogeneities of the wind field along the cross-section of the channel. In this part, we do want to revisit such centralized and synchronized control choice and leverage our unique test-bed to investigate alternative coordination strategies. We have therefore chosen to primarily focus the control effort described in this part on coordination between flaps along the arrays. Thus, we do not further investigate other possible control strategies for the individual flaps, e.g., piece-wise linear or nonlinear, but adhering to the previously defined amplitude-gain and phase-shift control law. Below we repeat the synchronized control law presented in Part III (although here generalized in terms of the control input) for the leading and trailing edge flaps.

$$\alpha_l(t) = A e^{-i\phi_l} x(t) \quad (13.1a)$$

$$\alpha_t(t) = A e^{-i\phi_t} x(t) \quad (13.1b)$$

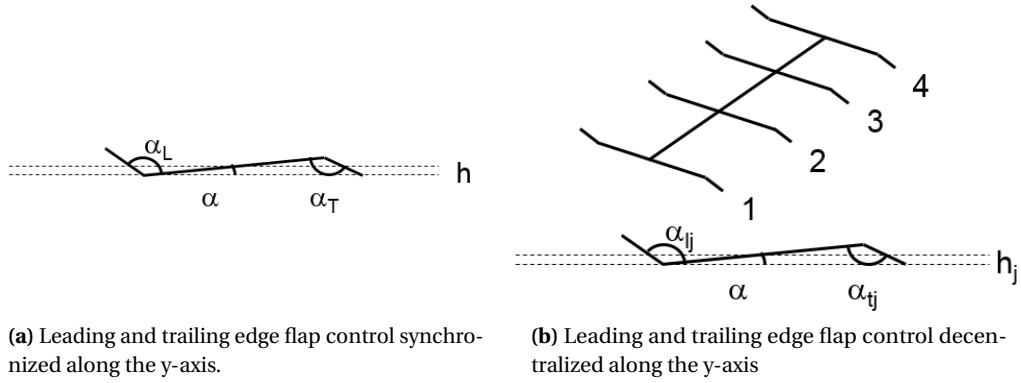


Figure 13.2 – Visualization of the synchronized and decentralized control approaches.

where A is the amplitude-gain, ϕ_l and ϕ_t are the leading and trailing edge phase-shifts, and $x(t)$ is the position of the deck in heave or pitch.

In order to study the individually controlled sections of the deck we have implemented the following decentralized flap control law

$$\alpha_{lj}(t) = Ae^{-i\phi_l} h_j(t) \quad (13.2a)$$

$$\alpha_{tj}(t) = Ae^{-i\phi_t} h_j(t) \quad (13.2b)$$

where $h_j(t)$ is the local heave position for section $j = 1:4$. The synchronized and decentralized control strategies are visualized in Figure 13.2.

Note that since the section model has a high torsional rigidity we cannot implement a meaningful individual control input for the deck's pitch DOF. However, locally individual heave positions can be achieved since the deck is free to move in the roll DOF. We will therefore in the following chapter also consider heave as control input, when comparing the synchronized and decentralized control approaches. Recall that, in theory, the deck oscillates at the same frequency and with constant amplitudes in the heave and in the pitch DOFs during flutter. Under these conditions controlling the deck using the pitch as input is equivalent to using the heave as input assuming that the amplitude-gain and phase-shift parameters are modified appropriately. Thus, we expect a similar performance regardless of the chosen control input for flutter suppression.

Note that we do not technically implement a decentralized control strategy, rather, we are emulating one in a centralized fashion. The individual heave positions are not given by local sensors, but are derived from the four laser sensors, and the individual flap set-points are calculated on the (single) control board. The control is however decentralized in the sense that each section is controlled based on local information, and that no information is shared among them.

13.1.3 Performance Metrics

In Part III, we showed already for the experimental model validation that we are able to control flutter, i.e., increase the flutter wind speed, providing that favorable control parameters have been implemented. However, as it is true for any control problem, additional actuation effort comes at a price. In order to facilitate the comparison between different control algorithms, it is convenient to quantify this cost in a single parameter. We have defined the actuation cost as the sum of the individual flap's kinetic energy, averaged for some finite time period. Analogously, it is of interest to evaluate the goodness of the control algorithm. Similarly to the actuation cost, the kinetic energy for the deck, provides meaningful information for determining the control efficiency. Since our goal is to limit the deck vibrations, a high kinetic energy is not desired. Thus, we have defined the benefit of the control as the inverse sum of the kinetic energy in the deck's three DOFs, averaged for the same finite time period. In the following equations our cost and benefit measures are described

$$C_f = \sum_{k=1}^n \sum_{i=1}^8 \frac{I_f \dot{\alpha}_i[k]^2}{2n} \quad (13.3a)$$

$$C_h = \sum_{k=1}^n \frac{m \dot{h}[k]^2}{2n} \quad (13.3b)$$

$$C_\alpha = \sum_{k=1}^n \frac{I_\alpha \dot{\alpha}[k]^2}{2n} \quad (13.3c)$$

$$C_\beta = \sum_{k=1}^n \frac{I_\beta \dot{\beta}[k]^2}{2n} \quad (13.3d)$$

$$B_X = \frac{1}{C_X} = \frac{1}{C_h + C_\alpha + C_\beta} \quad (13.3e)$$

where I_f is the flap mass inertia around the hinge $\dot{\alpha}_i[k]$ is the velocity of flap i for time sample k , and n is the total number of samples in the time series, i.e., the length of the step response. Furthermore, m , I_α , and I_β , are the deck's mass, pitch mass moment inertia, and roll mass moment inertia, respectively; and \dot{h} , $\dot{\alpha}$, and $\dot{\beta}$ are the velocities in the heave, pitch, and roll DOFs, respectively.

In the case of a generally favorable control law, we expect that increasing the amplitudes of the flaps, increases the cost, that will in turn dampen the deck vibrations more efficiently, thus, also increasing the benefit. In order to evaluate such trade-offs between the cost and the benefit of the control law, we would like to define a performance index that incorporates both benefit and cost effects.

Such a performance metric can be defined in many different ways. In the control theory literature, a cost function is commonly defined (in a similar format) as [96]

$$P_1 = C_X + wC_f \quad (13.4)$$

where w is a weight value. In optimal control, the aim is to find the control parameters that minimize the cost function P_1 (usually denoted J in control theory); and the weight value, w , determines whether the focus of the optimization leans towards minimizing the state movements (C_X), or the actuator movements (C_f). Thus, the weight is an important design parameter for determining the optimal solution. Determining control parameters through optimal control is not within the scope of this thesis. However, the definition of the cost function in Equation 13.4, is an interesting measure for evaluating the control performance. We have chosen to implement a weight value that normalizes the kinetic energy contributions of the deck and flaps; thus $w = m / \sum m_f$, where m_f is the weight of a single flap. However, as previously stated, assigning the weight is a design choice, and depending on the operation requirements, one could imagine to set a higher or lower value.

Another possible definition of the performance index, is to directly look at the ratio between the cost and the benefit, as follows

$$P_2 = \frac{C_f}{B_X} = C_f C_X \quad (13.5)$$

This performance index is perhaps more common in economical studies, and quantifies a "value for money" concept. It is certainly an interesting aspect to look at the return in control performance compared to the cost invested, in our case energy. However, one should be careful with interpreting this measure as it can be misleading. For instance, it would not be advisable to optimize control parameters to minimize Equation 13.5, although lower values are generally desirable, as we would easily find an optimal solution with no flap control, i.e., $C_f = 0$. In this case the performance is regarded as optimal regardless of the bridge state (whether fluttering or stable), and thus quite meaningless.

Both of the introduced performance metrics are based on the same definitions of cost and benefit, and they are both considered better for low values. Furthermore, note that the defined cost is highly correlated to the defined benefit; i.e, since the flap motions are determined by the control law using the bridge state as input, larger movements of the deck implies also (generally) larger flap movements.

Finally, all of the defined cost and performance metrics are calculated for a finite number of sample data, n . In Figure 13.3 the evolution of the measures are plotted against the length of the step response used in the calculations. The example is made for a control law capable of suppressing flutter. Therefore, the amplitudes of the bridge deck oscillations, and thus the flap actuation, decrease over time, which is reflected in the cost and benefit graphs. Furthermore, we observe that both defined performance metrics (Equations 13.4 and 13.5) decay over

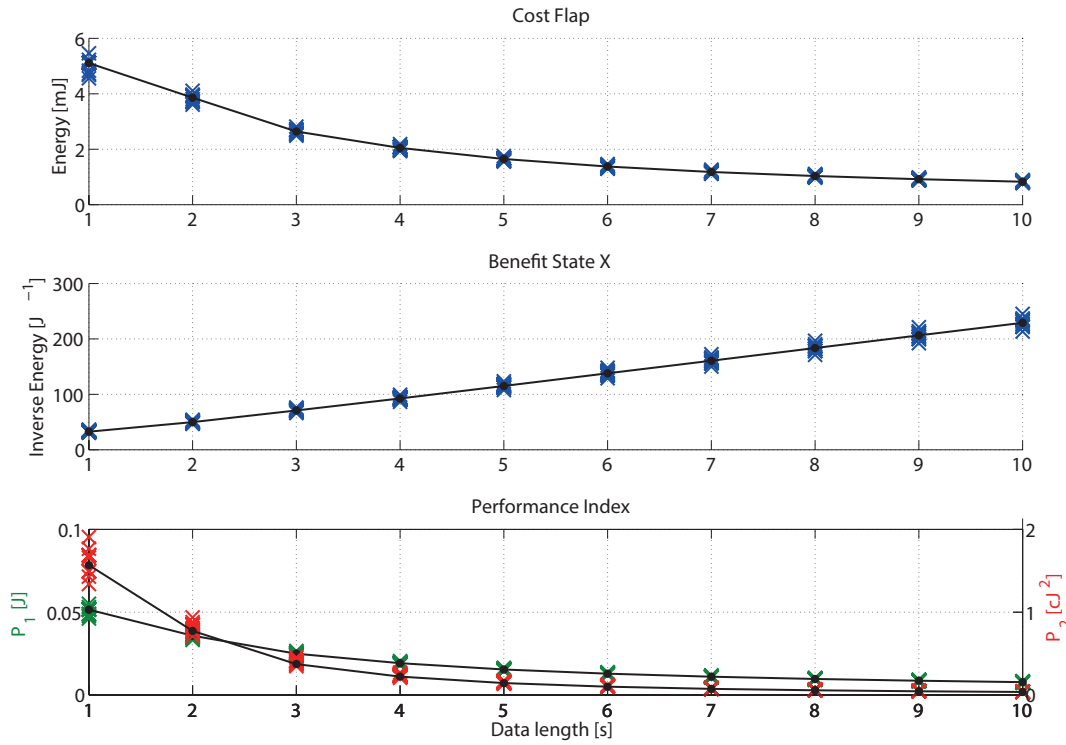


Figure 13.3 – The cost, benefit and performance indices calculated for synchronized flap movements under normal flow conditions. The same step response is considered for different data lengths, n .

time, however, at different rates. Note that the different metrics vary more for shorter time series, which is logical since the measures are averaged over the number of samples. Within reasonable limits, the number of considered data points is not of significant importance when comparing different control laws, assuming that the same number of samples are consistently used. We have therefore chosen a time length of 6 s ($n = 1200$), in accordance with the modeling estimation experiments in Part III.

13.2 Experimental Scenarios

The SmartBridge has a symmetric design and, as previously stated, we do not expect any significant dynamic variations along the y-axis of the deck in a uniform wind field. Consequently, we do not anticipate significant differences in the control performance between the synchronized and decentralized approaches under such ideal conditions. Therefore, we will in addition to the symmetric situation, create more interesting scenarios, so that the robustness of the control strategies for perturbed conditions can be evaluated. Moreover, such perfect conditions are unrealistic when considering a real full-scale bridge, where both disturbances of the wind field (e.g., angle of attack, turbulence level) and the deck (e.g., traffic) are constant factors.

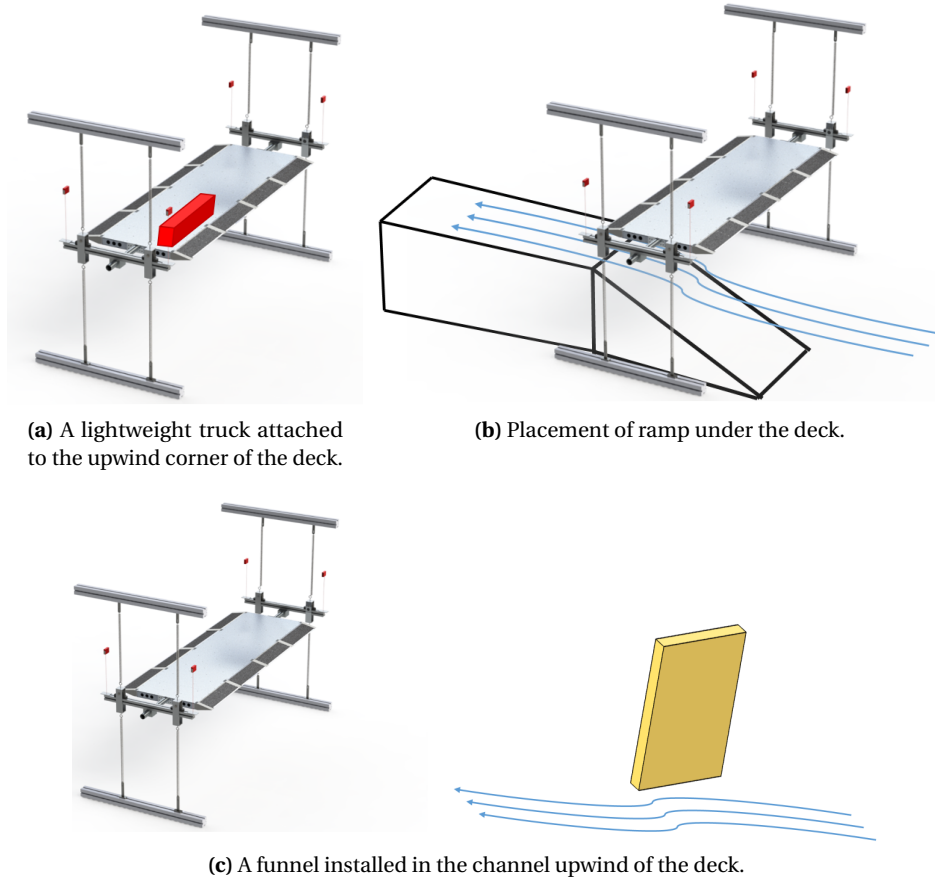


Figure 13.4 – Sketches of the different experimental scenarios (not to scale).

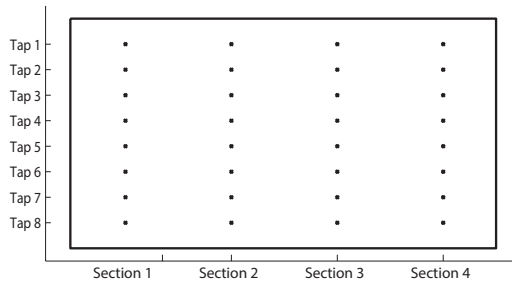
The different scenario's investigated are categorized into introducing asymmetries to the deck itself, and into creating a nonuniform wind field. In the following subsections, the investigated perturbed experimental conditions are further described.

13.2.1 Asymmetric Deck

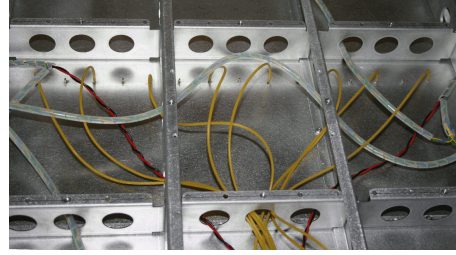
Asymmetry of the section model can be achieved in many different ways; we have focused on creating an imbalance in the actuation of the flaps and to create a nonuniform aerodynamic profile of the deck.

Actuating different flap combinations

The SmartBridge is divided into four sections each equipped with an independently controllable leading and trailing edge flap. Varying the number of segments actuated can address both questions of optimal coverage, i.e., ideal actuator length per length of deck, and of control



(a) Tap locations on deck viewed from above.



(b) Pressure tubes attached to the taps on the deck inside.

Figure 13.5 – Arrangement of the pressure sensor measurement system for the experiments.

robustness to malfunctioning flaps.

Modifying the aerodynamic profile of the deck

In order to create an aerodynamic asymmetry of the deck, we have placed a symbolic truck on the driving lane, as depicted in Figure 13.4a. The truck is a wooden block with dimensions $5 \times 8 \times 20 \text{ cm}^3$, and lightweight so that the impact on the structural dynamics of the deck is negligible. Furthermore, the truck is attached with strong magnets that can latch onto any of the iron screws that are keeping the aluminum panels in place. Thus, it can be easily placed at several different locations on the deck surface.

13.2.2 Modifying the Wind Profile

We have investigated two different scenarios for manipulating the wind field around the section model; in both cases the uniform wind field is disturbed by objects placed in the channel. In this section, we will characterize the different perturbed scenarios as well as the regular undisturbed wind flow.

In order to better understand how the wind field is affected when additional objects are introduced into the flow, we created CFD simulations of the flow in the channel around our section model. This design effort to create interesting wind profiles was achieved using the Solidworks Flow Simulation package¹.

Furthermore, in order to validate the expected wind field characteristics, we have leveraged the pressure sensor system, and the traversing system equipped with a hot-wire anemometer probe, that were introduced in Part II. The 64 pressure taps were equally distributed on the deck surface with eight local measurements on the lower and upper side of the deck per section of the SmartBridge. In Figure 13.5a the tap placements are presented; the same pattern of 32 taps are reproduced on both the upper and lower sides of the deck. The pressure tubes

¹<http://www.solidworks.com/sw/products/simulation/flow-simulation.htm>

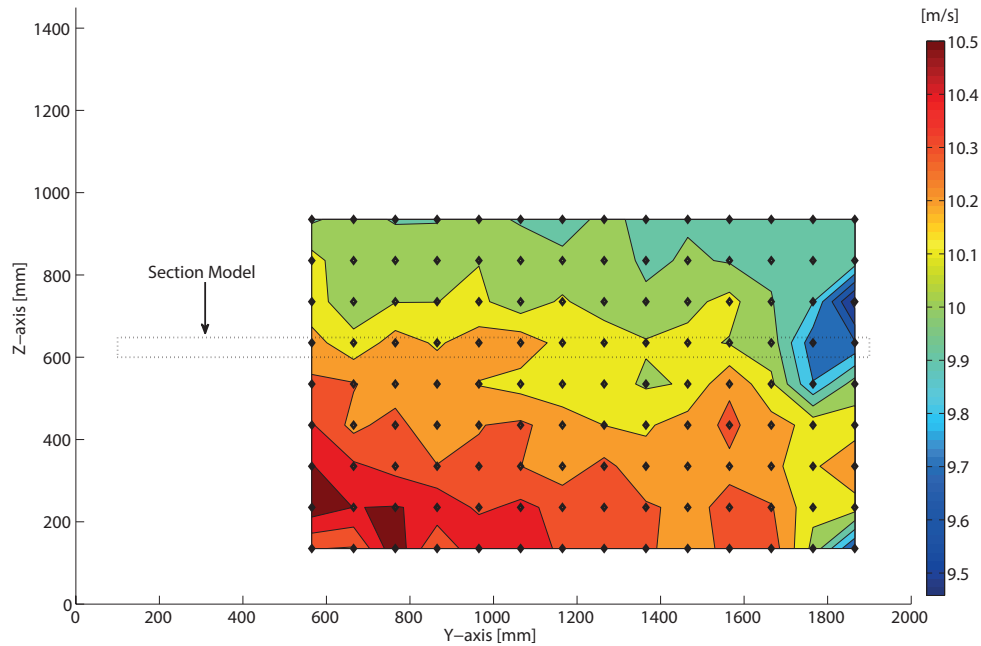


Figure 13.6 – Hot-wire measurements taken with the traversing system during normal flow in front of the bridge deck.

connected to the taps inside the deck are pictured in Figure 13.5b. The pressure measurements presented in this section were taken for the deck fixed by the decoupling system, thus excluding aeroelastic effects from the resulting measures. Each measurement batch was sampled at 2 Hz per channel during 60 s.

The unperturbed wind field

The characteristics of the wind field under normal conditions have been measured using a hot-wire probe attached to the traversing system's arm. This instrument allows us to create a wind speed map of the channel's cross-section, as presented in Figure 13.6. The data was gathered close to the flutter condition, and the measurements were taken slightly up-wind (~ 1 m) of the section model. A total of 14x9 data batches were collected with 10 cm intervals along the y-axis and the z-axis, each sampled at 100 Hz during 1 s. The turbulence intensity, i.e., the standard deviation divided by the mean wind velocity, averaged over the entire cross-section was of 1.8%. Due to the construction of the movable arm of the traversing system the movements in the y-direction and z-direction are restricted as indicated by the borders of the color map. Thus, we lack wind speed measurements for the first subsection of the deck. However, the coverage is sufficiently large to determine that even under these undisturbed flow conditions, the wind field is not precisely uniform; higher velocities are measured in the left, lower, part of the channel.

Furthermore, this result is consistent with the pressure tap measurements observed for the

undisturbed condition, presented in Figure 13.8 and Figure 13.10. Note that a high negative pressure on the deck surface indicates high wind speeds in the orthogonal direction to the pressure tap, i.e., for the x-component of the wind speed (also measured by the hot-wire probe). The pressure measurements in Figure 13.8 imply that the highest wind speeds are observed on the lower panel side of the deck towards the left side of the channel. In Figure 13.10 the pressure differences between the corresponding taps on the lower and upper sides of the deck are presented, thus providing a different representation of the same results.

Nonuniform wind field in one DOF

To achieve different flow conditions for the individual sections of the SmartBridge, a varying wind field along the y-axis of the channel is required. A basic technique to impose such conditions is to create a funnel effect, as seen in Figure 13.4c. The flat surface attached at an angle to the wall of the channel directs the flow into a narrower stream, thus creating an asymmetry in the y-direction without major perturbations in the z-direction. In Figure 13.7a and Figure 13.7c the pressure and velocity simulations on the funnel side of the channel are presented; and in Figure 13.7b and Figure 13.7d the pressure and velocity simulations on the opposite side of the channel are illustrated. We observe that the wind velocities approaching the deck at the funnel side are significantly lower than on the opposite side of the channel. Also the pressure is slightly higher on the side opposite of the funnel.

In Figure 13.8, the average pressure on the upper and lower sides of each section, measured locally on the deck, are presented. Indeed, we observe a change in pressure, relative to that of the normal condition, indicating lower wind velocities on the funnel side of the deck at section 4, thus supporting the simulated results. Note that we have defined the global positive pressure in the positive direction of the z-axis. Thus, the negative pressure measured locally on the upper side of the deck (out from surface) becomes positive pressure in the global context, while the negative pressure measured on the lower side of the deck remains negative.

Nonuniform wind field in two DOFs

In order to further disturb the deck and increase the importance of the roll DOF, we additionally created a scenario where the wind field is varying along the y-axis and z-axis, i.e., also above and under the deck. These conditions can be achieved by placing a ramp underneath the deck, as seen in Figure 13.4b.

In Figure 13.9a and Figure 13.9c the pressure and velocity simulations on the ramp side of the channel are presented; and in Figure 13.9b and Figure 13.9d the pressure and velocity simulations on the opposite side of the channel are found. We observe that the pressure is high under the deck in front of the ramp, and as anticipated by Bernoulli's principle regarding the conservation of energy, the corresponding wind velocities are low. Moreover, according to the same principle we observe the opposite effect in the narrow space in between the top of

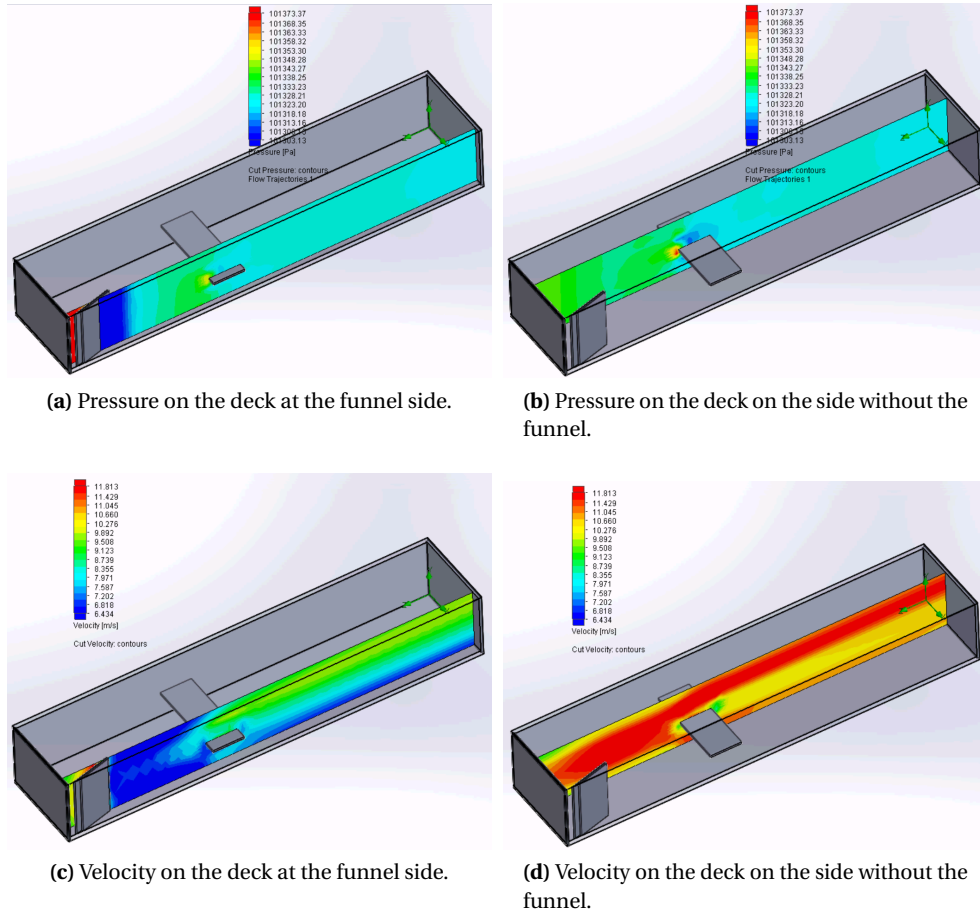


Figure 13.7 – Simulated pressure and velocity over the deck with a funnel placed upwind.

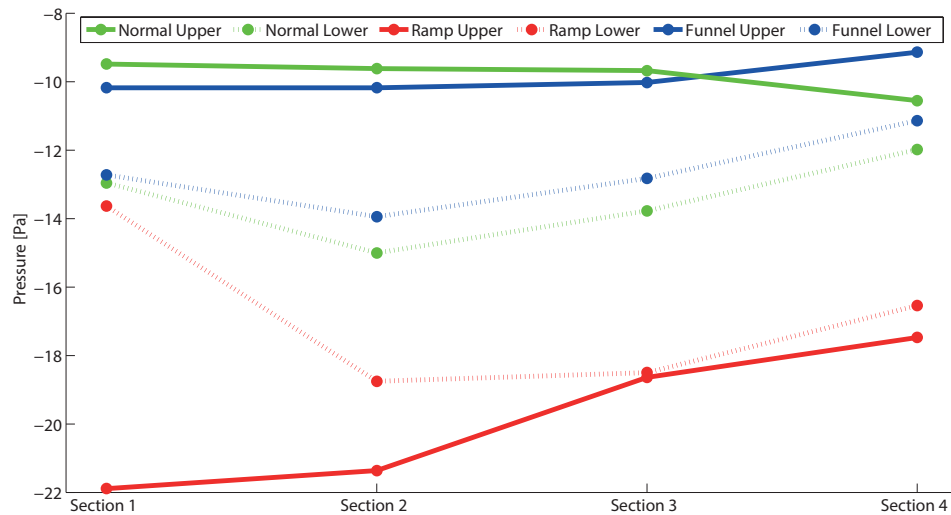


Figure 13.8 – Pressure measurements taken at the deck surface during normal “uniform” flow (green), with the funnel placed upwind (blue) on the side of section 3 and 4, and with a ramp placed under and downwind of the deck (red) on the side of section 1 and 2.

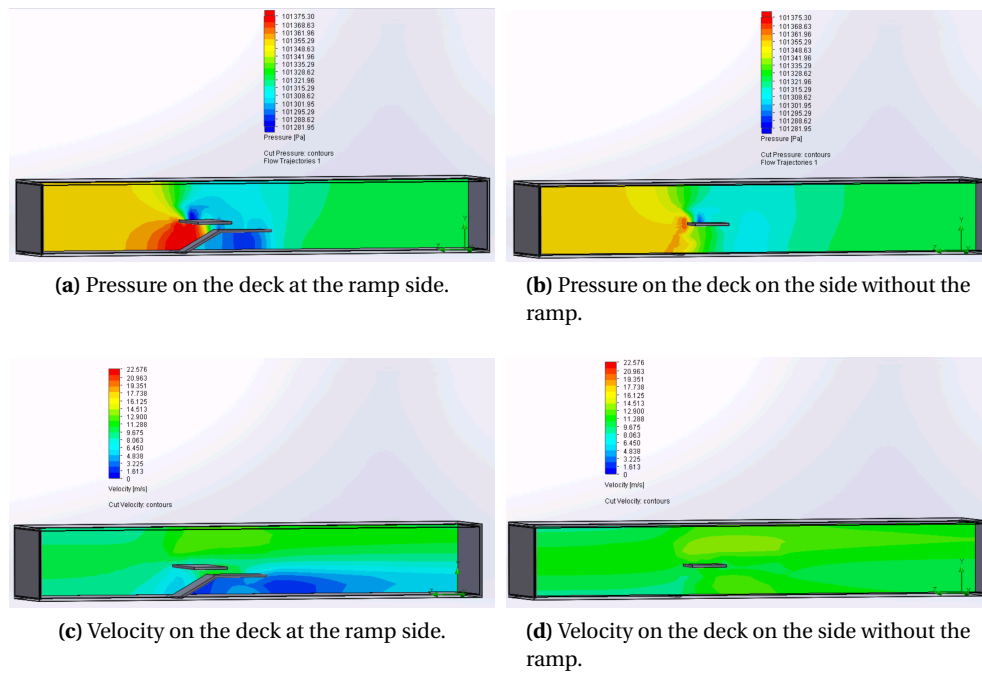


Figure 13.9 – Simulated pressure and velocity over the deck and ramp.

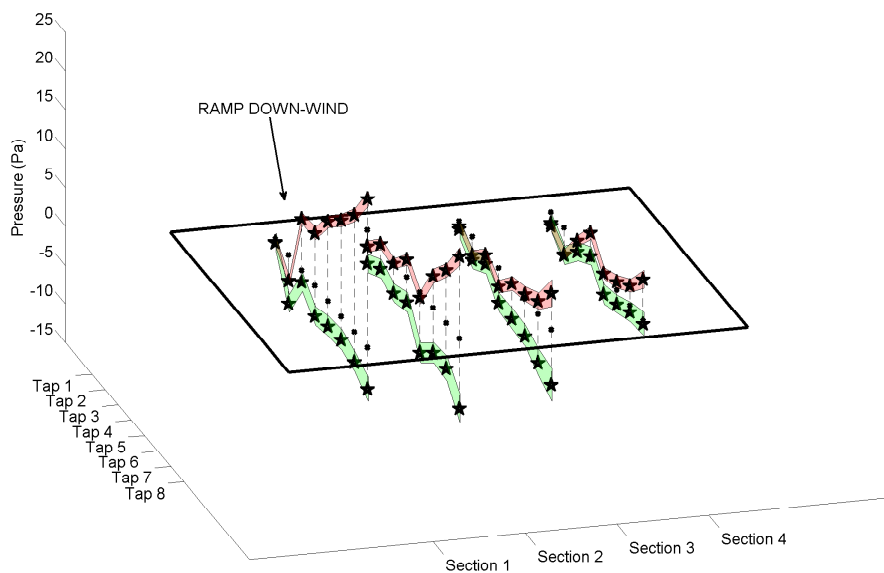


Figure 13.10 – Pressure difference between measurements from the upper and lower surfaces of the deck during normal "uniform" flow (green) and with the ramp placed downwind (red) on the side of section 1 and 2.

the ramp and the deck (lower pressure and higher speed). On the side of the channel without the ramp the pressure and velocity differences are significantly smaller in the z-direction.

The simulated results are supported by the local pressure tap measurements. The change in pressure along y-axis is presented, in comparison to the funnel and normal conditions, in Figure 13.8. In Figure 13.10 the effective pressure on the deck is visualized for the ramp and normal conditions. The imbalance in pressure along the z-axis is significant when the ramp is introduced. Furthermore, the from simulation anticipated significant pressure difference along the x-axis is evident for the perturbed scenario.

Summary

In this chapter we have described the methodology employed for the control part of this thesis. In particular, we have established a framework for conducting the experiments and evaluating the control performance. First, we introduced the concept of a section model in three-dimensional terms. Then, we described the synchronized and the decentralized control approaches we intend to evaluate, and defined the performance metrics that enables such a comparison. Finally, we presented a careful characterization of the different perturbed experimental scenarios that will be presented in the following chapters.

14 Synchronized Flap Control

SYNCHRONIZED movements within the flap arrays is our established control coordination baseline. We have already presented such a synchronized coordination between flaps in combination with a local amplitude-gain and phase-shift control law in the context of validating the analytical flutter model in Chapter 10. We will in this chapter further investigate the performance of this control strategy for ideal and perturbed experimental scenarios. In the first sections, different combinations of actuated flaps are evaluated under normal conditions. Finally, we assess the robustness of the different synchronized control strategies when considering additional disturbances in the approaching wind field.

14.1 Synchronized Control: Flap Combinations along the X-Axis

In Part III, we observed, in theory and in practice, that the implemented identical control parameters that were beneficial for the leading flaps, were harmful for the trailing flaps' performance, thus establishing that the aerodynamic forces produced are asymmetric. In this section we aim to further explore the combinatory effects of a synchronized flap control between the leading and trailing edge flaps, i.e., along the x-axis. Furthermore, we will adhere to the amplitude-gain and phase-shift control law using the deck pitch as input. In order to achieve a fair comparison between the leading and trailing edge performances we implemented different, and individually favorable, phase-shift values, while assigning equal amplitude-gains to the control laws. Furthermore, the performance using both trailing and leading edge flaps simultaneously were studied.

We have leveraged the previously introduced two-dimensional analytical flutter model in order to find efficient control parameters. Note that this study was conducted prior to the experimental model parameter estimation in Chapter 10. Therefore, we leveraged the canonical structural model in combination with the theoretical aerodynamic parameters, for the theoretical analysis.

Table 14.1 – Section Model Parameters

Parameter	SmartBridge
Mass (m) [kg]	30.5
Mass moment inertia (I) [kgm ²]	1.02
Damping ratio pitch (ζ_α)	0.015
Damping ratio heave (ζ_h)	0.006
Circular natural frequency pitch (ω_α) [rad/s]	14.75
Circular natural frequency heave (ω_h) [rad/s]	11.85
Circular natural frequency flutter (ω_f) [rad/s]	12.95

14.1.1 Theoretical Analysis

Recall the analytical framework presented in Part III. We have in the following analysis leveraged the model described in Equations 9.5 and 9.6, however, without considering inertia effects of the flaps or eccentricities of the deck. Furthermore, a combination of theoretical and experimentally obtained model parameters were implemented. Specifically, the theoretical flutter derivatives and the experimentally estimated structural model parameters were employed. Note that the experiments were conducted using a slightly different configuration of the SmartBridge (spring stiffness, distance between springs, dummy mass weight) compared to the model validation presented in Chapter 10. The divergent structural parameters are listed in Table 14.1. It follows that the structural and aeroelastic dynamics of the deck are affected, e.g., reflected in the observed flutter wind speed of the uncontrolled deck.

We can analyze the effect that the control will have on the actively controlled bridge deck by doing a parameter sweep of the control parameters, i.e., the amplitude-gains and the phase-shifts. In Figure 14.1, the estimated flutter wind speed is presented for varying phase-shifts and amplitude-gains when controlling each side of the deck separately, thus only actuating flaps on one side of the deck at a time. The zero amplitude represents the flutter wind speed of the bridge deck without control, and is estimated to 11.0 m/s. It is observed that the optimal phase-shifts of the trailing and leading flaps are dependent on the chosen amplitude-gains. Generally speaking, the optimal phase-shift values seem to decrease with higher amplitude-gains. For the leading flap the optimal phase-shift is 102° when the amplitude-gain is 0.2, while it is 66° when the amplitude-gain is set to 1.19. Whereas for the trailing flap the phase-shift is optimal at 252° for an amplitude-gain of 0.2, while it is optimal at 222° when the gain is set to 0.42. Note that flutter does not even occur for a wide range of angles, when increasing the amplitude-gains further, as seen in Figure 14.1 (for instance, for the leading flap control for a gain of 1.6 and phases-shifts between 24° and 102°). Furthermore, it is observed that increasing the amplitude-gains always increase the effect of the controller, for better or for worse. Moreover, the trailing edge flap is capable of eliminating flutter at lower amplitude-gains than the leading edge flap, if optimal phase-shift parameters are chosen. These observations are also comparable to the theoretical analysis of Hansen et al. [27].

14.1. Synchronized Control: Flap Combinations along the X-Axis

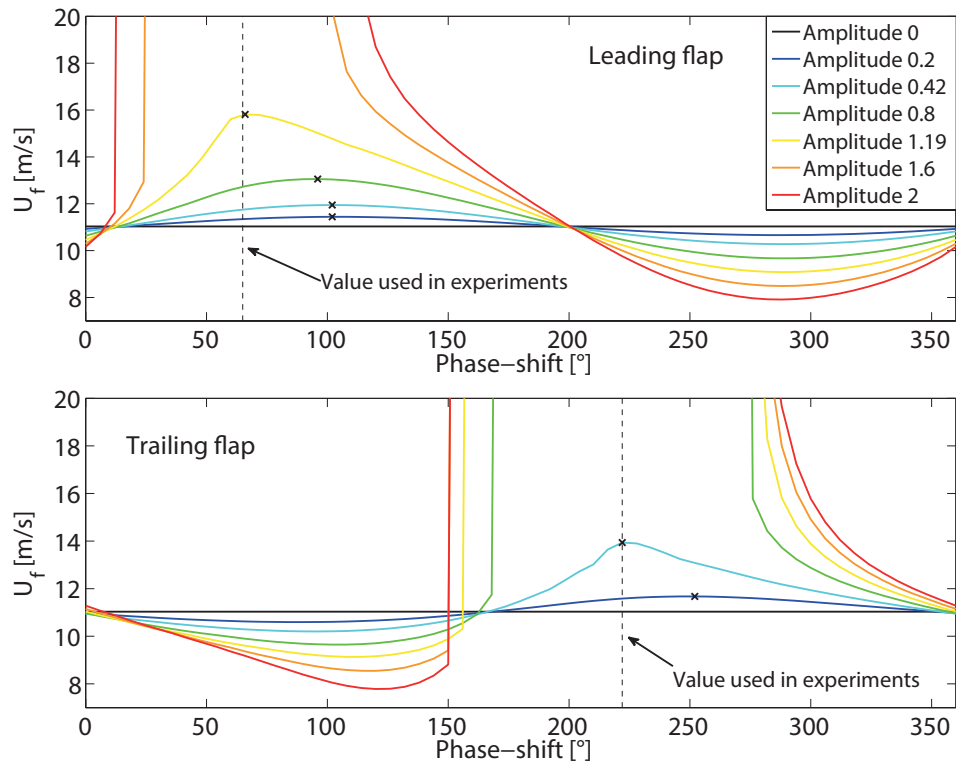


Figure 14.1 – Parameter sweep of the phase-shifts and amplitude-gains of the for the individual trailing and leading edge flaps.

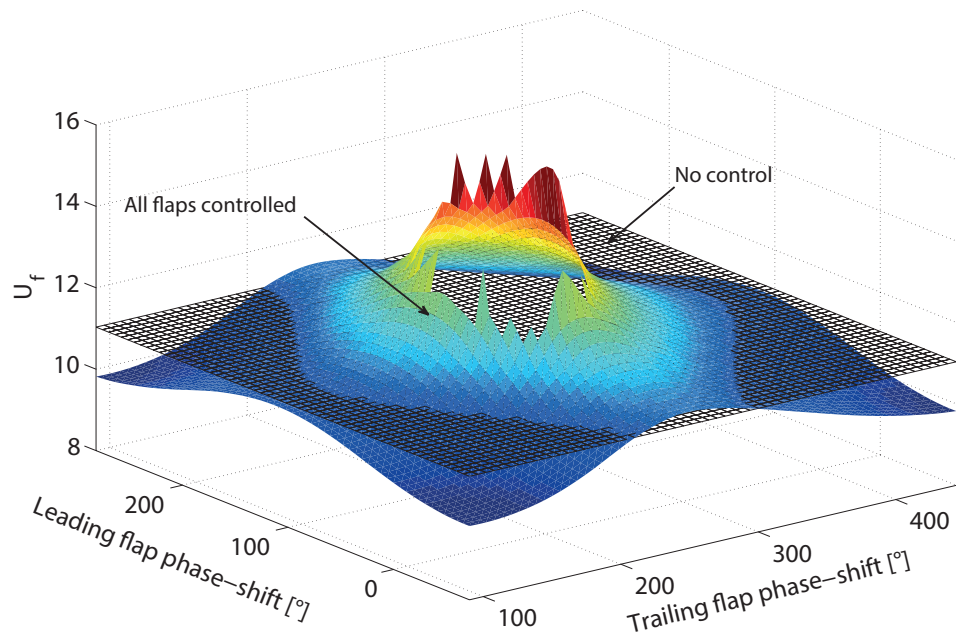


Figure 14.2 – The effect of the phase-shift parameter sweep when both flaps are controlled; the amplitude value is set to 0.35 here. The plane represents flutter wind speed of the bridge deck without control.

Table 14.2 – Wind Tunnel Experiments

Flaps used in Control	Nr of experiments	Parameter	Value
None	1	$\phi_l [^\circ]$	65
All flaps	10	$\phi_t [^\circ]$	222
Leading edge flaps	10	A_l	2
Trailing edge flaps	10	A_t	2

Furthermore, we analyzed the effect of controlling both flap arrays simultaneously, as can be seen in Figure 14.2. Here, we analyze the flutter wind speed for different phase-shifts at a fixed amplitude-gain of 0.35 for all flaps. Observe that the flutter wind speed was increased but never completely eliminated when controlling the flaps separately at this amplitude-gain, as seen in Figure 14.1. However, when the flaps on both sides are controlled simultaneously, their combined effect manage to also completely eliminate flutter (which is represented by the hole region on the surface). However, in a real scenario, other types of aerodynamic instabilities can occur at higher wind speeds that are not accounted for in our model, as has previously been pointed out by [24].

14.1.2 Wind Tunnel Experiments

The performance of the control laws were validated with wind tunnel experiments for the regular flow condition. The number of experiments performed per combination of actuated flaps, as well as the implemented control parameters can be found in Table 14.2. An amplitude-gain of two should, according to our analytical study, be capable of eliminating flutter for a rather wide range of phase-shift values. We chose the phase-shift values that were close to the optimal (for the highest observable amplitude-gain) found in theory for the individual flap control, as seen in Figure 14.1. As previously discussed in Chapter 10, the resulting phase-shift is dependent on the oscillation frequency of the deck, due to the constant time-delay implementation, and thus somewhat difficult to assign precisely. To be clear, the phase-shift values presented in the table correspond to the actual observed values.

As a reference point, we observed from the wind tunnel experiments the deck without control fluttering at 12.5 m/s. This value is comparable to the estimated wind speed from the theoretical model, 11.0 m/s. However, the experimental flutter wind speed was obtained for the bridge deck starting in a resting position, i.e., without performing a step response. In Chapter 10 we address the ambiguity regarding experimentally obtained flutter wind speeds and the dependence on the amplitude of the step response. Thus, the observed discrepancy between theoretical and experimental critical wind speed was likely due to the lack of initial perturbation (hence the higher experimental value).

Furthermore, the controlled experiments were conducted without an initial step response. The control laws were only triggered after the onset of flutter, when any of the displacement

14.1. Synchronized Control: Flap Combinations along the X-Axis

sensors (placed at the corners of the deck) was oscillating with an amplitude above 40 mm. A comparison between the uncontrolled deck and the control of the bridge deck using all the flaps is presented in Figure 14.3. Note that the wind was turned off manually during the experiment without control, otherwise the self-induced vibrations of the flutter could damage the deck. It is also clear from the figure that the control is capable of suppressing the flutter (i.e., deter the development of self-induced vibrations). Furthermore, the flutter remained suppressed as the wind speed was increased to the upper bound of 16 m/s.

The comparison between the different control algorithms, using all flaps, using only leading edge flaps, and using only trailing edge flaps, is presented in Figure 14.4 and in Figure 14.5. The qualitative difference between the three laws are visualized in Figure 14.4, where it is clear that using all flaps for the control is more efficient than using flaps on a single edge. However, there does not seem to be a significant difference between using only flaps on the leading edge or only on the trailing edge, especially in the heave DOF.

Note that also the heave amplitude is more efficiently suppressed when using all the flaps, although this DOF is not actively controlled. The qualitative analysis is also supported by the performance comparison over all runs, including the uncontrolled case, in Figure 14.5. The performance metric was for this study defined as the damping ratio of the bridge pitch estimated from the 5 seconds following the control being triggered (in the case of no control, the point where the control would have been triggered was identified from the displacement sensor data). For the uncontrolled case the damping ratio is negative due to the growing amplitude during flutter. It is shown that the control strategy using all flaps is both performing better and with a smaller variance, than the other strategies. Again, no significant advantage for using either leading or trailing edge flaps when only one side is controlled can be seen, although, a strategy based on the leading edge flap appears to be more repeatable (smaller variance). Theoretically the trailing edge flap should be more efficient (assuming at least close to optimal phase-shift values), as seen in Figure 14.1. This reverse relation could be explained either by a non-optimal phase-shift value for the trailing edge, and/or an inadequate analytical model.

Concerning the optimal control parameters, we have observed that the phase-shift implemented in the control has a significant impact on the performance, as seen in Figure 14.1. Furthermore, the same observation regarding the phase-shifts influence on the flutter wind was also made in Chapter 10 for the improved model and with experimental results. Note that we can not directly extrapolate conclusions regarding the optimal phase-shift values in this configuration from the experimental results presented there. Firstly, because the structural and aerodynamic dynamics were different. Secondly, because those results were gathered for a lower amplitude-gain. These issues can easily be addressed by applying corrected structural and control parameters (the aerodynamic have not changed), resulting in an expected infinite flutter wind speed regardless of controlling the leading edge flaps, the trailing edge flaps, or all of them. However, because of the optimal phase-shift's dependence on the amplitude, as seen in Figure 14.1, it can not be precisely defined by looking at the expected flutter wind speed in

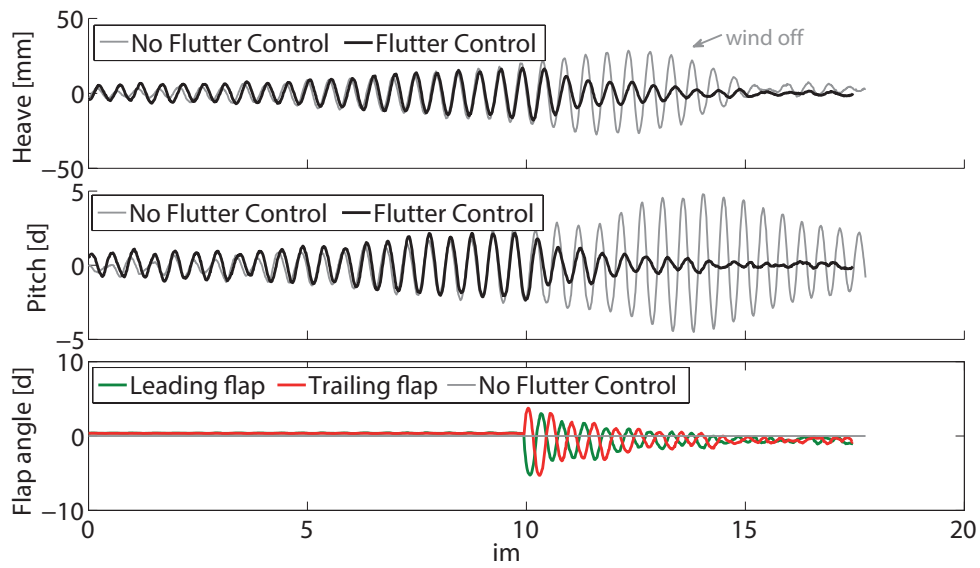


Figure 14.3 – The control using all flaps on the deck is compared to the deck without actively controlled flaps.

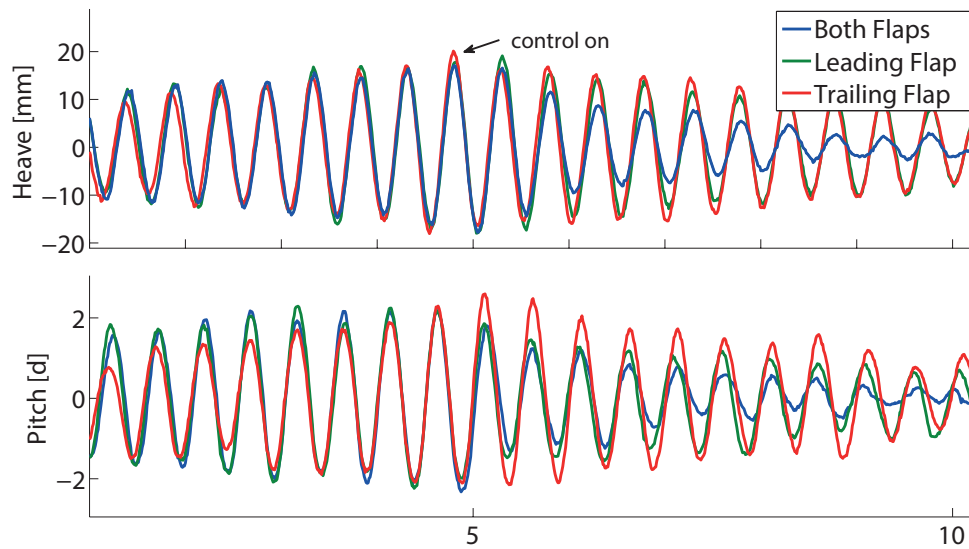


Figure 14.4 – The heave and pitch of the deck for the different control strategies. Note that the control is triggered at approximately 5 seconds.

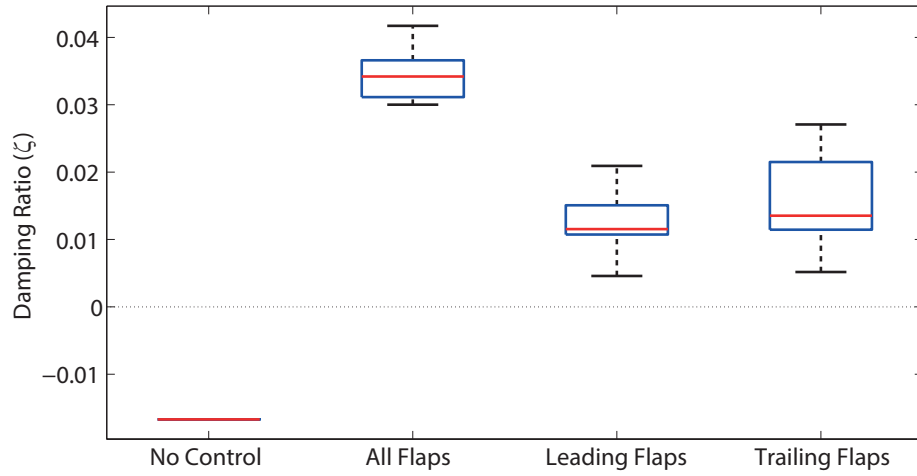


Figure 14.5 – Boxplot of the pitch damping ratios after 5 seconds of control for the four control strategies.

the case of complete flutter suppression. Thus, we can not guarantee that optimal phase-shift parameters were used in the experiments.

In Chapter 10, we have established that the structural model better captures the aeroelastic behavior of the deck when considering flap inertia and eccentric deck effects. Moreover, the model predictions are greatly improved if the aerodynamic parameters, in particular those of the trailing flap, are estimated from the experimental setup. Finally, our results indicated that movements of upwind elements do disturb the flow over, and consequently the effectiveness of the downwind elements, similarly to the observation that has subsequently been made by Gouder et al. [23]. Considering these supplementary insights, we presume that the discrepancies between the modeled and the experimental results presented in this chapter are mainly due to the factors not captured in the analytical model in combination with the use of theoretical model parameters instead of the experimentally calibrated ones.

Nevertheless, we can with certitude assess that all of the three control laws lie within the “positive region” predicted by the model and that controlling the bridge deck using flaps on both sides is more effective (in terms of damping ratio) than using only flaps on a single side.

14.2 Synchronized Control: Flap Combinations along the Y-Axis

In the previous section, we analyzed the control performance using different combinations of flaps along the wind direction. The work presented in this section focused instead on the performance and robustness of a synchronized control strategy actuating different flap combinations in the cross-wind direction, i.e., along the y-axis of the channel.

We addressed already in Chapter 13 that in order to make a meaningful comparison between the synchronized and decentralized control strategies, the heave DOF should be used as input

Table 14.3 – Implemented Control Parameters (Heave Input)

Time-delay[ms]	Value	Phase-shift[°]	Value	Amplitude-Gain	Value
τ_l	30	ϕ_l	18.8	A_l	6
τ_t	295	ϕ_t	184.9	A_t	6

instead of the pitch DOF. Recall also that in theory the aerodynamic effect is identical for either control input, assuming that the control parameters are modified appropriately. We have therefore used the heave position of the deck as control input in this and the following sections and chapter. Furthermore, we chose to no longer pursue the investigation on optimal phase-shift values: for the following experiments, they were assigned after an initial manual tuning. The parameters were chosen so that they provided, individually, a favorable performance in the flutter condition; and as we observed when using the pitch input, the performance was improved when simultaneously actuating the leading and trailing flaps. Moreover, we assume that any potential performance differences between the leading and the trailing flap controls are inconsequential, since we focus the subsequent analysis on variations along the y-axis. Providing that each section of the SmartBridge is controlled symmetrically in the x-direction, i.e., the leading and the trailing flaps are either both actuated or both still. The implemented control parameters are given in Table 14.3. Note that we report the default amplitude-gains here; however, we have explicitly stated where others were implemented. As previously discussed, the time-delay is a fixed constant while the resulting phase-shift is dependent on the oscillation frequency, the values reported in the table are based on the natural heave frequency at 10.94 rad/s.

The experiments were performed at 790 rpms of the wind tunnel fan. This corresponds to 9.7 m/s for the unperturbed wind field, thus close to the flutter wind speed (10.58 m/s) of the uncontrolled deck. The same fan speed was used for the perturbed conditions, however, we can not easily assess the resulting average wind speed in these cases from our point measurement of the fixed pitot-tube (it is attached to the wall close to section 1). Nevertheless, we measure 10.0 m/s in the funnel experiments, and 10.2 m/s in the ramp experiments, with the fixed pitot-tube.

In contrast to the procedure presented in Section 14.1, the following results are based on step responses performed in the mixed heave and pitch DOFs, where the upwind side of the deck was released from a height of 30 mm.

Finally, note that the following experiments were conducted with the same configuration of the setup as in Part III, thus, the corresponding structural parameters can be found in Table 10.2.

14.2. Synchronized Control: Flap Combinations along the Y-Axis

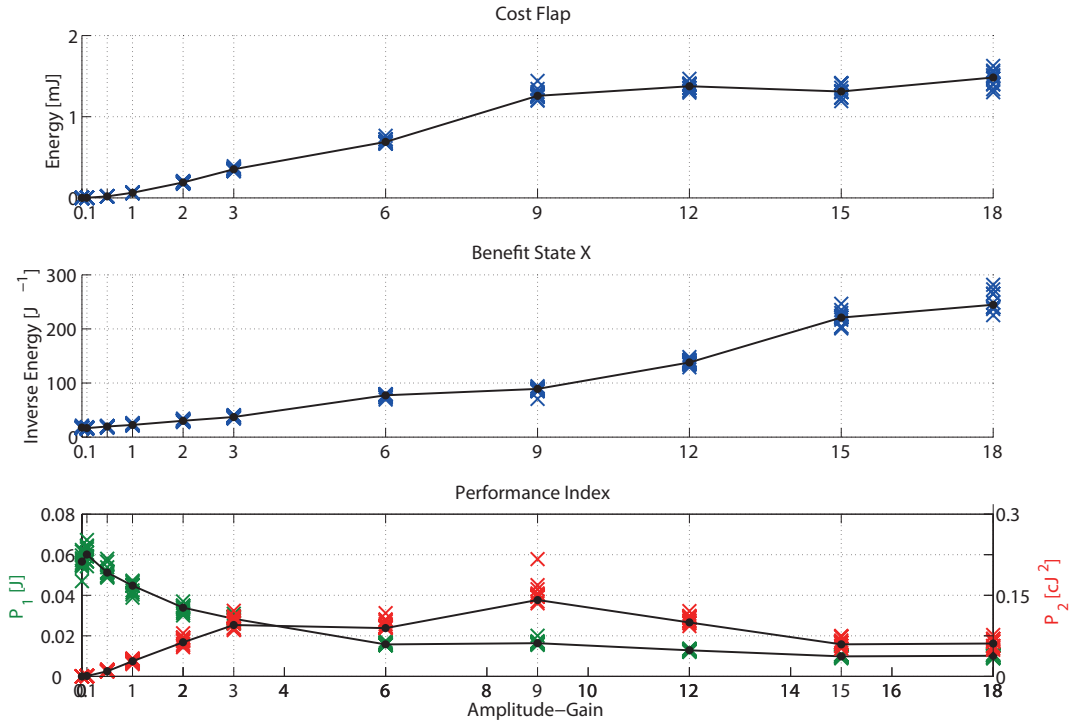


Figure 14.6 – Performance and cost for synchronized flap movements under normal flow conditions as a function of the amplitude-gains.

14.2.1 Varied Actuation Rate in Normal Wind Conditions

In this subsection, we aim to study the trade-off between the cost of actuation and the benefit in terms of bridge deck damping in normal flow conditions. Our setup allows us to vary the amount of energy invested in flap actuation in two different manners. First, we evaluate the performance of the defined synchronized control law for a range of the amplitude-gains using all the flaps. Secondly, we investigate the effect of controlling only a subset of the available flaps, with a fixed amplitude-gain.

Effect of changing the amplitude-gain

We have observed theoretically, and validated with wind tunnel experiments, that changing the phase-shift value has a significant effect on the flutter control. Furthermore, the model results in Figure 14.1 indicate, that the control effect (good or bad) is enhanced with a higher amplitude-gain for a fixed phase-shift value. However, we have not experimentally investigated the impact of changing this parameter. To this effect, we performed a series of step responses for a range of different amplitude-gain values, and the result was evaluated according to the cost, benefit and performance metrics established in Chapter 13. For each of the 11 parameter setting, 10 runs were performed, for which the result is presented in Figure 14.6. Quite intuitively, we observe that higher gain values yield a higher flap cost, and in turn the

benefit metric increase as the deck is better damped. Interestingly, we observe that the flap cost plateaus after an amplitude-gain of about nine, which is explained by the the substantial state improvement, i.e., the average flap movement remains constant because the increase of the amplitude-gain is matched by the decrease in heave amplitude of the deck. This is consistent with the decrease, i.e., improvement, of the performance indices defined in Equations 13.4 and 13.5, above this gain value. However, we observe that the two metrics give diverse appreciations of the achievement over the whole parameter range. This is especially apparent for the lower amplitude-gain values. As previously addressed, the cost-benefit ratio is ambiguous at extremely low gains since the result becomes independent of the state of the bridge. However, we observe that the performance according to the ratio index is better even at low, non-negligible, amplitude-gains, in contrast to the one based on control theory. Note that if we had assigned a very high weight, w , in Equation 13.4, it would have yielded a performance index with an identical trend to the flap cost, and therefore also indicating a better performance for low amplitude values. In a sense, the ratio index provides a more general appreciation of the performance since it does not require a specific parameter choice. However, the control-based index allows us to adjust the outcome depending on concrete system requirements. Thus, the two indices provide complementary insights to the system's performance.

Effect of changing the operated flap coverage degree

We have established that changing the amplitude-gain impacts the cost of flap actuation and the performance of the control in a non-linear fashion. Another parameter that influences the total cost of actuating the flaps, is the number of actuators operated.

In Figure 14.7, the evaluation of the different combinations of operated flaps is presented. The label Axxxx indicates each of the amplitude values implemented for a particular section, e.g., A6000 means that an amplitude-gain of 6 was implemented for section 1, and that the rest were not controlled. Note that uncontrolled segments imply that the flaps were held fixed at a 0° angle, and that controlled segments operated both leading and trailing flaps simultaneously. Furthermore, 10 runs were made for each of the 15 different configurations.

The graphs in Figure 14.7 are separated into four parts, thus grouping data by the number of sections used for the control; one, two, three, and four. We observe that even though the operated flaps are changing, the performance remains rather constant within the group, thus supporting the uniformity assumption of our unperturbed flow scenario. Moreover, we observe that using 25% of the available control surfaces is the least expensive in terms of flap cost, and that increasing the number of actuators generally costs more. However, with the exception of using 100% of the flaps, which is in fact cheaper than using 75% of them. This effect is again explained by the substantial increase of the deck's damping, i.e., even though more actuators are used, it is cheaper because each individual flap is required to move less.

Intuitively, the benefit of the control is augmented as the controlled flap rate is increased.

14.2. Synchronized Control: Flap Combinations along the Y-Axis

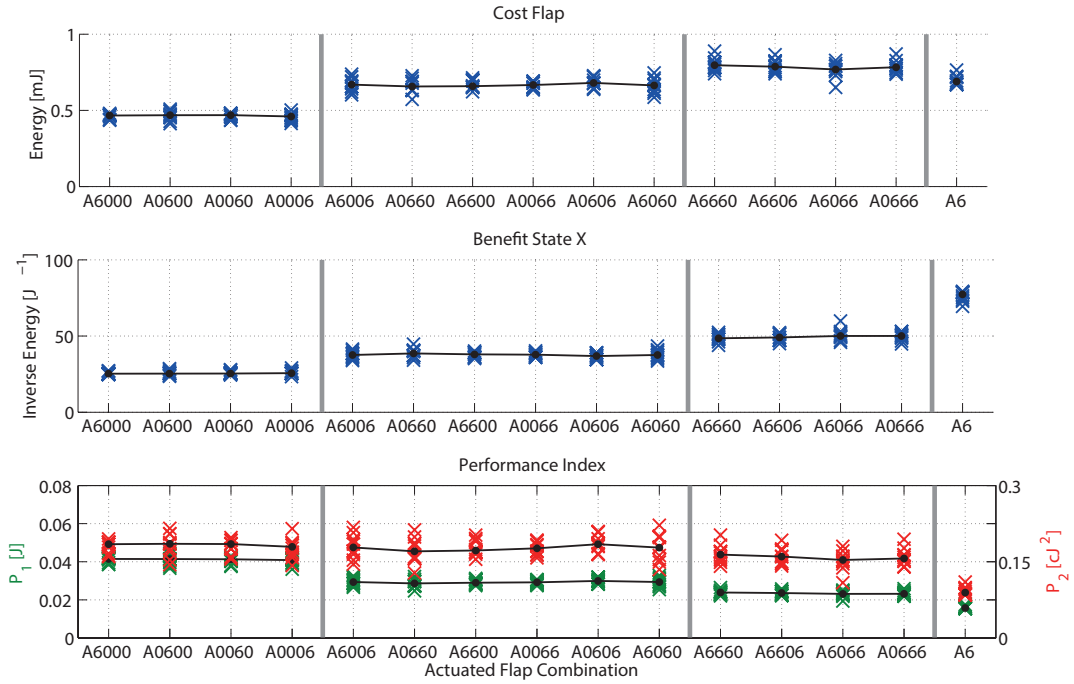


Figure 14.7 – Performance and cost for synchronized flap movements under normal flow conditions and different flap combinations.

The trade-off between the cost and benefit is reflected in the two performance indices, and indicate that using all the available actuators is best. However, the control-based index, P_1 , shows an incremental improvement as the number of actuators is increased, while the cost-benefit ratio, P_2 , is more or less constant for any subset of controlled segments. The ratio index really highlights the drastic, and rather unexpected, improvement for the 100% control coverage case.

14.2.2 Varying Controlled Flap Coverage for a Nonuniform Wind Profile

In this section, we investigate the effect of using the different flap control combinations for a perturbed flow scenario. In particular, we will look at the performances obtained when the wind flow is redirected by a funnel placed upwind of the deck, as described in Chapter 13.

In Figure 14.8, we present the resulting performance metrics when varying the degree of actuated flaps for the perturbed flow created by the funnel. We performed 10 runs for each of the 9 different combinations investigated, note that we did not investigate the 75% usage for the funnel scenario. As in the case of the undisturbed flow, we observe an increase in the cost and the benefit as more flaps are actuated. Furthermore, both of the performance indices, P_1 and P_2 , indicate that using all of the flaps is preferable. However, this control configuration is not nearly as superior as we observed for the normal wind flow. In fact, the median of the cost-benefit ratio, P_2 , is almost at a constant level, for all flap combinations, although it is

Chapter 14. Synchronized Flap Control

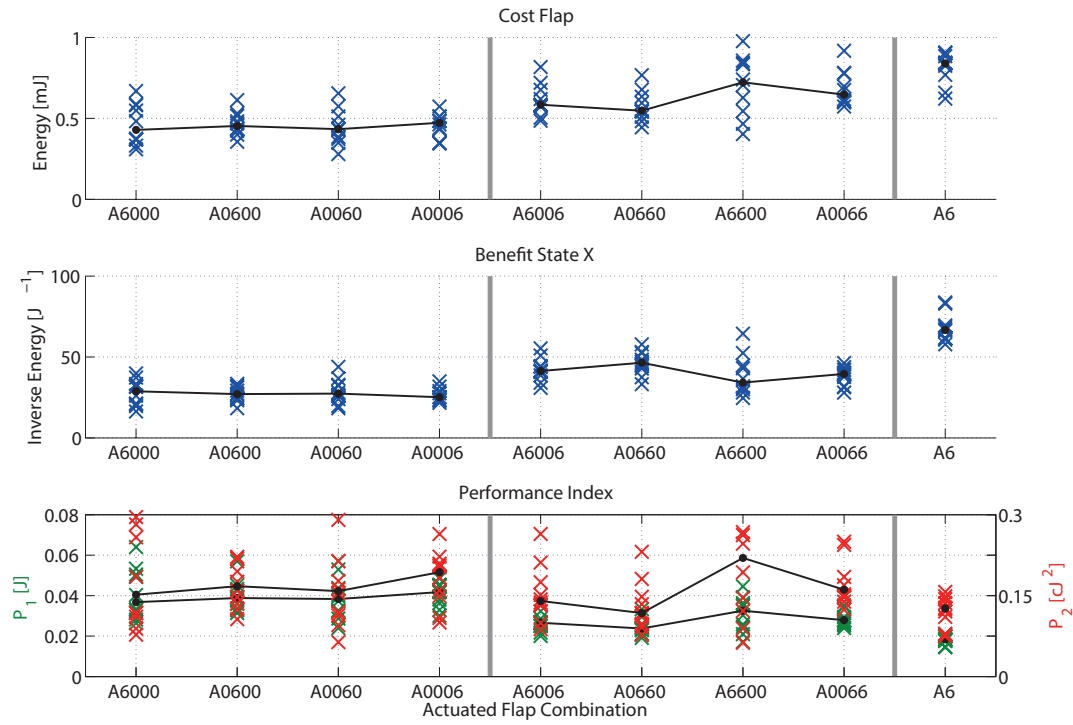


Figure 14.8 – Performance and cost metrics for different combinations of synchronized flap movements for the case of a nonuniform wind field created by the upwind funnel.

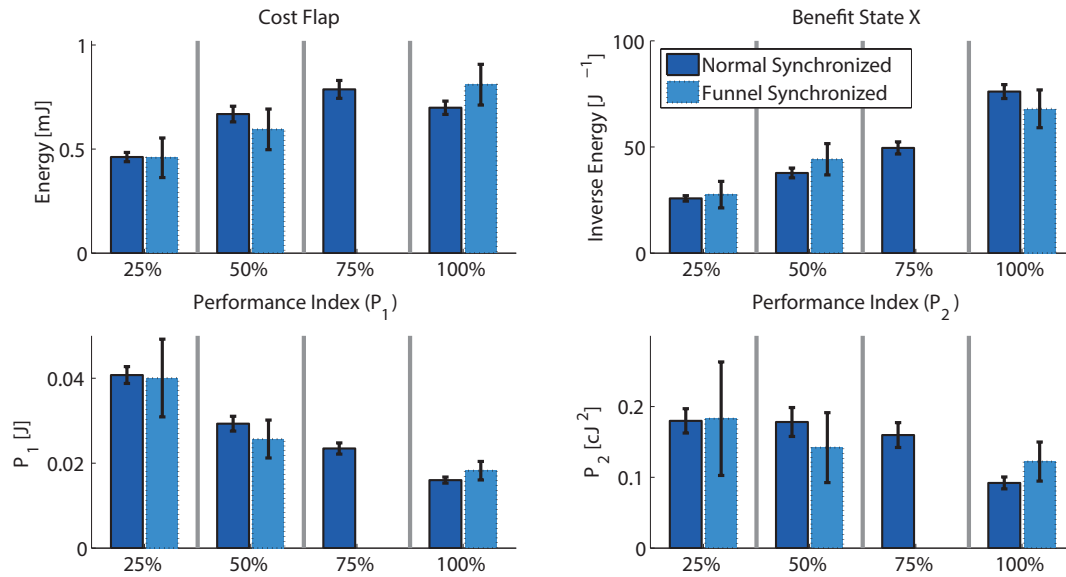


Figure 14.9 – Performance and cost for different combinations of synchronized flap movements under normal and perturbed flow conditions. The percentage indicate the ratio of used segments compared to the full capacity of the deck, independent of the actual control surfaces being used.

14.2. Synchronized Control: Flap Combinations along the Y-Axis

significantly less noisy when all the flaps are used. The control-based index P_1 adheres to the terrace-like evolution we observed for the normal flow as the degree of used flaps increases, although it is here less defined. Generally speaking, the result is much more scattered in the perturbed scenario. Moreover, we observe more divergent results when the same number, but different combinations, of control surfaces are used. A result that is natural considering the nonuniform wind field.

In Figure 14.9 we present the mean and standard deviation of the performance metrics for all of the data points reported in Figures 14.7 and 14.8. This representation highlights the observed tendencies that have already been discussed; i.e., that the improved performance when using all flaps is less evident, and that the results are noisier, for the funnel flow scenario.

Summary

We have in this chapter performed a substantial analysis of the performance of our synchronized, baseline, control algorithm. First, we investigate control coordination between the leading and trailing edge flaps, i.e., along the x-axis of the channel, for normal wind conditions. Then, we studied the effect on the control when only part of the defined subsections are operated, i.e., considering control coordination along the y-axis. Furthermore, the latter study was conducted both for normal and perturbed wind conditions. In the next chapter, we will build on top of these results and investigate also the decentralized control strategy, using local control input.

15 Decentralized Flap Control

LOCAL sensory information distinguishes our decentralized control approach from the centralized and synchronized coordination strategy. In this chapter, we aim to thoroughly evaluate the two different control methods for the experimental scenarios described in Chapter 13, a study we are uniquely equipped to carry out using the SmartBridge. We will first establish a baseline comparison for the uniform wind field. We will then explore the robustness of the control laws for various perturbations of the deck, both for normal and asymmetric wind fields.

15.1 Control Law Comparison in Normal Wind Conditions

In this section we compare the synchronized and decentralized control laws for the regular and asymmetric deck under normal flow conditions.

15.1.1 Decentralized vs. Synchronized Control: Baseline

Let us first establish a baseline comparison between the synchronized and decentralized control coordination approaches. These experiments were performed using all of the flaps, in the unperturbed flow condition. Note that the same control parameters, found in Table 14.3, were implemented in both cases, however, the decentralized flap approach considers local heave input for each individual subsection. Furthermore, 10 runs were performed per control law.

The result for the entire set of step responses is presented in Figure 15.1. Even from a qualitative aspect, we observe that there is a small, but distinct, difference in performance between the two strategies, especially in the roll DOF. In Figure 15.2, we report the corresponding cost and performance metrics. Considering the cost associated with each of the deck's DOFs separately, we can conclude that both the heave and the pitch are better damped with the synchronized approach, and that the effect is opposite for the roll DOF. In fact, the median

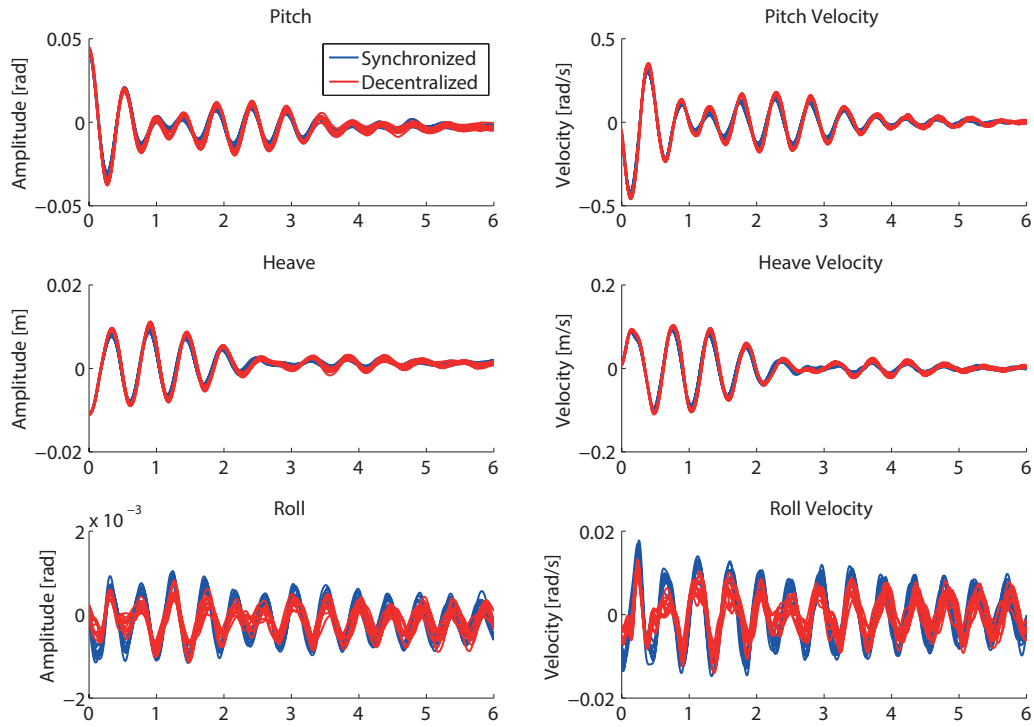


Figure 15.1 – The step responses for synchronized and decentralized flap movements under normal flow conditions.

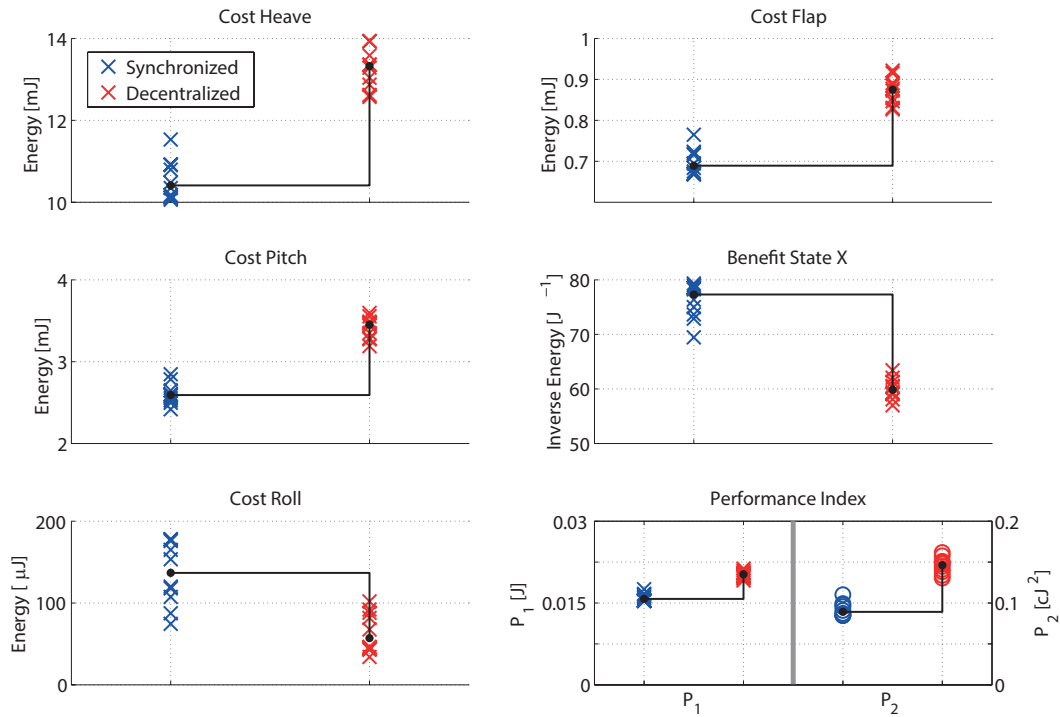


Figure 15.2 – Cost and performance calculated for the synchronized and decentralized flap movements under normal flow conditions.

cost is 28.0% higher for the decentralized approach in the heave DOF, and 33.2% bigger for the pitch DOF, while it is 58.27% lower for the roll DOF. However, since the absolute values for the roll DOF are orders of magnitudes lower than those of the heave and pitch, this improvement is insignificant when considering the aggregated calculation of the benefit metric. Thus, in terms of the defined actuation cost, control benefit, and performance indices, the synchronized control performs better on all accounts.

15.1.2 Asymmetric Aerodynamic Profile of the Deck

In order to perturb the system by creating a nonuniform aerodynamic profile of the deck, we placed a symbolic truck on top of the deck, as described in Chapter 13. In Figure 15.3 the results for two different placements of the truck are presented, in the downwind corner, marked DW in the figure, and the upwind corner, marked UW in figure, of the deck on the side of section 1. Furthermore, we performed two different types of step responses per truck placement scenario; upwind side pulled up (mixture of heave and pitch), marked P in the figure, and corner of the deck (producing a mixture of heave, pitch and roll), marked with C in the figure. For each of the experimental conditions, and each of the control approaches, 5 runs were executed. Note that the oncoming wind flow was not disturbed in these cases, the asymmetric wind forces are generated locally at the deck. Furthermore, all of the available flaps were employed in the control efforts.

From Figure 15.3, we can assess that the downwind or upwind placement has a general big impact on the system response. In fact, the truck placed on the downwind side of the deck causes a bigger disturbance and noisier results are obtained. The differences between the types of step responses and the control types are less significant. Generally, the synchronized approach yield a better performance regarding all of the defined metrics. However, the differences between the control approaches are much less significant compared to those of the unperturbed deck.

15.1.3 Decentralized vs. Synchronized Control: Flap Combinations

We investigated the effect of using subsets of the available actuators for the synchronized control in the previous chapter. In this subsection we will compare those results with the corresponding ones for the decentralized control. Thus, we adhered to the unperturbed wind condition, and we performed additional experiments of 10 runs per the 15 different flap combinations.

The resulting performance metrics for both of the control strategies are presented in Figure 15.4. We observe that the decentralized approach performances generally follow the same trends that we noted for the synchronized flap movements. Except for when all of the flaps are used for controlling the deck. In this case the decentralized control performs significantly worse. In fact, when regarding the decentralized approach the cost of the flap actuation is

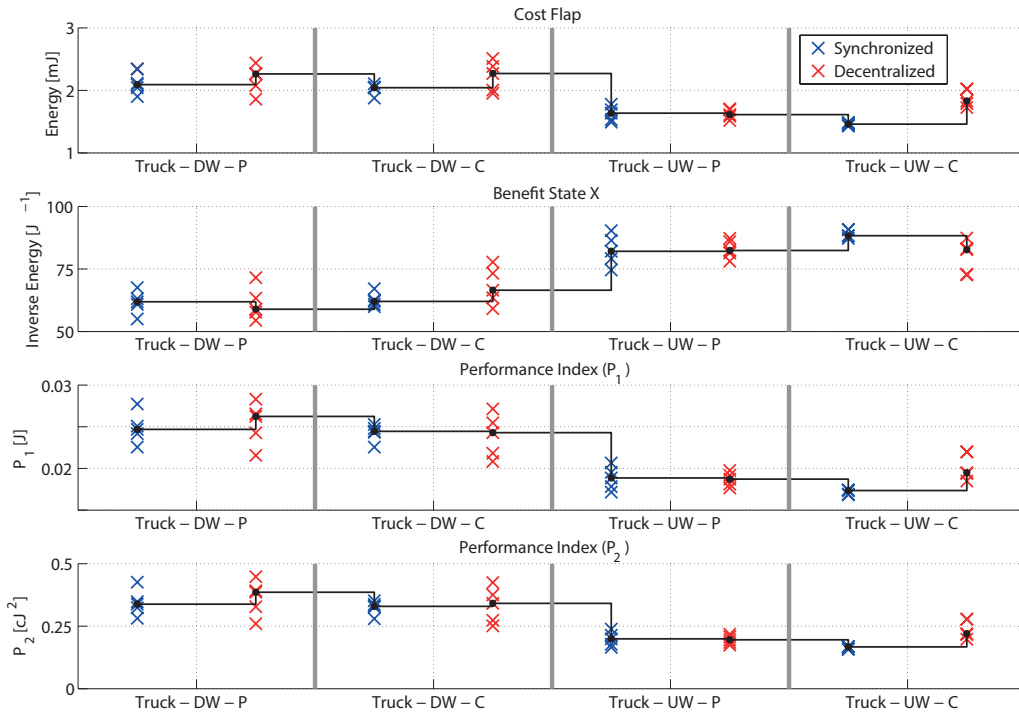


Figure 15.3 – Performance and cost for the synchronized and decentralized coordination strategies, under normal flow conditions, with a truck attached to the bridge deck.

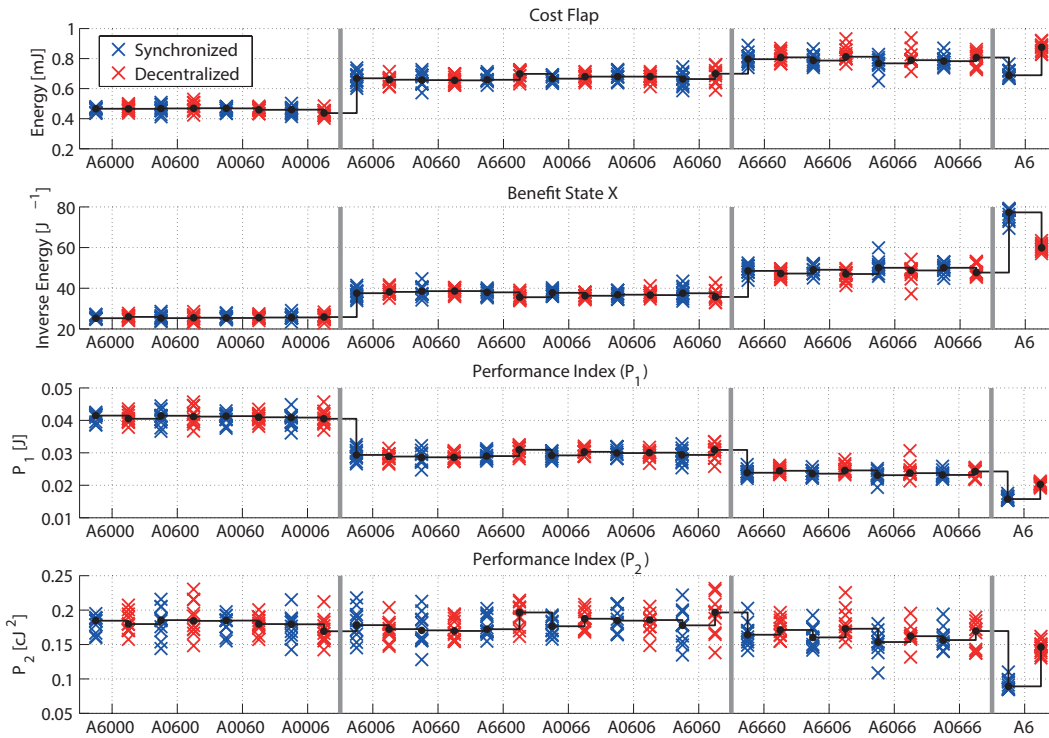


Figure 15.4 – The cost and performances for the synchronized and decentralized flap movements under normal flow conditions using different flap combinations.

slightly higher than when using 75% of the flaps, when for the synchronized control case it was lower. Moreover, the benefit of the control increases more or less linearly as more of the flaps are used in actuation for the decentralized approach. On the other hand, the two strategies perform very similarly for all other flap combinations.

Furthermore, we can detect that the decentralized approach performs slightly better, albeit a little noisier, when only one section is operated. This is not surprising since the local heave input provides more accurate state information. However, when several segments are controlled independently this benefit seems to be outweighed by aerodynamic and/or structural interactions that introduce additional unintended perturbations.

15.2 Control Law Comparison for Nonuniform Wind Profiles

In this section, we study the synchronized and decentralized control approaches for perturbed wind flow scenarios. In particular, we will look at the performances obtained when the wind flow is redirected by the funnel placed upwind of the deck for different flap control combinations. Furthermore, we will assess the controlled deck's behavior when the wind flow is perturbed by the ramp, a scenario described in Chapter 13.

15.2.1 Funnel Perturbation

Similarly to the experiments presented for the synchronized control strategy, we will additionally investigate the effect of operating different combinations of the deck's sections using the decentralized control law for the funnel scenario.

For this purpose, we conducted 10 runs for a total of 7 distinct flap combinations. Note again, that as in the case of the synchronized control we did not investigate the 75% usage for the funnel scenario. In Figure 15.5, the results are presented in comparison to the corresponding values of the synchronized control. The evolution of the different cost and performance measures as the number of actuators are increased is very similar to the results obtained in the normal wind condition for the decentralized control. Regarding the synchronized control, the trend of the control-based performance metric, P_1 , is less well-defined, but similar, to the results presented in Figure 15.4, while the cost-benefit ratio, P_2 , remains almost constant in the perturbed case. Moreover, the two control approaches perform very similarly in the funnel scenario, even when all of the actuators are employed. Thus further consolidating the observation that the performance of the synchronized control law is less robust in respect to perturbations, than that of the decentralized.

In Figure 15.6 we present the mean and standard deviation of the performance metrics for all of the data points reported in Figures 15.4 and 15.5. Analogously to the comparison made in the previous chapter, in Figure 14.9, we observe that the control performances for both approaches are less predictable for the funnel flow scenario. However, as already discussed, although the

Chapter 15. Decentralized Flap Control

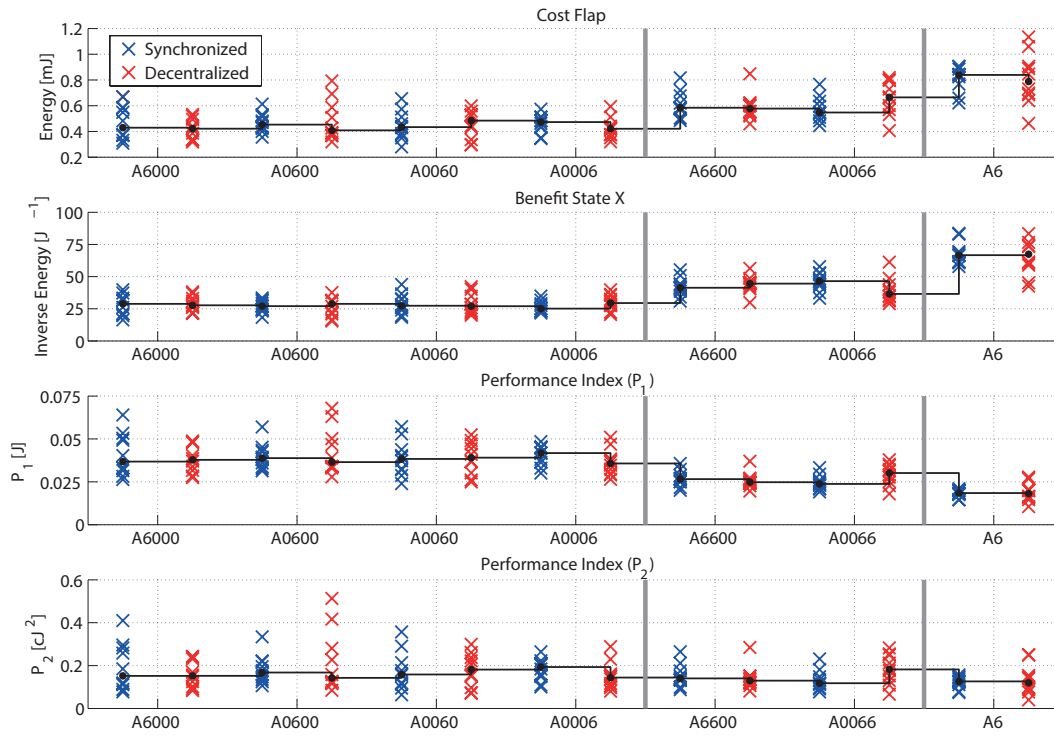


Figure 15.5 – The cost and performances for the synchronized and decentralized flap movements, for the funnel perturbed conditions, using different flap combinations.

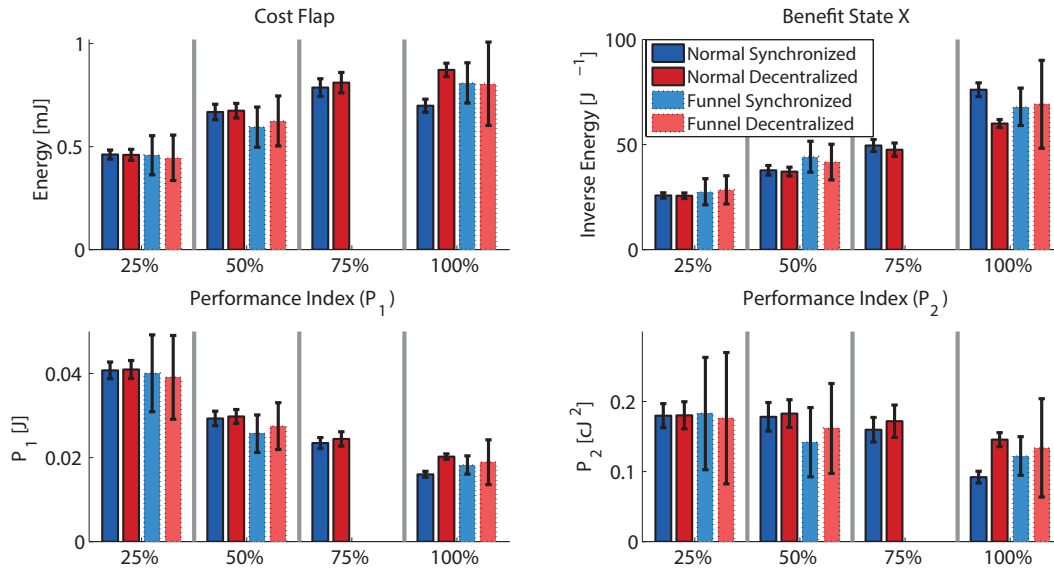


Figure 15.6 – Average performances and costs for decentralized and synchronized flap movements per number of flaps employed under normal and perturbed flow conditions. The percentage indicate the ratio of used segments compared to the full capacity of the deck, independent of the actual control surfaces being used.

15.2. Control Law Comparison for Nonuniform Wind Profiles

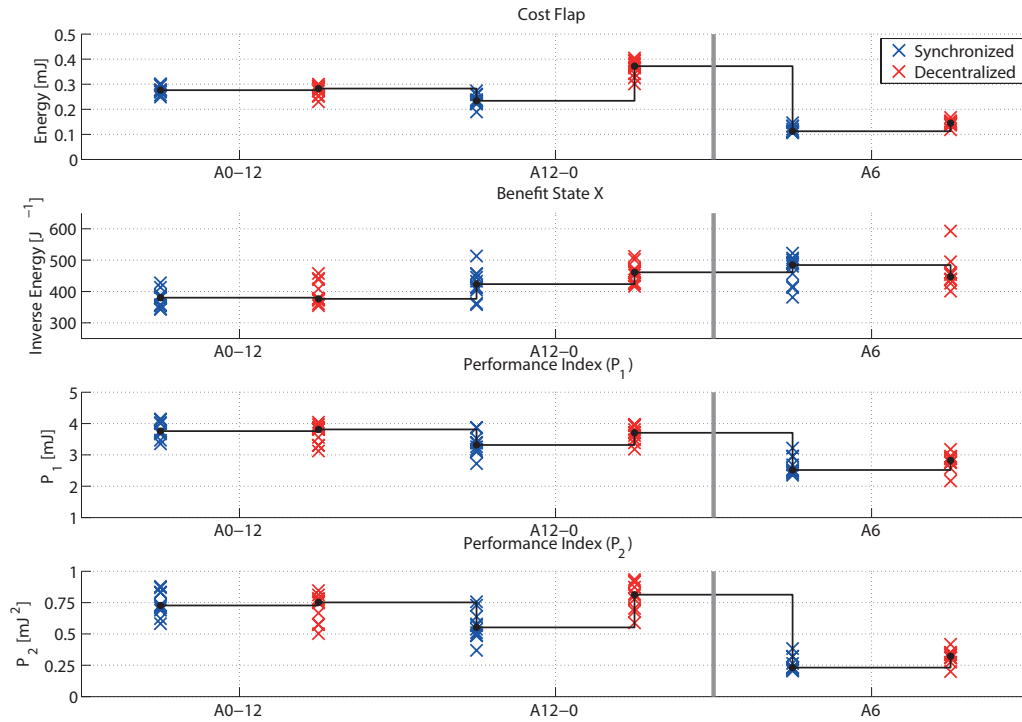


Figure 15.7 – Comparison of the synchronized and decentralized approaches for a wind field perturbed by the ramp.

decentralized approach is typically performing slightly worse than the synchronized, it is less affected by additional perturbations.

15.2.2 Ramp Perturbation

Finally, we performed a series of experiments comparing the synchronized and decentralized control approaches when the wind field was perturbed by the ramp placed underneath the deck, which implies asymmetries in more than one DOF. We conducted 10 runs for 3 different flap combinations per control law. The performances of the decentralized and synchronized approaches are presented in Figure 15.7. Note that for these experiments we kept the total sum of the individual flaps constant when changing from 50% to 100% usage of flaps, i.e., amplitude-gains were set to 12 when half of the available flaps were operated and set to 6 when all of them were controlled. Even though we compensate the fewer number of flaps case with higher individual actuation rates, the uniform control operation is superior for both the synchronized and decentralized strategy. Moreover, we observe that the control performances are asymmetric in regards to which side is being operated, however, this is logical since the wind field is highly nonuniform. These results indicate that control laws also considering local wind input could bring an improved performance.

Summary

We have in this chapter thoroughly bench-marked the decentralized and synchronized control strategies for a wide range of experimental scenarios. In particular, we evaluated the effect on the control performance by introducing local perturbations to the SmartBridge, and/or introducing objects in the channel that disturbed the wind flow. Generally, we observed that the two approaches perform similarly: although the synchronized control overall achieves slightly better results, it is more sensitive to internal and external perturbations.

16 Conclusion

COORDINATION between and within flap arrays is an important aspect to consider for flutter control of a bridge deck. The SmartBridge is uniquely equipped to perform such studies, since, to the best of our knowledge, there exists no other setup that is endowed with more than one flap on each side of the girder. We have in this part of the thesis performed an extensive, experimental exploration of different coordination strategies for the control of the multi-flap system.

First of all, we established a framework for conducting the experiments and evaluation of the system performance. In particular, we introduced the concept of sections of the SmartBridge, which, operated in different combinations, introduces a control asymmetry of the deck. Such perturbations allows us to study the effect of malfunctioning flaps and the cost-benefit trade-offs related to the rate of actuator coverage along the y-axis. Moreover, we established our main two control strategies: a centralized, synchronized approach and a decentralized approach, which is using an emulated local control input. In order to evaluate the goodness of the control laws, we define a number of measures that are related to the kinetic energy required for actuation, and the resulting kinetic energy of the deck movements. Finally, we sought to fully exploit the capabilities of the SmartBridge and the overall setup by properly establishing different experimental scenarios that have significantly distinct perturbation effects on the deck, and moreover relevant for a real bridge deployment. For this purpose, we have carefully characterized a set of experimental conditions leveraging the local pressure measurement system and a CFD simulation tool.

In a first step, we evaluated the synchronized control law for a series of different inter-flap/multi-flap coordination strategies that can be divided into two categories, along the x-axis and along the y-axis. Essentially, the strategy along the x-axis of the channel targets the coordination between the leading and the trailing edge flaps and has been studied also in the previous part. The amplitude-gain and phase-shift control based on the bridge deck's pitch was implemented in theory and with wind tunnel experiments in normal flow conditions. We leveraged the analytical framework presented in the previous part, although not utilizing the

full formulation and only employing theoretical aerodynamic parameters, since this particular study was made prior to the experimental validation of the model. Three different strategies were compared: using all flaps available on both sides of the deck, and using only flaps on a single side of the deck, either on the leading or trailing edge. All of the proposed strategies proved capable, both theoretically and experimentally, of suppressing flutter. Moreover, it was shown that using all the available flaps is the most efficient and reliable strategy, in theory as well as in practice. However, we did observe a discrepancy between theory and real experiments regarding the performance using only the trailing flaps and using only the leading flaps. In theory, the trailing flaps should perform better than the leading flaps, while in practice they have a similar performance. Thus, this observation is consistent with the previous results and can be corrected for with experimentally obtained model parameter and the inclusion of structural effects of the flaps. However, even without such corrections, the analytical model was proven a useful tool in order to locate the regions where the control phase-shifts should be most efficient.

Additionally, we studied the effects of varying the amount of energy invested for the synchronized control strategy. The cost of the flaps were varied in two fashions: changing the amplitude-gain for all of the flaps controlled simultaneously, or alternating the sections employed for controlling the deck. The performance changes rapidly for lower amplitude values, and depending on which metric is considered, it could be for the better or the worse. However, at larger amplitude gains the evolution is more stable and bigger movements is consistently better in regard to both of the defined performance metrics.

The investigation of the synchronized coordination strategy along the y-axis was achieved by alternating the operating sections, and enabled us to evaluate the cost-benefit trade-offs from a different angle, literally. We show that trends of the cost, benefit, and performance indices are quite consistent for all flap combinations and the total number of sections used in the operation, except for the case when 100% of the available resources are used. In this case, we observe a significant discontinuity, indicating a significant improvement of the control. However, we do not observe the same discrepancy in the metrics' trend evolution, when the same analysis is performed for a wind field that is perturbed by a funnel placed upwind of the SmartBridge.

Analogously, we investigated the decentralized coordination strategy along the y-axis, for a normal wind field and perturbed by the funnel and the ramp. We observed that while the synchronized approach is overall performing slightly better than the decentralized strategy, it is also more sensitive to the perturbations created by the funnel. In the ramp scenario we studied the effect of varying the number of flaps operated while maintaining a constant sum of all amplitude-gains; we observe that such compensations do not balance up the performance difference for using less flaps. Furthermore, our results indicated that a local wind input could be a promising approach. Moreover, we compared the two control laws with a local aerodynamic change, realized by a truck placed at different locations on the deck. For this analysis, all flaps were actuated, and similarly to the funnel comparison, we note that

the decentralized performs a little below the synchronized coordination; however, the delta between the two approaches is less than for a normal symmetric scenario.

Summary

In this chapter we conclude the control part of the thesis. We identified profitable control parameters for the leading and the trailing edge flaps using the analytical model based on Theodorsen's theory. Furthermore, we have evaluated the results obtained from an experimental study of different control coordination aspects. We conclude that in perfect conditions a synchronized control strategy is superior to a decentralized one; however, this difference is rapidly reduced when any type of internal or external perturbations are considered.

Conclusion Part V

17 Conclusion

WE have in this thesis investigated the flutter control problem of long-span bridges using arrays of flaps as actuators. The research effort is resting on three main pillars: the mechatronic development of our experimental setup, the analytical modeling effort to capture the dynamics of an actively controlled bridge section model, and the evaluation of different control coordination strategies. The main benefit of increasing the flutter wind speed for long-span bridges is that longer spans can be achieved. Furthermore, the proposed active solution might also be applicable during the erection of a bridge, when wind-induced vibration problems are also significant, independently from the future span-length of the bridge. Finally, reduced vibrations of the bridge deck imply less fatigue of the structure and thus a longer life time of the bridge, and additionally improve the comfort for people traversing the bridge. Wind-induced vibration problems are not limited to long-span bridges, thus the proposed sensor-actuator system might be relevant for other long/tall lightweight structures. It is our hope that the preliminary results we have obtained in this work, based on wind tunnel experiments on a section model, will rekindle the civil engineering community's interest for such innovative control techniques of large structures. To this effect, we trust that the lessons learned and insights gained that are described in this manuscript will constitute a valuable source of information for future studies within this field.

17.1 Summary

The first main part of this manuscript describes the mechatronic design process. We summarize our contributions as follows:

- We developed the SmartBridge, an actively controlled section model that is equipped with eight flaps and installed in a boundary layer wind tunnel. The SmartBridge represents a unique experimental platform worldwide, since previous experimental studies in this area have exclusively been carried out using a single flap on both sides of the bridge section.

- We explicitly motivated the various design choices made during the design process of the SmartBridge. For instance, we outlined the choice of actuators and sensors, deck dimensions, and described the flap design and its anchoring to the deck.
- We provided a thorough characterization of a single flap. For this purpose, we derived a model well-anchored to physical reality, which is capable of properly capture the nonlinear interaction between wind and the structure. Moreover, we leveraged this model in order to tune the control parameters of the single flap and to further push the performance limit of the actuator.

The second main part of this manuscript describes the analytical modeling effort. We summarize our contributions as follows:

- We based our analytical model of the active section model during flutter on a mixture of well-established theoretical formulations for a canonical bridge deck, and those of airplane wings equipped with trailing ailerons and tabs. In particular, we proposed to include the structural dynamics inherent to the flap movements, a property that have been largely ignored in the context of an actively or passively controlled section model.
- We derived the solution of the flutter equations for our proposed model, thus allowing a prediction of the flutter wind speed of the actively controlled deck. In particular, this contribution constitutes an extension to a well-established method for solving the flutter condition of a canonical bridge deck.
- We estimated all of the structural and aerodynamic model parameters from free vibration experiments in the wind tunnel. Furthermore, we provided a comprehensive description of our methodology.
- The fidelity of our proposed model, considering both theoretical and experimentally obtained model parameters, was rigorously evaluated with wind tunnel experiments. We showed that the analytical model is able to predict quite accurately the flutter wind speed, even for a wide range of different control parameters, when the leading flaps and trailing flaps are considered individually. Furthermore, our result highlights the importance of experimentally extracted model parameters and the significant impact of considering also the structural dynamics of the flaps.
- Although the analytical model satisfactory captures the resulting behavior of the deck controlled by the leading and trailing flaps separately, we observed significant discrepancies between the model prediction and the results obtained from wind tunnel tests when both sides were controlled simultaneously. Our intuition is that this is due to perturbations of the wind flow over downwind elements caused by the movements of upwind elements, an effect that is not considered in the model.
- Finally, we performed a sensitivity analysis of the model, by investigating possible redundant terms in the formulation. Notably, we find that we can reduce the number of aerodynamic model parameters related to the leading flap, from four to one, without causing a significant impact on the flutter prediction.

The third main part of this manuscript describes the investigation of different coordination

control strategies for multi-flap control. We summarize our contributions as follows:

- We provided an extensive, experimental study comparing the individual control contribution from the leading and trailing edge flaps.
- Additionally, the experimental validation of the model in the second part shows also novelty from a control perspective.
- We have performed a pioneering experimental investigation into flap coordination within the leading and trailing flap arrays. For this purpose, we established two basic control approaches, a synchronized and a decentralized one, and we defined a performance evaluation framework.
- We show that a synchronized control strategy, employing all the available flaps, at the largest amplitude-gain, provides not only the best vibration damping of the deck, but also at the cheapest cost for the defined performance measures.
- Finally, we evaluated the robustness of the two coordination approaches under more realistic, perturbed scenarios. The synchronized control law generally performs better even for perturbed scenarios. However, it degenerates quickly to the level of the decentralized approach even in the case of small disturbances.

17.2 Discussion and Outlook

This work constitutes a first step towards understanding the characteristics of the interaction between a wind field and an underlying structure (nonlinear, spatially heterogeneous, time-variant, and noisy), including the additional degrees of freedom introduced by the collective dimension of the flap system, and ultimately exploiting this knowledge in order to mitigate wind-induced vibrations. Although, we have tackled many aspects towards this goal, several remain to be taken into consideration. First of all, we will discuss compelling research thrusts that can be undertaken leveraging the current setup and techniques on a methodological level, i.e., concerning modeling and control aspects. Finally, we will broaden our view and extend the outlook beyond the current state of affairs.

Even though we have showed in this thesis that a version of the most commonly employed analytical model of flutter for a bridge deck equipped with movable flaps is capable of capturing the system dynamics to a satisfactory degree when the flaps are controlled one edge at the time, we recognized that this is not the case when both edges are operated simultaneously. We believe that these significant discrepancies are due to perturbations in the wind flow created by moving upwind elements. In order to validate this hypothesis, and possibly ameliorate the analytical formulation, it would be valuable to leverage our experimental setup equipped with pressure taps, which would provide further insights to understanding the underlying physical mechanisms. Moreover, since the SmartBridge allowed us to perform pioneering research of flap coordination along the arrays, we chose not to exhaustively study the synchronized control strategy. However, it would be interesting to further investigate variations of linear, synchronized, control laws, leveraging our analytical model, to achieve possibly

superior performances. For instance, adaptive control laws have shown promising results in a few theoretical studies, but never been validated experimentally. Furthermore, a thorough analysis of global properties of the system (e.g., stability, observability, and controllability) could be addressed using our experimental facility and theoretical framework. In particular, we believe that considering the principles of robust control to deal with the model's uncertainties is a promising approach. Finally, although we targeted the research in this thesis to the study and control of bridge deck flutter, we could in future studies investigate the SmartBridge capabilities to control also other aeroelastic phenomena such as buffeting or torsional divergence.

It is clear that for a final solution, i.e. a real long-span bridge equipped with multiple arrays of flaps, the control strategies of the individual flaps and in particular the collaboration between them is of the highest importance. The setup we developed in this thesis was necessary to answer basic research questions, such as validating the two-dimensional analytical model and investigate real-time flap control. However, we recognize that a rigid section model is not ideal for experimental investigation of collaborative control laws, mainly because the collaborative flap control schemes will be most effectual when controlling a flexible structure. In order to circumvent this, we sought out to perturb the deck by various internal and external factors. Although these additional experimental scenarios provided valuable insights concerning the robustness of the control strategies to disturbances, we had anticipated a more significant difference in performance between the synchronized and decentralized approach. This in turn would have stimulated us to further develop more sophisticated distributed control schemes, which eventually we decided to not investigate within this thesis because of the dominant performances of a centralized and synchronized control solution given the current setup. Thus, we believe that the production of a full-bridge model or a taut strip model controlled by multiple miniaturized flaps, would provide the next logical step towards (experimentally validated) advanced distributed control strategies. In terms of modeling, a flexible bridge structure could be approached with an analytical multi-mode model building on top of our two-dimensional model, or with a numerical FSI model where the fluid flow is modeled by CFD. Moreover, analogously to the theoretical and experimental work found in the literature, we have only considered an input vector to the control being the bridge model state. The mean wind speed and/or local wind measurements could also serve as control inputs. Finally, other sensory information such as accelerometers and inclinometers could be considered. These types of sensors are a more natural input for control on a real bridge.

A Solution of the Flutter Equations

In Part III, Chapter 9, we show that the fluttering bridge deck is described by

$$Y(t) \underbrace{\left[-\omega_f^2 M_s + \omega_f (C_s - C_{se}) i + (K_s - K_{se}) \right]}_A = 0 \quad (\text{A.1})$$

and that solving the determinant of system matrix A defines the flutter condition.

One method for finding this solution is Theodorsen's method, described for instance in [84]. Here we derive the solution, using the same approach, for an eccentric bridge deck controlled by leading and trailing flaps¹ (including both structural and aerodynamic flap contributions).

The strategy of the Theodorsen's method is to rearrange the system matrix A so that the flutter condition is solved for the non-dimensional variable X , and the system matrix only depends on the reduced frequency, K .

We introduce the variable $X = \omega/\omega_h$ and divide system matrix A by ω^2 . Note that the system frequency is denoted ω and is assumed equal for the heave and pitch DOF. However, this is only true for a flutter case situation where the solution of the matrix determinant, $|A/\omega^2| = 0$, will provide the system frequency ω_f at flutter. Thus, the notation difference between ω and ω_f mainly serves to distinguish the problem formulation from the solution (the value of ω is varied in order to find the solution ω_f). The new system matrix, A' , assuming the system in Equations 9.19 in Chapter 9, is described by

$$A' = \frac{A}{\omega^2} = -M_s + (C_s - C_{se}) \frac{i}{\omega} + (K_s - K_{se}) \frac{1}{\omega^2} = -M_s + (C'_s - C'_{se}) i + (K'_s - K'_{se}) \quad (\text{A.2})$$

¹The solution is restricted to an amplitude-gain and phase-shift of the pitch DOF control law. However, other linear control laws could be derived using a similar approach.

Appendix A. Solution of the Flutter Equations

where

$$M_s = \begin{bmatrix} m & \textcolor{red}{S} + S_t A_t (\cos(-\phi_t) + i \sin(-\phi_t)) + S_l A_l (\cos(-\phi_l) + i \sin(-\phi_l)) \\ \textcolor{red}{S} & I + I'_t A_t (\cos(-\phi_t) + i \sin(-\phi_t)) + I'_l A_l (\cos(-\phi_l) + i \sin(-\phi_l)) \end{bmatrix} \quad (\text{A.3a})$$

$$C'_s = \frac{C_s}{\omega} = \begin{bmatrix} 2m\zeta_h \frac{\omega_h}{\omega} & 0 \\ 0 & 2I\zeta_\alpha \frac{\omega_\alpha}{\omega} \end{bmatrix} = \begin{bmatrix} 2m\zeta_h \frac{1}{X} & 0 \\ 0 & 2I\zeta_\alpha \frac{\gamma}{X} \end{bmatrix} \quad (\text{A.3b})$$

$$K'_s = \frac{K_s}{\omega^2} = \begin{bmatrix} m \frac{\omega_h^2}{\omega^2} & 0 \\ 0 & I \frac{\omega_\alpha^2}{\omega^2} \end{bmatrix} = \begin{bmatrix} m \frac{1}{X^2} & 0 \\ 0 & I \frac{\gamma^2}{X^2} \end{bmatrix} \quad (\text{A.3c})$$

$$C'_{se} = \frac{C_{se}}{\omega} = \frac{1}{2} \rho B \frac{UK}{\omega} \begin{bmatrix} H_1^* & BH_2^{*'} \\ BA_1^* & B^2 A_2^{*'} \end{bmatrix} = \frac{1}{2} \rho B^2 \begin{bmatrix} H_1^* & BH_2^{*'} \\ BA_1^* & B^2 A_2^{*'} \end{bmatrix} \quad (\text{A.3d})$$

$$K'_{se} = \frac{K_{se}}{\omega^2} = \frac{1}{2} \rho \frac{U^2 K^2}{\omega^2} \begin{bmatrix} H_4^* & BH_3^{*'} \\ BA_4^* & B^2 A_3^{*'} \end{bmatrix} = \frac{1}{2} \rho B^2 \begin{bmatrix} H_4^* & BH_3^{*'} \\ BA_4^* & B^2 A_3^{*'} \end{bmatrix} \quad (\text{A.3e})$$

where $\gamma = \frac{\omega_\alpha}{\omega_h}$. Recall that the flutter derivatives are functions of the reduced frequency K even though the notation is removed from the equations for readability. Furthermore, we write the model parameter associated with an eccentric deck mass in **red**, and model parameters associated with the flap inertia in **green**. Note that by ignoring the **red** and **green** terms the solution reverts to the one of the symmetric, canonical bridge deck described for instance in [84].

Further note that the cross-diagonal flutter derivatives $H_2^{*'}, A_2^{*'}, H_3^{*'} and $A_3^{*'}$ are the aggregated terms for the controlled deck, as expressed in Appendix B, Equations B.10.$

Thus, the system matrix A' is written as follows

$$\begin{aligned} A' = & - \begin{bmatrix} m & \textcolor{red}{S} + S_t A_t (\cos(-\phi_t) + i \sin(-\phi_t)) + S_l A_l (\cos(-\phi_l) + i \sin(-\phi_l)) \\ \textcolor{red}{S} & I + I'_t A_t (\cos(-\phi_t) + i \sin(-\phi_t)) + I'_l A_l (\cos(-\phi_l) + i \sin(-\phi_l)) \end{bmatrix} \\ & + \left(\begin{bmatrix} \frac{2m\zeta_h}{X} & 0 \\ 0 & \frac{2I\zeta_\alpha\gamma}{X} \end{bmatrix} - \frac{\rho B^2}{2} \begin{bmatrix} H_1^* & BH_2^{*'} \\ BA_1^* & B^2 A_2^{*'} \end{bmatrix} \right) i + \left(\begin{bmatrix} \frac{m}{X^2} & 0 \\ 0 & \frac{I\gamma^2}{X^2} \end{bmatrix} - \frac{\rho B^2}{2} \begin{bmatrix} H_4^* & BH_3^{*'} \\ BA_4^* & B^2 A_3^{*'} \end{bmatrix} \right) \\ & = \begin{bmatrix} -m + \left(\frac{2m\zeta_h}{X} - \frac{\rho B^2}{2} H_1^* \right) i + \left(\frac{m}{X^2} - \frac{\rho B^2}{2} H_4^* \right) & -\textcolor{red}{S} - S_t A_t (...) - S_l A_l (...) - \frac{\rho B^3}{2} (H_2^{*'} i + H_3^{*'}) \\ -\textcolor{red}{S} - \frac{\rho B^3}{2} (A_1^* i + A_4^*) & -I - I'_t A_t (...) - I'_l A_l (...) + \left(\frac{2I\zeta_\alpha\gamma}{X} - \frac{\rho B^4}{2} A_2^{*'} \right) i + \left(\frac{I\gamma^2}{X^2} - \frac{\rho B^4}{2} A_3^{*'} \right) \end{bmatrix} \end{aligned} \quad (\text{A.4})$$

The determinant of A' is calculated as follows

$$\begin{aligned}
|A'| = & \left(-m + \left(\frac{2m\zeta_h}{X} - \frac{\rho B^2}{2} H_1^* \right) i + \left(\frac{m}{X^2} - \frac{\rho B^2}{2} H_4^* \right) \right) \\
& \left(-I - I'_t A_t(\dots) - I'_l A_l(\dots) + \left(\frac{2I\zeta_{\alpha}\gamma}{X} - \frac{\rho B^4}{2} A_2^{*'} \right) i + \left(\frac{I\gamma^2}{X^2} - \frac{\rho B^4}{2} A_3^{*'} \right) \right) \\
& - \left(-\textcolor{red}{S} - S_t A_t(\dots) - S_l A_l(\dots) - \frac{\rho B^3}{2} (H_2^{*'} i + H_3^{*'}) \right) \\
& \left(-\textcolor{red}{S} - \frac{\rho B^3}{2} (A_1^* i + A_4^*) \right) = 0
\end{aligned} \tag{A.5}$$

Keep developing the determinant

$$\begin{aligned}
|A'| = & mI + mI'_t A_t(\cos(-\phi_t) + i \sin(-\phi_t)) + mI'_l A_l(\cos(-\phi_l) + i \sin(-\phi_l)) \\
& - m \left(\frac{2I\zeta_{\alpha}\gamma I}{X} - \frac{\rho B^4}{2} A_2^{*'} \right) i - m \left(\frac{I\gamma^2}{X^2} - \frac{\rho B^4}{2} A_3^{*'} \right) - I \left(\frac{2m\zeta_h}{X} - \frac{\rho B^2}{2} H_1^* \right) i \\
& - I'_t A_t(\cos(-\phi_t) + i \sin(-\phi_t)) \left(\frac{2m\zeta_h}{X} - \frac{\rho B^2}{2} H_1^* \right) i \\
& - I'_l A_l(\cos(-\phi_l) + i \sin(-\phi_l)) \left(\frac{2m\zeta_h}{X} - \frac{\rho B^2}{2} H_1^* \right) i \\
& - \left(\frac{2m\zeta_h}{X} - \frac{\rho B^2}{2} H_1^* \right) \left(\frac{2I\zeta_{\alpha}\gamma}{X} - \frac{\rho B^4}{2} A_2^{*'} \right) + \left(\frac{2m\zeta_h}{X} - \frac{\rho B^2}{2} H_1^* \right) \left(\frac{I\gamma^2}{X^2} - \frac{\rho B^4}{2} A_3^{*'} \right) i \\
& - I \left(\frac{m}{X^2} - \frac{\rho B^2}{2} H_4^* \right) - I'_t A_t(\cos(-\phi_t) + i \sin(-\phi_t)) \left(\frac{m}{X^2} - \frac{\rho B^2}{2} H_4^* \right) \\
& - I'_l A_l(\cos(-\phi_l) + i \sin(-\phi_l)) \left(\frac{m}{X^2} - \frac{\rho B^2}{2} H_4^* \right) + \left(\frac{m}{X^2} - \frac{\rho B^2}{2} H_4^* \right) \left(\frac{2I\zeta_{\alpha}\gamma}{X} - \frac{\rho B^4}{2} A_2^{*'} \right) i \\
& + \left(\frac{m}{X^2} - \frac{\rho B^2}{2} H_4^* \right) \left(\frac{I\gamma^2}{X^2} - \frac{\rho B^4}{2} A_3^{*'} \right) - \left(\textcolor{red}{S}^2 + \textcolor{red}{S} \frac{\rho B^3}{2} (A_1^* i + A_4^*) \right) \\
& + \textcolor{red}{S} S_t A_t(\cos(-\phi_t) + i \sin(-\phi_t)) + S_t A_t(\cos(-\phi_t) + i \sin(-\phi_t)) \frac{\rho B^3}{2} (A_1^* i + A_4^*) \\
& + \textcolor{red}{S} S_l A_l(\cos(-\phi_l) + i \sin(-\phi_l)) + S_l A_l(\cos(-\phi_l) + i \sin(-\phi_l)) \frac{\rho B^3}{2} (A_1^* i + A_4^*) \\
& + \textcolor{red}{S} \frac{\rho B^3}{2} (H_2^{*'} i + H_3^{*'}) - \frac{\rho^2 B^6}{4} (H_3^{*'} A_4^* - H_2^{*'} A_1^*) - \frac{\rho^2 B^6}{4} (H_2^{*'} A_4^* + H_3^{*'} A_1^*) i = 0
\end{aligned} \tag{A.6}$$

Appendix A. Solution of the Flutter Equations

Further calculation of the determinant

$$\begin{aligned}
 |A'| = & mI + mI'_t A_t \cos(-\phi_t) + mI'_t A_t \sin(-\phi_t) i + mI'_l A_l \cos(-\phi_l) + mI'_l A_l \sin(-\phi_l) i \\
 & - m \left(\frac{2I\zeta_\alpha \gamma I}{X} - \frac{\rho B^4}{2} A_2^{*'} \right) i - m \left(\frac{I\gamma^2}{X^2} - \frac{\rho B^4}{2} A_3^{*'} \right) - I \left(\frac{2m\zeta_h}{X} - \frac{\rho B^2}{2} H_1^* \right) i \\
 & - I'_t A_t \cos(-\phi_t) \left(\frac{2m\zeta_h}{X} - \frac{\rho B^2}{2} H_1^* \right) i + I'_t A_t \sin(-\phi_t) \left(\frac{2m\zeta_h}{X} - \frac{\rho B^2}{2} H_1^* \right) \\
 & - I'_l A_l \cos(-\phi_l) \left(\frac{2m\zeta_h}{X} - \frac{\rho B^2}{2} H_1^* \right) i + I'_l A_l \sin(-\phi_l) \left(\frac{2m\zeta_h}{X} - \frac{\rho B^2}{2} H_1^* \right) \\
 & - \left(\frac{2m\zeta_h}{X} - \frac{\rho B^2}{2} H_1^* \right) \left(\frac{2I\zeta_\alpha \gamma}{X} - \frac{\rho B^4}{2} A_2^{*'} \right) + \left(\frac{2m\zeta_h}{X} - \frac{\rho B^2}{2} H_1^* \right) \left(\frac{I\gamma^2}{X^2} - \frac{\rho B^4}{2} A_3^{*'} \right) i \\
 & - I \left(\frac{m}{X^2} - \frac{\rho B^2}{2} H_4^* \right) - I'_t A_t \cos(-\phi_t) \left(\frac{m}{X^2} - \frac{\rho B^2}{2} H_4^* \right) - I'_t A_t \sin(-\phi_t) \left(\frac{m}{X^2} - \frac{\rho B^2}{2} H_4^* \right) i \\
 & - I'_l A_l \cos(-\phi_l) \left(\frac{m}{X^2} - \frac{\rho B^2}{2} H_4^* \right) - I'_l A_l \sin(-\phi_l) \left(\frac{m}{X^2} - \frac{\rho B^2}{2} H_4^* \right) i \\
 & + \left(\frac{m}{X^2} - \frac{\rho B^2}{2} H_4^* \right) \left(\frac{2I\zeta_\alpha \gamma}{X} - \frac{\rho B^4}{2} A_2^{*'} \right) i + \left(\frac{m}{X^2} - \frac{\rho B^2}{2} H_4^* \right) \left(\frac{I\gamma^2}{X^2} - \frac{\rho B^4}{2} A_3^{*'} \right) \\
 & - \left(S^2 + S \frac{\rho B^3}{2} (A_1^* i + A_4^*) + S S_t A_t \cos(-\phi_t) + S S_l A_l \sin(-\phi_l) i \right. \\
 & + S_t A_t \cos(-\phi_t) \frac{\rho B^3}{2} (A_1^* i + A_4^*) + S_t A_t \sin(-\phi_t) \frac{\rho B^3}{2} (-A_1^* + A_4^* i) \\
 & + S S_l A_l \cos(-\phi_l) + S S_l A_l \sin(-\phi_l) i \\
 & + S_l A_l \cos(-\phi_l) \frac{\rho B^3}{2} (A_1^* i + A_4^*) + S_l A_l \sin(-\phi_l) \frac{\rho B^3}{2} (-A_1^* + A_4^* i) \\
 & \left. + S \frac{\rho B^3}{2} (H_2^{*'} i + H_3^{*'}) \right) - \frac{\rho^2 B^6}{4} (H_3^{*'} A_4^* - H_2^{*'} A_1^*) - \frac{\rho^2 B^6}{4} (H_2^{*'} A_4^* + H_3^{*'} A_1^*) i = 0
 \end{aligned} \tag{A.7}$$

Consider real and imaginary part separately

$$\begin{aligned}
\Re(|A'|) = & mI + mI'_t A_t \cos(-\phi_t) + mI'_l A_l \cos(-\phi_l) - mI\gamma^2 \frac{1}{X_r^2} + m \frac{\rho B^4}{2} A_3^{*'} \\
& + I'_t A_t \sin(-\phi_t) \left(\frac{2m\zeta_h}{X_r} - \frac{\rho B^2}{2} H_1^* \right) + I'_l A_l \sin(-\phi_l) \left(\frac{2m\zeta_h}{X_r} - \frac{\rho B^2}{2} H_1^* \right) \\
& - \left(mI\zeta_h \zeta_\alpha \gamma \frac{4}{X_r^2} - m\zeta_h \frac{\rho B^4}{X_r} A_2^{*'} - I\zeta_\alpha \gamma \frac{\rho B^2}{X_r} H_1^* + \frac{\rho^2 B^6}{4} H_1^* A_2^{*'} \right) - mI \frac{1}{X_r^2} + I \frac{\rho B^2}{2} H_4^* \\
& - I'_t A_t \cos(-\phi_t) \left(\frac{m}{X_r^2} - \frac{\rho B^2}{2} H_4^* \right) - I'_l A_l \cos(-\phi_l) \left(\frac{m}{X_r^2} - \frac{\rho B^2}{2} H_4^* \right) \\
& + \left(mI\gamma^2 \frac{1}{X_r^4} - m \frac{\rho B^4}{2X_r^2} A_3^{*'} - I\gamma^2 \frac{\rho B^2}{2X_r^2} H_4^* + \frac{\rho^2 B^6}{4} H_4^* A_3^{*'} \right) \\
& - \mathbf{S}(\mathbf{S} + S_t A_t \cos(-\phi_t) + S_l A_l \cos(-\phi_l)) - \frac{\rho B^3}{2} (\mathbf{S} A_4^* + S_t A_t \cos(-\phi_t) A_4^* \\
& - S_t A_t \sin(-\phi_t) A_1^* + S_l A_l \cos(-\phi_l) A_4^* - S_l A_l \sin(-\phi_l) A_1^* + \mathbf{S} H_3^{*'}) \\
& - \frac{\rho^2 B^6}{4} (H_3^{*'} A_4^* - H_2^{*'} A_1^*) = 0
\end{aligned} \tag{A.8}$$

$$\begin{aligned}
\Im(|A'|) = & mI'_t A_t \sin(-\phi_t) + mI'_l A_l \sin(-\phi_l) - 2mI\zeta_\alpha \gamma \frac{1}{X_i} + m \frac{\rho B^4}{2} A_2^{*'} - 2mI\zeta_h \frac{1}{X_i} \\
& + I \frac{\rho B^2}{2} H_1^* - I'_t A_t \cos(-\phi_t) \left(\frac{2m\zeta_h}{X_i} - \frac{\rho B^2}{2} H_1^* \right) - I'_l A_l \cos(-\phi_l) \left(\frac{2m\zeta_h}{X_i} - \frac{\rho B^2}{2} H_1^* \right) \\
& + \left(2mI\zeta_h \gamma^2 \frac{1}{X_i^3} - m\zeta_h \frac{\rho B^4}{X_i} A_3^{*'} - I\gamma^2 \frac{\rho B^2}{2X_i^2} H_1^* + \frac{\rho^2 B^6}{4} H_1^* A_3^{*'} \right) \\
& - I'_t A_t \sin(-\phi_t) \left(\frac{m}{X_i^2} - \frac{\rho B^2}{2} H_4^* \right) - I'_l A_l \sin(-\phi_l) \left(\frac{m}{X_i^2} - \frac{\rho B^2}{2} H_4^* \right) \\
& + \left(2mI\zeta_\alpha \gamma \frac{1}{X_i^3} - m \frac{\rho B^4}{2X_i^2} A_2^{*'} - I\zeta_\alpha \gamma \frac{\rho B^2}{X_i} H_4^* + \frac{\rho^2 B^6}{4} H_4^* A_2^{*'} \right) \\
& - \mathbf{S}(S_t A_t \sin(-\phi_t) + S_l A_l \sin(-\phi_l)) - \frac{\rho B^3}{2} (\mathbf{S} A_1^* + S_t A_t \cos(-\phi_t) A_1^* \\
& + S_t A_t \sin(-\phi_t) A_4^* + S_l A_l \cos(-\phi_l) A_1^* + S_l A_l \sin(-\phi_l) A_4^* + \mathbf{S} H_2^{*'}) \\
& - \frac{\rho^2 B^6}{4} (H_2^{*'} A_4^* + H_3^{*'} A_1^*) = 0
\end{aligned} \tag{A.9}$$

Appendix A. Solution of the Flutter Equations

Multiply the real part in A.8 by X_r^4

$$\begin{aligned}
 \Re(|A'|)X_r^4 = & \left[mI + m\frac{\rho B^4}{2}A_3^{*'} + I\frac{\rho B^2}{2}H_4^* + \frac{\rho^2 B^6}{4}(-H_1^*A_2^{*'} + H_4^*A_3^{*'} + H_2^{*'}A_1^* - H_3^{*'}A_4^*) \right. \\
 & + \left(m + \frac{\rho B^2}{2}H_4^* \right) (I_t' A_t \cos(-\phi_t) + I_l' A_l \cos(-\phi_l)) \\
 & - \frac{\rho B^2}{2}H_1^* (I_t' A_t \sin(-\phi_t) + I_l' A_l \sin(-\phi_l)) \\
 & - \mathbf{S}(\mathbf{S} + S_t A_t \cos(-\phi_t) + S_l A_l \cos(-\phi_l)) - \frac{\rho B^3}{2}(\mathbf{S}(A_4^* + H_3^{*'})) \\
 & + A_4^*(S_t A_t \cos(-\phi_t) + S_l A_l \cos(-\phi_l)) - A_1^*(S_t A_t \sin(-\phi_t) + S_l A_l \sin(-\phi_l)) \Big] X_r^4 \\
 & + \left[m\zeta_h \rho B^4 A_2^{*'} + I\zeta_\alpha \gamma \rho B^2 H_1^* + 2m\zeta_h (I_t' A_t \sin(-\phi_t) + I_l' A_l \sin(-\phi_l)) \right] X_r^3 \\
 & + \left[-mI\gamma^2 - 4mI\zeta_h \zeta_\alpha \gamma - mI - m\frac{\rho B^4}{2}A_3^{*'} - I\gamma^2 \frac{\rho B^2}{2}H_4^* \right. \\
 & \left. - m(I_t' A_t \cos(-\phi_t) + I_l' A_l \cos(-\phi_l)) \right] X_r^2 \\
 & + mI\gamma^2 = 0
 \end{aligned} \tag{A.10}$$

Multiply the imaginary part in A.9 by X_i^3

$$\begin{aligned}
 \Im(|A'|)X_i^3 = & \left[m\frac{\rho B^4}{2}A_2^{*'} + I\frac{\rho B^2}{2}H_1^* + \frac{\rho^2 B^6}{4}(H_1^*A_3^{*'} + H_4^*A_2^{*'} - H_2^{*'}A_4^* - H_3^{*'}A_1^*) \right. \\
 & + m(I_t' A_t \sin(-\phi_t) + I_l' A_l \sin(-\phi_l)) + \left(\frac{\rho B^2}{2}H_1^* \right) (I_t' A_t \cos(-\phi_t) + I_l' A_l \cos(-\phi_l)) \\
 & + \left(\frac{\rho B^2}{2}H_4^* \right) (I_t' A_t \sin(-\phi_t) + I_l' A_l \sin(-\phi_l)) \\
 & - \mathbf{S}(S_t A_t \sin(-\phi_t) + S_l A_l \sin(-\phi_l)) - \frac{\rho B^3}{2}(\mathbf{S}(A_1^* + H_2^{*'})) \\
 & + A_1^*(S_t A_t \cos(-\phi_t) + S_l A_l \cos(-\phi_l)) + A_4^*(S_t A_t \sin(-\phi_t) + S_l A_l \sin(-\phi_l)) \Big] X_i^3 \\
 & + \left[-2mI\zeta_\alpha \gamma - 2mI\zeta_h - m\zeta_h \rho B^4 A_3^{*'} - I\zeta_\alpha \gamma \rho B^2 H_4^* \right. \\
 & \left. - 2m\zeta_h (I_t' A_t \cos(-\phi_t) + I_l' A_l \cos(-\phi_l)) \right] X_i^2 \\
 & + \left[-I\gamma^2 \frac{\rho B^2}{2}H_1^* - m\frac{\rho B^4}{2}A_2^{*'} - m(I_t' A_t \sin(-\phi_t) + I_l' A_l \sin(-\phi_l)) \right] X_i \\
 & + 2mI\gamma(\zeta_h \gamma + \zeta_\alpha) = 0
 \end{aligned} \tag{A.11}$$

Finally, the polynomials in Equations A.10 and A.11 are simultaneously solved for X_r and X_i , for a range of values of the reduced frequency K . The flutter condition is defined as the point, (X_f, K_f) , where the curves of $X_r(K)$ and $X_i(K)$ cross. Since the amplitude of the system at the flutter condition is assumed to be constant, i.e. neither damped nor growing, only real solutions to the polynomials are considered. In the case of multiple crossings of the curves,

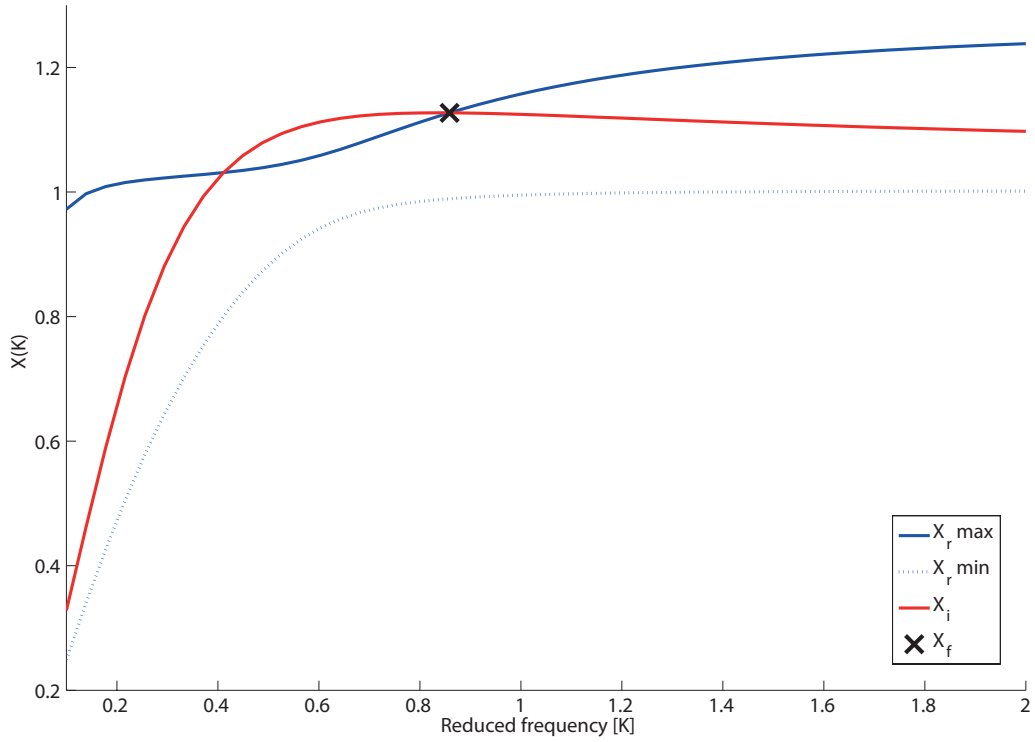


Figure A.1 – Plotting the real and imaginary parts of the determinant solution for a range of reduced frequencies. The flutter condition is defined by the crossing point of the imaginary and real curves.

the highest value of the reduced frequency, K , (i.e. the lowest wind speed U), corresponds to the flutter point. From the solution (X_f, K_f) the flutter frequency and flutter wind speed are calculated as follows

$$\omega_f = X_f \omega_h \quad (\text{A.12a})$$

$$U_f = B \omega_f / K_f \quad (\text{A.12b})$$

In case the curves do not cross, the flutter condition is never fulfilled, and thus the system will, at least in theory, never flutter.

In Figure A.1, we show the solution given for the uncontrolled eccentric bridge deck. Note, that the real part of the solution has two real positive roots. However, in this example, only one of the real roots cross the imaginary solution. Although, the curves cross twice, the flutter condition is defined by the crossing point at the highest reduced frequency, as marked in the figure.

B Expressing Flap Positions in the Form of the Bridge State

Assuming an amplitude-gain and phase-shift control law using the bridge deck pitch as input, we can express the trailing and leading edge flaps' positions accordingly

$$\alpha_t(t) = A_t e^{-i\phi_t} \alpha(t) \quad (\text{B.1a})$$

$$\alpha_l(t) = A_l e^{-i\phi_l} \alpha(t) \quad (\text{B.1b})$$

where A_l and A_t are the amplitude gains, and ϕ_l and ϕ_t are the phase-shifts of the leading and trailing edge flaps respectively, and α is the deck position.

Recall that the flutter condition allows us to describe the pitch state and its time derivatives as follows

$$\alpha(t) = \alpha_0 e^{-i\phi_f} e^{i\omega_f t} \quad \dot{\alpha}(t) = i\omega_f \alpha(t) \quad \ddot{\alpha}(t) = -\omega_f^2 \alpha(t) \quad (\text{B.2})$$

This allows us to express the flap position and velocity in terms of pitch position and velocity as follows

$$\begin{aligned} \alpha_x(t) &= A_x e^{-i\phi_x} \alpha(t) = A_x (\cos(-\phi_x) + i \sin(-\phi_x)) \alpha(t) \\ &= A_x \left(\cos(-\phi_x) \alpha(t) + i \sin(-\phi_x) \frac{\dot{\alpha}(t)}{i\omega} \right) \\ &= A_x \left(\cos(-\phi_x) \alpha(t) + \frac{1}{\omega} \sin(-\phi_x) \dot{\alpha}(t) \right) \end{aligned} \quad (\text{B.3})$$

Appendix B. Expressing Flap Positions in the Form of the Bridge State

$$\begin{aligned}
 \dot{\alpha}_x(t) &= A_x e^{-i\phi_x} \dot{\alpha}(t) = A_x (\cos(-\phi_x) + i \sin(-\phi_x)) \dot{\alpha}(t) \\
 &= A_x (\cos(-\phi_x) \dot{\alpha}(t) + i \sin(-\phi_x) i \omega \alpha(t)) \\
 &= A_x (\cos(-\phi_x) \dot{\alpha}(t) - \omega \sin(-\phi_x) \alpha(t))
 \end{aligned} \tag{B.4}$$

where x denotes either the leading or the trailing flap and the corresponding control parameters.

We can now insert the expression for the flap position and velocity as given in Equations B.3 and B.4 into the expression for the aerodynamic forces described in Equations 9.6 as follows

$$\begin{aligned}
 L_t &= \frac{1}{2} \rho U^2 B K \left[H_5^* \frac{B \dot{\alpha}_t}{U} + H_6^* K \alpha_t \right] \\
 &= \frac{1}{2} \rho U^2 B K \left[H_5^* \frac{B}{U} A_t (\cos(-\phi_t) \dot{\alpha}(t) - \omega \sin(-\phi_t) \alpha(t)) \right. \\
 &\quad \left. + H_6^* K A_t \left(\cos(-\phi_t) \alpha(t) + \frac{1}{\omega} \sin(-\phi_t) \dot{\alpha}(t) \right) \right] \\
 &= \frac{1}{2} \rho U^2 B K \left[H_5^* A_t \frac{B}{U} \cos(-\phi_t) \dot{\alpha}(t) - H_5^* A_t \frac{B \omega}{U} \sin(-\phi_t) \alpha(t) \right. \\
 &\quad \left. + H_6^* K A_t \cos(-\phi_t) \alpha(t) + H_6^* \frac{K}{\omega} A_t \sin(-\phi_t) \dot{\alpha}(t) \right]
 \end{aligned} \tag{B.5}$$

Note that the flutter derivatives are functions of the reduced frequency K even though the notation is removed from the equations for readability. Given that $K = B\omega/U$, the expression in Eq. B.5 can be simplified as follows

$$\begin{aligned}
 L_t &= \frac{1}{2} \rho U B^2 K \left[H_5^* A_t \cos(-\phi_t) + H_6^* A_t \sin(-\phi_t) \right] \dot{\alpha}(t) \\
 &\quad + \frac{1}{2} \rho U^2 B K^2 \left[-H_5^* A_t \sin(-\phi_t) + H_6^* A_t \cos(-\phi_t) \right] \alpha(t)
 \end{aligned} \tag{B.6}$$

Analogously for the leading edge flap lift and the trailing and leading edge flap moments

$$L_l = \frac{1}{2} \rho U B^2 K \left[H_7^* A_l \cos(-\phi_l) + H_8^* A_l \sin(-\phi_l) \right] \dot{\alpha}(t) + \frac{1}{2} \rho U^2 B K^2 \left[-H_7^* A_l \sin(-\phi_l) + H_8^* A_l \cos(-\phi_l) \right] \alpha(t) \quad (\text{B.7})$$

$$M_t = \frac{1}{2} \rho U B^3 K \left[A_5^* A_t \cos(-\phi_t) + A_6^* A_t \sin(-\phi_t) \right] \dot{\alpha}(t) + \frac{1}{2} \rho U^2 B^2 K^2 \left[-A_5^* A_t \sin(-\phi_t) + A_6^* A_t \cos(-\phi_t) \right] \alpha(t) \quad (\text{B.8})$$

$$M_l = \frac{1}{2} \rho U B^3 K \left[A_7^* A_l \cos(-\phi_l) + A_8^* A_l \sin(-\phi_l) \right] \dot{\alpha}(t) + \frac{1}{2} \rho U^2 B^2 K^2 \left[-A_7^* A_l \sin(-\phi_l) + A_8^* A_l \cos(-\phi_l) \right] \alpha(t) \quad (\text{B.9})$$

Thus, we are now able to express the extended system purely in terms of the bridge pitch and the control parameters. Finally, we modify the flutter derivatives H_2^* , H_3^* , A_2^* and A_3^* so that the aerodynamic forces of the extended system is fully taken into account. Given the proposed control laws in Eqs.B.1a and B.1b the modified flutter derivatives become

$$H_2^{*'} = H_2^* + H_5^* A_t \cos(-\phi_t) + H_6^* A_t \sin(-\phi_t) + H_7^* A_l \cos(-\phi_l) + H_8^* A_l \sin(-\phi_l) \quad (\text{B.10a})$$

$$H_3^{*'} = H_3^* - H_5^* A_t \sin(-\phi_t) + H_6^* A_t \cos(-\phi_t) - H_7^* A_l \sin(-\phi_l) + H_8^* A_l \cos(-\phi_l) \quad (\text{B.10b})$$

$$A_2^{*'} = A_2^* + A_5^* A_t \cos(-\phi_t) + A_6^* A_t \sin(-\phi_t) + A_7^* A_l \cos(-\phi_l) + A_8^* A_l \sin(-\phi_l) \quad (\text{B.10c})$$

$$A_3^{*'} = A_3^* - A_5^* A_t \sin(-\phi_t) + A_6^* A_t \cos(-\phi_t) - A_7^* A_l \sin(-\phi_l) + A_8^* A_l \cos(-\phi_l) \quad (\text{B.10d})$$

Bibliography

- [1] K. Ostenfeld, *A system and a method of counteracting wind induced oscillations in a bridge girder*, Feb. 1993.
- [2] K. Ostenfeld and A. Larsen, "Bridge engineering and aerodynamics", in *Proceedings of the First International Symposium on Aerodynamics of Large Bridges*, 1992, pp. 3–22.
- [3] D. Smith, "A case study and analysis of the tacoma narrows bridge failure", Dept Mech Eng, Carleton University, Tech. Rep., Mar. 1974.
- [4] M. S. Andersen, J. R. Læsø, M. Lenius, and J. Johansson, "Non-flutter design principle for twin boxes", in *14th International Conference on Wind Engineering (ICWE)*, Jun. 2015.
- [5] J. Nobuto and Y. Fujino, "A study on the effectiveness of tmd to suppress a coupled flutter of bridge deck", *J Struct Mech Earthquake Eng*, vol. 398, pp. 413–416, 1988.
- [6] X. Chen and A. Kareem, "Efficacy of tuned mass dampers for bridge flutter control", *J Struct Eng*, vol. 129, no. 10, pp. 1291–1300, 2003.
- [7] R. Koerlin and U. Starossek, "Wind tunnel test of an active mass damper for bridge decks", *Journal of Wind Engineering and Industrial Aerodynamics*, vol. 95, no. 4, pp. 267–277, 2007.
- [8] J. Scheller and U. Starossek, *Wind tunnel tests on active flutter control by twin rotor damper*, Jul. 2011.
- [9] U. Starossek and J. Scheller, *A novel active mass damper for vibration control of bridges*, Jul. 2008.
- [10] N. N. Dung, T. Miyata, and H. Yamada, "Application of robust control to the flutter in long-span bridges", *Journal of Structural Engineering*, vol. 42A, pp. 847–854, 1996.
- [11] J. Raggett, *Stabilizing winglet pair for slender bridge decks*, 1987.
- [12] M. G. Savage and G. L. Larose, "An experimental study of the aerodynamic influence of a pair of winglets on a flat plate model", *J Wind Eng Ind Aerodyn*, vol. 91, no. 1–2, pp. 113–126, 2003.
- [13] G. Liu, F. Meng, and X. Wang, *Mechanism of flutter control of suspension bridge by winglets*, 2006.
- [14] H. Kobayashi and H. Nagaoka, "Active control of flutter of a suspension bridge", *Journal of Wind Engineering and Industrial Aerodynamics*, vol. 41, no. 1–3, pp. 143–151, 1992.

Bibliography

- [15] K. Wilde, Y. Fujino, and T. Kawakami, "Analytical and experimental study on passive aerodynamic control of flutter of a bridge deck", *Journal of Wind Engineering and Industrial Aerodynamics*, vol. 80, no. 1 - 2, pp. 105–119, 1999. DOI: [http://dx.doi.org/10.1016/S0167-6105\(98\)00196-2](http://dx.doi.org/10.1016/S0167-6105(98)00196-2).
- [16] S.-D. Kwon, M. S. Sungmoon Jung, and S.-P. Chang, "A new passive aerodynamic control method for bridge flutter", *Journal of Wind Engineering and Industrial Aerodynamics*, vol. 86, no. 2-3, pp. 187–202, 2000. DOI: [http://dx.doi.org/10.1016/S0167-6105\(00\)00010-6](http://dx.doi.org/10.1016/S0167-6105(00)00010-6).
- [17] U. Starossek and H. Aslan, "Passive control of bridge deck flutter using tuned mass dampers and control surfaces", in *7th European Conference on Structural Dynamics*, 2008, pp. 7–9.
- [18] D.-H. Phan and H. Kobayashi, "An experimental study of flutter and buffeting control of suspension bridge by mechanically driven flaps", *Wind and Structures*, vol. 14, no. 2, pp. 152–163, 2011.
- [19] D.-H. Phan and H. Kobayashi, "Analytical and experimental study on aerodynamic control of flutter and buffeting of bridge deck by using mechanically driven flaps", *Structural Engineering and Mechanics*, vol. 46, no. 4, pp. 549–569, 2013. DOI: 10.12989/sem.2013.46.4.549.
- [20] D.-H. Phan and N.-T. Nguyen, "Flutter and buffeting control of long-span suspension bridge by passive flaps: experiment and numerical simulation", *International Journal of Aeronautics and Space*, vol. 14, no. 1, pp. 46–57, 2013. DOI: 10.5139/IJASS.2013.14.1.46.
- [21] X. Zhao, K. Gouder, D. Limebeer, and J. Graham, "Experimental flutter and buffet suppression of a sectional suspended-bridge", in *Proceedings of the 53rd IEEE Conference on Decision and Control*, Dec. 2014.
- [22] X. Zhao, K. Gouder, J. M. R. Graham, and D. J. Limebeer, "Buffet loading, dynamic response and aerodynamic control of a suspension bridge in a turbulent wind", *Journal of Fluids and Structures*, vol. 62, pp. 384–412, 2016. DOI: <http://dx.doi.org/10.1016/j.jfluidstructs.2016.01.013>.
- [23] K. Gouder, X. Zhao, D. J. N. Limebeer, and J. M. R. Graham, "Experimental flutter suppression of a long-span suspension bridge section", in *First International Symposium on Flutter and its Application*, International Federation of Automatic Control, Mar. 2016.
- [24] H. Kobayashi, R. Ogawa, and S. Taniguchi, "Active flutter control of a bridge deck by ailerons", in *Second World Conference on Structural Control*, 1998, pp. 1841–1848.
- [25] H. I. Hansen and P. Thoft-Christensen, "Wind tunnel testing of active control system for bridges", in *15th Congress Structural Eng*, Stollfuss Verlag Bonn GmbH and Co. KG, 1996, pp. 775–780.
- [26] H. I. Hansen and P. Thoft-Christensen, "Wind tunnel experiments with active control of bridge section model", in *IABSE Symp on "Long-span and High-rise Structures"*, 1998, pp. 199–204.

- [27] H. I. Hansen and P. Thoft-Christensen, "Active vibration control of long suspension bridges", PhD thesis, Aalborg University, 1998.
- [28] H. I. Hansen, P. Thoft-Christensen, P. A. Mendes, and F. A. Branco, "Wind-tunnel tests of a bridge model with active vibration control", *Structural Engineering International*, vol. 10, no. 4, pp. 249–253, 2000. DOI: doi:10.2749/101686600780481239.
- [29] H. I. Hansen and P. Thoft-Christensen, "Active flap control of long suspension bridges", *Journal of Structural Control*, vol. 8, no. 1, pp. 33–82, 2001. DOI: 10.1002/stc.4300080104.
- [30] P. Thoft-Christensen, "Active control of suspension bridges", in *2nd Euro Conf on Structural Control*, 2000.
- [31] P. Thoft-Christensen, "Improving the dynamics of suspension bridges using active control systems", in *2nd Int Work on Life-Cycle Cost Analysis and Design of Civil Infrastructure Systems*, 2001, pp. 293–304.
- [32] **M. Boberg**, G. Feltrin, and A. Martinoli, "Model and control of a flap system mitigating wind impact on structures", in *Robotics and Automation (ICRA), 2014 IEEE International Conference on*, May 2014, pp. 264–269. DOI: 10.1109/ICRA.2014.6906620.
- [33] **M. Boberg**, G. Feltrin, and A. Martinoli, "A novel bridge section model endowed with actively controlled flap arrays mitigating wind impact", in *Robotics and Automation (ICRA), 2015 IEEE International Conference on*, May 2015, pp. 1837–1842. DOI: 10.1109/ICRA.2015.7139437.
- [34] **M. Boberg**, G. Feltrin, and A. Martinoli, "Experimental validation of the wing-aileron-tab combination applied to an actively controlled bridge section model", in *14th International Conference on Wind Engineering (ICWE)*, Jun. 2015.
- [35] **M. Boberg**, G. Feltrin, and A. Martinoli, "An analytical and experimental investigation of an actively controlled bridge section model", *Journal of Wind Engineering and Industrial Aerodynamics*, in preparation.
- [36] **M. Boberg**, G. Feltrin, and A. Martinoli, "Flutter suppression of a bridge section model endowed with actively controlled flap arrays", in *Intelligent Robots and Systems (IROS), 2015 IEEE/RSJ International Conference on*, Sep. 2015, pp. 5936–5941. DOI: 10.1109/IROS.2015.7354221.
- [37] E. Simiu and R. H. Scanlan, *Wind Effects on Structures: Fundamentals and Application to Design*. New York: John Wiley & Sons, 1996.
- [38] K. Wilde, P. Omenzetter, and Y. Fujino, "Suppression of bridge flutter by active deck-flaps control system", *J Eng Mech*, vol. 127, no. 1, pp. 80–89, 2001.
- [39] Z. Chen, X. Yu, G. Yang, and B. Spencer, "Wind-induced self-excited loads on bridges", *J Struct Eng*, vol. 131, no. 12, pp. 1783–1793, 2005.
- [40] B. Cao and P. P. Sarkar, "Identification of rational functions by forced vibration method for time-domain analysis of flexible structures", in *Proceedings: the fifth international symposium on computational wind engineering*, Chapel Hill, 2010.

Bibliography

- [41] T. Argentini, D. Rocchi, S. Muggiasca, and A. Zasso, "Cross-sectional distributions versus integrated coefficients of flutter derivatives and aerodynamic admittances identified with surface pressure measurement", *Journal of Wind Engineering and Industrial Aerodynamics*, vol. 104–106, pp. 152–158, 2012, 13th International Conference on Wind Engineering. DOI: <http://dx.doi.org/10.1016/j.jweia.2012.03.009>.
- [42] A. Sarkic, R. Fisch, R. Hoeffler, and K.-U. Bletzinger, "Bridge flutter derivatives based on computed, validated pressure fields", *J Wind Eng Ind Aerodyn*, vol. 104, pp. 141–151, 2012.
- [43] A. Larsen, *Aerodynamics of Large Bridges*. Taylor & Francis, 1992.
- [44] C. Neuhaus, S. Roesler, R. Hoffer, M. Hortmanns, and W. Zahlten, "Identification of 18 flutter derivatives by forced vibration tests - a new experimental rig", in *5th Euro and African Conf on Wind Eng*, 2009.
- [45] E. Hjorth-Hansen, "Section model tests", in *Proceedings of the First International Symposium on Aerodynamics of Large Bridges*, 1992, pp. 95–112.
- [46] J. Brownjohn and J. Jakobsen, "Strategies for aeroelastic parameter identification from bridge deck free vibration data", *Journal of Wind Engineering and Industrial Aerodynamics*, vol. 89, no. 13, pp. 1113–1136, 2001.
- [47] M. Matsumoto, K. Mizuno, K. Okubo, and Y. Ito, "Torsional flutter and branch characteristics for 2-d rectangular cylinders", *Journal of Fluids and Structures*, vol. 21, no. 5 - 7, pp. 597–608, 2005. DOI: <http://dx.doi.org/10.1016/j.jfluidstructs.2005.07.021>.
- [48] P. Sarkar, A. G. Chowdhury, and T. B. Gardner, "A novel elastic suspension system for wind tunnel section model studies", *Journal of Wind Engineering and Industrial Aerodynamics*, vol. 92, pp. 23–40, 2004.
- [49] J. M. Fowler and R. D'Andrea, "A formation flight experiment", *Control Systems, IEEE*, vol. 23, no. 5, pp. 35–43, 2003.
- [50] A. Visioli, *Practical PID Control*. Springer, 2006.
- [51] I. Abbott and A. Von Doenhoff, *Theory of wing sections, including a summary of airfoil data*, ser. Dover books on physics and chemistry. Dover Publications, 1959.
- [52] R. Sheldahl, P. Klimas, U. S. D. of Energy, and S. N. Laboratories, *Aerodynamic Characteristics of Seven Symmetrical Airfoil Sections Through 180-degree Angle of Attack for Use in Aerodynamic Analysis of Vertical Axis Wind Turbines*. Sandia National Laboratories, 1981.
- [53] Y. Fung, *An Introduction to the Theory of Aeroelasticity*, ser. Dover Phoenix Edition: Engineering. Dover Publications, 2002.
- [54] T. Theodorsen, "General theory of aerodynamic instability and the mechanism of flutter", *NACA Tech. Rep. no. 496*, 1935.

- [55] R. Scanlan, N. Jones, and L. Singh, "Inter-relations among flutter derivatives", *Journal of Wind Engineering and Industrial Aerodynamics*, vol. 69–71, pp. 829–837, 1997, Proceedings of the 3rd International Colloquium on Bluff Body Aerodynamics and Applications. DOI: [http://dx.doi.org/10.1016/S0167-6105\(97\)00209-2](http://dx.doi.org/10.1016/S0167-6105(97)00209-2).
- [56] R. H. Scanlan, and J. J. Tomko, "Airfoil and bridge deck flutter derivatives", *Journal of the Engineering Mechanics Division*, vol. 97, no. EM 6, pp. 1717–1736, 1971.
- [57] K. Wilde and Y. Fujino, "Variable-gain control applied to aerodynamic control of bridge deck flutter", in *35th IEEE Decision and Control*, vol. 1, 1996, pp. 682–687.
- [58] P. Omenzetter, K. Wilde, and Y. Fujino, "Suppression of wind-induced instabilities of a long span bridge by a passive deck-flaps control system: part i: formulation", *J Wind Eng Ind Aerodyn*, vol. 87, no. 1, pp. 61–79, 2000.
- [59] K. Wilde and Y. Fujino, "Aerodynamic control of bridge deck flutter by active surfaces", *J Eng Mech*, vol. 124, no. 7, pp. 718–727, 1998.
- [60] P. Omenzetter, K. Wilde, and Y. Fujino, "Suppression of wind-induced instabilities of a long span bridge by a passive deck-flaps control system: part ii: numerical simulations", *J Wind Eng Ind Aerodyn*, vol. 87, no. 1, pp. 81–91, 2000.
- [61] P. Omenzetter, K. Wilde, and Y. Fujino, "Study of passive deck-flaps flutter control system on full bridge model. i: theory", *J Eng Mech*, vol. 128, no. 3, pp. 264–279, 2002.
- [62] P. Omenzetter, K. Wilde, and Y. Fujino, "Study of passive deck-flaps flutter control system on full bridge model. ii: results", *J Eng Mech*, vol. 128, no. 3, pp. 280–286, 2002.
- [63] J. M. R. Graham, D. J. N. Limebeer, and X. W. Zhao, "Aeroelastic control of long-span suspension bridges", *J Appl Mech - Trans Asme*, vol. 78, no. 4, 2011.
- [64] J. M. R. Graham, D. J. N. Limebeer, and X. Zhao, "Aeroelastic modelling of long-span suspension bridges", in *18th IFAC World Congress*, International Federation of Automatic Control, 2011, pp. 9212–9217.
- [65] D. J. N. Limebeer, J. M. R. Graham, and X. Zhao, "Buffet suppression in long-span suspension bridges", *Annual Reviews in Control*, vol. 35, no. 2, pp. 235–246, 2011.
- [66] Z. Xiaowei, D. J. N. Limebeer, and J. M. R. Graham, "Flutter control of long-span suspension bridges", in *50th IEEE Conf on Decision and Control and European Control Conf*, 2011, pp. 4195–4200.
- [67] X. Zhao, D. J. Limebeer, and J. M. R. Graham, "Modelling and control of a suspended-span bridge section", in *World Congress*, vol. 19, 2014, pp. 5211–5216.
- [68] K. Li, Y. Ge, Z. Guo, and L. Zhao, "Theoretical framework of feedback aerodynamic control of flutter oscillation for long-span suspension bridges by the twin-winglet system", *Journal of Wind Engineering and Industrial Aerodynamics*, vol. 145, pp. 166–177, 2015. DOI: <http://dx.doi.org/10.1016/j.jweia.2015.06.012>.
- [69] A. Jain, N. P. Jones, and R. H. Scanlan, "Coupled aeroelastic and aerodynamic response analysis of long-span bridges", *J Wind Eng Ind Aerodyn*, vol. 60, no. 0, pp. 69–80, 1996.

Bibliography

- [70] S.-D. Kwon and S.-P. Chang, "Suppression of flutter and gust response of bridges using actively controlled edge surfaces", *Journal of Wind Engineering and Industrial Aerodynamics*, vol. 88, no. 2–3, pp. 263–281, 2000.
- [71] D. Arco and A. Aparicio, "Improving suspension bridge wind stability with aerodynamic appendages", *Journal of Structural Engineering*, vol. 125, no. 12, pp. 1367–1375, 1999. DOI: 10.1061/(ASCE)0733-9445(1999)125:12(1367). eprint: [http://dx.doi.org/10.1061/\(ASCE\)0733-9445\(1999\)125:12\(1367\)](http://dx.doi.org/10.1061/(ASCE)0733-9445(1999)125:12(1367)).
- [72] H. D. Nissen, P. H. Sørensen, and O. Jannerup, "Active aerodynamic stabilisation of long suspension bridges", *J Wind Eng Ind Aerodyn*, vol. 92, no. 10, pp. 829–847, 2004.
- [73] D. Sun, J. S. Owen, and N. G. Wright, "Application of the k-omega turbulence model for a wind-induced vibration study of 2d bluff bodies", *J Wind Eng Ind Aerodyn*, vol. 97, no. 2, pp. 77–87, 2009.
- [74] M. W. Sarwar, T. Ishihara, K. Shimada, Y. Yamasaki, and T. Ikeda, "Prediction of aerodynamic characteristics of a box girder bridge section using the les turbulence model", *J Wind Eng Ind Aerodyn*, vol. 96, no. 10–11, pp. 1895–1911, 2008.
- [75] A. Larsen and J. H. Walther, "Aeroelastic analysis of bridge girder sections based on discrete vortex simulations", *Journal of Wind Engineering and Industrial Aerodynamics*, vol. 67–8, pp. 253–265, 1997.
- [76] A. Larsen and J. H. Walther, "Discrete vortex simulation of flow around five generic bridge deck sections", *Journal of Wind Engineering and Industrial Aerodynamics*, vol. 77–8, pp. 591–602, 1998.
- [77] J. B. Frandsen, "Numerical bridge deck studies using finite elements. part i: flutter", *J Fluids Struct*, vol. 19, no. 2, pp. 171–191, 2004.
- [78] S. Preidikman and D. T. Mook, "A new method for actively suppressing flutter of suspension bridges", *J Wind Eng Ind Aerodyn*, vol. 69–71, no. 0, pp. 955–974, 1997.
- [79] K. Li and L. Zhao, "Cfd simulation of the feedback controlled twin-winglet system for flutter suppression of long-span suspension bridges", in *14th International Conference on Wind Engineering (ICWE)*, Jun. 2015.
- [80] Z. Chen, Y. Han, Y. Luo, and X. Hua, "Identification of aerodynamic parameters for eccentric bridge section model", *Journal of Wind Engineering and Industrial Aerodynamics*, vol. 98, no. 4–5, pp. 202–214, 2010. DOI: <http://dx.doi.org/10.1016/j.jweia.2009.10.016>.
- [81] P. Sarkar, N. Jones, and R. Scanlan, "Identification of aeroelastic parameters of flexible bridges", *Journal of Engineering Mechanics*, vol. 120, no. 8, pp. 1718–1742, 1994. DOI: 10.1061/(ASCE)0733-9399(1994)120:8(1718). eprint: [http://dx.doi.org/10.1061/\(ASCE\)0733-9399\(1994\)120:8\(1718\)](http://dx.doi.org/10.1061/(ASCE)0733-9399(1994)120:8(1718)).
- [82] R. Scanlan and R. Rosenbaum, *Introduction to the study of aircraft vibration and flutter*. Dover Publications, 1951.
- [83] T. Theodorsen and I. E. Garrick, "Nonstationary flow about a wing-aileron-tab combination including aerodynamic balance", *NACA Tech. Rep. no. 736*, 1942.

-
- [84] C. Dyrbye and S. Hansen, *Wind Loads on Structures*. Wiley, 1997.
- [85] A. Selberg, "Oscillation and aerodynamic stability of suspension bridges", *Acta Polytechnica Scandinavica Civil Engineering and Building Construction Series*, vol. 13, 1961.
- [86] X. Chen and A. Kareem, "Revisiting multimode coupled bridge flutter: some new insights", *Journal of Engineering Mechanics*, vol. 132, no. 10, pp. 1115–1123, 2006. DOI: 10.1061/(ASCE)0733-9399(2006)132:10(1115).
- [87] Y. Nakamura, "An analysis of binary flutter of bridge deck sections", *Journal of Sound and Vibration*, vol. 57, no. 4, pp. 471–482, 1978. DOI: [http://dx.doi.org/10.1016/0022-460X\(78\)90539-4](http://dx.doi.org/10.1016/0022-460X(78)90539-4).
- [88] G. Bartoli and C. Mannini, "A simplified approach to bridge deck flutter", *Journal of Wind Engineering and Industrial Aerodynamics*, vol. 96, no. 2, pp. 229–256, 2008. DOI: <http://dx.doi.org/10.1016/j.jweia.2007.06.001>.
- [89] G. Bartoli and M. Righi, "Flutter mechanism for rectangular prisms in smooth and turbulent flow", *Journal of Wind Engineering and Industrial Aerodynamics*, vol. 94, no. 5, pp. 275–291, 2006. DOI: <http://dx.doi.org/10.1016/j.jweia.2006.01.014>.
- [90] C. Mannini, "Flutter vulnerability assessment of flexible bridges", PhD thesis, University of Florence, 2006.
- [91] J. N. Juang and R. S. Pappa, "An eigensystem realization algorithm for modal parameter identification and model reduction", *Journal of Guidance, Control, and Dynamics*, vol. 8, no. 5, pp. 620–627, 1985.
- [92] P. Sarkar, *New Identification Methods Applied to the Response of Flexible Bridges to Wind*. Johns Hopkins University, 1992.
- [93] L. Ljung, *System Identification: Theory for the User*, ser. Prentice Hall information and system sciences series. Prentice Hall PTR, 1999.
- [94] M. Verhaegen, "Special issue on statistical signal processing and control identification of the deterministic part of mimo state space models given in innovations form from input-output data", *Automatica*, vol. 30, no. 1, pp. 61–74, 1994. DOI: [http://dx.doi.org/10.1016/0005-1098\(94\)90229-1](http://dx.doi.org/10.1016/0005-1098(94)90229-1).
- [95] W. E. Larimore, "Canonical variate analysis in identification, filtering, and adaptive control", in *Decision and Control, 1990., Proceedings of the 29th IEEE Conference on*, Dec. 1990, 596–604 vol.2. DOI: 10.1109/CDC.1990.203665.
- [96] G. C. Goodwin, S. F. Graebe, and M. E. Salgado, *Control System Design*, 1st. Upper Saddle River, NJ, USA: Prentice Hall PTR, 2000.



Curriculum Vitae

Maria Boberg

Education

2010-2016	PhD in Robotics, Control, and Intelligent Systems <i>Ecole Polytechnique Fédérale de Lausanne (EPFL), Switzerland</i>
2004-2009	MS in Mechatronics <i>Royal Institute of Technology (KTH), Stockholm, Sweden</i>
2001-2003	Gymnasium degree in the Natural Sciences program. <i>Höglandskolan, Bromma, Sweden</i>

Experience

2009-2010	Research Assistant <i>Ecole Polytechnique Fédérale de Lausanne (EPFL)</i>
2009	Student Intern <i>Scania AB, Södertälje, Sweden</i>
2008	Teaching Assistant <i>Royal Institute of Technology (KTH), Stockholm, Sweden</i>

Publications and Working Papers

1. **M. Boberg**, G. Feltrin, and A. Martinoli, “Model and control of a flap system mitigating wind impact on structures”, in *Robotics and Automation (ICRA), 2014 IEEE International Conference on*, May 2014, pp. 264–269. DOI: 10.1109/ICRA.2014.6906620.
2. **M. Boberg**, G. Feltrin, and A. Martinoli, “A novel bridge section model endowed with actively

controlled flap arrays mitigating wind impact”, in *Robotics and Automation (ICRA), 2015 IEEE International Conference on*, May 2015, pp. 1837–1842. DOI: 10.1109/ICRA.2015.7139437.

3. **M. Boberg**, G. Feltrin, and A. Martinoli, “Experimental validation of the wing-aileron-tab combination applied to an actively controlled bridge section model”, in *14th International Conference on Wind Engineering (ICWE)*, Jun. 2015.
4. **M. Boberg**, G. Feltrin, and A. Martinoli, “Flutter suppression of a bridge section model endowed with actively controlled flap arrays”, in *Intelligent Robots and Systems (IROS), 2015 IEEE/RSJ International Conference on*, Sep. 2015, pp. 5936–5941. DOI: 10.1109/IROS.2015.7354221.
5. **M. Boberg**, G. Feltrin, and A. Martinoli, “An analytical and experimental investigation of an actively controlled bridge section model”, *Journal of Wind Engineering and Industrial Aerodynamics*, in preparation.

Project Supervision

1. Tiago Morais, Semester Project (2014)
System Identification and Calibration of an Active Bridge Deck Section Model
2. Vincent MAZOYER, Semester Project (2012)
Control of Active Flap in Wind Tunnel
3. Nicolò VALIGI, Summer Internship (2011)
Wind Profiling and Pressure Distribution for an Airfoil Model in a Wind Tunnel

Languages

Swedish	native
English	fluent
French	proficient

Personal Details

Date of birth:	23 July 1984
Place of birth:	Stockholm, Sweden
Citizenship:	Sweden

